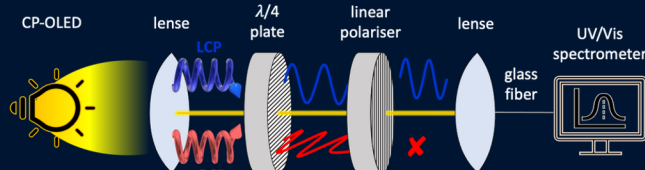
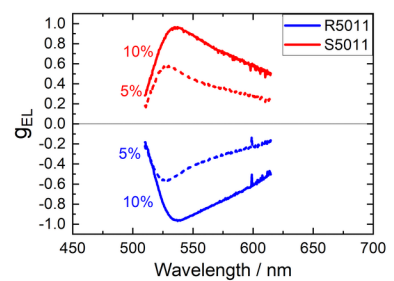
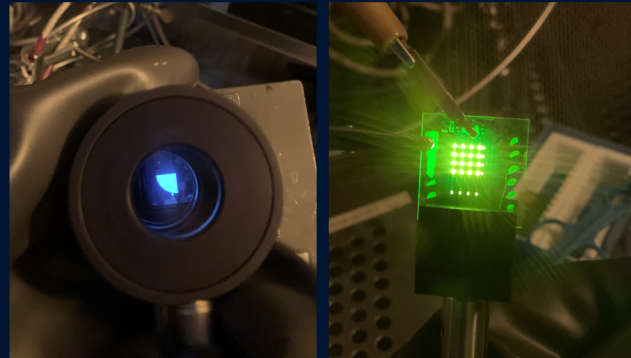
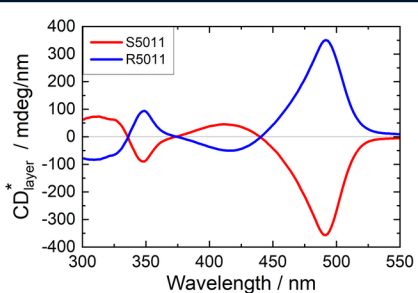


Optimisation and Analysis of a Circularly Polarised Organic Light Emitting Diode (CP-OLED)

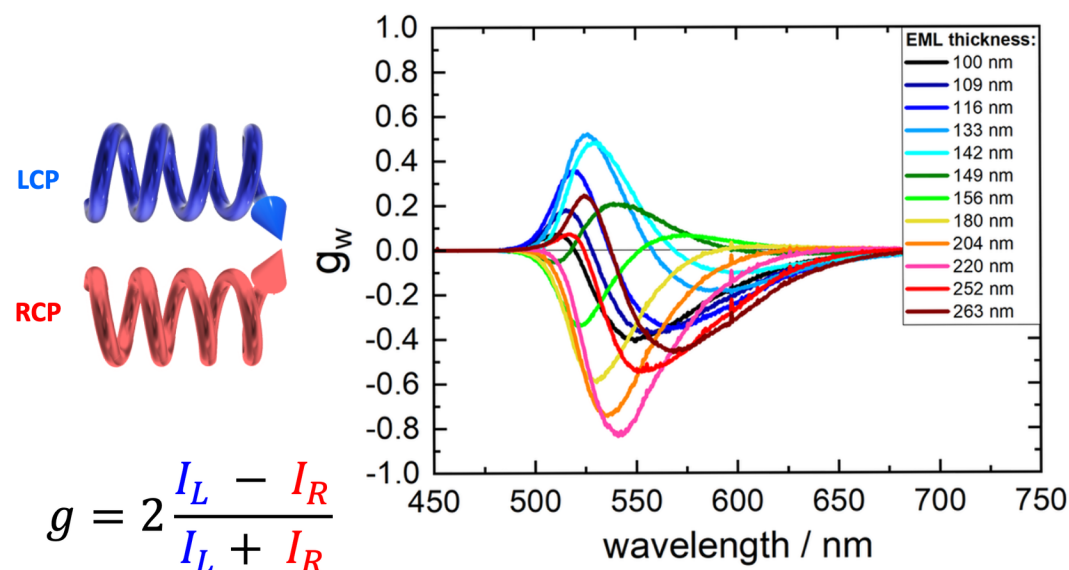
Claudia Dillmann



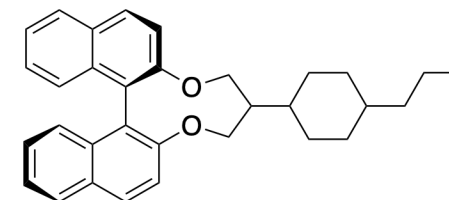
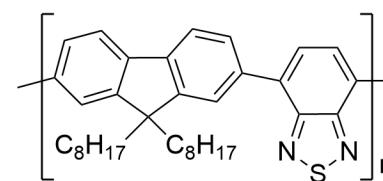
This work introduces strategies to design and characterise circularly polarised organic light emitting diodes (CP-OLEDs).

A suitable measurement set-up is presented to analyse devices from three device categories: intrinsic (**I-CPL**) helicene based emitters, **one component systems** of chirally functionalised polyfluorenes, and **mixed systems** consisting of the achiral emissive polymer F8BT and different non-emissive chiral inducers. Results are quantified via circular dichroism (**CD**) for absorption, and via the dissymmetry factor g for electroluminescence.

To optimise polarisation of the outcoupled light, the influence of different material and device aspects are studied. This includes emissive polymer **molecular weight**, **annealing** procedures, layer **thickness** and chiral inducer **concentration**.



$$g = 2 \frac{I_L - I_R}{I_L + I_R}$$





Optimisation and Analysis of a Circularly Polarised Organic Light Emitting Diode (CP-OLED)

Inaugural-Dissertation

zur

Erlangung des Doktorgrades

der Mathematisch-Naturwissenschaftliche Fakultät

der Universität zu Köln

vorgelegt von

Claudia Dillmann

aus

Nürtingen

Köln, März 2023

Berichtersteller:

Prof. Dr. Klaus Meerholz

Prof. Dr. Arne Lützen

Tag der mündlichen Prüfung: 07.06.2023

Die experimentellen Untersuchungen für die vorliegende Arbeit wurden von März 2019 bis Oktober 2022 in der Physikalischen Chemie der Universität zu Köln unter der Anleitung von Prof. Dr. Klaus Meerholz angefertigt.

Abstract

Because of their excellent properties and low energy requirement, organic light emitting diodes (OLEDs) are commonly used in display applications. Improvements and new concepts are widely studied, scientifically as well as commercially. This advancement has brought forward novel, innovative technologies like bendable or transparent displays, as well as increased efficiency and stability of established devices. Nevertheless, due to their amorphous nature, regular OLEDs only emit unpolarised light.

In this thesis, the development of a highly functional circularly polarised OLED (CP-OLED) is pursued, characterised by both, excellent device performance and large circular polarisation (CP) effects. To quantify these effects, a measurement set-up for circularly polarised electroluminescence (CP-EL) is assembled, and different ways to evaluate and present this data are developed. For best expressiveness and comparability, the g value at the wavelength of the EL spectrum maximum ($g@maxEL$) is reported here.

As chosen CP-OLED systems, devices from three categories are analysed:

1. **I-CPL emitters**
2. **one component systems**
3. **mixed systems**

With the exception of intrinsic CPL approaches, all systems require thermal annealing to produce a chiral liquid crystalline phase, which is responsible for later CPL emission. For this, ideal curing conditions are developed for each system. All materials were evaluated in thin film as well as in OLED devices.

Firstly, two helicene based molecules, **H1-Me₂** and **ThiahelalkBZT**, are utilized as potential intrinsic CPL emitters. As expected from calculations and similar materials in literature, no measurable CP-effect is found. Additionally, both

molecules are tested as chiral inducers within an F8BT matrix. As such, they achieve g_{maxEL} values of up to 0.42 and 0.41, respectively.

Secondly, multiple chirally functionalised polyfluorenes (PFs) are analysed as one component CP-OLED systems. Both, homo- and co-polymers are compared. To minimize complexity, CP-OLEDs are also built in a cavity system, thereby reducing the number of emission peaks. The disruptive influence of keto-defects within the chirally functionalised polymer is explained. Based on the position of the chiral centre, an odd-even-effect resulting in opposite handedness for circular dichroism (CD) and g_{EL} curves is found. Over all, g_{maxEL} values of up to -0.55 are measured with chiral side chain functionalised PFs.

Thirdly, an F8BT based mixed CPL system is analysed in depth. The opposite CP-effect of both chiral inducer enantiomers, R5011 and S5011, is demonstrated. As was done for all polymer based systems, ideal curing conditions to achieve maximum CP-effects are developed. Supported by DSC measurements, required curing times and temperatures increase with increasing molecular weight of the polymer. Best CD and g_{EL} values are found for a M_w of 7 - 21 kg/mol. The result of thickness variations of different layers within this stack are explained and strategies to reduce cathode reflections leading to optical interference are proposed. The influence of the chiral inducer concentration is analysed. It is demonstrated that using different enantiomeric excess (*e.e.*) ratios of both chiral inducer enantiomers with a constant combined chiral inducer concentration produces more comparable results than changing the chiral inducer concentration directly. CP-effects of a specific effective chiral inducer enantiomer concentration are equivalent to the same chiral inducer concentration with only one enantiomer used. Over all, g_{maxEL} values of up to -1.12 are found with F8BT + R5011 mixed systems.

Table of Contents

Table of Contents	iv
1 Aims and concept	1
1.1 Introduction	2
1.2 Concept	5
2 Theory	7
2.1 Photophysical properties	8
2.1.1 Photoluminescence	9
2.1.2 Electroluminescence	11
2.2 Organic light emitting diodes (OLEDs)	13
2.2.1 OLED basic processes	13
2.2.2 OLED generations and emitter development	16
2.2.3 OLED architecture and design	21
2.2.4 Deposition methods	22
2.2.5 Cross-linking	23
2.3 Polymeric OLED materials	26
2.3.1 Polyfluorenes (PF)	28
2.3.2 Poly(dioctylfluorene-co-benzothiadiazole) (F8BT)	31
2.4 Polarised light	32
2.4.1 Polarisation effects	34
2.4.2 Optical interference	35
2.4.3 Transfer-matrix model	39
2.4.4 Ellipsometry	42
2.4.5 Müller Matrix ellipsometry	43
2.5 Chirality	46
2.6 Polarised OLEDs	48
2.6.1 Linearly Polarised OLEDs	48
2.6.2 Circularly Polarised OLEDs	51
2.6.3 Intrinsic CPL (I-CPL)	52

Table of Contents

2.6.4	Extrinsic CPL (E-CPL)	55
2.6.5	Development of CP-OLEDs	59
2.6.6	Applications of CP-OLEDs	63
3	Results and Discussion	67
3.1	Measurement set-up for CP-OLEDs	68
3.1.1	Measurement set-up and procedure	68
3.1.2	Typical data	71
3.1.3	CP-EL Artefacts	76
3.1.4	Possibilities and limitations of CD measurements	79
3.2	Polymeric emitters in thin film and OLED	82
3.2.1	PF thin films	82
3.2.2	F8BT thin films	85
3.2.3	PF OLEDs	86
3.2.4	F8BT OLEDs	91
3.3	F8BT molecular weight	103
3.4	Thermal annealing of F8BT thin films	107
3.4.1	F8BT thin film volume reduction	107
3.4.2	F8BT surface roughness	109
3.4.3	F8BT aggregation	112
3.4.4	F8BT curing temperature	116
3.4.5	F8BT annealing conclusion	125
3.5	CP-OLED strategies	127
3.6	Chiral small molecules as CPL-emitters	128
3.6.1	H1-Me ₂	129
3.6.2	ThiahelalkBZT	131
3.7	One component systems	133
3.7.1	BINOL functionalised polyfluorenes	134
3.7.2	Polyfluorenes with chiral side chains	138
3.7.3	Cavity CP-OLEDs	148
3.7.4	Oxidation of chirally functionalised PFs	151
3.7.5	Odd-Even-Effect	156
3.7.6	Chirally functionalised homo- vs. co-polymers	160

3.7.7 Chirally functionalised F8BT	166
3.8 Mixed systems	175
3.8.1 Chiral inducers for E-CPL mixed systems	176
3.8.2 F8BT + R5011 operating voltage	181
3.9 Thermal annealing of F8BT + R5011 thin films	182
3.9.1 F8BT + R5011 thin film volume reduction	183
3.9.2 F8BT + R5011 curing temperature	185
3.10 F8BT + R5011 layer thickness variation	190
3.10.1 HTL thickness variation	190
3.10.2 EML thickness variation	194
3.10.3 ETL thickness variation	200
3.11 F8BT + R5011 molecular weight	203
3.12 F8BT + R5011 chiral inducer concentration	206
3.12.1 F8BT + R5011 total chiral inducer concentration	208
3.12.2 F8BT + R5011 chiral inducer <i>e.e.</i>	215
4 Conclusion and perspectives	227
4.1 Summary and Conclusion	228
4.2 Perspectives	232
5 Experimental Section	237
5.1 General Procedures	238
5.1.1 Substrates	238
5.1.2 Materials	238
5.1.3 Spin-coating of organic materials	238
5.1.4 PEDOT:PSS deposition	239
5.1.5 Cross-linking	239
5.1.6 Alignment layer preparation	239
5.1.7 Vacuum deposition	240
5.2 Analytical Methods	240
5.2.1 UV/Vis spectroscopy (UV/Vis)	240
5.2.2 Photoluminescence spectroscopy (PL)	241
5.2.3 Photoluminescence quantum yield (PLQY)	241

Table of Contents

5.2.4 Profilometry	241
5.2.5 Ellipsometry	241
5.2.6 Electric characterization (LIV) and electroluminescence (EL) of OLEDs	242
5.2.7 Electroluminescence (EL) and polarised electroluminescence	242
5.2.8 Microscopy	243
5.2.9 Differential scanning calorimetry (DSC)	243
5.2.10 Gel permeation chromatography (GPC)	244
6 Appendix	245
6.1 Materials	246
Bibliography	255

1 Aims and concept

1.1 Introduction

With the first publication about organic light emitting diodes (**OLEDs**) by Tang and Van Slyke [1], a new scientific field was initiated. Generally, an OLED only requires a single layer of an organic emitter material between two electrodes. However, through the addition of multiple supporting layers, device performance and efficiency can be increased significantly. For this reason, all modern OLEDs consist of multi-layer stacks of precisely matched materials.

Early OLED systems relied solely on fluorescence as origin for emission. In electroluminescence, however, spin statistics restricts the amount of singlet excitons required for fluorescence to only 25 %. To bypass the severely limited maximum achievable internal quantum yield, later OLED generations also utilised the generated triplet excitons. This was achieved by the introduction of phosphorescent emitters, and later thermally activated delayed fluorescence (TADF) emitters.

Since then, OLEDs have not only been a topic of interest in science, but found widespread commercial application. A wide variety of high performance materials with different features is already available, and countless more specifications can be implemented through synthesis.

OLED displays established a new benchmark and are, therefore, widely used today in TVs, tablets, mobile phones and microdisplays. They stand out for their excellent quality, even in comparison to the much older and therefore perfected LED technology. OLED displays excel through crisp and sharp colour contrasts and deep blacks thanks to individual access to each pixel instead of using a uniform background lighting panel, as is typically the case in LCD displays. Also, the low energy consumption and high efficiency makes them perfect for display technologies. Because of these benefits, OLEDs have found a permanent spot, especially in high class portable electronics like mobile phones and smart watches.

Besides these typical applications, OLEDs can facilitate new and interesting features. Because of the amorphous nature of the materials, OLEDs can be created

on flexible substrates. This allows for the production of bendable or even rollable displays. Flexible light elements could even be incorporated into clothing. By replacing the typically reflective metallic electrodes with transparent materials, it is also possible to create transparent displays. These extraordinary devices can be used as design elements, for example in interior decoration or show windows.

While OLEDs have only a very small market share in lighting applications today, they have the potential to be used as high quality light panels, since organic emitter materials with broad emission spectra generate warm, natural light.

A common aspect for all OLEDs, however, is the polarisation state of their emission. Most organic materials used in OLEDs are amorphous, which means the chromophores are randomly oriented. This leads to an over all unpolarised emission. By incorporating an element of order, however, it is possible to directly generate polarised emission.

In 1995, Inganäs *et al.* published an early example of a linearly polarised OLED. By stretch-orienting their emitter polymer, they achieved an intensity ratio of 2.4:1 between the electroluminescence measured parallel and perpendicular to the orientation direction [2].

Through incorporation of a chiral element, it is even possible to achieve direct emission of circularly polarised light. In 1997, Meijer *et al.* reported the first example of a partially circularly polarised OLED (CP-OLED) [3]. Since then, several such examples have been published with various methods. The most obvious approach to generate CP-OLEDs is using a chiral chromophore. However, while several different chiral emitters have been reported, they typically only exhibit very small CP-effects, or poor OLED device performance. Much better results have been achieved by generating a chiral phase in emissive polymers. This can be done by chiral functionalisation of the polymer, or by adding a chiral inducer. The best result of a CP-OLED with good device performance achieved a g_{EL} of 1.13, which represents the presence of 78 % of the dominant handedness [4].

1 Aims and concept

Current OLED research mostly addresses two main areas. On one hand, already existing concepts are improved. This is done by enhancing systems, or creating new materials and techniques. Studied topics include increased efficiency, improved device architectures for light outcoupling, and variation of emission features. On the other hand, new application concepts are created.

The CP-OLEDs investigated in this work can contribute to both areas. In displays with anti-glare filters, they can significantly increase the outcoupling efficiency, which is especially valuable for portable devices with a limited power source. As a novel application, CP-OLEDs could provide the next generation of 3D displays. They could combine all the previously mentioned benefits of OLEDs with stunning 3D technology, replacing current bulky and poorly performing 3D technologies.

1.2 Concept

The aim of this work is the fabrication and characterisation of CP-OLEDs.

A suitable OLED stack architecture needs to be chosen. This includes the choice of material for supporting layers and matrix materials, as well as their layer thicknesses. For all systems, ideal preparation conditions are to be found, consisting of curing times and temperatures. Other strategies, like the implementation of alignment layers (ALs) or solvent vapour annealing (SVA) treatment, are investigated. As an indicator for chiral environments, circular dichroism (CD) curves can be calculated from *Müller Matrix* (MM) ellipsometry measurements.

To quantify circularly polarised (CP) effects, a measurement set-up for polarised electroluminescence needs to be constructed. Appropriate sample measurement and data evaluation procedures have to be developed.

Three distinct systems will be investigated and their usability as materials for CP-OLEDs is to be evaluated:

1. Intrinsic CPL emission from chiral molecules.

The two helicene based molecules **H1-Me₂** and **ThiahelalkBZT** are examined as potential I-CPL emitters embedded in a PVK matrix. Additionally, their functionality as non-emissive chiral inducers within an F8BT matrix is to be compared.

2. Extrinsic CPL emission from chirally functionalised polymers (one component systems).

Different chirally functionalised polyfluorenes (PFs) are compared, representing homo- or co-polymers. The alkyl side chains differ in length and the position of the chiral centre. The influence of the polymer molecular weight is to be estimated. The disruptive effect of keto-defects within such polymers is to be evaluated.

3. Extrinsic CPL emission from a mix of achiral emissive polymer and non-emissive chiral inducer (mixed systems).

As an example for a mixed system, the emissive polymer F8BT with the chiral inducer R5011 is to be studied. The influence of different system variations is to be explored. This includes the CPL performance of different F8BT batches with various molecular weights, as well as different chiral inducer concentrations.

2 Theory

2.1 Photophysical properties

Many organic molecules with a large conjugated π -system can display photoluminescence (PL), which is the emission of light upon relaxation of an excited state. For emitted light in the visible spectrum, a band gap ΔE_{H-L} of 1.7 eV to 3.0 eV between the highest occupied molecular orbital (HOMO) and the lowest unoccupied molecular orbital (LUMO) is necessary [5]. While many different forms of luminescence are possible, this work focuses on the two types PL and electroluminescence (EL).

The possible radiative (coloured arrows) and non-radiative (wavy arrows) transitions between different energetic levels are best illustrated with a *Jablonski* diagram. The electronic (thick lines) and vibrational (thin lines) energy levels shown in fig. 2.1 are superimposed to focus only on the transitions. A more accurate representation of this diagram based on the *Morse*-potential is given in chapter 2.1.1.

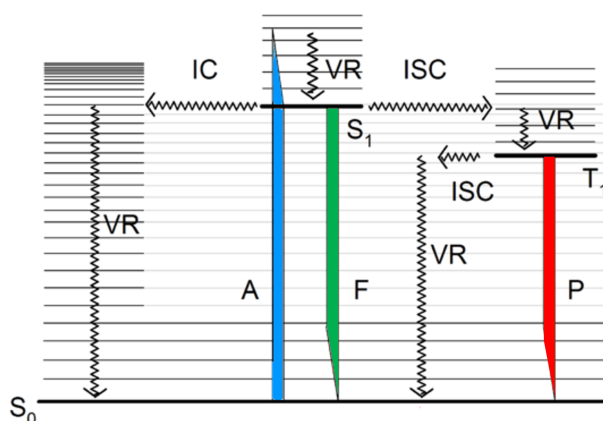


Fig. 2.1: Optical excitation and light emission in organic semiconductors. The *Jablonski* diagram depicts the ground state S_0 as well as a singlet excited state (S_1) and triplet excited state (T_1); with A: absorption, F: fluorescence, P: phosphorescence, VR: vibronic relaxation, IC: internal conversion, ISC: intersystem-crossing. Based on a model from [6].

Here, the excited species is generated through optical excitation. After absorption (A, blue arrow) of light with sufficient energy, an exciton is formed. Several transitions can occur from there, which also apply to excitons created through

other processes, for example electrical excitation. Vibronic relaxation (VR, vertical wavy arrow) represents a non-emissive deactivation process. The transition between a singlet and triplet state is called intersystem crossing (ISC, horizontal wavy arrow). A horizontal transition between two states of the same multiplicity is called internal conversion (IC, horizontal wavy arrow). As emissive deactivation processes, fluorescence (F, green arrow) or phosphorescence (P, red arrow) are possible. The sequence and conditions for each pathway are explained in chapter [2.1.1](#).

2.1.1 Photoluminescence

If a material is excited optically, for example through irradiation with a light source, the deactivation process is called [PL](#). Depending on the excitation light wavelength, absorption (A) from a singlet ground state S_0 to a singlet excited state S_1 occurs. In accordance with the *Franck-Condon* principle, "vertical" transitions with similar vibrational wavefunctions of ground and excited state are preferred. Therefore, the initial excitation is most likely to occupy a vibronically excited level of an upper electronic state. The empiric *Kasha* rule suggest a subsequent non-radiative vibrational relaxation (VR) into the lowest vibrational level of S_1 . From here, **fluorescence** (F), a radiative transition between two singlet states, can occur. The *Franck-Condon* principle still applies, leading to relaxation into multiple vibrational ground state levels which results in a vibrational microstructure in emission spectra [\[7, 8, 9\]](#).



Fig. [2.2](#) shows the sequence of steps leading to fluorescence. The transitions are analogous to the *Jablosnki* diagram shown in fig. [2.1](#). However, this illustration features *Morse* potential energy curves.

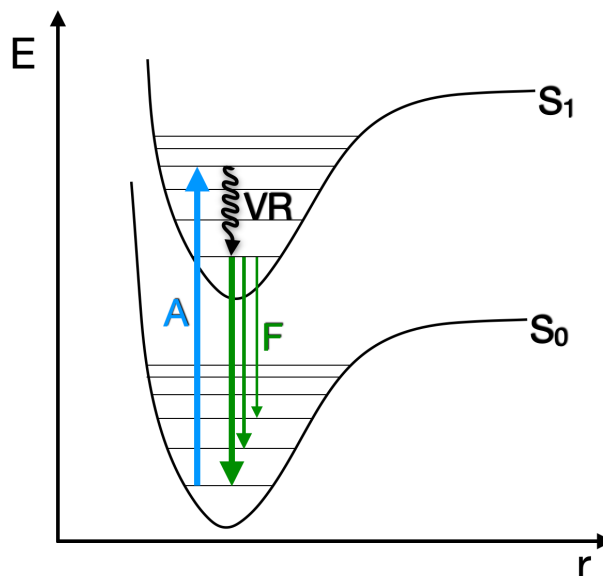


Fig. 2.2: Sequence of steps leading to fluorescence. After absorption (A, blue arrow) from the ground state S_0 , vibronic relaxation (VR) into the lowest vibronic level of S_1 occurs. From here, fluorescence (F, green arrow) back into S_0 can follow. Morse potential curves show potential energy levels over intermolecular separation r . Based on a model from [8].

From a vibrational ground state of an electronically excited state $S_{n,v=0}$, horizontal transitions into high vibrational levels of a lower electronic state can occur. This transition is called internal conversion (IC) if it occurs between states of the same multiplicity (e.g. singlet to singlet). IC is usually followed by VR, which represents the most unfavourable course if strong light emission is desired.

The horizontal transition between a singlet and triplet state is called intersystem-crossing (ISC) and involves a quantum mechanically "forbidden" spin flip. For nonradiative horizontal transitions, overlapping vibrational levels are beneficial. ISC is favoured by strong spin-orbit coupling, which dissolves the forbidden nature of the transition, and can therefore be promoted by the presence of heavy metal atoms like iridium. The radiative transition from T_1 to S_0 is called **phosphorescence** (P). Since this transition, too, requires a "spin-forbidden" flip, excited triplet states usually display much higher lifetimes than singlet states [10, 11].

Fig. 2.3 shows the sequence of steps leading to phosphorescence.

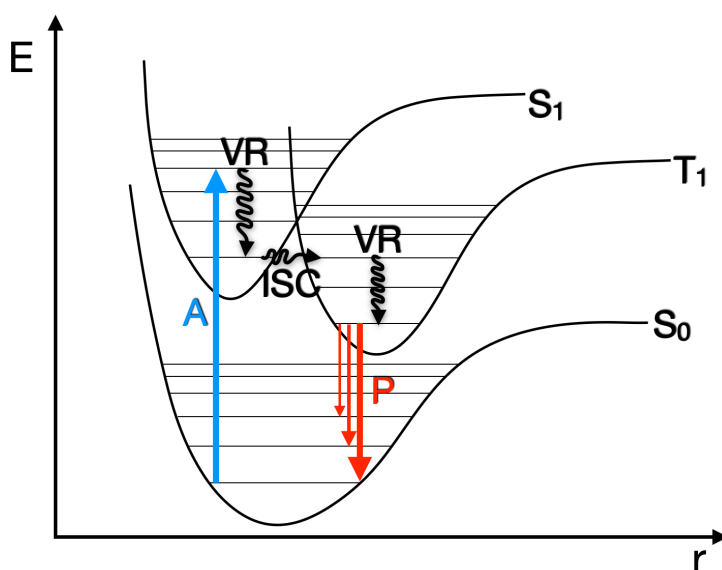


Fig. 2.3: Sequence of steps leading to phosphorescence. After absorption (A, blue arrow) from the ground state S_0 , vibronic relaxation (VR) into the lowest vibronic level of S_1 occurs. The spin "forbidden" intersystem-crossing (ISC) into the triplet T_1 state, as well as a subsequent VR into the lowest vibronic level, follows. From here, phosphorescence (P, red arrow) back into S_0 can occur. Morse potential curves show potential energy levels over intermolecular separation r . Based on a model from [8].

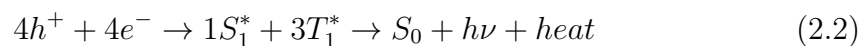
2.1.2 Electroluminescence

For [PL], the molecules are excited directly. Therefore, only one molecule is required to form an exciton. For [EL], multiple molecules are involved in the exciton generation process. Positive (holes, h^+) and negative (electrons, e^-) charge carriers are injected from their respective electrodes, from where they are transported towards the opposite electrode. The exciton (S_1^*) is formed through recombination. A detailed explanation of the basic processes in OLEDs is given in chapter 2.2.1.

This has a direct impact on spin statistics for the multiplicity of the generated excitons. In [PL], the excitation of a singlet ground state will also produce a singlet

2 Theory

excited state. To produce a triplet excited state, a spin "forbidden" ISC would be required. In [EL](#), however, the recombination step of the two opposite charge carriers involves two molecules. Depending on the spin of the hole and electron, the chances to form a singlet or triplet exciton are 25 % and 75 %, respectively [\[12\]](#).



While the number of triplet excitons is typically much higher in [EL](#) than in [PL](#), fluorescence and phosphorescence can occur in both processes. Chapter [2.2.2](#) explains how these processes were utilised in different OLED generations.

2.2 Organic light emitting diodes (OLEDs)

For display applications, OLEDs have already achieved a considerable market share. Advantages of OLED systems include lower power consumption, potentially lower production costs and the possibility to use bendable substrates. While OLED lighting applications are less common, OLED displays for TVs, cellphones or wearables are quite popular today due to their high colour contrast and extremely low black level. As difficulties with stability and lifetime are being conquered, new and exciting technologies like transparent display TVs and flexible display cellphones are moving from the prototype stage on to the market [13, 14, 15, 16, 17, 18].

2.2.1 OLED basic processes

The simplest OLED structure consists of an emissive organic semiconductor between two electrodes. The operation principle of an OLED can be described in four steps:

1. charge carrier **injection**
2. charge **transport**
3. charge **recombination** and exciton formation
4. light **emission** upon exciton decay

These four steps are illustrated in fig. 2.4.

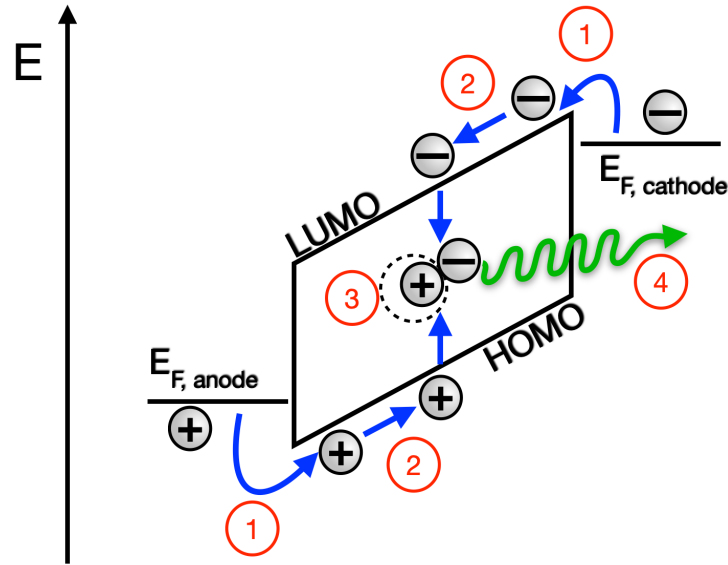


Fig. 2.4: Schematic illustration of the basic processes in a single-layer OLED. Upon applying a sufficient voltage, charge carriers are injected (1). From the anode, holes are injected into the HOMO, and from the cathode, electrons are injected into the LUMO of the organic semiconductor. Charge carriers are transported towards their opposite electrode (2) along the FMOs. Upon recombination (3), an exciton is formed. Through radiative decay of this exciton, light is emitted (4).

Upon applying a voltage at the electrodes, charge carriers can be **injected** into the organic semiconductor. This voltage must be large enough to overcome the injection barrier between the *Fermi* level of the electrodes and the frontier molecular orbitals (FMOs) of the organic material. From the anode, holes are injected into the HOMO, and from the cathode, electrons are injected into the LUMO of the organic material.

In contrast to the discrete energy levels in the valence and conduction band of inorganic semiconductors, the amorphous structure of organic materials leads to a statistical distribution of FMO energy levels. This so called density of energetic states (DOS) shown in fig. 2.5 follows a *Gaussian* distribution [7, 14, 19, 20].

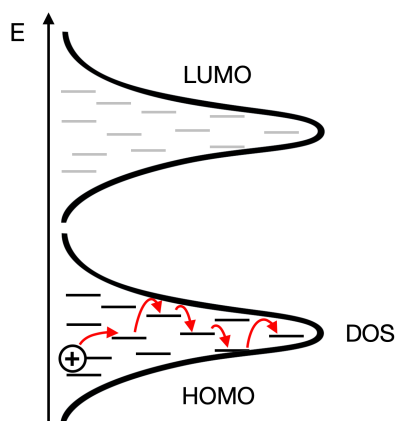


Fig. 2.5: Density of states (DOS) and hopping transport for organic semiconductors. Filled (HOMO) and empty (LUMO) energy levels are indicated in black and grey, respectively.

After injection, charge carriers travel towards the oppositely charged electrode. Charges are delocalised within a conjugated π -system, which can be located within one molecule, or a section of a polymer. This limits their drift length to a molecule or a few nanometers in a polymer chain segment. **Charge transport** can be described as a "hopping" process, where charges jump from one molecule or polymer section to the next.

Within the statistically distributed [DOS](#), individual energy sites can be slightly higher or lower than the average. Each hopping step is a thermally activated process. Deeper local potential energetic barriers are typically called traps. While shallow traps can be overcome by thermal activation, the required energy for deep traps can be too high. This can lead to light emission at a higher wavelength, or even loss of the charge carrier to vibronic relaxation [\[7, 14, 19, 21, 22\]](#).

While opposite charge carriers migrate through the bulk towards their corresponding electrode, *Coulomb* attraction leads to their **recombination** and the formation of an exciton. Spin-statistics state that the ratio of singlet to triplet excitons is 1:3 [\[7, 23\]](#). Possible radiative and non-radiative pathways for excitons are analogous to the processes described in chapter [2.1](#).

Radiative decay of those excitons and subsequent **emission** of light is called **EL**. Depending on whether the emission originated from a singlet or triplet exciton, fluorescence or phosphorescence can occur. The wavelength of the emitted photon is determined by the difference of energetic levels. While not desirable, non-radiative relaxation is also a possible pathway, which often accumulates in decaying devices [7, 23].

As stated in the beginning of this chapter, these basic OLED processes can already occur in a single-layer device. However, by introducing additional layers of energetically matching materials, device efficiency can be increased dramatically. Such multi-layer OLEDs are explained in chapter 2.2.3. Different emitter materials also provide individual advantages. An overview of emitter material development and OLED generations is given in chapter 2.2.2.

2.2.2 OLED generations and emitter development

Historically, OLEDs can be categorised in different generations, based on emitter functionality. As the processes on a molecular level have been introduced in previous chapters, this section will focus on the historic evolution of emitter materials.

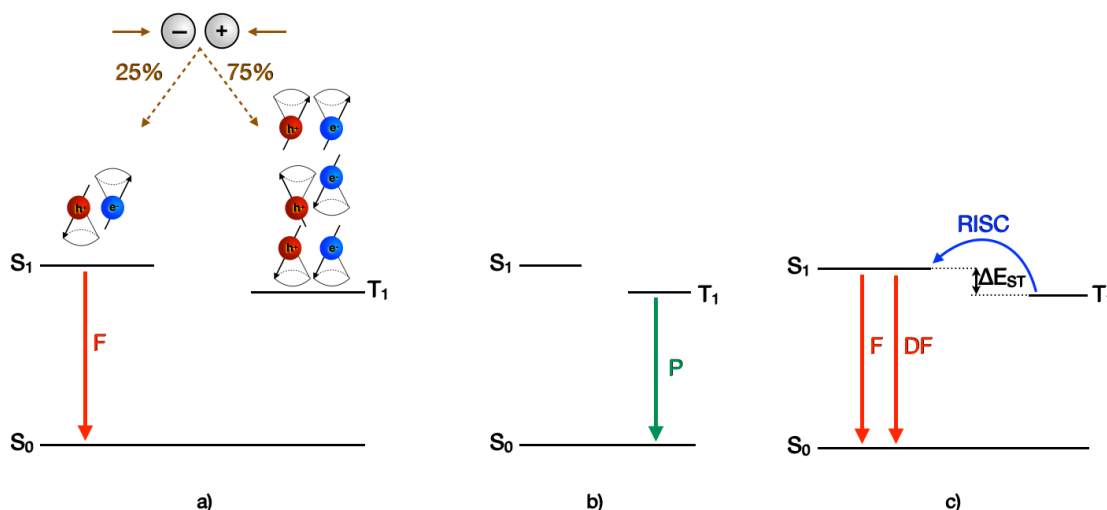


Fig. 2.6: Simplified schematic outline of the emission processes for fluorescence F (a), phosphorescence P (b) and TADF with delayed fluorescence DF (c). Exemplary, the first schematic also includes the spin statistics for electrically generated excitons.

The first generation of OLEDs, introduced by VanSlyke *et al.* in 1987, uses **fluorescence** emitters like 8-hydroxyquinoline aluminium (Alq_3 , fig. 2.7 (a)). A simplified schematic of fluorescence emission is shown in fig. 2.6 a). This model also illustrates the spin statistics of electrically generated excitons. Fluorescent OLED systems often employ organic dyes which are relatively easy to synthesise and can be found in all colours. However, spin statistics dictates that the ratio of singlet to triplet excitons generated in an OLED are 25% to 75%. Since radiative decay of triplet states is spin-forbidden in fluorescence emitters, 75% of generated excitons will be "lost" to vibronic relaxation, thereby limiting the maximum internal quantum efficiency (IQE) to 25% [13, 24, 25].

To increase OLED efficiency, it was indispensable to achieve an IQE of 100%. The second generation of OLEDs therefore utilises **phosphorescence** to access the remaining 75% for light generation. The schematic of phosphorescence emission is shown in fig. 2.6 (b). A prominent example for phosphorescent emitters is *fac*- $\text{Ir}(\text{ppy})_3$ (fig. 2.7 (b)) [26, 27, 28]. To increase spin-orbit coupling, incorporation for heavy metal atoms like platinum or iridium is required in phosphorescent emit-

2 Theory

ters. Additionally, phosphorescence emitters typically exhibit broader EL spectra, which makes them less suitable for display applications.

Third generation OLEDs utilise both, singlet and triplet excitons, without requiring heavy metals through **thermally activated delayed fluorescence (TADF)**. The schematic of TADF emission is shown in fig. 2.6 (c). Like in the widely known sky-blue emitter DMAC-DPS (fig. 2.7 (c)), a small singlet-triplet energy splitting (ΔE_{ST}) facilitates efficient reverse intersystem crossing (RISC) from T_1 to S_1 at room temperature. This way, all triplet excitons can potentially contribute through delayed fluorescence [10, 26, 29, 30].

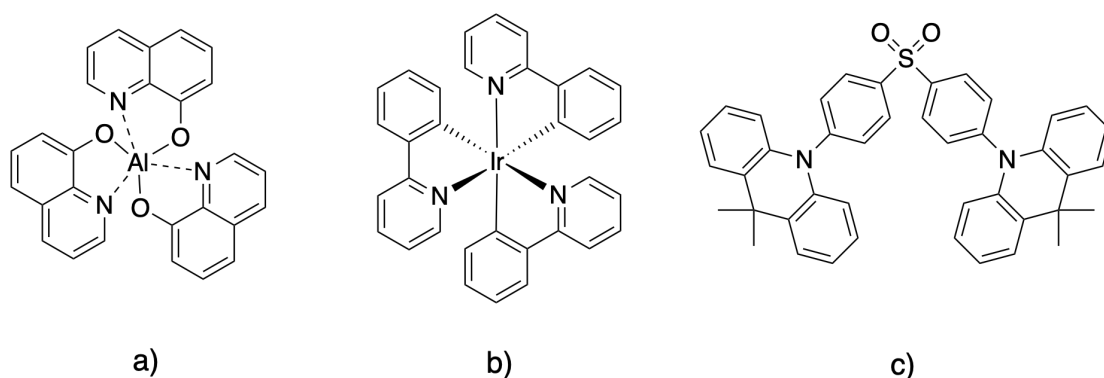


Fig. 2.7: Structures of the fluorescent emitter Alq₃ (a), the phosphorescent emitter *fac*-Ir(ppy)₃ (b) and the TADF emitter DMAC-DPS (c).

While **TADF** is an established and popular approach, the complicated molecular design process and a tendency for short device lifetimes give room for improvement. For the next generation of OLEDs, high efficiencies, long lifetimes and good colour purity need to be achieved. While no fourth generation process has yet been established, several sophisticated cascade energy transfer systems have been proposed.

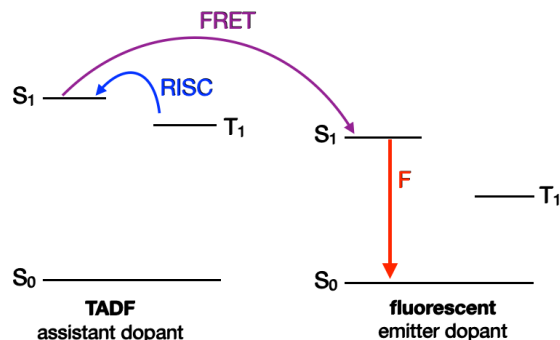


Fig. 2.8: Simplified schematic outline of the emission process for hyperfluorescence. A non-emissive host is mixed with a TADF-based assistant dopant, from which an efficient FRET onto a fluorescent emitter dopant is achieved.

Adachi *et al.* showed examples of **hyperfluorescence** OLEDs with different emission colours. The EML is based on a typical non-emissive host material and two dopants. Electrically generated excitons are passed onto a TADF-based assistant dopant (typically 1 wt%), which can upconvert the triplet into singlet excitons via **RISC**. From there, a Förster resonance energy transfer (**FRET**) into the S^1 of the fluorescent emitter dopant (typically 25 - 50 wt%) occurs. From here, the regular fluorescence pathway for light emission follows. This method combines all advantages of first generation fluorescence emitters with third generation **TADF** emitters. Depending on the emission colour, maximum external quantum efficiencies up to 18 % are reported, which is almost a one order of magnitude increase compared to devices without the TADF assistant dopant [26, 28, 31].

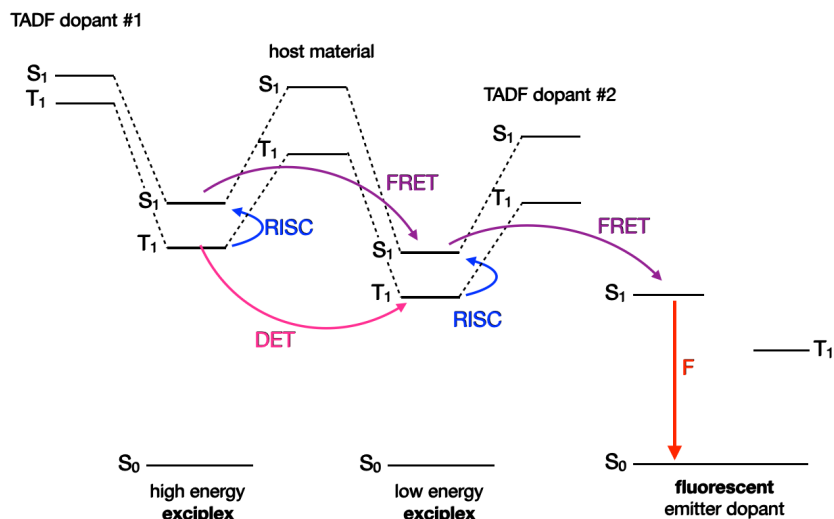


Fig. 2.9: Simplified schematic outline of the emission process for cascade singlet-harvesting (CSH). Two TADF-based molecules form a high energy and a low energy exciplex with the host material. DET can occur between the triplet states of the exciplexes. An efficient FRET from the high energy exciplex onto the low energy exciplex and onto a fluorescent emitter dopant is achieved.

A system shown by Lee *et al.* follows a similar strategy, but additionally incorporates a second TADF-based assistant dopant. The concept is called **cascade singlet-harvesting (CSH)** and utilises a so called singlet exciton harvesting matrix, consisting of two TADF molecules, which form a high energy and low energy exciplex with the non-emissive host material, respectively. A **FRET** cascade from the high energy exciplex S_1 into the low energy exciplex S_1 and subsequently into the fluorescent emitter S_1 , followed by fluorescent emission, occurs. Additionally, a Dexter energy transfer (DET) can occur from the high energy exciplex T_1 onto the low energy exciplex T_1 . Since both exciplexes are based on TADF technology, triplet excitons can be upconverted into singlet excitons. This way, no significant losses due to unfavourable Dexter-type energy transfers into the fluorescent emitter T_1 are suffered. With this strategy, an external quantum efficiency up to 19.9 % is reported, compared to 10.4 % for the same system with only one exciplex [28, 32].

2.2.3 OLED architecture and design

As described in chapter 2.1.2, electrons and holes are injected into an OLED. Those charges are transported along the energetic HOMO and LUMO DOS of the organic semiconductor materials and recombine to form excitons, which, upon relaxation, emit light. In this chapter, OLED device architecture shall be discussed on an application based level.

Generally, an OLED consists of at least one semiconducting, electroluminescent material, sandwiched between two electrodes. But single-layer OLEDs usually perform poorly due to large injection barriers and charge carrier imbalance.

To optimise device performance, a multi-layer architecture should be designed. Thereby, materials and their respective layer thicknesses are chosen depending on their energetic HOMO and LUMO levels, their charge transport properties and optical aspects like the interference pattern of light in forward direction and light reflected from the cathode (see chapter 3.2.4). This way, an ideal position of the recombination zone can be achieved, which maximises emission and reduces negative effects like luminance quenching.

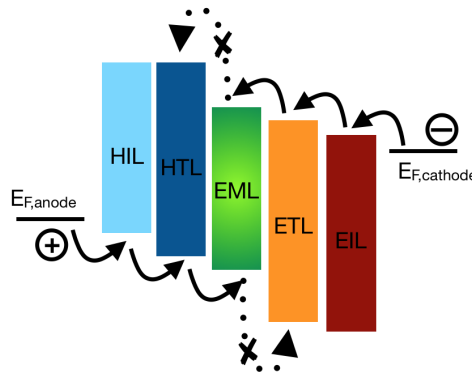


Fig. 2.10: Schematic energy diagram of a multi-layer OLED. 1) charge carrier injection 2) charge transport 3) recombination to an exciton 4) exciton degradation and emission of light. Crossed out arrows represent energetic barriers of blocking layers.

Fig. 2.10 shows a stylised multi-layer OLED stack. In addition to the emissive layer (EML), it features hole- and electron-injection layers (light blue and red) as well as -transport layers (dark blue and orange). On the anode side, HOMO energy levels of hole-injection layer (HIL) and hole-transport layer (HTL) divide the hole injection barrier from anode to EML into two smaller steps which can be

overcome easier. At the same time, the **HTL** functions as electron blocking layer. It has a significantly higher LUMO energy level than the **EML**, which prevents electrons from moving beyond the **EML**, thereby maximising charge carrier concentration within the **EML** and subsequently increasing recombination probability. Analogously on the cathode side, the same effects take place with the LUMO as base energy level [7].

2.2.4 Deposition methods

One of the main benefits of OLEDs is that the devices work with very thin layers and therefore only require very small amounts of the organic semiconducting materials. To produce highly efficient multi-layer OLEDs, it is necessary to apply subsequent layers of different materials without removing or intermixing with the previously deposited layers. This can be achieved either in a vacuum deposition process, e.g. physical vapour deposition (PVD), or in a solution based process, e.g. spin-coating or offset and ink-jet printing.

Vacuum deposition uses low pressure chambers that scale to the substrate size and require large quantities of energy and time to evaporate material into the gas phase. Despite its high cost, vacuum deposition is the most common process in OLED fabrication today. PVD allows a precise layer thickness control and very high material purity since it can be considered as an additional purification step. This has a positive influence on device performance and lifetime, which makes it so popular.

While deposition of organic layers can easily be done solution based, application of the metal cathode always requires vacuum deposition.

Solution based deposition methods are an attractive alternative because they are fast and significantly cheaper. They allow the use of materials that cannot be evaporated, like polymers, since thermal degradation poses no problem. In laboratories, spin-coating is the most commonly used solution based method. Here, the material solution is deposited onto a substrate. Through rotation, excess material

is spun off the substrate and the residue layer dries. Layer thickness can be varied through rotation speed and solution concentration.

For multi-layer stacks, precautions have to be made to prevent intermixing or dissolving of previously applied layers during the next solution based deposition step. This challenge can be overcome either by an orthogonal solvent approach, or by making the layers insoluble [33, 34].

2.2.5 Cross-linking

One method to make layers insoluble is cross-linking. This can be achieved by functionalising the active materials, for example the triphenylamine (TPA) derivatives QUPD and OTPD (for chemical structures, see chapter 6.1) used here as hole-transport materials (HTMs), with active groups like oxetanes. Cross-linking proceeds by photoinitiated cationic ring-opening polymerization (CROP), as illustrated in fig. 2.11. By increasing the number of oxetane functionalities per molecule, an even denser and more interconnected network can be created, thereby ensuring layer insolubility and reducing intermixing with subsequent layers. Separating the oxetane functionality from the core molecule through an alkyl chain reduces shrinkage in the cross-linked layer and thereby prevents problems like cracking or delamination.

2 Theory

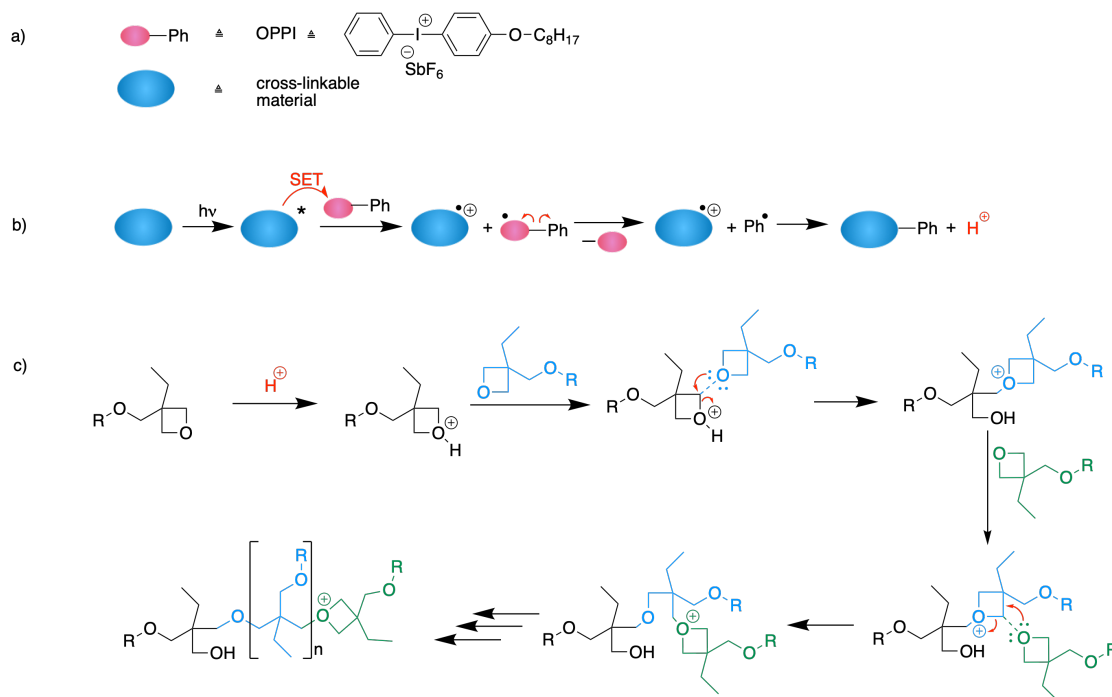


Fig. 2.11: (a) Chemical structure of the photo acid OPPI and schematic illustration of a cross-linkable material; (b) Photoinduced reaction mechanism to generate the proton necessary to initiate a CROP reaction; (c) CROP mechanism for the cross-linking of an oxetane-functionalised **HTM**.

To initialise the **CROP** process, small quantities the photo acid (4-octyloxyphenyl) phenyliodonium hexafluoroantimonate (**OPPI**) (fig. 2.11) (a) are added to the **HTM** solution.

To activate the reaction (fig. 2.11) (b), a free proton is required, which is produced photochemically through illumination with UV light. For the here used triphenylamine (TPA) based **HTMs**, this means irradiation at 365 nm. Alternatively, to cross-link molecules without an extensive π -system, OPPI can be activated directly through irradiation at 315 nm. A photoinduced single electron transfer (SET) from the activated TPD onto the photo acid OPPI occurs, leaving a TPD radical cation. The OPPI radical splits into a phenyl radical and a neutral 4-octyloxyphenyl iodonium hexafluoroantimonate. The phenyl radical undergoes rearomatisation with the TPD radical cation.

2.2 Organic light emitting diodes (OLEDs)

The hereby released proton (red) can now initiate the **CROP** reaction (fig. 2.11 (c)) by activating an oxetane group (black). Through electrophilic attack, this activated oxetane can now react with another oxetane function (blue). The first oxetane ring opens, thereby leaving the second oxetane activated, which is now able to attack a third oxetane function (green), and so on. This way, a 3D polymer network is gradually created. Depending on the number of oxetane functionalities, this network can be more or less interconnected and dense [34, 35, 36].

2.3 Polymeric OLED materials

Polymers make excellent materials for solution based deposition methods like spin-coating. Due to their high molecular weight, they usually cannot be used for vacuum based deposition methods, however. In contrast to small molecule materials, polymers feature unique physical and electronic properties. In π -conjugated polymers, a charge can be delocalised. But defects, kinks and twists can interrupt the conjugation of a polymer and create traps. Depending on the curvature of the polymer backbone, charge transport is faster in delocalised areas and slower where kinks and twists have to be overcome via hopping [7]. As co-polymers, multiple molecular components like donor- and acceptor-functionalities can be combined in an ideal ratio and position to each other which would not be possible by simply mixing them.

Cross-linking a material after deposition creates a mesh-like polymer network. This technique, which is explained in detail in chapter 2.2.5, has the additional benefit of rendering the layer insoluble.

The phase behaviour of polymers differs from small molecules and even for the same polymer, depending on the molecular weight. Polymerisation usually results in a mixture of shorter and longer chains. Instead of an exact molecular weight, polymers are usually described through a molecular weight distribution.

The molar fraction x_i can be calculated as the ratio of the number of polymer chains n_i consisting of i monomer units to the total number of all polymer chains n_{total} .

$$x_i = \frac{n_i}{n_{total}} \quad (2.3)$$

The number average molecular mass M_n defines an arithmetic average of the molecular masses of the individual polymer chains M_i .

$$M_n = \sum x_i M_i \quad (2.4)$$

Similarly, the weight fraction w_i is calculated as the ratio of the weight of those polymer chains, derived from the product of n_i and M_i , to the total weight of all polymer chains $n_{total}M_{total}$.

$$w_i = \frac{n_i M_i}{n_{total} M_{total}} \quad (2.5)$$

The weight average molecular mass M_w defines a weight average of the polymer chains.

$$M_n = \sum w_i M_i \quad (2.6)$$

Typically, polymers are a mixture of different polymer chain lengths. An exemplary distribution curve is shown in fig. 2.12.

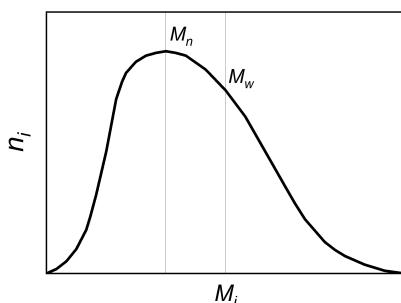


Fig. 2.12: Example molecular distribution curve of a polymer consisting of different chain lengths, with M_n and M_w marked. Based on a model from [37].

As a measure of dispersity, the polydispersity index (PDI) can be calculated as the ratio of M_w and M_n

$$PDI = \frac{M_w}{M_n} \quad (2.7)$$

The PDI represents the width of the molecular weight distribution, a value of 1 meaning monodisperse, and with larger values more and more polydisperse.

To fully characterise a polymer, all three values, M_n , M_w and PDI, are required. But often, only one molecular mass value is given or used for comparison. While M_n is the number average molecular mass, M_w also factors in the larger size of longer polymers. Since molecular size has a great impact on many physical properties, longer polymer chains will have a greater impact on them. While each polymer behaves differently, it can be assumed that a higher M_w usually results in

2 Theory

a higher glass transition temperature (T_g) and melting temperature (T_m) [37].

Besides the glassy or crystalline phase and isotropic melt, additional phases can often be seen. Especially when chiral elements are present, liquid crystalline phases can occur. Some of those phases are even thermodynamically stable after cooling. For polydisperse polymers, more complex phase transitions can be an issue, though. In thin layers, phase separation can occur, with shorter chains rising to the top, or unmelted crystallites of longer chains embedded.

In this work, two types of polymers were used: PF and F8BT. Their properties and characteristics will be explained in the following section.

2.3.1 Polyfluorenes (PF)

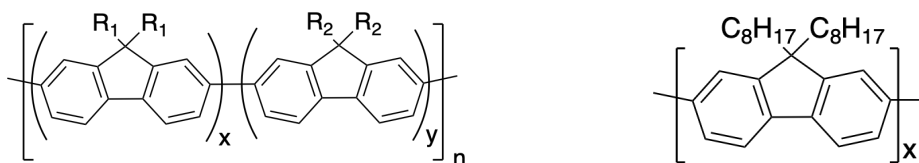


Fig. 2.13: General structure of a PF co-polymer (left) and one of the most common PF examples, poly(9,9-dioctylfluorene) (PFO) (right).

Polyfluorenes (PFs) are homo- or co-polymers from fluorene monomers. Fig. 2.13 (left) shows the general structure of a PF based co-polymer, analogous to many of the materials used in this work. Additionally, one of the most common PF examples, PFO (right), is shown.

Fluorene consists of two benzene rings bridged in para position over a cyclopentadiene, creating a planar, aromatic unit with fully delocalised π electrons. To increase solubility, the PF backbone is usually functionalised with alkyl chains, the most common PF featuring two octyl chains per fluorene unit, hence being called PFO (poly(9,9-dioctylfluorene)). But other chains, even branched or chiral ones, are also common. PFs are synthesised via a Suzuki- or Yamamoto-coupling

reaction. As conjugated polymers with blue electroluminescence, PFs are well suited as emitter materials in organic electronics [38].

Of especial interest, particularly for the application in CP-OLEDs, is the phase behaviour of PFs. The three most commonly mentioned phases are named α , γ and β . An overview of their distinguishing parameters is given in tab. 2.1. Spectra of PFO in α , γ and β phase are shown in chapter 3.2.1.

The α phase, also called amorphous or glassy phase, consists of bent polymer chains with a randomly distributed torsion angle between monomers around 135° . It is the predominant phase for pristine PF thin films. Quick solvent evaporation (like in spin-coating) or heating and subsequent slow cooling to room temperature lead to this phase [39, 40]. A relatively broad absorption peak around 383 nm is typical [41]. For individual polymer chains, PL peaks around 411 nm for the first electronic (0-0) transition and 438 nm for the first vibronic (0-1) transition can be measured. The ratio of those peaks depends on the degree of bending of the polymer chain, with bent chains displaying a more prominent (0-1) peak [40]. In thin layers however, the two peaks often merge into a combined PL peak around 428 nm [42].

The β phase represents the most planar, rigid and linear conformation, with a torsion angle between monomers of $160 - 180^\circ$. Slow solvent evaporation, solvent vapour annealing (SVA), or cooling to -196°C and reheating to room temperature predominantly leads to β phase. While an absorption peak around 400 nm is associated with delocalised π - π transitions on the backbone of β phase PFs, the characterising feature is an additional absorption shoulder or peak around 433 nm. The more planar structure results in a PL emission red-shift of approximately 20 - 30 nm compared to α phase. Peaks around 438 nm ((0-0) transition) and 465 nm ((0-1) transition) can be observed, whereas aggregates will be red-shifted compared to individual chains [39, 40, 42].

2 Theory

Between α and β phase, the nematic or γ phase occurs. The torsion angle between monomers of $140 - 160^\circ$ resides between α and β conditions. The γ phase can be produced through heating and subsequent rapid quenching, or occurs naturally during the transition of α to β phase. It can be characterised by a schlieren texture observed in microscopy with crossed polarisers. As a mixed phase, the absorption and PL features are located somewhere between α and β as well. The absorption peak experiences a gradual red-shift and may lie somewhere between 383 nm and 433 nm. For PL, peaks around 430 nm ((0-0) transition) and 455 nm ((0-1) transition) are reported [38, 39].

Tab. 2.1: Overview of torsion angles as well as absorption and PL peaks of the α , γ and β phases of PFs.

	α	γ	β
Torsion angle	broad distribution	narrow distribution (140 - 160°)	narrow distribution (160 - 180°)
Abs	383 nm	383 - 400 nm (mixed phase)	433 nm (characteristic feature)
PL	411 nm (0-0) 438 nm (0-1)	430 nm (0-0) 455 nm (0-1)	438 nm (0-0) 465 nm (0-1)

For chiral materials, mesophases are possible. The so called blue phase was first reported in 1888, where Reinitzer described a "bright blue-violet colour phenomenon" during the cooling of cholesterol benzoate [43]. Thermally, up to three blue phases can be located between the helical phase and isotropic phase. While they are similar to the helical phase, blue phases are reported to have a viscosity in the order of 10^6 higher. Also, despite being a liquid phase, they experience a small, yet surprising non-zero elastic shear modulus [44].

Blue phases can occur for highly chiral, thermotropic liquid crystals, and have therefore been reported in association with chirally functionalised PFs [4, 45, 46, 47].

2.3.2 Poly(dioctylfluorene-co-benzothiadiazole) (F8BT)

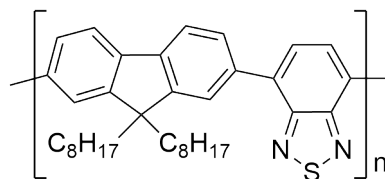


Fig. 2.14: Structure of poly(9,9-dioctylfluorene-*alt*-benzo thiadiazole) (F8BT).

F8BT is an alternating co-polymer of fluorene with two octyl side chains (F8) and benzothiadiazole (BT) units. Since the LUMO of BT lies 1.56 eV below the LUMO of F8, electron density is strongly localised on the BT unit [48]. The high electron affinity of F8BT also enables an easy electron injection, allowing a simpler device architecture without necessarily requiring an electron-transport layer (ETL) [49]. A high luminance efficiency and balanced charge transport properties makes F8BT an excellent green emitter material [50].

To increase OLED performance and efficiency, 5 - 10% of F8BT are often mixed into a PFO matrix. Due to the spectral overlap between F8 emission and BT absorption bands in the polymer mixture, a highly efficient FRET occurs. The resulting PL or EL emission spectrum is almost identical to a pure F8BT emission spectrum. The high electron mobility of F8BT and high hole mobility of PFO combines to improved charge transfer properties compared to either material alone [49].

2.4 Polarised light

In terms of electromagnetic theory, light can be described by two perpendicularly relative waves. Fig. 2.16 (a) shows the electric (E, red) and magnetic (B, blue) component of an electromagnetic wave, with the light propagating in z -direction. Their phase and intensity are tied together by the *Maxwell* equations. To simplify models, light is often only represented by the wave plain of the electric component, which is much larger than the magnetic component. Alternatively, it can be described in terms of a cartesian coordinate system, with the direction of light propagation z and two orthogonal, linearly polarised components x and y . Based on the most common convention, **polarisation effects shall be defined from the point of view of the detector or an observer, looking towards the light source.** A 3D representation of a left-handed circularly polarised (LCP) (blue) and a right-handed circularly polarised (RCP) (red) light beam is shown in fig. 2.15.

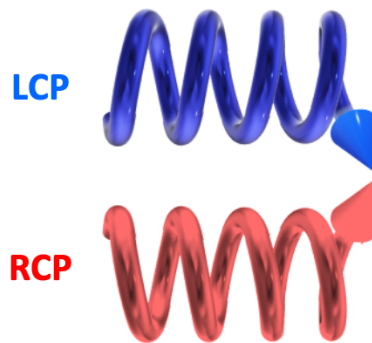


Fig. 2.15: Helical projection of LCP (blue) and RCP (red) light.

Unpolarised light can be viewed as the sum of many, randomly oriented wave plains, or $x = y = 1$.

For linearly polarised light, only one wave plain remains, e.g. $x = 1$ and $y = 0$.

For circularly polarised light, the wave plain forms a spiral or cork screw. The electric field vector rotates around z . A clockwise rotation represents RCP, and a counter-clockwise rotation represents LCP. In terms of the coordinate system, the magnitude of the two linear components are equal $x = y = 1$, but have a phase

shift in relation to each other. A phase shift of $-\pi/2$ represents **RCP**, and a phase shift of $+\pi/2$ represents **LCP**.

To have a consistent understanding of polarisation directions in this work, 0° shall be set in 12 o'clock position. This characterises a linear polariser with a vertical transmission direction, or linearly polarised light in a vertical plane. For quarter-wave plates (**qwps**), the fast axis of the material shall define 0° .

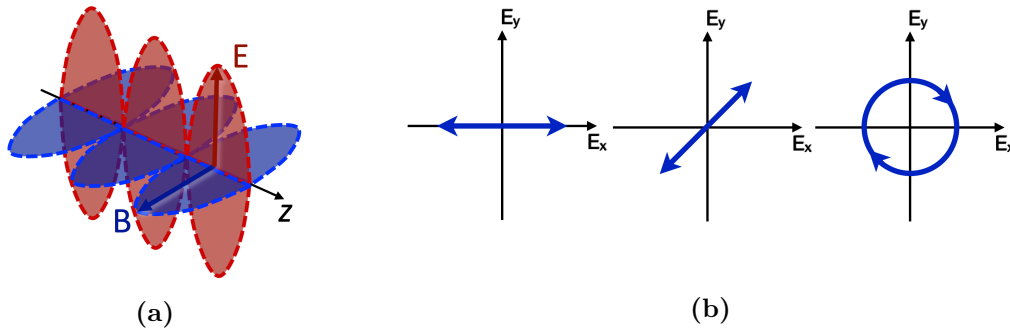


Fig. 2.16: (a) Electromagnetic wave model with orthogonal electric (red) and magnetic (blue) components. (b) *Jones* vector diagrams for horizontal LP, vertical LP and right-handed CPL.

To describe polarisation, the *Jones* vector (Eq. 2.8) can be used. It requires the two electric field components in x - and y -direction. The polarization state consists of the amplitudes E_{0x} and E_{0y} and the phase angles δ_x and δ_y , with $i = \sqrt{-1}$ [51].

$$\begin{bmatrix} E_x \\ E_y \end{bmatrix} = \begin{bmatrix} E_{0x}e^{i\delta_x} \\ E_{0y}e^{i\delta_y} \end{bmatrix} \quad (2.8)$$

By tracing the oscillation of the electric field vector in the x - y -plane, basic polarisation states can be visualised. As examples, fig. 2.16 (b) shows horizontally and vertically linearly polarised (**LP**) light, as well as right-handed circularly polarised (**CP**) light.

2.4.1 Polarisation effects

Most natural and artificial light sources emit unpolarised light. This incoherence results from combining the uncorrelated, randomly polarised emission from individual atoms or molecules. In [OLEDs](#), this is due to the amorphous nature of the organic semiconductor layers. The polarisation state can be influenced either through interaction of the light wave with a specific environment, or by changing the material properties of the emitter and implementing molecular order.

The following section will introduce and explain some of the physical effects associated with polarisation, while a more in-depth analysis of circularly polarised OLEDs ([CP-OLEDs](#)) can be found in in chapter [2.6](#).

Birefringence is the difference in refractive indices of a material depending on the light propagation direction. At the right conditions, one polarisation state can be converted into another. For example, if a birefringent medium has different refractive indices in x - and y -direction (slow and fast axis), one light component will be retarded compared to the other, affecting the resulting polarisation state depending on the material thickness in z -direction. This effect is used in waveplates (retarders), which consist of a retarding material like quartz or mica.

In a quarter-wave plate ($\lambda/4$ plate), a [LP](#) light beam with an angle of $+45^\circ$ or -45° in respect to the fast axis will be converted into [RCP](#) or [LCP](#), respectively.

A half-wave plate ($\lambda/2$ plate) on the other hand will rotate [LP](#) light by 90° . A similar effect, rotation of the polarisation plane of [LP](#) light, can be observed in optical rotation, which is usually associated with solutions of chiral materials like sucrose.

Circular dichroism ([CD](#)) on the other hand describes the preferential absorption of [RCP](#) or [LCP](#) light. This effect can be used in solid as well as liquid samples and is the base for [CD](#) spectroscopy [\[52, 53\]](#).

2.4.2 Optical interference

When two light beams are superimposed, they experience optical interference. Waves are called coherent, when they have the same frequency. As shown in fig. 2.17, coherent waves will experience constructive interference, while non-coherent waves experience destructive interference.

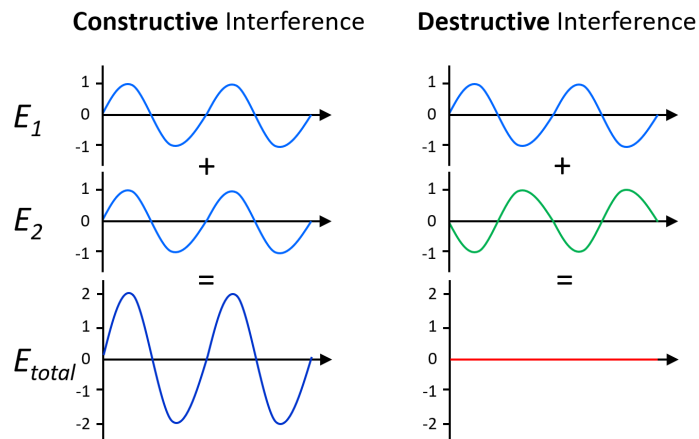


Fig. 2.17: Coherent waves will lead to constructive interference (left), while non-coherent waves experience destructive interference (right).

The resulting interference pattern can be calculated as the vector sum of the individual waves. Fig. 2.18 shows the intensity distribution of two interfering light waves.

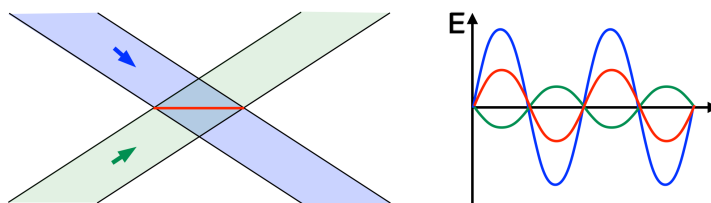


Fig. 2.18: Two superimposed light beams will experience interference (left). The standing wave interference pattern of the cross section marked in red is shown (right).

2 Theory

The interference pattern can be calculated with eq. 2.9 and 2.10. A schematic is shown in fig. 2.19.

After passing a double slit, two light beams will create an interference pattern on a screen. If the distance D to the screen is much larger than the slit distance d , the angle of each light beam is nearly identical to the angle θ of the combined light path. If the path length difference n , also called order of interference, in the grating equation eq. 2.9 is an integral number multiple of the wavelength λ ($n = 0, 1, -1, 2, -2, \dots$), constructive interference occurs. Likewise, destructive interference occurs for half-integral number multiples of λ ($n = \frac{1}{2}, -\frac{1}{2}, \dots$).

$$n\lambda = d \sin \theta \quad (2.9)$$

The distance s between successive interference maxima is calculated with eq. 2.10 [53].

$$s = \frac{n\lambda D}{d} \quad (2.10)$$

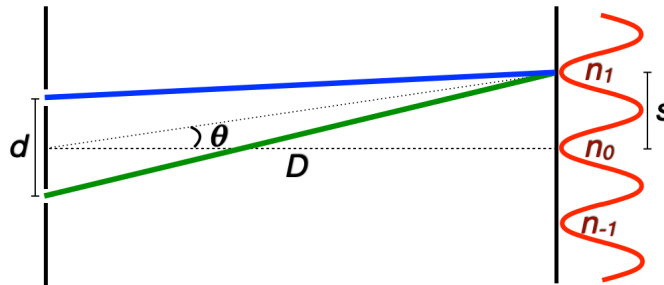


Fig. 2.19: Interference of two light beams (green and blue) in an angle θ through a double slit with the distance d at a much larger distance D to the screen produces an interference pattern with intensity peaks of the order n at a distance s to the centre of the screen.

In OLEDs, interference of different light waves and the subsequent intensity distribution ultimately influences the shape of the outcoupled light spectrum. This can be explained by several factors.

Due to the amorphous nature of organic emitter layers, the emission direction of generated light is random in all directions. This means equal amounts of light travel in forward direction towards the transmissive anode, and in backward direction towards the metal cathode, where it is reflected. As explained in chapter 2.4.3, however, each interface can result in partial reflection as well. Interference occurs for all involved light beams. This leads to a complex interference pattern, which depends on the position of the recombination zone, the angle of observation, as well as refractive indices and thickness of all involved layers.

Analogous to the intensity distribution, interference also influences the polarisation state. Fig. 2.20 show the polarisation state of two interfering light beams with identical intensities, but different incident polarisation states, depending on their phase difference. In the example on top, the interference between an LCP and an RCP light wave produces LP light. In the bottom example, the interference between two orthogonal LP light waves produces LP, elliptical or circularly polarised light waves.

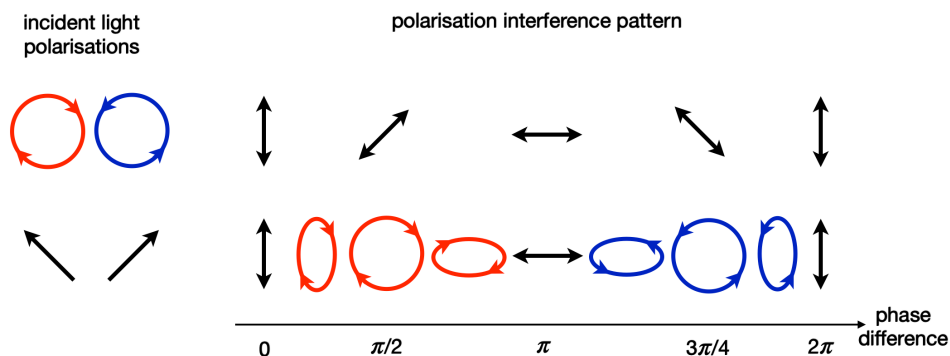


Fig. 2.20: Incident (left) and resulting (right) polarisation state of two interfering light waves with identical intensities. Results are shown for several phase differences.

In the top example, interference between two CP light waves of opposite handedness results in LP light.

In the bottom example, interference between two orthogonal LP light waves results in LP, elliptical or CP light.

2 Theory

In CP-OLEDs, reflection results in a reversal of CP handedness (see fig. 2.21). While OLEDs experience partial reflection on every interface according to the *Fresnel* equations, the most significant reflection occurs at the cathode. Reflection of CPL leads to a reversal in handedness. Interference between light waves with different polarisation states leads to a polarisation distribution, effectively reducing the experimentally measured g-value. The polarisation state of the outcoupled light depends on the initial polarisation state of generated light, the position of the recombination zone, as well as thickness and potentially CP-selective absorption (CD) of each layer [46, 53, 54].

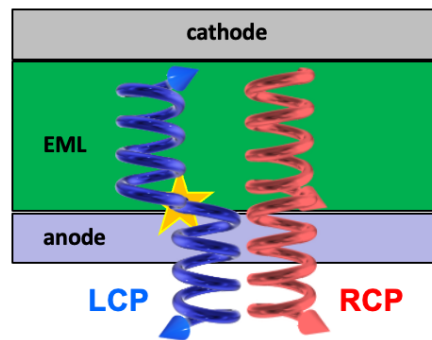


Fig. 2.21: Reversal of CP handedness after reflection on the cathode. Interference between light waves with different polarisation states leads to a polarisation distribution.

Interference can be actively used to influence and tune the outcoupled emission spectrum. In cavity OLEDs, a second semitransparent metal layer is introduced. This way, light is consecutively reflected on both electrodes before it is eventually outcoupled. Like in a *Fabry-Pérot* resonator, light waves with the correct resonance wavelength can create a standing wave. The resonance wavelength depends on the distance between both mirrors, which is called cavity length. Through constructive and destructive interference, this specific wavelength is amplified compared to other wavelengths, a process originally used for lasing. This way, the originally broad OLED emission spectrum can be narrowed to a precise peak at a tunable wavelength.

Within the cavity, an infinite number of resonant modes j are possible, depending on resonant wavelength λ_j of the j^{th} mode, the refractive index n and the thickness of the organic layer d .

$$\frac{j\lambda_j}{2} = nd \quad \text{with } j = 1, 2, 3, \dots \quad (2.11)$$

The refractive index n of organic materials is typically between 1.5 and 2. For the emissive polymer F8BT used in this work, for example, a refractive index of 1.69 at 577 nm is reported [55]. For an OLED with 200 nm thickness, the fundamental resonant mode $j = 1$ and second order resonant mode $j = 2$ would result in $\lambda/2$ resonant peaks of 676 nm and 338 nm, respectively [56].

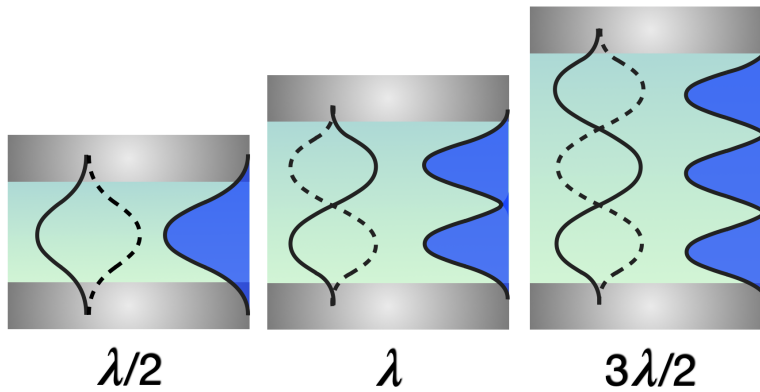


Fig. 2.22: Schematic of cavity OLEDs with different organic layer (green) thicknesses. Shown are the $\frac{\lambda}{2}$ (left), λ (middle) and $\frac{3\lambda}{2}$ (right) resonant modes as standing waves and as intensities (blue).

2.4.3 Transfer-matrix model

A critical aspect about OLEDs is that the light propagates through multiple layers consisting of different materials. On every interface, at least partial reflection occurs. This leads to outcoupled emission losses due to waveguiding to the edge of the substrate. Depending on the position of the recombination zone in relation to the reflective cathode, interference between the individual light beams can also influence the **EL** spectrum and the polarisation state of outcoupled light. It is,

2 Theory

therefore, fundamental to understand the optical processes occurring in an OLED, which is done with the transfer-matrix model.

For a single interface between two optical media 0 and 1, the behaviour of a light beam can be predicted based on the *Fresnel* equations and *Snell's* law:

$$n_1 \sin(\theta_1) = n_2 \sin(\theta_2) \quad (2.12)$$

With the refractive indices n_0 and n_1 of the two materials and the angles of incidence θ_1 and refraction θ_2 , the reflection and transmission of a light beam passing an interface can be calculated.

The multi-layer environment in OLEDs with several interfaces is, however, more complex. A partially reflected light beam can again experience partial reflection and transmission on another interface. Additionally, all involved light beams can interfere, and light can be absorbed by the layer in which it travels.

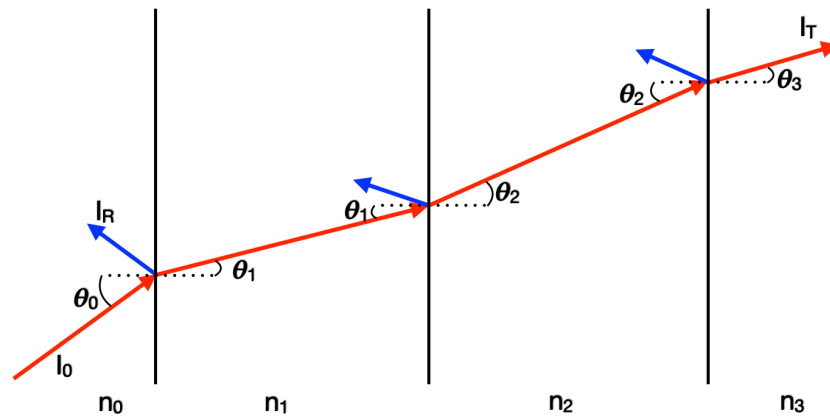


Fig. 2.23: Schematic of a light beam propagating through a multi-layer stack at propagation angles θ_i . Each of the layers i has a refractive index of n_i . The light intensities are represented by I_0 for incident light, I_R for reflected light and I_T for transmitted light.

According to *Maxwell's* equations, the electric field across an interface must follow a continuity condition. It can, therefore, be calculated using a matrix approach.

$$\begin{bmatrix} E_{0B}^R \\ E_{0B}^L \end{bmatrix} = D_{0,1} \cdot \begin{bmatrix} E_{1A}^R \\ E_{1A}^L \end{bmatrix} \quad (2.13)$$

Eq. 2.13 represents the transmission of a light beam from layer 0 to layer 1, with the electric field vectors E^r in right and E^l left direction. The boundary condition at the interface is indicated by the index A and B for the right and left side of an interface, so the transmission at the interface equals a transition from B to A.

The transmission matrix $D_{0,1}$ can be calculated with the *Fresnel* coefficients for reflection $r_{0,1}$ and transmission $t_{0,1}$ at the interface. Since the *Fresnel* coefficients for s- and p-polarised light are different, the transmission matrix $D_{0,1}$ is polarisation dependent.

$$D_{0,1} = \frac{1}{t_{0,1}} \cdot \begin{bmatrix} 1 & r_{0,1} \\ r_{0,1} & 1 \end{bmatrix} \quad (2.14)$$

After transmission of the interface, the light beam propagates through layer 1, where it can experience absorption. Propagation can, again, be represented by a matrix, equalling a transition from A to B.

$$\begin{bmatrix} E_{1A}^R \\ E_{1A}^L \end{bmatrix} = P_1 \cdot \begin{bmatrix} E_{1B}^R \\ E_{1B}^L \end{bmatrix} \quad (2.15)$$

The propagation matrix P_1 can be calculated as

$$P_1 = \begin{bmatrix} e^{i\phi_1} & 0 \\ 0 & e^{-i\phi_1} \end{bmatrix} \quad (2.16)$$

and

$$\phi_1 = \frac{2\pi}{\lambda} \cdot \tilde{n}_1 \cdot d_1 \cdot \cos\theta_1 \quad (2.17)$$

2 Theory

with the wavelength of the light beam λ , the complex refractive indices \tilde{n}_1 (see eq. [2.19](#)), the layer thicknesses d_1 and the propagation angles θ_1 .

By comparing equations [2.13](#) and [2.15](#), it can be seen that one matrix element appears in both terms. The transmission from layer 0 into layer 1 and subsequent propagation through layer 1 can, therefore, be combined.

$$\begin{bmatrix} E_{0B}^R \\ E_{0B}^L \end{bmatrix} = D_{0,1} \cdot P_1 \cdot \begin{bmatrix} E_{1B}^R \\ E_{1B}^L \end{bmatrix} \quad (2.18)$$

The product of all transmission and propagation matrices, in this case $D_{0,1}$ and P_1 , is called transfer matrix [\[57, 58\]](#).

This principle is instrumental for ellipsometry and further details are given in chapters [2.4.4](#) and [2.4.5](#).

2.4.4 Ellipsometry

The refractive index n determines how much a light beam will bend when moving from one material to another. *Snell's law* (eq. [2.12](#)) brings the angles of incidence and refraction θ into relation with the refractive indices of the materials, while the *Fresnel equations* describe the reflection and transmission at the interface. When n is wavelength dependent, dispersion, a splitting of light into its constituent colours, occurs. To describe absorbing materials, a complex refractive index \tilde{n} is required (eq. [2.19](#)), with the index of refraction n and extinction coefficient k .

$$\tilde{n} = n - ik \quad (2.19)$$

In ellipsometry, an incident light beam is reflected from - and transmitted into - a sample, which leads to a change in phase and amplitude of the electric and magnetic vectors of this light beam. Depending on angle and polarisation direction (p or s), this interaction can be described by the *Fresnel coefficients* \tilde{r}_p and \tilde{r}_s . Ellip-

sometry measures a change in polarisation of the reflected light and gives the ratio of the complex *Fresnel* coefficients (eq. 2.20), where Ψ relates to the amplitude ratio and Δ relates to the phase change.

$$\frac{\tilde{r}_p}{\tilde{r}_s} = \tan(\Psi)e^{i\Delta} \quad (2.20)$$

To derive the optical material constants n and k as well as the layer thickness d from the measured values Ψ and Δ , a regression analysis can be performed. A suitable layer study is assumed and the parameters are fitted to match the measured data. The accuracy of the calculated optical constants strongly depends on the aptitude of the assumed model. For more complicated systems, e.g. for the presence of anisotropies, multiple measurements can be combined and fitted with one set of assumptions. Measurements can be performed in reflection or transmission. A common measurement strategy is the variation of the angle of incidence of the light beam, called variable angle spectroscopic ellipsometry (VASE) [58].

While standard ellipsometry is very useful for isotropic materials, anisotropic layers benefit from a more extensive mode of measurement, called *Müller* matrix (MM) ellipsometry.

2.4.5 Müller Matrix ellipsometry

The polarisation state of a light beam can be characterised with the *Stokes* vector (eq. 2.21). It consists of four intensity observables S_0 through S_3 , which are expressed through basic polarisation states: I_p , I_s , I_{+45° and I_{-45° represent linear polarisation (LP) parallel (p), orthogonal (s) and at a $\pm 45^\circ$ angle relative to the plane of incidence, whereas I_R and I_L refer to right- and left-handed circular polarisation. The total intensity described by S_0 is usually normalised to 1. S_1 and S_2 represent the relation of horizontal to vertical and $+45^\circ$ to -45° LP light, respectively. Lastly, S_3 describes the relation of RCP to LCP light [58, 59].

$$S = \begin{bmatrix} S_0 \\ S_1 \\ S_2 \\ S_3 \end{bmatrix} = \begin{bmatrix} I_p + I_s \\ I_p - I_s \\ I_{+45^\circ} - I_{-45^\circ} \\ I_R - I_L \end{bmatrix} \quad (2.21)$$

While the *Stokes* vector defines the polarisation state of a light beam, the transformation of this light while passing through a medium can be described with a *Müller* matrix \mathbf{MM} (eq. 2.22).

$$\begin{bmatrix} S_0 \\ S_1 \\ S_2 \\ S_3 \end{bmatrix}_{out} = \begin{bmatrix} m_{00} & m_{01} & m_{02} & m_{03} \\ m_{10} & m_{11} & m_{12} & m_{13} \\ m_{20} & m_{21} & m_{22} & m_{23} \\ m_{30} & m_{31} & m_{32} & m_{33} \end{bmatrix} \cdot \begin{bmatrix} S_0 \\ S_1 \\ S_2 \\ S_3 \end{bmatrix}_{in} \quad (2.22)$$

\mathbf{MM} is a valuable tool in ellipsometry. During measurement of a sample, the incident light properties S_{in} are known, and the properties of the light beam exiting the sample S_{out} can be measured. Therefore, the \mathbf{MM} elements can be calculated, thereby allowing conclusions about the properties of the measured material and even calculation of \mathbf{CD} values [58, 60, 61].

The M-2000 ellipsometer used in this group has one compensator, which means only the first three rows of a \mathbf{MM} can be recorded. Through symmetry considerations however, it is possible to calculate the fourth row (indicated in grey) of the \mathbf{MM} as well. For non-depolarising samples, calculating the logarithm of this \mathbf{MM} \mathbf{M} will deliver the differential \mathbf{MM} \mathbf{L} (eq. 2.23), the elements of which can be interpreted as circular dichroism (\mathbf{CD}), circular birefringence (\mathbf{CB}) and horizontal (LD, LB) and 45° vertical (LD', LB') linear dichroism and birefringence, respectively.

$$\mathbf{L} = \ln(\mathbf{M}) = \begin{bmatrix} 0 & -LD & -LD' & CD \\ -LD & 0 & CB & LB' \\ -LD' & -CB & 0 & -LB \\ CD & -LB' & LB & 0 \end{bmatrix} \quad (2.23)$$

From this matrix, the circular dichroism value CD can be derived [\[61\]](#).

Some materials cannot be described by simple optical material constants due to their anisotropic nature. Examples for this are birefringent crystals or spin-coated polymers. To define those materials, multiple measurements from different angles, measurements in reflection and transmission and MM ellipsometry can be necessary.

2.5 Chirality

Chirality is a property of symmetry and shape. Like our left and right hand are mirror images of each other, chiral structures consist of identical but non-superimposable structures. Chirality can be observed across different length-scales, from the subatomic spins of electrons or photons, over molecules and even in macroscopic natural structures like seashells. In molecules, chiral mirror images are called enantiomers.

Molecular chirality can have different origins. The most obvious is a chiral centre, e.g. a C-atom with four different substituents. Based on the *Cahn-Ingold-Prelog* (CIP) priority rules, each chiral centre is assigned an *R* or *S* descriptor which unambiguously describes the spatial arrangement of atoms. This is achieved by assigning priorities to each group attached to a chiral centre based on their atomic number and rotating the molecule accordingly (see leftmost structure in fig. 2.24).

Structures with axial chirality don't necessarily have a chiral centre, but display an axis or plane of chirality. Typical examples are BINAP or helicenes (see respective structures in fig. 2.24). To apply CIP rules in this case, the molecule is observed along the chiral axis and the "near" substituents are given priority over "far" substituents.

For helical structures, the *M* and *P* nomenclature is more common. *M* ("minus") refers to a left-handed helix and *P* ("plus") refers to a right-handed helix. There is no precise line when to use which classification, but generally *R* is comparable with *M* and *S* is comparable with *P* [62].

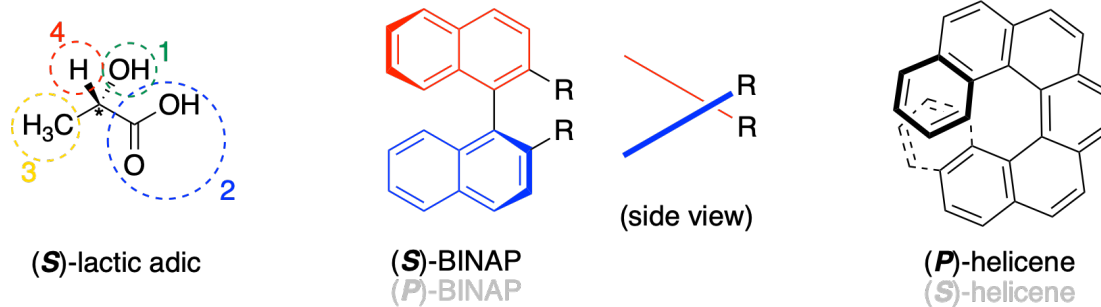


Fig. 2.24: Examples of different kinds of chirality. Lactic acid displays molecular chirality. Priorities of the groups attached to the chiral centre (marked with star) are ranked in accordance with CIP rules. BINAP- and helicene-structures display axial chirality and can therefore be named either with CIP rules, or with *M* and *P* nomenclature. The more common name is printed in black, respectively.

Chirality can also occur on a supramolecular level. For CP-OLEDs, chiral phases in thin films are of especial interest. They can occur for chiral molecules, chiral polymers, polymers with an added chiral inducer, or through surface-induced chirality.

2.6 Polarised OLEDs

Regular OLEDs, due to the amorphous nature of the organic material, emit unpolarised light. However, using a chiral phase **EML** or chiral chromophores allows for the construction of an OLED that can directly emit linearly or circularly polarised light. The following chapters give an introduction into development, properties and applications of LP- and CP-OLEDs.

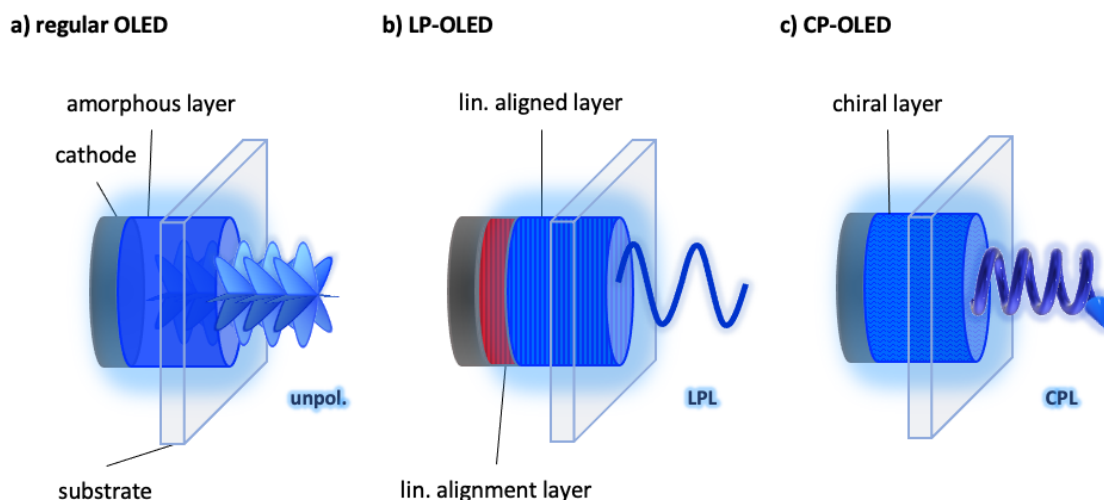


Fig. 2.25: Schematic structure of three different OLEDs: (a) a regular OLED with amorphous organic layers will emit unpolarised light. (b) A LP-OLED requires an **AL** and subsequently linear alignment of the organic layer. (c) A CP-OLED contains chiral elements within the chromophore (intrinsic CPL) and/or a chiral supramolecular structure (extrinsic CPL).

2.6.1 Linearly Polarised OLEDs

Linear polarisation is a common property, for example in liquid crystal (LC) displays. There, the light from a often LED based backlight panel has to pass through two orthogonal linear polarisers. The space between those polarisers is filled with a winding liquid crystalline, often twisted nematic, material which is aligned at the upper and lower interface through alignment layers (**ALs**). To maintain both orthogonal alignment directions, the molecules form a twisted nematic (TN) structure which rotates the linearly polarised light from the backlight panel along the

rotation axis, enabling it to also pass the second orthogonal linear polariser. A dark pixel is achieved by applying an electric field between the **ALs**, causing the LC molecules to reorient along this electric field. Subsequently, LP light from the backlight is no longer rotated and cannot pass the second linear polariser - the pixel appears dark.

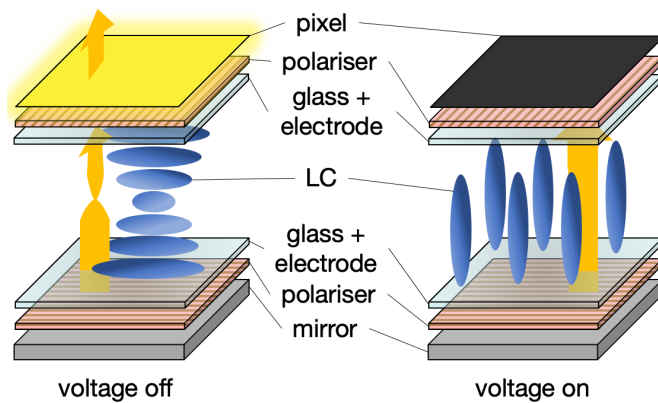


Fig. 2.26: Schematic structure of a TN cell. On the left side, voltage is turned off so the liquid crystalline molecules can adapt a twisted nematic structure, which rotates the light and allows it to pass the second polariser. The pixel appears light. On the right side, voltage is applied, which forces the molecules in the liquid crystal layer to orient along the electric field. The light is no longer rotated and cannot pass the second polariser. The pixel appears dark.

LC-displays use unpolarised light in combination with linear polarisers, which results in the same decreased outcoupling efficiency as mentioned in chapter [2.6.6](#). It would, however, also be possible to use linearly polarised OLEDs (LP-OLEDs) as backlight, eliminating this problem. Typically, such devices would require an **AL** and an emissive material, usually a polymer, that can be linearly aligned. The most common alignment technique includes physical rubbing of the **AL** and subsequent annealing of the emitter layer [\[63\]](#).

Linear alignment is quantified with the dichroic ratio D (eq. [2.24](#)), which can be defined for absorption, PL or EL for example. I_{\parallel} and I_{\perp} represent the intensity of light with linear polariser in parallel or orthogonal position in respect to the alignment direction.

$$D = \frac{I_{\parallel}}{I_{\perp}} \quad (2.24)$$

For alignment, polyimide (PI) is usually used. Due to their insulating properties, AL materials used in LCDs are not suitable for applications within an OLED stack. But many alternative approaches for ALs can be found in literature. Tab. 2.2 shows an overview of different alignment strategies and the resulting dichroic ratios D .

For rubbed PI with intermixed HTMs to increase conductivity, $D_{\text{abs}} = 15$ [64] and $D_{\text{EL}} = 22$ [65] are reported. In comparison, rubbed PEDOT is reported with $D_{\text{EL}} = 24.6$ [66]. Apart from rubbing, other alignment methods can be found as well, for example floating transfer of the emitter layer ($D_{\text{EL}} = 7.7$ [66]), photoalignment of the HTL ($D_{\text{EL}} = 14$ [67]), friction-transfer ($D_{\text{EL}} = 51$ [39]) and rubbing in combination with ion-beam treatment of a MoS₂ AL ($D_{\text{EL}} = 166.7$ [68]).

Tab. 2.2: Examples of different LP-OLED systems and their dichroic ratio D .

alignment layer	D_{abs}	D_{EL}	Reference
rubbed PI + HTM	15	22	[64, 65]
rubbed PEDOT	n.a.	24.6	[66]
floating EML transfer	n.a.	7.7	[66]
photoalignment of the HTL	n.a.	14	[67]
friction-transfer	n.a.	51	[39]
rubbing + ion-beam treatment of a MoS ₂ AL	n.a.	166.7	[68]

2.6.2 Circularly Polarised OLEDs

In the mid 1990s, the idea arose to incorporate chiral components into OLEDs for devices that could directly emit circularly polarised light (CPL). CPL is typically quantified through the CPL dissymmetry factor g (eq. 2.25), which can take values between 0, for completely unpolarised light, and ± 2 , for completely circularly polarised light of one handedness only [3].

$$g = 2 \cdot \frac{I_L - I_R}{I_L + I_R} \quad (2.25)$$

The g -value is typically found in context with absorption, PL or EL. But other definitions like photocurrent dissymmetry in the CPL-selective photodiodes can also be found [3, 69].

The CP-effect of CP-OLEDs is quantified by measuring the polarisation state of the outcoupled light. It has to be remembered, however, that the measured polarisation state is not identical to the original polarisation state of the EL. Also, it is not possible to distinguish the ratios of R-CPL, L-CPL and unpolarised light, since the measurement takes place after interference. For example, a combination of 75 % R-CPL and 25 % L-CPL will result in a g value of 1. However, the same g value is achieved for a combination of 50 % R-CPL with 50 % unpolarised light. The 25 % L-CPL will interfere with the R-CPL, resulting in a combined 50 % unpolarised light, and a reduced intensity for R-CPL. After interference, both examples are indistinguishable.

Many different strategies and materials for CP-OLEDs have been published, but they can be categorised into one of two main principles: intrinsic (see chapter 2.6.3) and extrinsic (see chapter 2.6.4) CPL.

2.6.3 Intrinsic CPL (I-CPL)

Intrinsic CPL (I-CPL) requires the π -system of the chromophore to be chiral, allowing the molecule to directly emit CPL. Therefore, chiral absorption and emission should be measurable in solution and film. I-CPL can be calculated with equation [2.26](#), where $g_{intrinsic}$ depends on the electric (μ) and magnetic (m) transition dipole moment, and the angle θ between them [70](#).

$$g_{intrinsic} = \frac{4|\mu||m| \cos(\theta)}{D} \quad (2.26)$$

with the dipole strength D

$$D = |\mu|^2 + |m|^2 \quad (2.27)$$

It has to be pointed out that the dipole strength D is not identical with the dipole moment.

An ideal $|g_{intrinsic}|$ of 2 would require μ and m to be of the same magnitude ($\mu/m = 1$) and parallel or antiparallel ($\theta = 0, 180^\circ$). Unfortunately, this constellation is usually not met in organic materials, especially not in good emitter molecules with a high fluorescent quantum yield ϕ_F . The electric contribution m is two to three orders of magnitude larger than the magnetic contribution μ , resulting in low $g_{intrinsic}$ values [71](#), [72](#). Kubo *et al.* calculated transition dipole moment values for a figure-eight-shaped [5]helicene dimer (shown in fig. [2.27](#)) specifically designed to be used as I-CPL emitter. They report a μ of 50×10^{-20} esu·cm (0.5 D) and a m of 3.1×10^{-20} erg/G (3.1×10^{-17} A·m²), resulting in a calculated and experimentally confirmed g_{PL} of 1.5×10^{-2} [73](#), [74](#).

For better comparability, μ and m values are often given in CGS units, because symmetric Gaussian system assumes the electric and magnetic field in the same dimension. Here, the examples were also converted into SI units, for better relatability¹.

¹Conversion of m and μ from Gaussian CGS units:

1 D (debye) = 10^{-18} esu·cm

1 A·m² = 1000 erg/G (Gauss) and $1 \mu_B$ (Bohr magneton) = $9.274 \cdot 10^{-24}$ A·m²

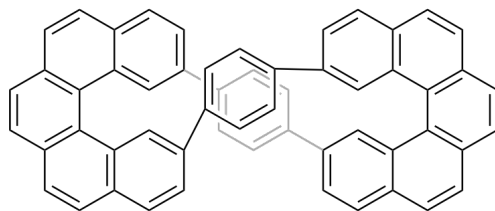


Fig. 2.27: Chemical structure of a figure-eight-shaped [5]helicene dimer, designed to be an I-CPL emitter [73].

Reported I-CPL emitter systems either have a large g -value but very low luminance, or high luminance but small g -value.

As an example for the first case, Zinna *et al.* reported a chiral europium emitter (shown in fig. 2.28), which achieved a maximum $g_{\text{EL}} = -1.0$ for the ${}^5\text{D}_0 \rightarrow {}^7\text{F}_1$ transition. The intensity of this emission, however, is very low. g_{EL} of the main transition ${}^5\text{D}_0 \rightarrow {}^7\text{F}_2$ is $+0.19$, with a device brightness of max. $L = 17 \text{ Cd/m}^2$ [75, 76].

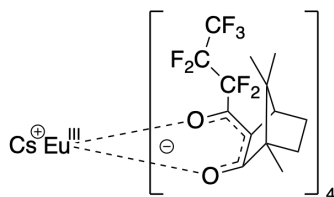


Fig. 2.28: Chemical structure of a chiral europium based I-CPL emitter [76].

As an example for the second case, Wu *et al.* reported a chiral octahydro-binaphthyl based I-CPL TADF emitter (shown in fig. 2.29). While this system achieved good OLED performance with max. $L = 25,000 \text{ Cd/m}^2$, it only had a small CP-effect of $g_{\text{EL}} = 2.9 \times 10^{-3}$ [77].

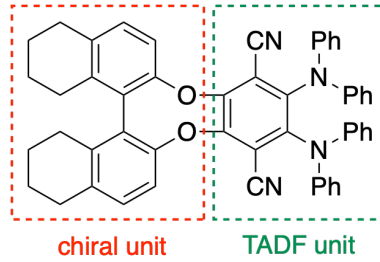


Fig. 2.29: Chemical structure of a chiral octahydro-binaphthyl based I-CPL TADF emitter [77].

Since intrinsic CPL emitters would be the most attractive, current research focusses on increasing g_{EL} either through molecular design, or smart combination with other materials.

One such example is given by Wade *et al.* for an oxa[7]superhelicene (shown in fig. 2.30). The g_{PL} of a neat thin film sample of this emitter is reported to be 3×10^{-4} . However, if the helicene is mixed into an F8BT matrix and the thin film annealed, g_{PL} is increased to 0.15. It has to be noted that here, even though F8BT is an emissive polymer, CPL emission specifically originates from the helicene. This 500-fold increased CP-effect is explained to be the result of a CP-selective FRET process from the chiral phase F8BT matrix onto the helicene [46].

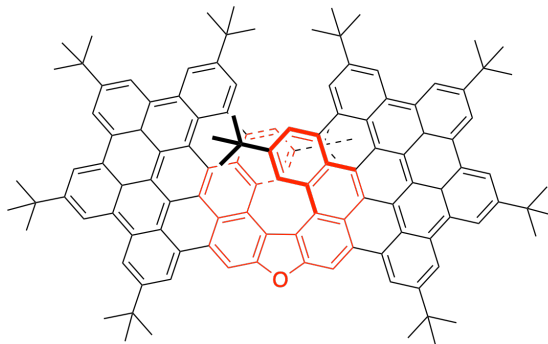


Fig. 2.30: Chemical structure of a oxa[7]superhelicene I-CPL emitter [46].

2.6.4 Extrinsic CPL (E-CPL)

The second CP-OLED principle is called **extrinsic CPL** (E-CPL). Here, non-CP emission is turned into CPL through the chiral environment. The chromophore not necessarily needs to contain a chiral component within its π -system, so chiral absorption and emission can only be measured in treated films and not in solution.

E-CPL combines all other effects that can occur within a chiral OLED, and therefore also has an impact on intrinsic CP-OLEDs. Because intrinsic CPL emitters perform so poorly, many groups focused their strategy on extrinsic CPL elements. E-CP-OLEDs are based on chiral phases, in most cases through annealing above T_g . Such chiral phases are reported as cholesteric liquid crystalline phase [4, 78, 79], helical arrangements [80, 81, 82, 83] or blue phase [4, 45, 46, 47]. With this strategy, $|g_{EL}|$ values of up to 1.13 can be found [4]. Chiral phases are typically achieved through one of the following strategies.

Strategy 1 consists of co-polymerising an achiral emissive monomer (red) with a non-emissive chiral monomer (blue), which induces a chiral phase in the resulting co-polymer. Zhao *et al.* reported how such a co-polymer, here with a molar ratio of 7:3 between the chiral and achiral monomers, can adapt a helical architecture, resulting in g_{PL} values up to 0.26 in solution (10 mM in CHCl_3) and up to 0.05 in thin film (3 wt% polymer in a PMMA matrix, drop-cast, 0.3 mm film thickness) [82, 83]. While many examples for helical arrangements in solution can be found, they often struggle to retain their architecture in solid form, even if embedded into a matrix material.

A similar concept was also used in this work. Results can be found in chapter 3.7.1.

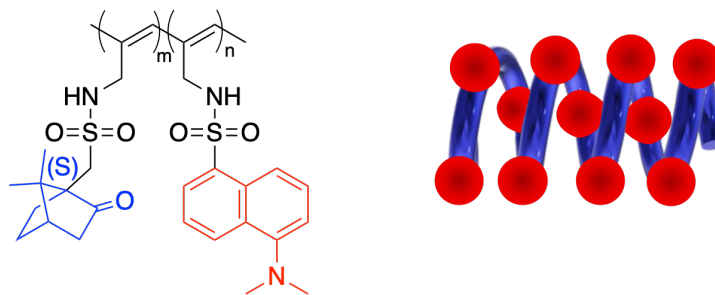


Fig. 2.31: Chemical structure and helical polymer architecture of a chiral copolymer, consisting of a non-emissive chiral monomer (blue, $m = 7$) an achiral emissive monomer (red, $n = 3$, shown here with the *S*-enantiomer) [82, 83].

Strategy 2 is the functionalisation of an emissive polymer with a chiral component. Oda *et al.* reported several examples of polyfluorene homo- and co-polymers with chirally functionalised side chains (one example shown in fig. 2.32). After annealing, single-layer CP-OLEDs of these polymers achieved g_{EL} values up to 0.25 [84].

Using polyfluorenes with chirally functionalised side chains is a concept that was also used in this work. Results can be found in chapters 3.7.2 to 3.7.7.

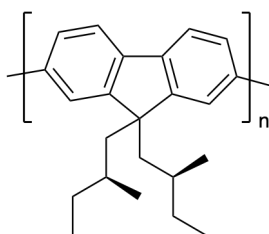


Fig. 2.32: Chemical structure of a polyfluorene with chirally functionalised side chains, used as E-CPL emitter [84].

Strategy 3 combines an achiral emissive polymer with a non-emissive chiral inducer molecule. During annealing, the polymer converts into a liquid crystalline phase, in which the chiral inducer forces the polymer into a preferential direction. The resulting chiral phase, which is responsible for the CP-effect, remains thermodynamically stable even after cooling. Lee *et al.* adapted this strategy

and reported the highest g_{EL} value of 1.13 for a well performing CP-OLED so far. They combined the achiral emissive polymer F8BT (see structure in fig. 2.14) with a non-emissive chiral inducer R5011 (see structure in fig. 3.63), resulting in strong CP emission (see fig. 2.33) [4, 85].

Such mixed systems were also used in this work. Results can be found in chapters 3.8 to 3.12.

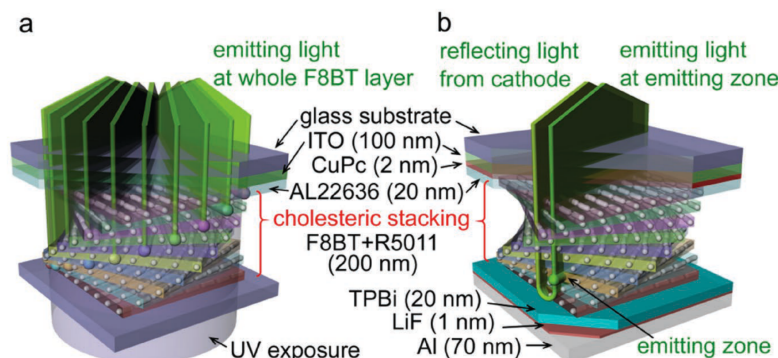


Fig. 2.33: Schematic illustration of CP-PL (a) and CP-EL (b) from a cholesteric F8BT + R5011 mixture. Picture was reproduced from [4].

Strategy 4 also uses an achiral emissive polymer capable of forming a liquid crystalline phase upon annealing, but does not require a chiral inducer molecule. Instead, this strategy relies on surface-induced chirality. Baek *et al.* reported a fabrication process (see fig. 2.34) with a PI-based AL and F8BT to achieve a g_{EL} of 0.64. After spin-coating of F8BT onto the rubbed AL, the F8BT surface is also rubbed, resulting in a groove structure. This surface anisotropy is fixed by covering the layer with an epoxy resin coat, which acts as second AL. Upon annealing, F8BT orients itself along the rubbing direction of both ALs. Since the bottom AL and F8BT surface are rubbed in different directions, the polymer is reported to adapt a continuously twisted structure. Once the desired chiral phase is achieved, the epoxy resin coat can be removed and a metal cathode can be evaporated.

2 Theory

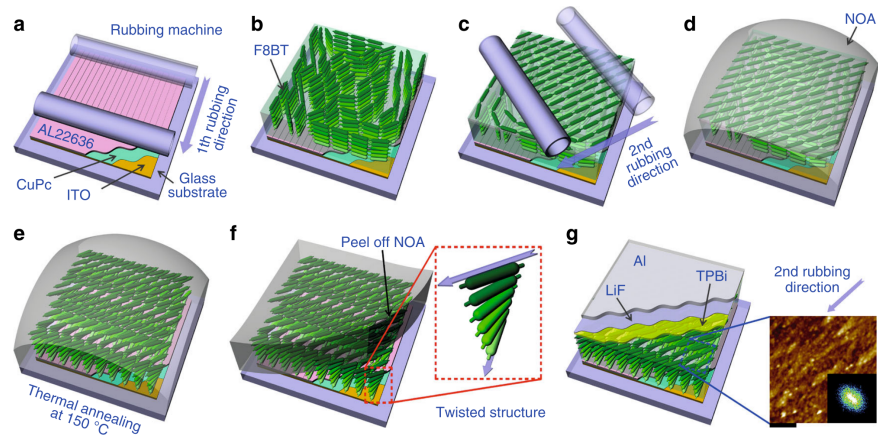


Fig. 2.34: Fabrication process of an F8BT based CP-OLED created through surface-induced chirality. Picture was reproduced from [86].

Chiral molecules or phases within an OLED stack lead to anisotropic optical behaviour, like CPL selective scattering, absorption, birefringence and optical rotation, which can partly be described through anisotropic optical constants (see chapter 2.4.5). Depending on the position of the recombination zone, (possibly anisotropic) refractive indices and thickness of all involved layers, an interference pattern of all light beams (see chapter 2.4.2), which can be described with the transfer-matrix method (see chapter 2.4.3), influences the final outcoupled EL spectrum and g_{EL} curve. This explains the strong layer thickness and wavelength dependence of g_{EL} , which has previously been reported in literature [70, 83, 87, 88].

2.6.5 Development of CP-OLEDs

Historically, I-CP-OLEDs and E-CP-OLEDs were developed in parallel. In 1997, Peeters *et al.* published the first example of CP-EL. They used poly(*p*-phenylenevinylene) (PPV) functionalised with enantiopure chiral side chains (see fig. 2.35) as active material and achieved a maximum $|g_{EL}| = 1.7 \times 10^{-3}$ [3].

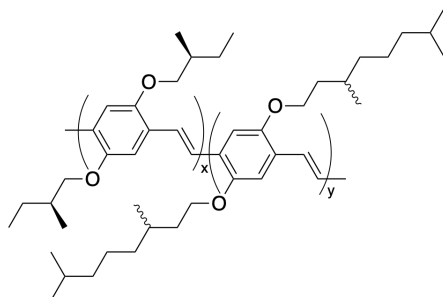


Fig. 2.35: Chemical structure of a PPV-based polymer with chiral side chains. Polymers with a x:y ratio of 1:0, 0.89:0.11 and 0:1 were analysed [3].

Shortly after, Oda *et al.* (see fig. 2.32) and Geng *et al.* analysed polyfluorenes with chiral side chains. They could already report maximum $|g_{EL}|$ values of 0.25 and 0.35, respectively [84, 89]. These groups analysed homo- and co-polymers of fluorene monomers with chiral, achiral and racemic mixture side chains.

In 2013, Yang *et al.* published the first example for CP-EL from a mixed system, consisting of the achiral emissive polymer F8BT in combination with a non-emissive aza[6]helicene as a chiral inducer. They reported g_{EL} values of up to 0.2 [90]. With the same approach, using R5011 as chiral inducer, Lee *et al.* later reported g_{EL} values of up to 1.13 (for further data, see fig. 2.33) [4, 85], the highest g_{EL} values reported so far for a CP-OLED with adequate performance.

The first examples of an I-CPL emitter used in a CP-OLED were published in 2015. Zinna *et al.* reported a chiral europium emitter, which achieved high g_{EL} values, but with a poor OLED performance (for chemical structure and further data, see fig. 2.28) [75, 76].

2 Theory

In the same year, Li *et al.* reported a chiral iridium emitter (see fig. 2.36). From a racemic mixture of chiral iridium complexes, they isolated and analysed four examples. While the device performance was excellent, with max. $L = 220,000 \text{ Cd/m}^2$ and max. $\text{Eff} = 73 \text{ Cd/A}$, only small CP-effects up to $g_{\text{EL}} = 2.6 \times 10^{-3}$ were reported [91], which is within the typical range of an I-CPL emitter, as explained in chapter 2.6.3.

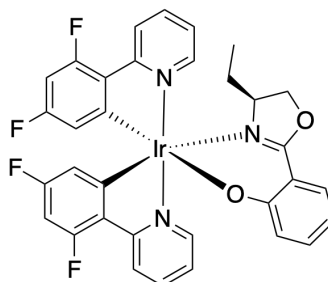


Fig. 2.36: Chemical structure of a chiral iridium complex. The shown complex configuration is called $\Lambda\text{-Ir}(\text{dfppy})_2(\text{R-edp})$ [91].

Since 2015, several more examples of CP-OLEDs have been published [79].

Further examples of E-CPL based CP-OLEDs include different chirally functionalised polymers [64, 78, 81, 82, 83, 87, 92, 93], or mixtures of achiral emissive polymers with a chiral inducer [4, 69, 70, 85, 88, 94, 95, 96, 97, 98, 99].

CP-OLEDs based on small molecule I-CPL emitters are found as metal complexes [54, 75, 76, 91, 100, 101, 102, 103] or organic molecules [12, 46, 71, 73, 74, 77, 99, 104, 104, 105, 106, 107, 108, 109, 110, 111, 112, 113].

Increasing the CP-effect of CP-OLEDs does not only include the development of new materials and systems, but also strategies to increase the g_{EL} value of outcoupled light. As explained in chapter 2.4.2, reflection on each interface of a CP-OLED, but especially on the metal cathode, and the subsequent interference leads to an intensity and polarisation distribution for the outcoupled light. To prevent this reduction of the maximum possible g_{EL} value, this reflection has to be suppressed.

Using a semitransparent cathode (see fig. 2.37) instead of a fully reflective cathode can reduce the interference effect. Light waves in backward direction are outcoupled from the backside of the CP-OLED instead of being reflected and interfering with light waves in forward direction. While these methods might increase the measured g -value, it has to be kept in mind that they achieve this effect by removing light from the outcoupling direction, which naturally decreases device brightness and efficiency.

Yan *et al.* tried to bypass polarisation interference by using a semitransparent cathode consisting of 1 nm CsF, 4 nm Al and 50 nm Ag, hence reducing the amount of reflected light of the wrong handedness. This increased g_{EL} in forward direction by 60% from 1.4×10^{-3} to 2.2×10^{-3} . In backward direction however, a g_{EL} of 5.1×10^{-3} was measured, close to value for g_{PL} for this emitter and an increase of 265% compared to the original device [54].

Zinna *et al.* also reported how increasing cathode transparency with decreasing aluminium thickness for a Ba/Al cathode could boost g_{EL} by 650% up to a value of 0.75. In comparison, the same device with a fully reflective cathode only achieved a g_{EL} of 0.1. However, this value only applied for the $^5\text{D}_0 \rightarrow ^7\text{F}_1$ transition of their CsEu(hfbc) europium complex (see fig. 2.28), which unfortunately had a very low EL intensity [75, 76]. Also, such a device with a cathode thickness of only 4 nm Ba and 6 nm Al could suffer from poor electrical connections and fast device degradation.

A promising alternative could be to use an ITO cathode, which would provide excellent transparency, conductivity and stability. ITO can only be sputtered, however, which brings the risk of higher fabrication temperatures. For the here used polymer based CP-OLEDs, this might provoke a phase change and reduce the CP-effect. Therefore, process conditions would have to be monitored closely.

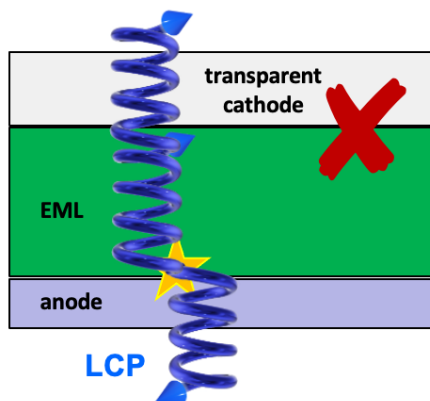


Fig. 2.37: By using a semitransparent cathode, light waves travelling in backward direction are outcoupled from the backside rather than reflected.

Apart from using a semitransparent cathode, no other approaches to reduce light reflection on the cathode in CP-OLEDs have been reported so far. However, other strategies to reduce interference and the resulting polarisation distribution are imaginable.

A scattering electrode, originally designed to increase the outcoupling efficiency in cavity OLEDs, might help remove reflected light with the wrong handedness in CP-OLEDs from the outcoupling direction [114].

Another approach might be the use of an absorbing ETL to filter light in backward direction and reflected light from the cathode.

Wan *et al.* recently published a paper about direction-dependent CP emission in their F8BT + aza[6]helicene mixed system. While it is widely accepted that CP emission in forward- and backward-direction have the same handedness, they state to have found an example where oppositely propagating CP light exhibits opposite handedness. For this, they compared conventional and inverted CP-OLED architectures and found that the inverted stack produced CPL of the opposite handedness as the conventional stack. The explanation for this observation, however, is controversial and shall, not be discussed in this work [98].

2.6.6 Applications of CP-OLEDs

The most immediate benefit of CP-OLEDs, even with only partial polarisation, is an increased light outcoupling efficiency in devices with anti-glare filters. Such filters are used in most display devices today, because the reflection of ambient light, especially sunlight, on the back electrode of displays interferes with the display image and leads to uncomfortable glare effects.

Anti-glare filters consist of a thin film linear polariser and qwp on top of the display (schematic and working principle illustrated in fig. 2.38 (a)). With this design, external light is converted into linearly polarised light (LPL) and subsequently into CPL. When this CPL is reflected on the back electrode, its handedness is reversed. By passing the anti-glare filter once more, the CPL is converted back into LPL. But due to the opposite handedness, this LPL was rotated by 90° compared to the original LPL and is now oriented in blocking direction of the linear polariser and subsequently filtered out. This way, display performance is not disturbed by external light.

Unfortunately, the use of anti-glare filters decreases the light outcoupling efficiency by approximately 50% since unpolarised light from the display also has to pass this filter. CPL, however, does not suffer this loss (see fig. 2.38 (b) and (c)).

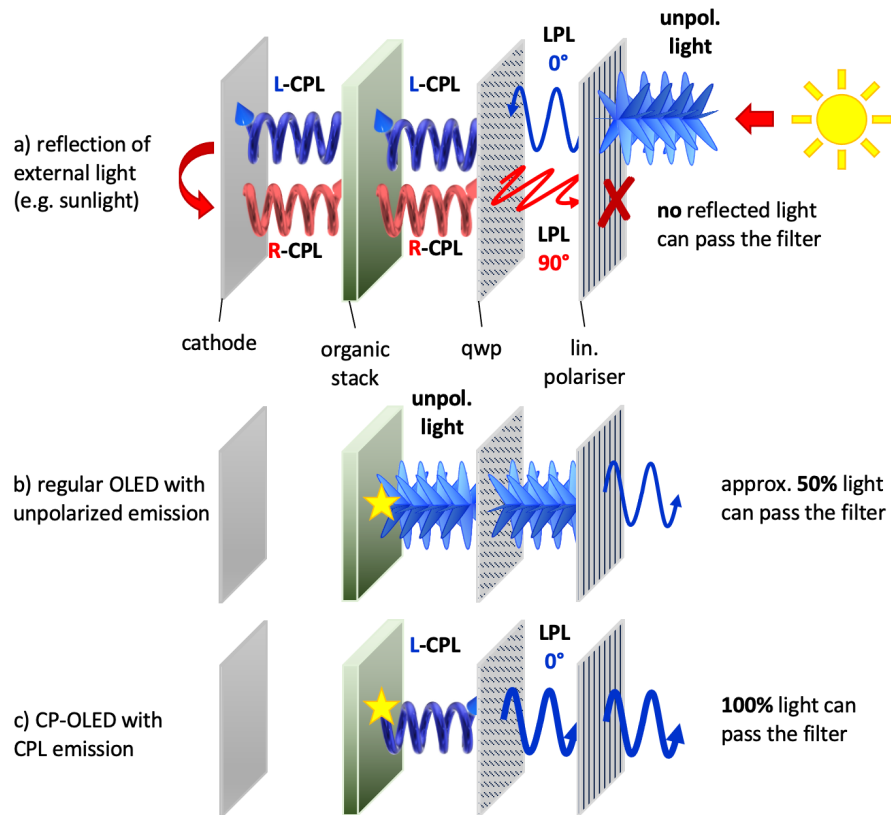


Fig. 2.38: Schematic illustration of an anti-glare filter consisting of (from right to left) a linear polariser, a **qwp**, the organic stack of an OLED and a reflective metal cathode. Shown are three working examples:

(a) Unpolarised sunlight (from the right side) passes the lin. polariser and will be converted into **LPL** (0° in respect to the lin. polariser transmission axis). Passing the qwp will convert it into R-CPL, which will also be retained while passing the organic material. Upon reflection at the cathode, the handedness is reversed to L-CPL. Passing the qwp will revert the light into **LPL** (90°), which, due to the flip in CPL-handedness, is now no longer able to pass the lin. polariser. This way, outside light does not influence display brightness and clarity.

(b) Example of unpolarised light generated from a regular OLED passing the anti-glare filter. Only approx. 50% light can be outcoupled.

(c) Example of CPL generated from a CP-OLED passing the anti-glare filter. 100% of the generated light can pass the filter.

Devices with even partially circularly polarised emission would already show significantly increased outcoupling efficiencies compared to unpolarised devices [12, 115]. Examples of this effect can already be found in literature.

Brandt *et al.* reported a 19% increase in brightness of a CP-OLED with $|g_{EL}| = 0.38$ compared to a non-polarised OLED, both with an anti-glare filter attached [102].

Wan *et al.* reported that the 50% current efficiency decrease for non-polarised devices with anti-glare filter could be reduced to 25% current efficiency decrease in CP-OLEDs with maximum $|g_{EL}|$ up to 1 [70].

Another application field for CP-OLEDs is 3D displays. To perceive a 3D image, a slightly shifted image for the left and right eye has to be projected. Both images must only be observed by their respective eye. The left eye, for example, should only see the left image, and vice versa.

Current 3D displays are based on shutter technology. This means, the left and right image are projected alternately. Through shutter glasses operating at the same frequency as the alternating images, vision through one or the other eye is blocked. This way, each image can only be observed by the corresponding eye. This technology, however, has severe limitations. Harmonizing the shutter frequency of the display and glasses is essential, but prone for errors. Only small margins for viewing angles and distances are possible. Shutter glasses are heavy, expensive and must be regularly charged.

CP-OLEDs, on the other hand, would adapt the same strategy as used in cinemas. The left and right image are projected simultaneously, for example by alternating the L-CP and R-CP pixels in a checker board pattern, or alternately, like in the previously explained shutter technology. To perceive the 3D image, only simple polariser glasses are necessary. Such glasses, as commonly used in cinemas, are much lighter, cheaper, do not require power and function in a much wider angle and distance range. If used without polariser glasses, the display can also be used in 2D mode, as long as all only one image instead of two is projected.

2 Theory

3D displays based on CP-OLEDs, however, would require very large g_{EL} values. Otherwise, the perceived 3D effect would be poor, or the image would be blurry. Therefore, further research and device optimisation is necessary for this technology [79].

3 Results and Discussion

3.1 Measurement set-up for CP-OLEDs

While LIV measurements and unpolarised spectral analysis of CP-OLEDs can be performed just like for regular OLEDs, quantification of the polarisation properties requires a special set-up.

This chapter introduces circularly polarised electroluminescence (CP-EL) measurements as well as interpretation of the results.

3.1.1 Measurement set-up and procedure

As described in chapter 2.4, it requires a qwp and linear polariser in a specific orientation to each other to only allow the RCP or LCP elements of light to pass. These optical components are inserted between the light source and detector. To ensure that as much light as possible reaches the detector, a series of lenses is used to create a collimated light beam. This light beam is directed into a UV/Vis-spectrometer via a large diameter (1500 μm) glass fibre. Fig. 3.1 schematically illustrates the components of this CP-EL measurement set-up.

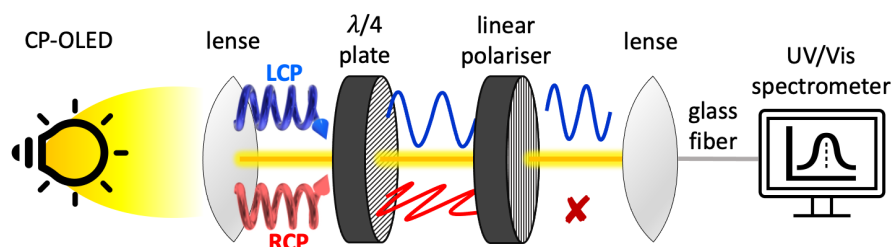


Fig. 3.1: Schematic illustration of a CP-EL measurement set-up, consisting of the CP-OLED, lenses to produce a collimated beam, a qwp, a linear polariser and a detector.

For the actual set-up as seen in fig. 3.2, some additional considerations have to be made. Since differently coloured OLEDs with broad spectra should be measurable, all optical components need to be achromatic in the visible spectrum. To assure a stable and consistent environment, the components are mounted on an optical rail. The device holder is set in a stage with adjustable x-, y- and z-positioning. This

way, different pixels can be centred into the focus for measurement. To operate the individual pixels of the OLED, the device holder features individual contact pins. Measurements are performed in Ar protective atmosphere.

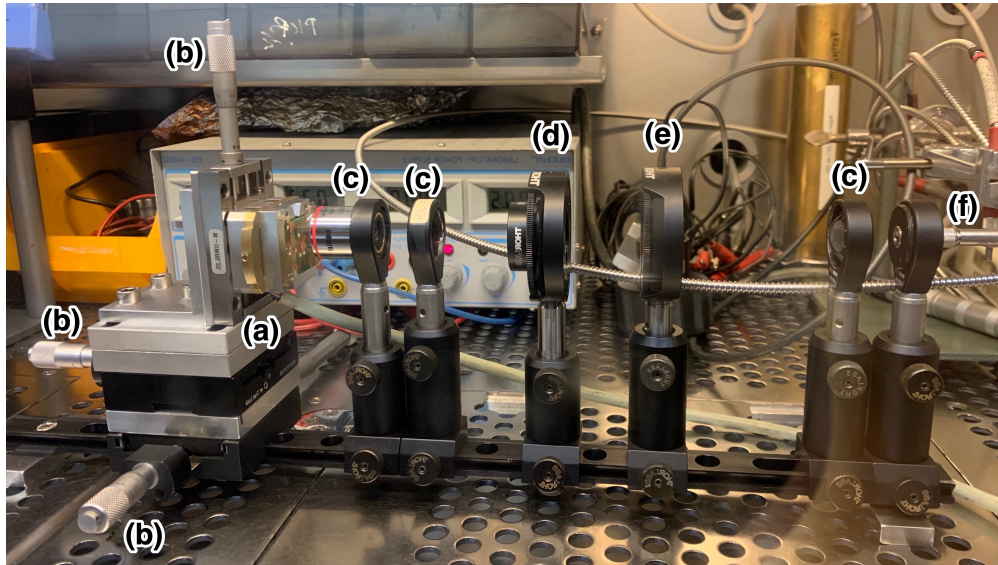


Fig. 3.2: Image of the CP-EL measurement set-up, consisting of a device holder (a) with adjustable stage (b), lenses to produce a collimated light beam (c), a QWP (d), a linear polariser (e), and a fibre cable leading to a UV/Vis spectrometer (f).

As detector, a UV/Vis spectrometer is used. A UV/Vis spectrometer has the benefit of providing a spectrally resolved dissymmetry factor, resulting in a g_{EL} curve rather than only one g_{EL} value.

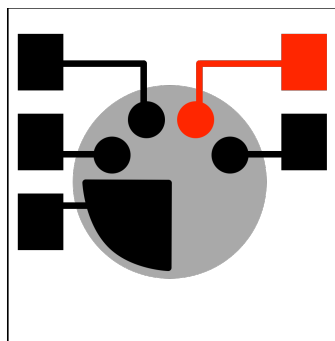


Fig. 3.3: Schematic pixel layout of a CP-OLED.

3 Results and Discussion

After testing different pixel layouts, a shadow mask with three different areas was deemed ideal for CP-OLED analysis with this set-up. Fig. 3.3 displays a schematic of the 1 inch² substrate, with the anode connection to the underlying ITO layer (grey) shown in red.

The three round pixels with an area of 7.87 mm² are used for LIV measurements. CP-EL measurements are performed on the larger pie-slice shaped pixel. Because of the distance between device and glass fibre, not all generated light can reach the detector. Even more light is lost through the polarisers, which leads to a poor signal to noise ratio when measuring smaller pixels or devices with lower maximum brightness. Lastly, an area is deliberately kept free for additional measurements on the organic layers, for example ellipsometry, UV/Vis-absorption and thickness measurement.

CP-EL measurements are performed by manually rotating the polarisers and measuring the remaining light spectrum. As stated in chapter 2.4, all angles are defined from the point of view of the detector, with 0° in 12 o'clock position. To measure L/RCP light, the angle between the transmission direction of the linear polariser (in 0° position) and the fast axis of the qwp has to be -45/+45°, respectively (see tab. 3.1).

Tab. 3.1: Polariser angles to measure L/RCP light, respectively.

linear polariser	qwp	light able to pass	g_{EL}
0°	+45°	LCP	positive
0°	-45°	RCP	negative

3.1.2 Typical data

After measuring the L/RCP light intensities of a CP-OLED, the dissymmetry factor g_{EL} (see eq. 2.25 in chapter 2.6.2) can be calculated. A complete dataset of unpolarised EL (yellow), L/RCP-EL (blue and green) and resulting g_{EL} curve (red) is displayed in fig. 3.4 (a).

While the dissymmetry factor g_{EL} is widely accepted in literature, its mathematical nature (see eq. 2.25 on page 51) makes it prone for errors at lower light intensities. As seen in fig. 3.4 (b), even small background noise outside of the measured EL spectrum leads to unphysical high g_{EL} values and lots of noise. For this reason, in this work, shown g_{EL} curves will be trimmed to a wavelength range in which the EL spectrum has at least 20 % of its maximum intensity (20 % intensity in fig. 3.4 is marked with a dashed line and the trimmed area is indicated in grey).

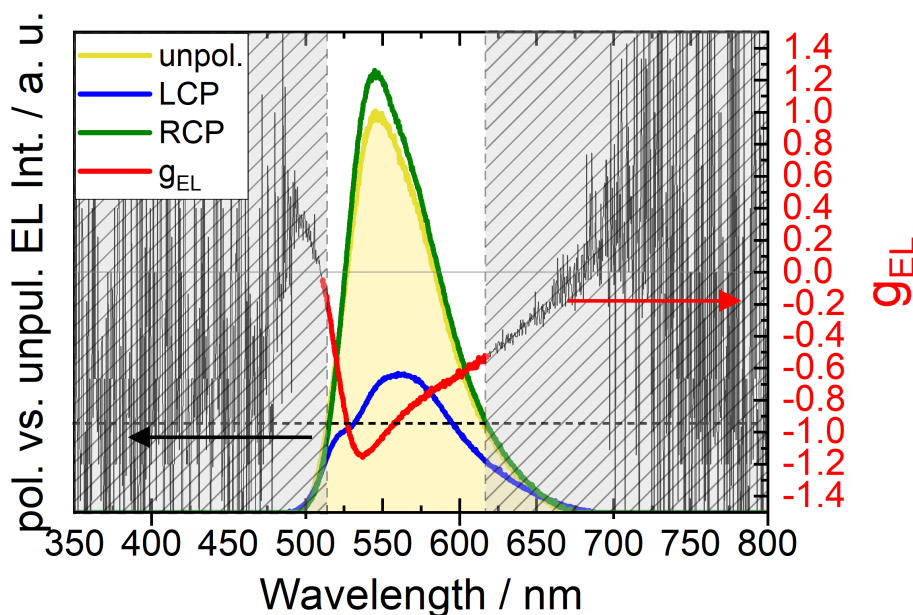


Fig. 3.4: Example of a complete CP-OLED dataset, consisting of the unpolarised EL (yellow), LCP-EL (blue), RCP-EL (green), and the resulting g_{EL} curve (black and red). The calculated complete g_{EL} curve (black) contains extreme noise. Therefore, the dataset outside of the EL-spectral range is trimmed (red) to values with CP-EL intensities above 20 % of the maximum intensity (dashed line and grey area).

3 Results and Discussion

It is, however, not practical to always show CPL data as EL spectra with g_{EL} curves. To easily quantify and compare different CP-effects, a single representative g_{EL} value needs to be chosen. Fig. 3.5 shows three representative examples of normalised EL spectra (green) with their corresponding g_{EL} curves: g_{EL} as calculated by eq. 2.25 and trimmed at 20 % max. EL intensity (blue), and g weighted EL spectrum (g_{w}) as calculated by eq. 3.1 (red), which will be explained on the next pages. For comparison, the EL maximum, as well as three representative g_{EL} values, are marked.

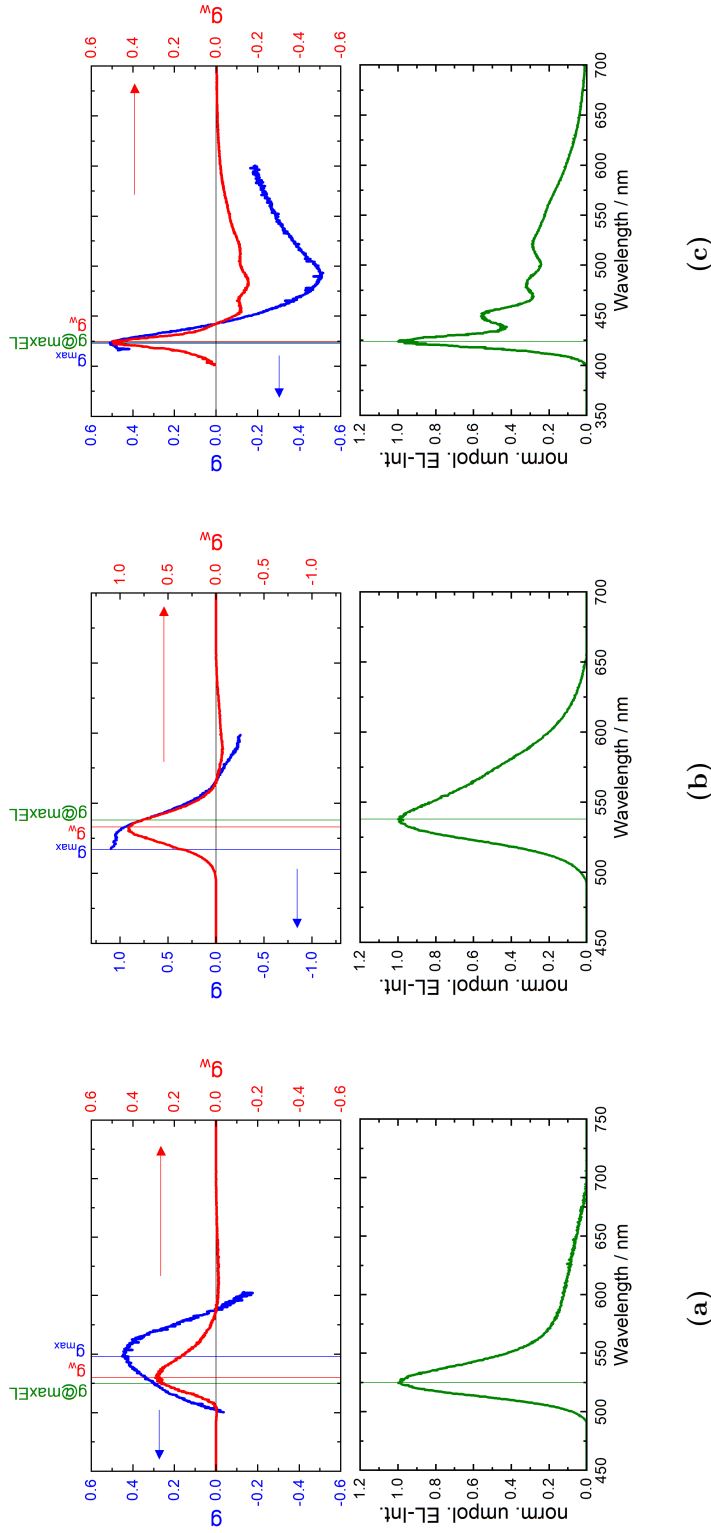


Fig. 3.5: Examples of three different CP-OLEDs, with unpolarised EL spectra (green), gEL curve (blue), and g_w curve (red). Values and corresponding wavelengths for g_{\max} , g_{\maxEL} and g_w are given in tab. 3.2

(a) Example with a well defined gEL curve, with a clear g_{\max}

(b) Example with a strong spectral shift between the LCP and RCP spectra. Here, g_{\max} depends on the trim conditions.

(c) Example of a CP-OLED with multiple EL peaks. While evaluation of the first peak is excellent, all subsequent peaks have a significantly reduced g_w compared to the classic g_{EL} values.

3 Results and Discussion

In most cases, the shape of the g_{EL} curve does not replicate the shape of the EL spectrum, nor is it a constant value. As explained in chapter 2.4.2, reflection on every interface and especially the metal cathode leads to optical interference, resulting in an intensity and polarisation distribution for the outcoupled light beam. Subsequently, a spectral shift between the LCP and RCP spectra occurs.

Depending on the size of this spectral shift between LCP and RCP spectra, maximum g-value (g_{max}) can be close to or far away from the maximum of the unpolarised EL spectrum, or it can even be shifted all the way to the side of the spectrum, where it becomes indistinguishable from the noise. In this case, g_{max} depends on the trim conditions (fig. 3.5 (b)).

As seen in fig. 3.5 (a) and (b), the g_{max} is usually located at a different wavelength than the EL maximum. For CP-OLED displays, however, the polarisation state of the most intense emission is most relevant. This condition is met by the g_{EL} value at the wavelength of the EL spectrum maximum ($g_{\text{@maxEL}}$). While in many cases, $g_{\text{@maxEL}}$ might be smaller than g_{max} , it better represents the useful CPL situation of the device. Therefore, if not otherwise stated, g_{EL} values given in this work will be $g_{\text{@maxEL}}$ values.

In literature, it is not always clear which g_{EL} value is reported, making it more difficult to compare given values from different sources. If possible, the given values should, therefore, always be compared to g_{EL} curves and EL spectra.

Instead of cutting off the g_{EL} curve, it is also imaginable to calculate the g_{w} by multiplying g_{EL} with the normalised unpolarised EL spectrum $\text{Int}_{\text{EL unpol. norm.}}$:

$$g_w = g \cdot \text{Int}_{\text{EL unpol. norm.}} \quad (3.1)$$

In contrast to the g_{EL} curve, g_{w} displays a clear maximum. The shape of the g_{w} curve is usually closer to the shape the EL spectrum than g_{EL} . Outside the wavelength area of the EL spectrum, g_{w} is zero. False g_{EL} values due to background noise and exaggerated g_{EL} values at the edges of the EL spectrum do not occur due

to the low EL intensity, providing a direct baseline correction.

It has to be noted that g_w can never be larger than g_{EL} . By using the normalised instead of the absolute EL spectrum for this calculation, g_{EL} is not increased. The g_{EL} curve will not be multiplied with values larger than one, so g_w remains comparable with other g_{EL} values.

g_w curves are especially valuable when comparing the CP-effect in a series of CP-OLEDs, for example with a varying layer thickness. Compared to g_{EL} curves, it is much easier to see trends like spectral shifts and polarisation maxima. Over all, g_w curves give a more useful image of the CP-effect of CP-OLEDs.

In fig. 3.5, three representative examples are shown, on which the advantages and disadvantage of the different g_{EL} values and curves can be seen.

In example (a), the shape of the g_{EL} curve is similar to the shape of the EL spectrum. Therefore, g_{max} can easily be extracted. The overall shape of g_w is cleaner than the g_{EL} curve. However, in this example, the benefits of g_w over g_{EL} are marginal.

In example (b), the g_{EL} curve does not have a clear maximum. Depending on the cut off conditions, g_{max} changes. Here, the benefits of g_w over g_{EL} are obvious. The g_w curve has a peak like shape with a clear maximum.

In both cases, however, the spectral position of g_{max} does not match the position of the EL maximum. Tab. 3.2, listing the corresponding g_{EL} values and their spectral positions, illustrates how g_w is closer to $g@maxEL$ than g_{max} .

Evidently, this method proves a very useful tool for EL spectra with only one peak. For EL spectra with multiple peaks, g_w is less convincing, as example (c) shows. For the largest EL peak, in this case the first peak, $g@maxEL$, g_{max} and g_w match almost perfectly. However, g_w values of all subsequent lower intensity EL peaks are dampened. While the g_w curve replicates the peaks from the EL

3 Results and Discussion

spectrum, the g_{EL} curve is smooth, indicating a continuous change of optical properties independent of vibronic progression in emission. This has to be considered when evaluating g_w data of multi peak EL spectra.

Tab. 3.2: Different g_{EL} values from fig. 3.5. Shown are $g@maxEL$, g_{max} and g_w and their corresponding wavelengths.

	(a)		(b)		(c) 1. peak		(c) 3. peak	
$g@maxEL$	+0.27	525 nm	-0.77	538 nm	-0.50	424nm	-0.48	480nm
g_{max}	+0.45	548 nm	-1.29	514 nm	-0.51	423 nm	-0.51	490nm
g_w	+0.33	530 nm	-0.83	530 nm	-0.50	424 nm	-0.16	480nm

3.1.3 CP-EL Artefacts

In principle, it would suffice to measure each constellation, LCP and RCP, only once. To minimise artefacts and errors, however, multiple measurements and averaging are recommended. In this work, a series of four measurements for each handedness provided good results. Each set of one LCP and one RCP measurement calculate one g_{EL} curve, resulting in four g_{EL} curves which can be averaged into one g_{EL} curve:

$$\underbrace{L_1 R_1}_{g_1} \underbrace{L_2 R_2}_{g_2} \underbrace{L_3 R_3}_{g_3} \underbrace{L_4 R_4}_{g_4} \quad (3.2)$$

$$\frac{g_1 + g_2 + g_3 + g_4}{4} = g_{ave}. \quad (3.3)$$

3.1 Measurement set-up for CP-OLEDs

It has to be considered, though, that all devices suffer from degradation over time, especially during operation, which possibly leads to artefacts. Therefore, it is essential to measure LCP and RCP data alternatively:

$$\underbrace{L_1 R_1}_{g_1} \underbrace{R_2 L_2}_{g_2} \underbrace{L_3 R_3}_{g_3} \underbrace{R_4 L_4}_{g_4} \quad (3.4)$$

Fig. 3.6 shows an example of a g_{EL} curve artefact through degradation in a unpolarised OLED. The measurement sequence used for this example is of the type "LRLR". Each set of L/RCP data, which subsequently generates one g_{EL} curve, starts out with an LCP measurement. In the given example, the device suffered from particularly fast degradation, resulting in differences between each LCP (blue) and RCP (red) measurement. Subsequently, this leads to the calculation of a false non-zero g_{EL} curve.

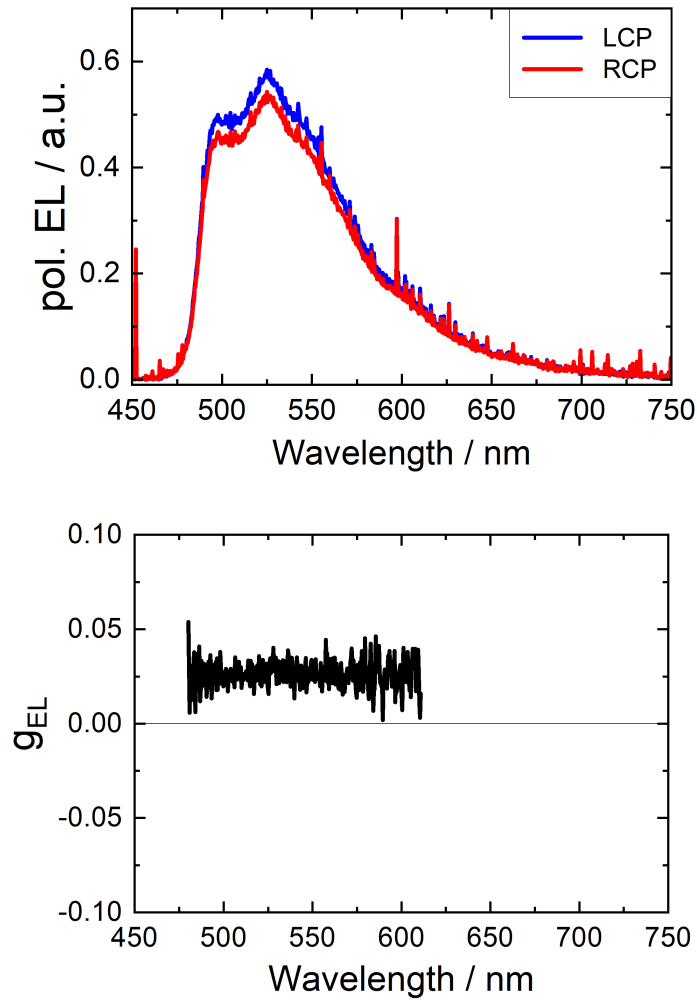


Fig. 3.6: Subsequently measured LCP (blue) and RCP (red) spectra (top) and subsequent artefact g_{EL} curve (bottom) for an unpolarised OLED. Degradation during the measurement can be seen by the difference between the LCP and RCP spectra, leading to an artefact non-zero g_{EL} curve.

To solve this problem, a measurement sequence of the type "LRRL" is proposed instead. While each pair and resulting g_{EL} curve might still contain an artefact, combining the two g_{EL} curves with opposite artefacts produces a more exact value, assuming that each IV curve led to a similar degradation. In this work, measurements performed with this sequence produced more reliable results, even for degrading devices.

3.1.4 Possibilities and limitations of CD measurements

As an indicator for chiral phase behaviour in thin films, circular dichroism (CD) measurements are extremely useful. For E-CPL systems based on chiral phases, CD results usually follow the same trends as CP-EL data. However, thin films can be prepared much easier than OLED devices. This makes CD measurements a great way to quickly analyse new material systems or assess the impact of different curing conditions.

Most CD spectrometers, however, are optimised for solution based measurements, which can cause problems when measuring thin film samples. Here, CD data is derived from ellipsometry measurements, specifically from *Müller* matrix (MM) measurements in transition. An extensive explanation of this measurement and evaluation process is given in chapter 2.4.5.

The CD signal depends on two aspects: the properties of the chiral phase and the thickness of the measured layer. Since MM ellipsometry measurements are performed in transition geometry, light absorption following the *Lambert-Beer* law has to be considered.

$$\log\left(\frac{I}{I_0}\right) = -\epsilon_\lambda \cdot c \cdot d \quad (3.5)$$

Through eq. 3.5, the absorption of light can be calculated, with the incident light I_0 and transmitted light I intensities, the molar extinction coefficient ϵ of the absorbing material for a given wavelength λ , as well as the concentration c and sample thickness d [116]. The same principle applies for the absorption of polarised light, as it is measured in MM ellipsometry to calculate CD data.

Depending on the sample properties, complete absorption of the incident light, or one polarisation state, is possible. This leads to the calculation of unphysical CD results. Fig. 3.7 illustrates such an example for different layer thicknesses of a chiral phase sample, here 74 nm to 206 nm of a cured F8BT + 10 wt%R5011 thin film (the properties of this system as well as the used materials will be introduced in chapter 3.8 and are not relevant at this point.)

3 Results and Discussion

CD values are usually normalised by dividing them through the layer thickness. This is comparable to the division of solution CD values by the concentration. The resulting values are called thickness-normalised CD coefficient CD^* . Analogous to the extinction coefficient ϵ in concentration dependent absorption, CD^* would be expected to be constant. However, this is not the case here, as seen in fig. 3.7 (bottom). This suggests that the size of the chiral domain responsible for the CD effect is larger than the layer thickness. In this work, this is the case for all shown E-CPL systems.

As expected, CD values increase with increasing layer thickness. To compare different samples, the maximum CD intensity of the largest signal, in this case at 490 nm (right dashed line), is typically chosen. Unfortunately, the sample with 206 nm layer thickness in this example exceeds the polarised absorption limit, leading to unphysical CD values in this spectral region. The CD signal peak around 490 nm is, therefore, missing.

It is, however, still possible to compare such samples at a different wavelength without unphysical values. This can be done, for example, at the position of the second largest signal peak, here 347 nm (left dashed line). Fig. 3.7 (bottom) compares CD^* data at both signals. Due to the previously explained absorption limit, the last data point of the 490 nm signal is missing.

While the 490 nm signal produces over all larger values and a larger slope than the 347 nm signal, both signals follow the same trend. In general, when comparing CD data of different samples, one should always confirm that values from the same signal peak are compared.

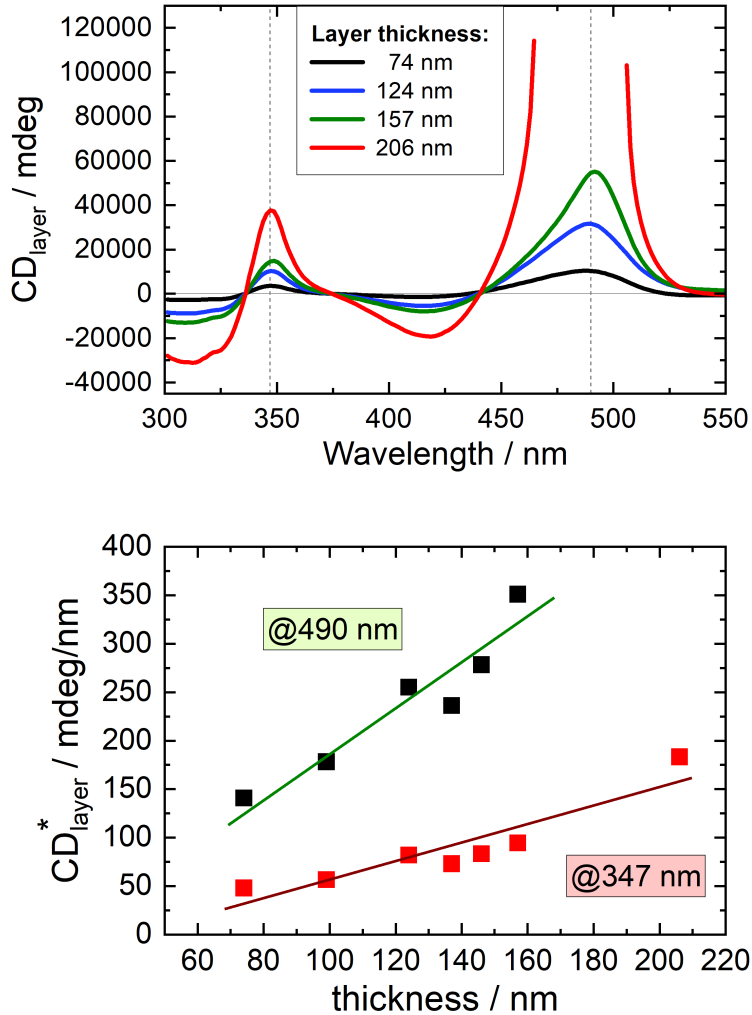


Fig. 3.7: CD curves (top) and CD^* values at 347 nm (red) and 490 nm (green) (bottom) of F8BT + 10 wt%R5011 thin films with different layer thicknesses. Samples were cured for 10 min at 190 °C to develop a chiral phase. Around 490 nm, the 206 nm thick sample reaches the polarised absorption limit, resulting in unphysical CD values which are removed.

3.2 Polymeric emitters in thin film and OLED

The application of π -conjugated polymers in organic electronics in general, as well as PFs and F8BT specifically, was introduced in chapter 2.3. The following chapters will focus on more detailed information of the thin film behaviour of these two polymers, as well as their application as EML in OLEDs. Before introducing chiral components in the form of chiral functionalities (chapter 3.7) or chiral inducers (chapter 3.6 and 3.8), the neat polymer properties and a well performing OLED device architecture need to be addressed.

For polymer based CP-OLEDs, thermal annealing, also called curing, is a crucial factor. The following chapters show some examples of annealing and how this influences the optical and electrical properties of thin films and OLEDs. Further details about curing are given in chapter 3.4.

3.2.1 PF thin films

The properties and phases of PFs were introduced in chapter 2.3.1. As a practical example, fig. 3.8 shows the absorption and PL spectra of a PFO thin film. Compared are a pristine sample (top) directly after spin-coating, a sample treated with SVA (middle), and a cured sample (bottom).

The pristine thin film of PFO shows an absorption peak around 382 nm, which is typical for the randomly oriented glassy or α phase. The PL spectrum features two main peaks at 423 nm and 439 nm, representing the first two vibronic transitions of the α phase. The first peak is slightly red-shifted compared to the value shown in tab. 2.1. This is a typical result of aggregation, which is to be expected in thin films.

After SVA¹ treatment, the main absorption peak is red-shifted and an additional peak at 433 nm appears, characteristic for the more planar β phase. Subsequently,

¹SVA 60 min in CHCl₃ vapour at RT.

PL peaks are also shifted to 439 nm and 466 nm.

Thermal annealing, also called curing, of either the pristine or **SVA** layer leads to an additional colour shift. The absorption peaks broaden and the characterising β absorption peak disappears. PL peaks are shifted to 432 nm and 455 nm, which represents the γ phase.

A more detailed overview of how curing effects polymer thin films is given in chapter **3.4** for F8BT. Analysed parameters include thin film volume reduction, surface roughness, and changes in absorption and PL behaviour for different molecular weights. While these experiments were not performed for PF, it is likely that PFs would behave similarly to F8BT in this regard.

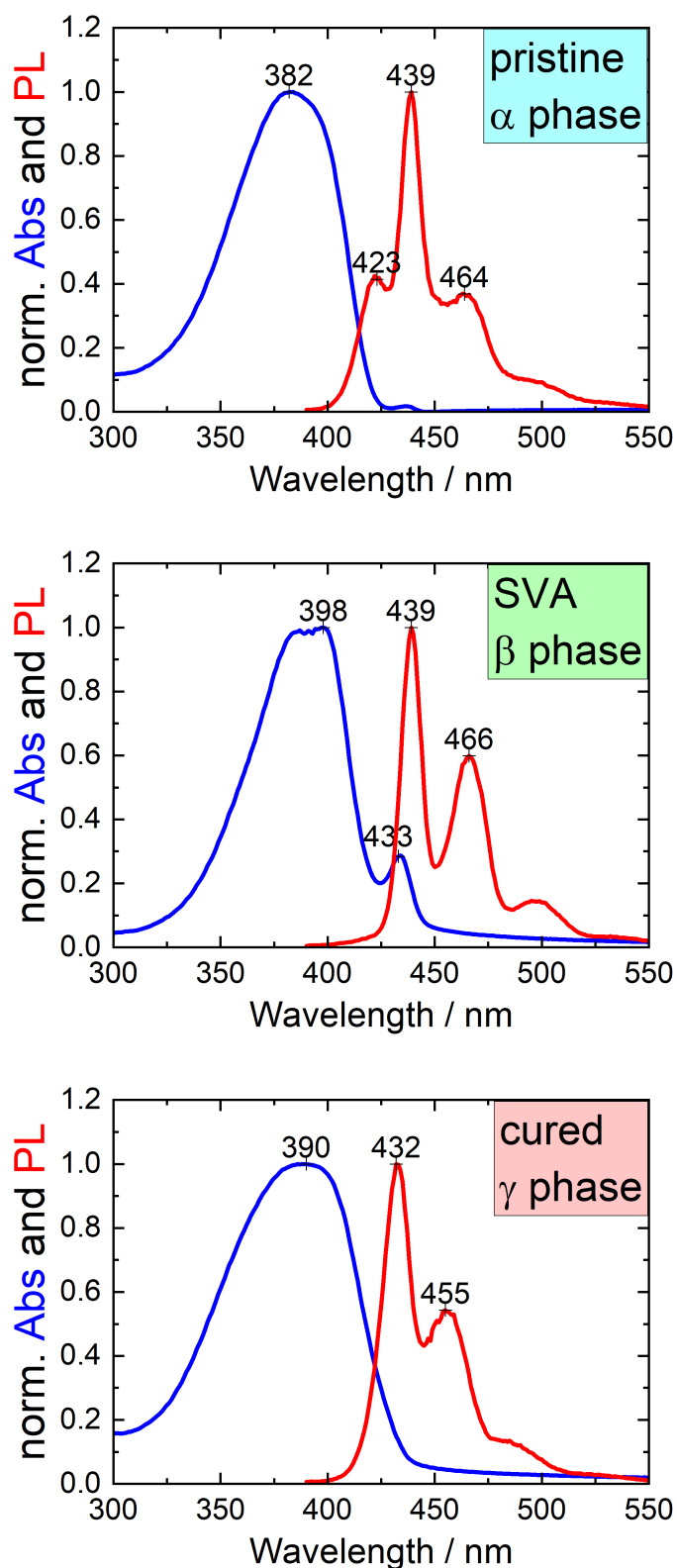


Fig. 3.8: Absorption (blue) and PL (red) spectra of PFO thin films ($M_w = 270$ kg/mol). The sample was measured pristine (top), after SVA treatment (middle), and cured 15 min at 200 °C (bottom); $\lambda_{ex} = 370$ nm.

3.2.2 F8BT thin films

The co-polymer F8BT was introduced in chapter [2.3.2](#). In this section, a focus shall be put on F8BT properties in thin films and devices, specifically.

Fig. [3.9](#) shows absorption spectra of a pristine F8BT thin film sample. Compared to PFs, F8BT features a second absorption peak around 460 nm. In contrast to the multi-peak PL vibronic fine structure of PFO, F8BT only has one broad emission peak around 550 nm. Both effects, the second absorption peak as well as the red-shifted PL, are a result of the co-polymerised BT unit.

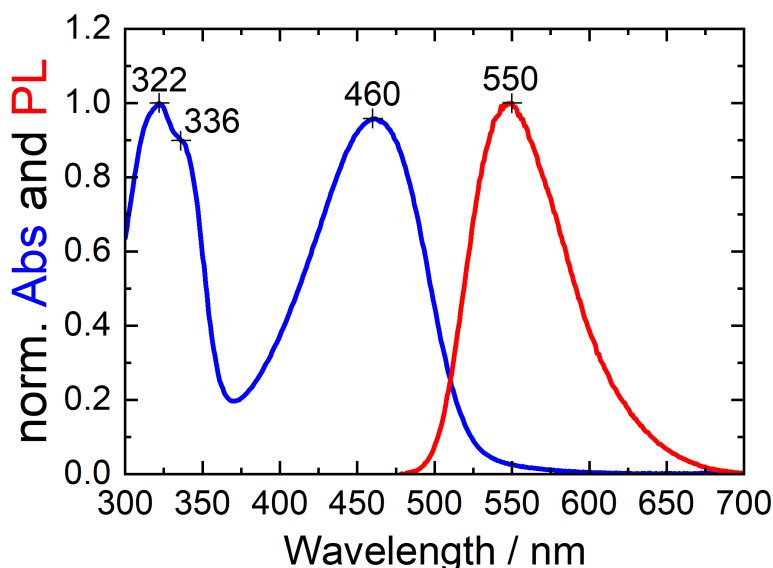


Fig. 3.9: Normalised absorption (blue) and PL (red) spectra of a pristine spin-coated F8BT thin film; $\lambda_{\text{ex}} = 460$ nm.

The absorption and PL behaviour of F8BT thin films can change significantly after curing. However, those phenomena strongly depend on the polymer molecular weight. An in depth analysis is given in chapter [3.4.4](#).

3.2.3 PF OLEDs

As explained in chapter 2.2.3, choosing a suitable multi-layer OLED architecture is crucial to maximise device brightness, efficiency and lifetime. This is especially important for CP-EL measurements, where low brightness or rapid device degradation can render such measurements impossible.

The standard stack used in this work for PF based OLEDs is shown in fig. 3.10 (b). In (a), the energetic properties of the materials reveal an energetic staircase for holes. While different polymers might have different properties, this device architecture applies to all PF based OLEDs used in this work, including chirally functionalised PFs in chapter 3.7.

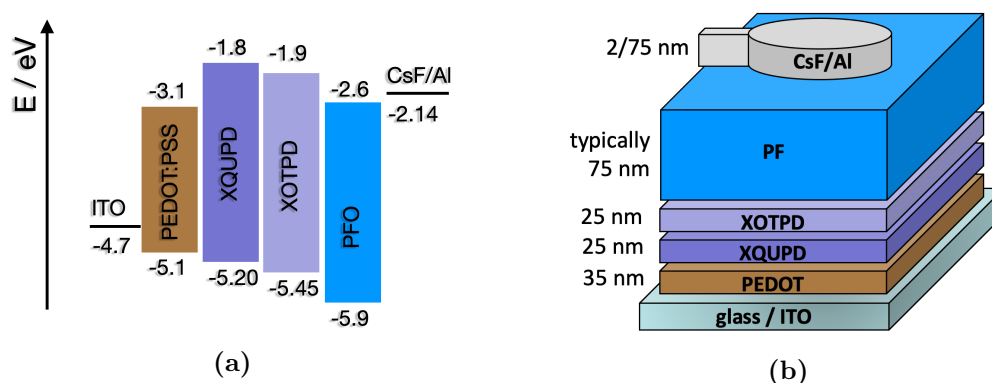


Fig. 3.10: Energetic levels (a) and OLED device architecture (b) of a standard PF based OLED.

To improve hole injection from the ITO anode, PEDOT:PSS is used as **HIL**. QUPD and OTPD are introduced as **HTLs**. After the **EML**, a CsF/Al cathode is added.

If not otherwise stated, all OLEDs in this work are based on this architecture. Detailed information on the used materials as well as device fabrication can be found in chapters 6.1 and 5.2.10, respectively. Stack variation and optimisation can be found in chapter 3.2.4.

Fig. 3.11 shows PL (top) and EL (bottom) spectra of PFO thin films and OLEDs.

This way, the PL and EL spectra of pristine, SVA treated and cured samples can be compared.

Despite the differences in molecular weight, curing temperature and layer thickness, it can be seen that the first EL peaks match the PL peaks of their respective phase. The pristine device with predominantly α phase features two sharp peaks at 423 nm and 440 nm. The SVA treated device features the typical β phase peaks at 440 nm and 468 nm. Typical for γ phase, the cured device features peaks at 436 nm and 459 nm.

In contrast to the PL spectra however, the EL spectra of all three devices also feature multiple red-shifted peaks of significant intensity around 500 nm, often even surpassing the main peak intensities. These peaks can be explained by the presence of multiple superimposed effects. The vibrational fine structure of the EML itself, emission of aggregates, as well as optical and cavity effects can play a role. Additionally, devices annealed at a higher temperature frequently suffer from degradation, resulting in the appearance of a broad, red-shifted emission band. In the following chapters, these effects will be introduced and analysed for both, unpolarised and polarised systems.

It has to be noted that the samples shown in fig. 3.11 have different layer thicknesses. While this is not relevant for the normalised PL spectra, EML thickness differences influence the shape of the outcoupled EL spectra and LIV performance, as explained below.

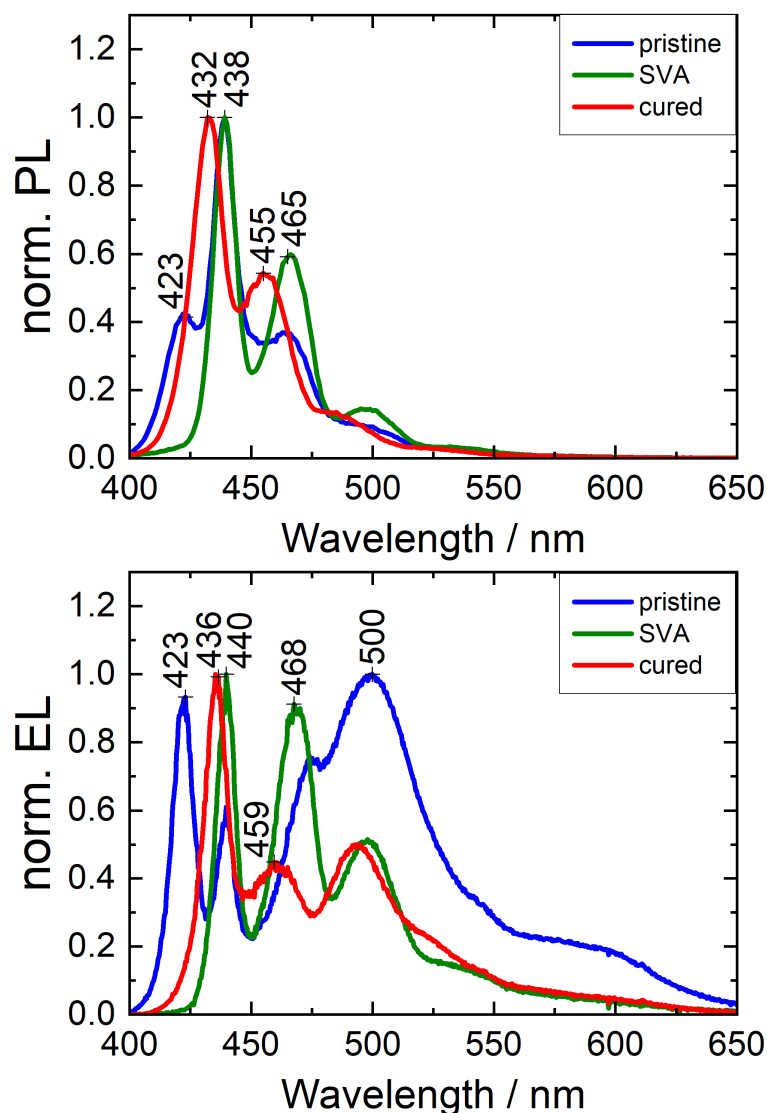


Fig. 3.11: Normalised PL (top) and EL (bottom) spectra of PFO thin films and OLEDs, pristine (blue), after SVA treatment (green) and cured (red). $\overline{M}_w = 32$ kg/mol (SVA EL data) and 270 kg/mol (all others). Curing $T = 180$ °C (EL) and 200 °C (PL). PFO layer thickness (pristine / SVA / cured) = 85 / 65 / 85 nm (PL) and 230 / 85 / 230 nm (EL). PL $\lambda_{\text{ex}} = 460$ nm.

In fig. 3.12, LIV performance data corresponding to the EL data in fig. 3.11 (bottom) is shown. LIV performance data consists of current density (J), device bright-

ness or luminance (L) and device efficiency (Eff) values plotted against operating voltage. It has to be considered, however, that, while the pristine and cured devices are comparable in molecular weight and EML thickness, the SVA treated device is not. With a significantly lower EML thickness, it shows a much lower turn on voltage (V_{on}) than the thicker devices. The influence of different EML thicknesses is shown in fig. 3.13. Also, the SVA treated device was built with a lower molecular PFO batch than the pristine and cured devices. While the influence of varying the molecular weight of the emissive polymer was not studied for PFO in this work, chapter 3.3 analyses this parameter for F8BT.

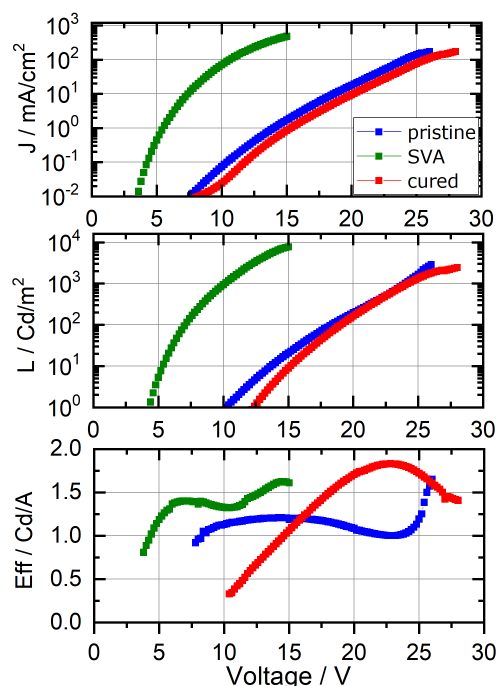


Fig. 3.12: LIV performance data for different PFO based OLEDs. Shown are current density (J), luminance (L) and efficiency (Eff) values plotted against operating voltage.

PFO (M_w = 32 kg/mol (SVA) and 270 kg/mol (pristine and cured)) is shown pristine (blue), SVA treated (green) and cured 15 min at 180 °C (red).

Device architecture: ITO / PEDOT / XQUPD / XOTPD / PFO / CsF/Al, EML thickness = 85 nm (SVA) and 230 nm (pristine and cured).

3 Results and Discussion

Fig. 3.13 illustrates the influence of different EML thicknesses on the shape of the EL spectrum and device performance. While this parameter is of no consequence for PL spectra, it has a significant impact on the relative position of the recombination zone to the reflecting cathode. Subsequently, the intensities and interference patterns of the outcoupled EL peaks are influenced. It is, therefore, extremely important to keep as many conditions as possible constant when comparing different devices. This phenomenon, which was explained in chapter 2.4.2, likewise applies to pristine and annealed PF and F8BT based OLEDs.

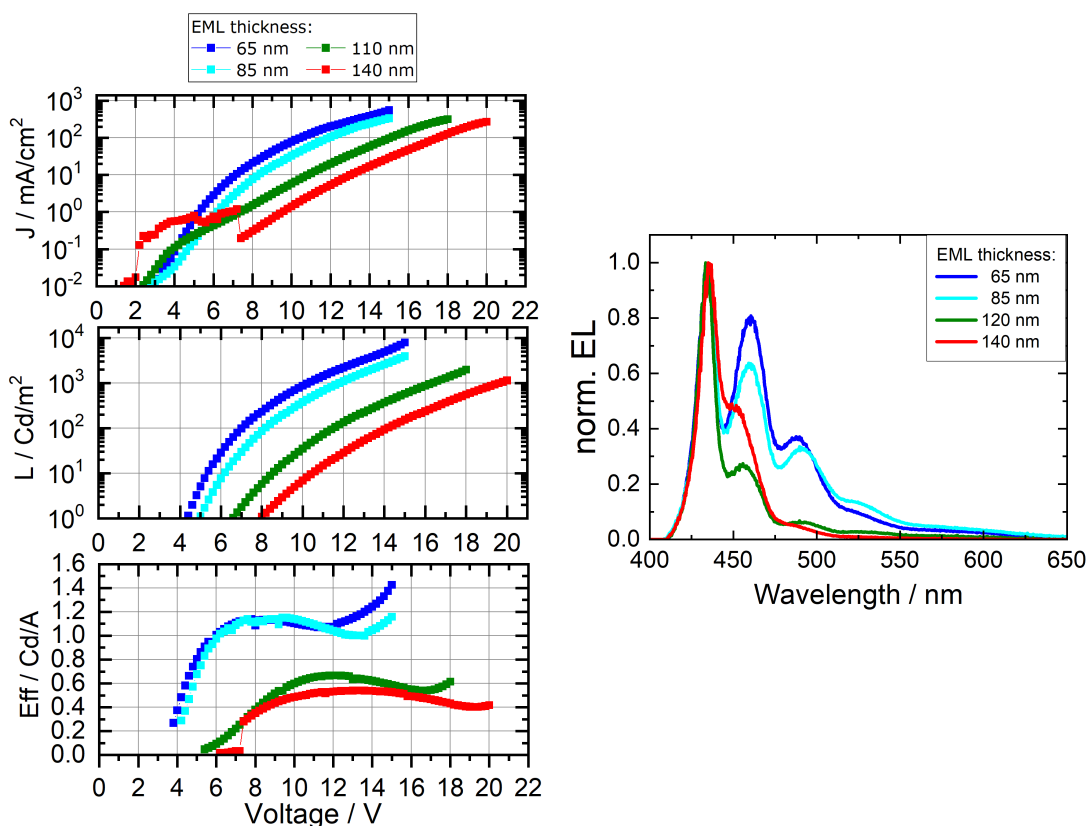


Fig. 3.13: LIV performance data (left) and EL spectra (right) of PFO based OLEDs. EML thickness is varied between 65 nm and 140 nm. Device architecture: ITO / PEDOT / XQUPD / XOTPD / PFO / CsF/Al, $M_w = 270$ kg/mol. EML thickness = 65 - 140 nm. Cured 15 min at 180 °C.

3.2.4 F8BT OLEDs

A suitable device stack is the base for good OLED performance. While the primary aim of this work is not to optimise the performance of polymer based OLEDs in general, good device performance, especially in terms of sufficient brightness, is incremental for CP-EL measurements of CP-OLEDs. In literature, many different approaches to F8BT based OLEDs can be found.

Yan *et al.* analysed the following device stack: ITO / PEDOT:PSS (50 nm) / F8BT (80 nm) / Ba (4 nm) / Al. They reported a maximum brightness of $L_{\max} = 7,000$ and $20,000$ Cd/m² and maximum efficiencies of $\text{Eff}_{\max} = 2.8$ and 6.0 Cd/A for uncured devices and device that were cured for 30 min at 120 °C [117].

F8BT is also used in mixed system CP-OLEDs, where it is combined with a chiral inducer. This approach was also used in this work.

Lee *et al.* analysed CP-OLEDs with the following stack: ITO / CuCP (2 nm) / polyimide (20 nm) / F8BT + 10 wt% R5011 (200 nm) / TPBi (20 nm) / LiF (1 nm) / Al, which were cured for 10 min at 150 °C. They reported a $L_{\max} = 4,000$ Cd/m² and $\text{Eff}_{\max} = 4.5$ Cd/A, as well as a $V_{\text{on}} = 5.7$ V [4].

Similarly, Wan *et al.* also analysed CP-OLEDs, but with a different chiral inducer. They used the following stack: ITO / PEIE-modified ZnO / F8BT + 10 wt% aza[6]helicene (180 nm) / TCTA (40 nm) / MoO₃ / Au, which were cured for 10 min at 140 °C. They reported a $L_{\max} = 28,500$ Cd/m² and $\text{Eff}_{\max} = 16.4$ Cd/A, as well as a $V_{\text{on}} = 2.3$ V [96].

In this work, in analogy to PF based OLEDs, a standard device architecture of ITO / PEDOT / XQUPD / XOTPD / F8BT / CsF/Al was chosen for F8BT based OLEDs. If not otherwise stated, all OLEDs in this work are based on this architecture. Detailed information on the used materials as well as device fabrication can be found in chapters [6.1] and [5.2.10], respectively.

3 Results and Discussion

With this stack, OLED performances up to $L_{\max} = 10,000 \text{ Cd/m}^2$, $\text{Eff}_{\max} = 10.0 \text{ Cd/A}$ at $V_{\text{on}} = 4 - 9 \text{ V}$. However, device performance strongly depends on layer thickness (see fig. 3.18), curing conditions (see fig. 3.19), chiral inducer concentration (see chapter 3.12) and F8BT molecular weight (see chapter 3.3). Also, depending on environmental and laboratory conditions, a noticeable batch to batch variation between individual experiment sets can occur. A typical CP-OLED in this work optimised for a large $g@_{\max\text{EL}}$ of 1.1 achieves $L_{\max} = 5,000 \text{ Cd/m}^2$ and $\text{Eff}_{\max} = 5.3 \text{ Cd/A}$ with $V_{\text{on}} = 6.5 \text{ V}$.

Fig. 3.14 shows the energetic levels (a) and stack architecture (b) for F8BT based OLEDs used in this work. For CP-OLEDs, the EML can also contain a chiral inducer.

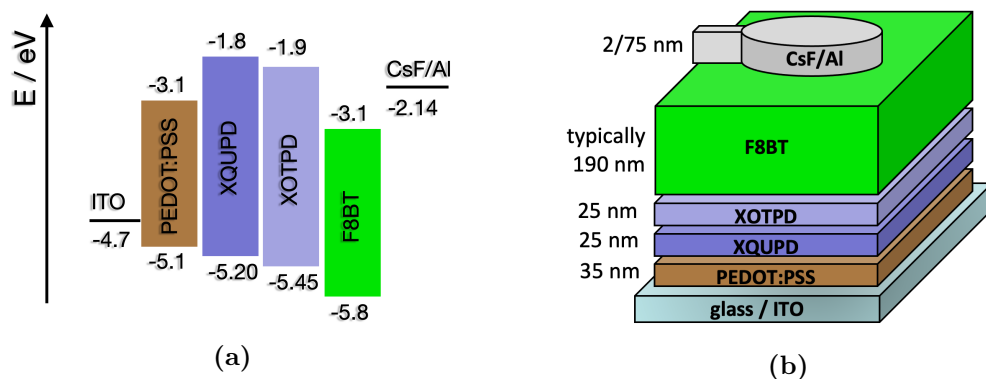
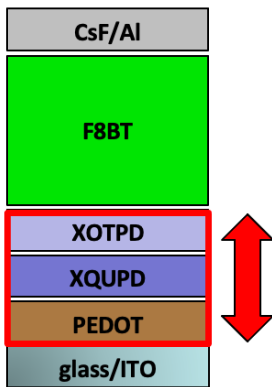


Fig. 3.14: Energetic levels (a) and OLED device architecture (b) of a standard F8BT OLED.

The LIV characteristics shown in fig. 3.15 point out the impact of architecture variations on device performance.



In (a), the stack composition is altered to highlight the beneficial effect of the chosen supporting layers, PEDOT, QUPD and OTPD. Three otherwise equivalent F8BT based OLEDs are compared. One without any HIL/HTL (blue), one only containing PEDOT:PSS as **HIL** (green), and the standard architecture with both, PEDOT:PSS as **HIL** and XQUPD and XOTPD as **HTL**s (red). Even with only the PEDOT layer, device performance is already improved significantly. This is noticeable through a greatly reduced V_{on} and increased L_{max} and Eff_{max} . Introducing QUPD and OTPD improves device performance even further. Not only is the efficiency increased, the layers also help device stability, decreasing the speed of degradation. This is particularly important for CP-OLEDs, as device degradation during CP-EL measurements lead to artefacts.

In (b), the layer thicknesses of the three supporting layers are varied. Within the shown thickness range, no significant differences in device efficiency are found. This is important for batch to batch comparability, since unintentional layer thickness variation of this magnitude can occur in laboratory scale OLED production. The impact of a more extensive XOTPD thickness variation on device performance is shown in fig. 3.73 in chapter 3.10.

3 Results and Discussion

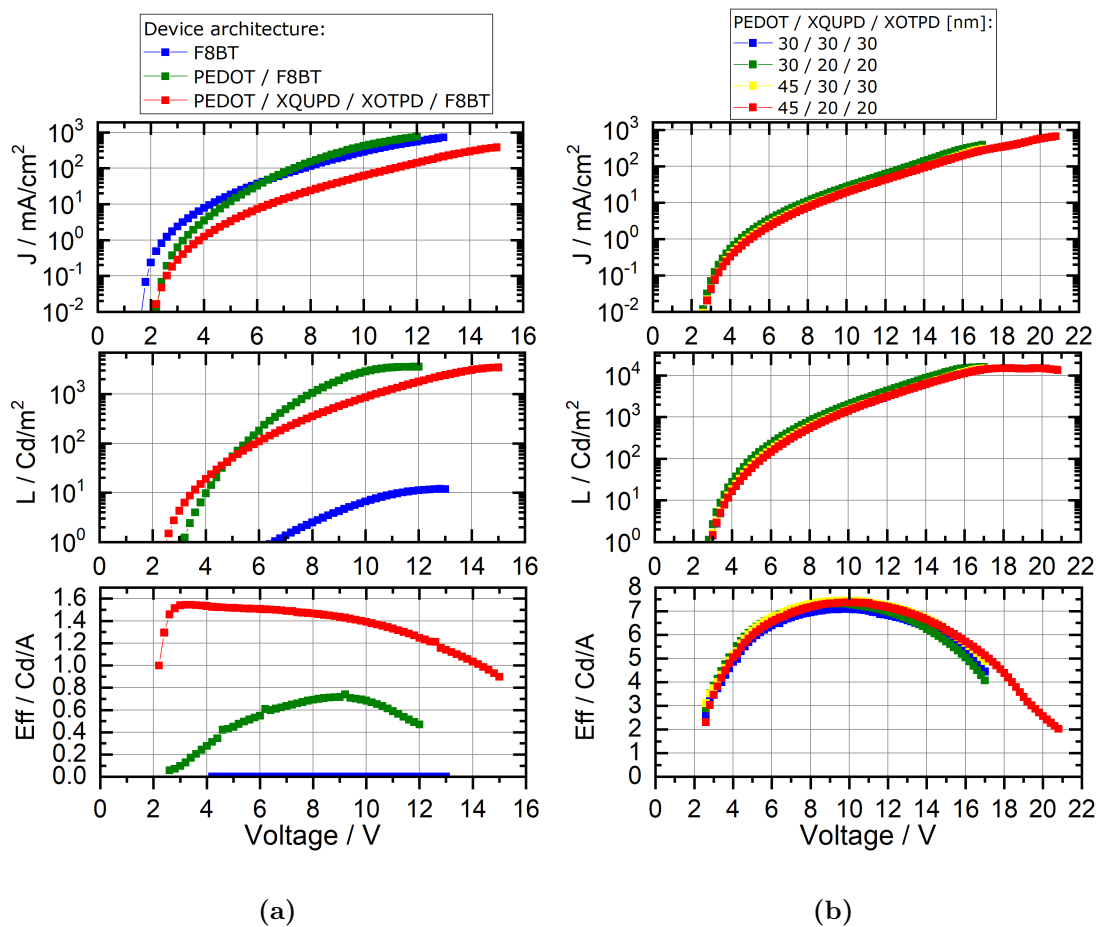


Fig. 3.15: LIV performance data for different F8BT based OLEDs. Shown are current density (J), luminance (L) and efficiency (Eff) values plotted against operating voltage.

(a) Architecture variation of otherwise equivalent F8BT based OLEDs. Compared are devices without any HIL/HTL (blue), with only PEDOT:PSS as **HIL** (green), and the standard architecture with both, PEDOT:PSS as **HIL** and XQUPD and XOTPD as **HTL**s (red).

(b) HTL thickness variation with a standard device architecture.

Device architecture: ITO / PEDOT / XQUPD / XOTPD / F8BT / CsF/Al. EML thickness = 115 nm (a) and 195 nm (b). M_w (F8BT) = 37 kg/mol.

EL spectra for the LIV data in fig. 3.15 are shown in fig. 3.16. The first three spectra belong to fig. 3.15 (a) and are coloured respectively. The orange spectrum belongs to fig. 3.15 (b). The first dataset with 30 nm PEDOT, 30 nm XQUPD and 30 nm XOTPD is chosen as representative, since all EL spectra of this set are almost identical.

The low brightness of the F8BT only device leads to a poor signal to noise ratio. Therefore, the EL spectrum is not shown here. Because of their higher brightness, the devices with PEDOT (green) and HTMs (red) exhibit smooth spectra. The difference between the two devices with HIL and HTMs is a result of the different EML thicknesses. As shown in fig. 3.18, EML thickness has a large impact on the spectral shape.

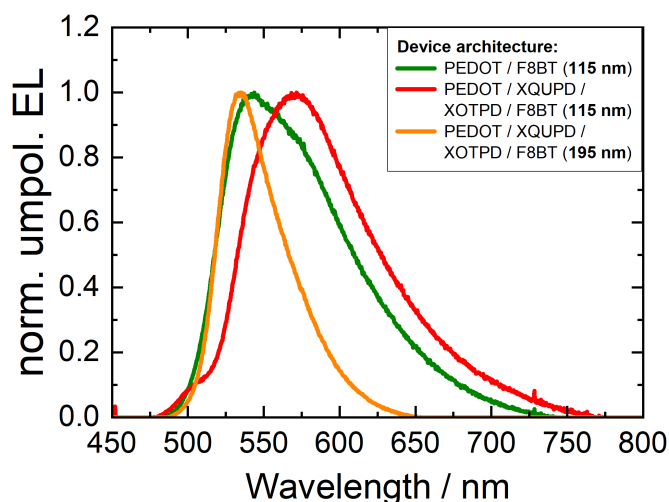
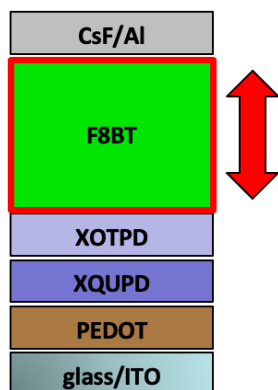


Fig. 3.16: EL spectra for the LIV data in fig. 3.15. The green and red spectra belong to fig. 3.15 (a) and are coloured respectively. The orange spectrum belongs to fig. 3.15 (b). The first dataset with 30 nm PEDOT, 30 nm XQUPD and 30 nm XOTPD is chosen as representative, since all EL spectra of this set are almost identical.

Device architecture: ITO / PEDOT (32 nm) / XQUPD (33 nm) / XOTPD (31 nm) / F8BT / CsF/Al. EML thickness = 115 nm (blue, green, red) and 195 nm (orange). M_w (F8BT) = 37 kg/mol.



Device performance is not only defined by the stack architecture, but also by the thickness of each layer. In this regard, EML thickness has the most significant influence. Fig. 3.18 (a) shows the effect of varying the EML thickness of an F8BT based OLED. With increasing EML thickness, resistance increases, resulting in a higher V_{on} . However, as shown in (c), there is no linear correlation between EML thickness and Eff_{max} . To understand this phenomenon, EL spectra shown in (b) have to be considered as well. It can be seen that the EML thickness variation leads to a spectral shift back and forth, with EL maxima between 517 nm and 593 nm. This shift can also be observed as a changing emission colour from green, to chartreuse, to yellow and orange. The highest L_{max} and Eff_{max} are found for an emission maximum around 535 nm. Within the shown range, an EML thickness around 190 - 200 nm showed the overall best performance. Therefore, it was chosen as standard EML thickness for F8BT based OLEDs in this work.

To highlight the spectral EL shift, the EL main and shoulder peaks are plotted in (d). The values are plotted over total device thickness. Initially, increasing the EML thickness shifts the emission peak towards higher wavelengths, which is indicated by trend-lines. Around a total thickness of 225 nm, a second EL peak appears at a lower wavelength. For this representation, the smaller of these two peaks (marked in red) is called shoulder peak. Increasing the EML thickness even further results in an inversion between those two peaks, thereby flipping the main emission back towards lower wavelengths. After this jump, the same emission wavelength increase with further increase of the EML thickness occurs as before. The same jump is also found around a total thickness of 375 nm, indicating a periodical effect. As introduced in chapter 2.4.2, these trend-lines represent different resonant modes, which could be $\frac{\lambda}{2}$ (left), λ (middle) and $\frac{3\lambda}{2}$ (right) [56].

This wave-like spectral shift can be explained by optical effects, which were described in chapter 2.4.2. Light emission within the amorphous EML radiates spherically in all directions. For simplification, it can be assumed that 50% of the gen-

erated light travels in forward direction, towards the transparent ITO anode and glass substrate, and 50% of the generated light travels in backward direction, towards the reflective Al cathode. After reflection, the light originally travelling in backward direction now also travels in forward direction. This reflected light beam can now interfere with the light in forward direction. Coherent waves will experience constructive and destructive interference, respectively. Therefore, depending on the position of the recombination zone in relation to the reflective cathode, different emission wavelengths are increased or dampened. This leads to a varying interference pattern for different EML thicknesses, similar to a cavity effect.

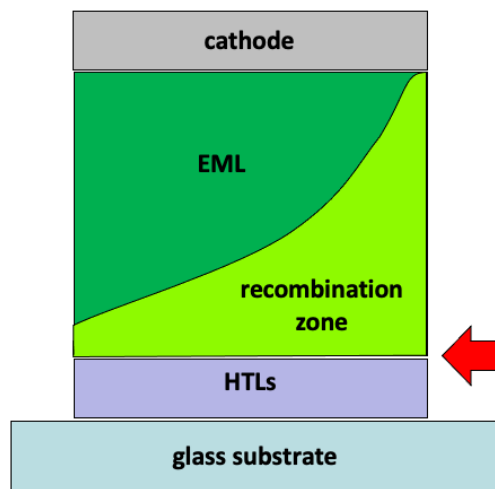


Fig. 3.17: Exponential decay of the recombination zone within the EML of an F8BT based OLED. The HTL/EML interface is indicated by a red arrow.

For cost and energy efficiency reasons (low drive voltage), regular OLEDs are usually designed with a lower total thickness than shown in this work. Therefore, such severe spectral shifts are rarely observed. For CP-OLEDs, however, larger EML thicknesses are a requirement to boost E-CP-effects. With a PL emission maximum around 550 nm for F8BT, such EML thicknesses are in the range of $\lambda/4$ to $\lambda/2$, resulting in significant changes in the interference pattern. Also, the stack architecture energetically promotes the recombination zone to be positioned close to the EML/HTL interface (see energetic levels in fig. [3.14](#) (a)). As illustrated in

3 Results and Discussion

fig. 3.17 the recombination zone within the EML of an F8BT based OLED decays exponentially with increasing distance to the HTL/EML interface (indicated by a red arrow). Therefore, changing the EML thickness has the greatest possible influence on the outcoupled interference pattern.

For the PF and F8BT based OLED systems used in this work, optical interference effects have a great influence on measured EL spectra. This concerns both, unpolarised and polarised results. To be able to analyse and improve CPL results, it is essential to distinguish them from optical effects. In chapter 4, several methods to decouple optical from CP-effects are proposed, including experimental changes in device architecture, and supporting simulations.

3.2 Polymeric emitters in thin film and OLED

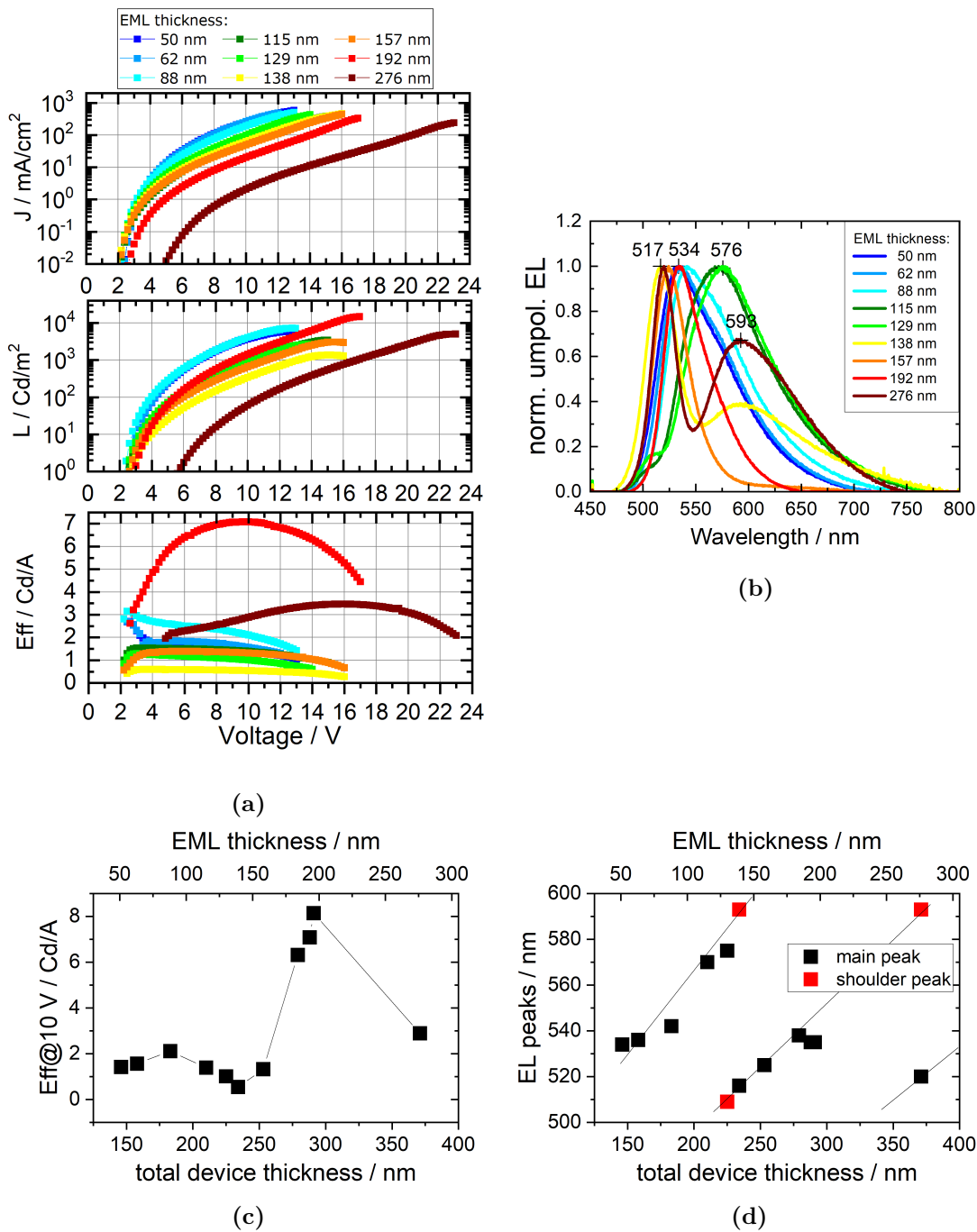


Fig. 3.18: LIV performance data (a) and normalised unpolarised EL spectra (b) of F8BT based OLEDs with different EML thicknesses. Efficiencies at 10 V (c) and main peak (black) and shoulder peak (red) spectral positions (d) are shown for different total device thicknesses. In (d), trend-lines of three resonant modes are added as guide to the eye. Device architecture: ITO / PEDOT (32 nm) / XQUPD (31 nm) / XOTPD (31 nm) / F8BT / CsF/Al. M_w (F8BT) = 37 kg/mol.

3 Results and Discussion

For F8BT based CP-OLEDs, a curing step needs to be incorporated into the fabrication to induce the formation of a chiral phase. While this chiral phase does not occur in devices without a chiral element, curing still has an effect on unpolarised OLEDs. Further information on the impact of curing on F8BT is given in chapter 3.4.

Fig. 3.19 shows the influence of different curing temperatures on device performance (a) and EL spectra (b). As shown in chapter 3.3, the molecular weight of the used F8BT batch influences the ideal curing temperature. For this example, F8BT-37 is used.

Compared to a pristine device (black), curing leads to a spectral red-shift. For lower curing temperatures, device performance improves and increases Eff_{max} . The best performances are achieved at 150 - 170 °C (blue to green). At a higher curing T, device performance gradually decreases again. This occurs because ITO conductivity starts to decline above 180 °C, as indicated by an increasing sheet resistance. Additionally, PEDOT:PSS degradation sets in above 200 °C. This degradation effect can be observed in the device cured at 300 °C (red). Device performance is deteriorated, with V_{on} increasing from 3 V to 10 V and L_{max} and Eff_{max} significantly reduced.

By replacing some of the materials used in those OLEDs, it would be possible to apply higher curing temperatures without damaging the device. Instead of ITO, fluorinated ITO (FTO) is usually chosen for applications with higher curing temperatures. Likewise, more thermally stable versions of PEDOT:PSS are commercially available. Those materials might be a better alternative for the higher M_w F8BT batches analysed in this work, which require higher curing temperatures for best CP-effects. For the present system, however, curing temperatures above 200 °C are not recommended.

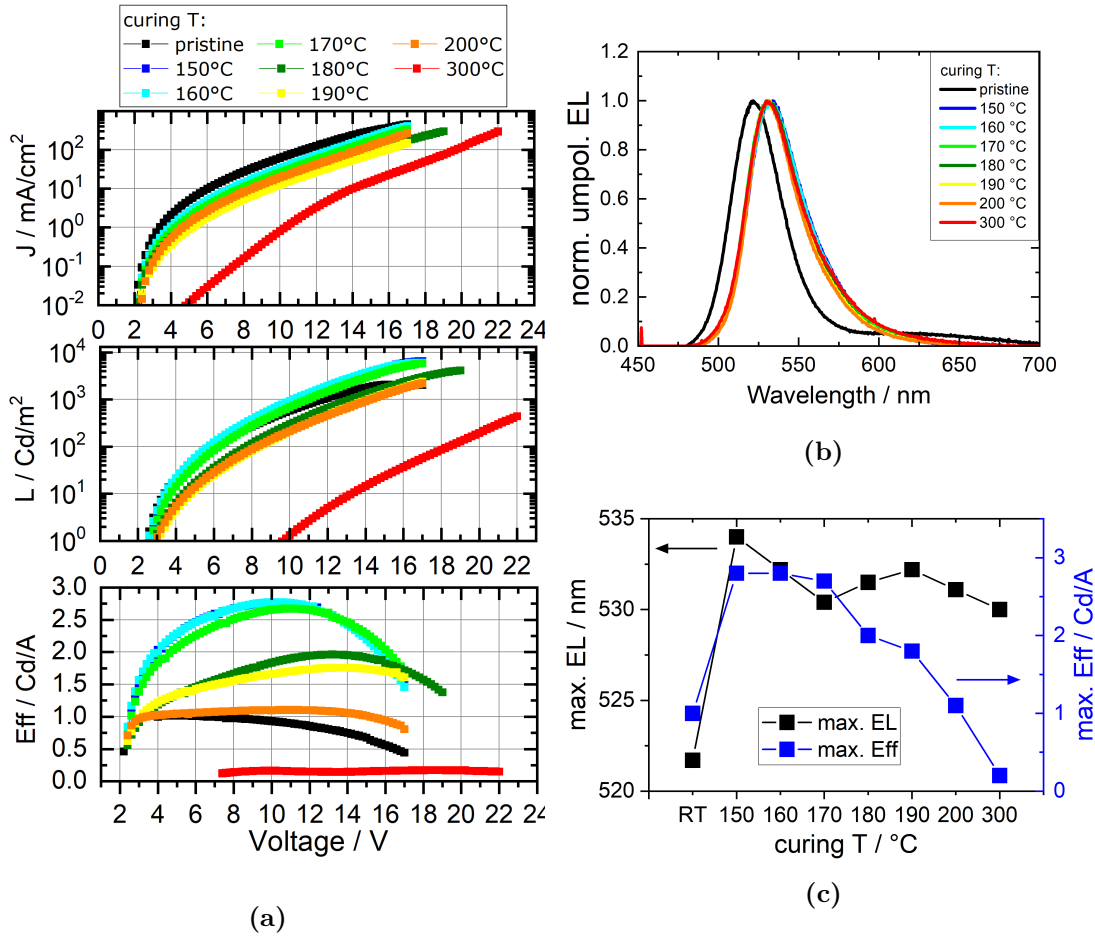


Fig. 3.19: LIV performance data (a) and EL spectra (b) of F8BT based OLEDs cured at different temperatures. Maximum EL wavelengths (black) and maximum efficiencies (blue) are given for all curing temperatures in (c). Device architecture: ITO / PEDOT (36 nm) / XQUPD (33 nm) / XOTPD (22 nm) / F8BT (150 nm) / CsF/Al (cured 20 min@RT - 300 °C). M_w (F8BT) = 37 kg/mol.

The curing step is performed directly after spin-coating of the EML. Curing instead after evaporation of the metal cathode leads to rapid device degradation. Curing of a complete OLED device leads to the deformation and breakdown of the cathode, as shown in fig. 3.20, rendering the device inoperable. Even a curing time of 2 min, which is a much shorter period than typically used for this system, results in the complete destruction of the device.

3 Results and Discussion

The examples shown in fig. 3.20 also contain 10 wt% of the chiral inducer R5011. It is, however, likely that devices without chiral inducer would behave similarly.

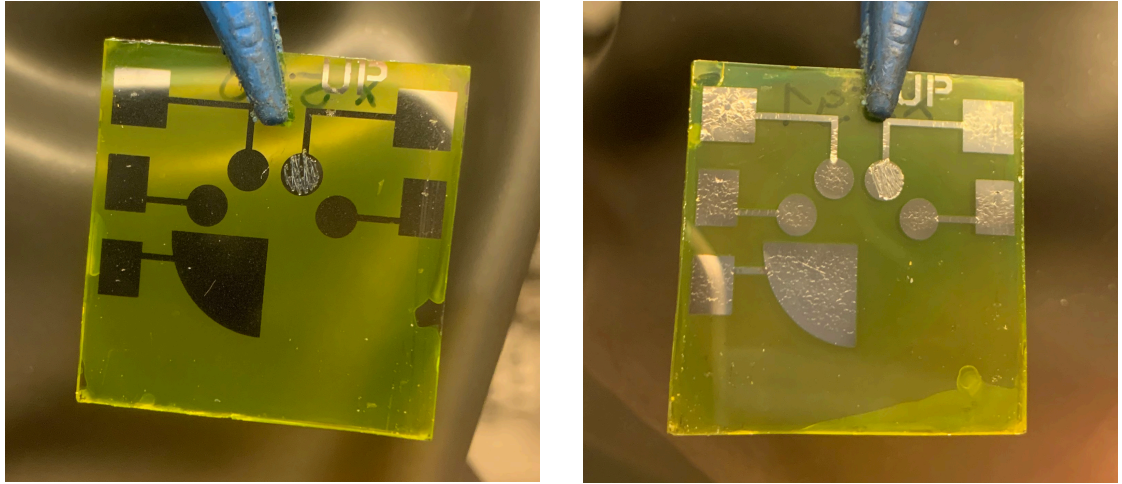


Fig. 3.20: Pictures of cured F8BT based OLEDs. The left device was cured for 20 min at 180 °C before evaporation of the cathode, resulting in a smooth cathode surface. The right device was cured for 2 min at 180 °C with the cathode already evaporated onto the stack, leading to a wrinkled and even ripped cathode surface.

Device architecture: ITO / PEDOT / XQUPD / XOTPD / F8BT + 10 wt% R5011 / CsF/Al. M_w (F8BT) = 37 kg/mol.

3.3 F8BT molecular weight

In this work, a wide range of molecular weights of F8BT polymers was analysed. An overview of the different batches is given in tab. 3.3. It is clear that, depending on the PDI, the average polymer length or number of monomer units calculated via M_w or M_n differs significantly. As explained in chapter 2.3, M_w factors in polymer size, which makes it the more relevant value when analysing physical properties like thermal behaviour. For this reason, the different F8BT batches are named and structured based on their M_w .

Tab. 3.3: F8BT batches with M_w , M_n and PDI. The average number of monomer units (F8-BT couples, endcaps excluded) was calculated based on the average molecular masses. Polymers marked with a star were synthesised by Dr. Jürgen Schelter in the group of Prof. Meerholz. All other polymers were purchased from *1 Material*.

Material	M_w / g/mol	M_n / g/mol	PDI	Monomer units (via M_w)	Monomer units (via M_n)
F8BT-2*	1,920	1,103	1.74	3	2
F8BT-3	2,590	1,880	1.38	5	3
F8BT-7*	6,850	2,403	2.85	13	4
F8BT-13	12,600	7,000	1.80	24	13
F8BT-21	21,100	12,500	1.68	40	24
F8BT-24*	24,400	9,138	2.67	46	17
F8BT-28	28,000	14,000	2.00	53	26
F8BT-37	36,800	17,300	2.13	70	33
F8BT-39	38,863	17,400	2.23	74	33
F8BT-54	53,700	28,400	1.89	102	54
F8BT-122*	122,000	13,260	9.20	233	25

3 Results and Discussion

To compare the thermal phase behaviour of F8BT polymers with different molecular weights, differential scanning calorimetry (DSC) measurements were performed. Fig. 3.22 shows the second or later heating curve of these DSC measurements. As widely accepted standard, (a) displays slow measurements with a heating rate of 10 °C/min. This heating rate benefits from high accuracy and good temperature resolution, but the features are often flat and difficult to analyse. To increase sensitivity and feature intensity, (b) shows fast DSC measurements with a heating rate of 30 °C/min. This method provides an easier detection of features, but can suffer from poor temperature resolution. Both measurements combined allow for an easy feature detection with fast DSC and exact temperature assignment of those features with slow DSC.

Explanation of the DSC signals is given on the example of F8BT-37, shown in fig. 3.21.

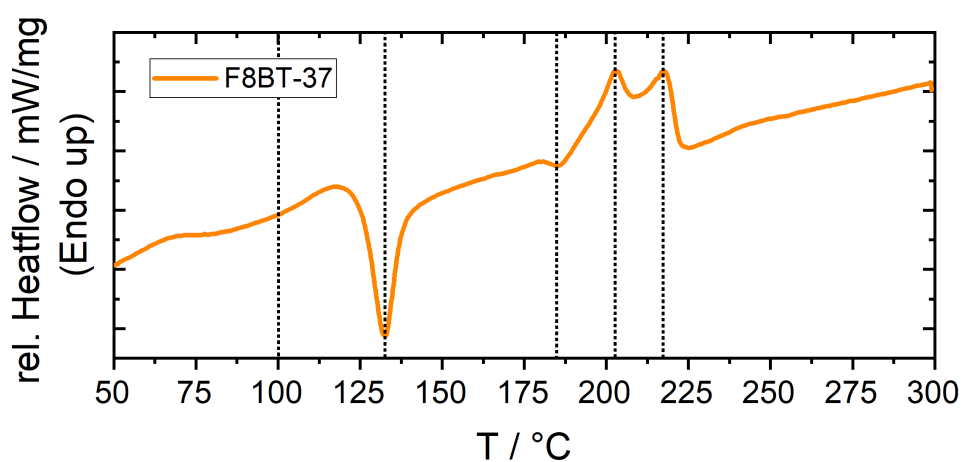


Fig. 3.21: DSC measurements of F8BT-37. Heating rate 10 °C/min, second heating scan. Heatflow was divided by sample mass.

F8BT-37 has a step-like signal around 100 °C, associated with T_g . Unfortunately, T_g can not clearly be identified in all batches, but depending on the molecular weight of the batch, values between 60 °C and 110 °C can be found.

At 133 °C, F8BT-37 exhibits a peak, which can be found around 130 - 150 °C in other batches as well. Since the peak is exothermic, it indicates some kind of phase formation.

The next feature, found at 185 °C for F8BT-37 and between 173 °C and 196 °C for other batches, is only small. However, for F8BT based CP-OLEDs, this peak is the most significant. While the exact nature of this phase is unclear, its thermal position aligns with the experimentally identified ideal curing temperature to achieve maximum g_{EL} or CD values. Its exothermic nature identifies this peak as another crystallisation. In fig. 3.22 (b), where measurements were performed with a faster heating rate, this signal is more clearly visible. However, the temperature resolution of faster measurements is not exact. Therefore, these faster measurements should only be used to better identify the signal.

F8BT-37 shows two endothermic peaks at 203 °C and 217 °C, which are associated with the polymer melting into a liquid crystalline phase (T_m). Especially for polymers with high polydispersities, multiple of such melting features could indicate fractionation. These features can be found between 180 °C and 260 °C in most F8BT batches [48, 63]. Above T_m , F8BT thin films typically experience volume reduction (see chapter 3.4.1.)

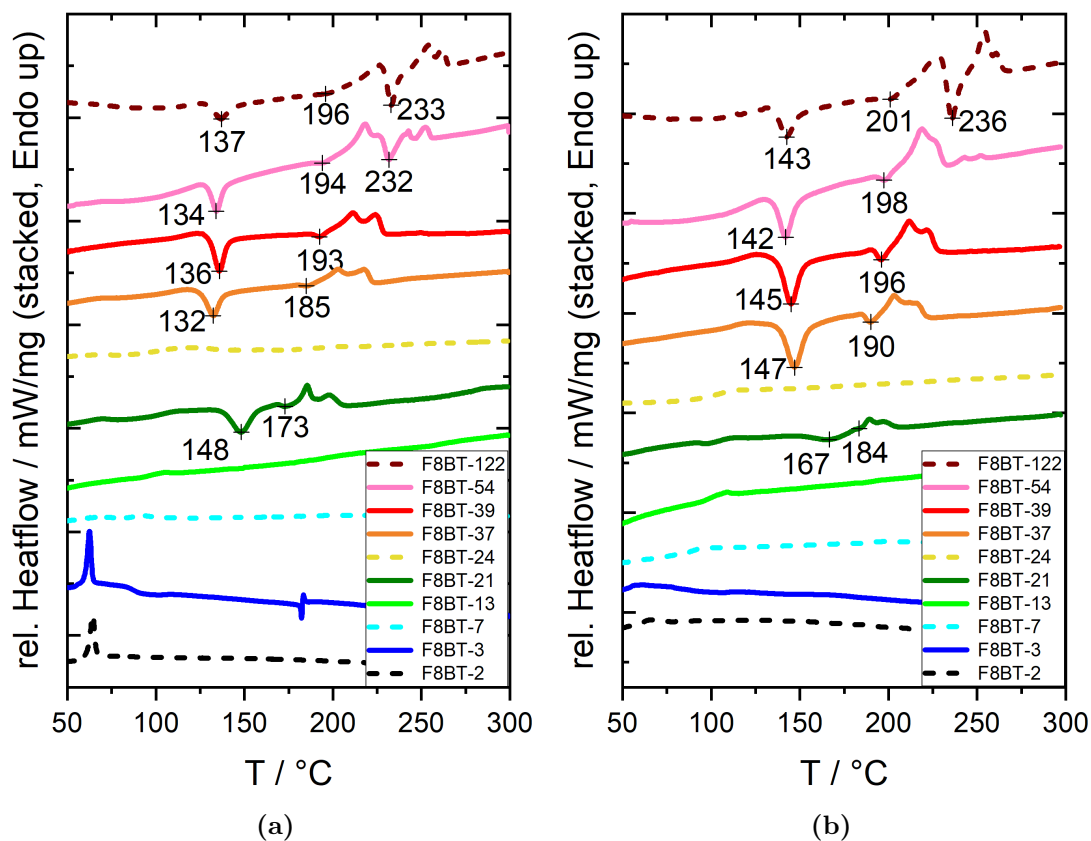


Fig. 3.22: DSC measurements of different F8BT batches. Heating rates were either slow with 10 °C/min (a) or fast DSC with 30 °C/min (b). Only second or later heating scans are shown. Heatflow was divided by sample mass, curves are stacked for better visibility. Solid lines represent F8BT batches purchased from *1Material*, dashed lines represent F8BT batches synthesised by Dr. Jürgen Schelter.

For mixed systems consisting of F8BT and a chiral inducer, the thermal phase behaviour changes slightly. R5011 acts as a plasticiser, thereby reducing the temperature at which the above mentioned phase transitions occur. In fig. [3.81](#), DSC measurements of such mixtures with different chiral inducer concentrations are shown.

3.4 Thermal annealing of F8BT thin films

Thermal annealing, also called curing, is an important factor for polymer based CP-OLEDs. The implications curing has on PF and F8BT thin films and OLEDs was already briefly introduced in chapters [3.2](#). Also, the molecular weight dependence of thermal phase behaviour was introduced in chapter [3.3](#).

In this chapter, the effect of curing on F8BT is analysed further. A focus is set on volume reduction (chapter [3.4.1](#)), surface roughness (chapter [3.4.2](#)), aggregation (chapter [3.4.3](#)) as well as changes in absorption, PL and PLQY (chapter [3.4.4](#)).

While these aspects were only studied for F8BT in this work, it can be presumed that other PF polymers behave similarly.

3.4.1 F8BT thin film volume reduction

It should be noted, that, especially at higher curing temperatures, F8BT thin films can experience shrinkage. Fig. [3.23](#) shows the layer volume reduction of a F8BT-37 based OLED through curing. The here used F8BT batch is identical to the DSC example in fig. [3.21](#).

At lower curing temperatures, the layer thickness remains constant. The shown thickness variations are in the range of typical sample to sample variations. Additionally, for higher curing temperatures and times, surface roughness can occur (see chapter [3.4.2](#)), which makes an exact layer thickness determination impossible.

Above T_m the layer thickness decreases. Here, for the example of F8BT-37, volume reduction sets in around 200 °C. In this example, the final layer thickness after curing decreased by 17 %.

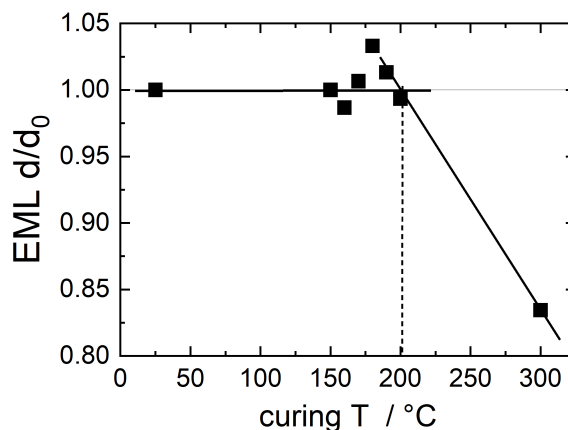


Fig. 3.23: Layer thickness volume reduction of F8BT based OLEDs through curing. $M_w(\text{F8BT}) = 37 \text{ kg/mol}$.

To explain this behaviour, the arrangement of the polymer and its behaviour during curing needs to be analysed. After spin-coating, the polymer chains tend to be entangled. Through curing, the chains can reorder into a more favourable position where the space between the polymer chains is reduced [48]. This effect becomes more intense at higher temperatures, especially above T_m . Because of the large impact of the EML thickness on the outcoupled EL spectrum and CPL properties, exact layer thickness measurements of every device are critical.

While volume reduction for F8BT thin films only occurs for temperatures above T_m it is much more significant in mixed systems with a chiral inducer. This aspect is highlighted in chapter 3.9.

In this work, no evaluation of the molecular weight dependent phase behaviour of PF based polymers was made. It can, however, be assumed, that they would show similar phases as F8BT.

3.4.2 F8BT surface roughness

Additional to shrinkage, development of surface roughness structures can be observed in many F8BT thin films after curing. This effect occurs likewise for neat samples and samples with mixed in additives and has previously been reported for F8BT [48].

Fig. 3.24 shows surface pictures of a pristine (a) and annealed (b) F8BT thin film. While the freshly spin-coated, pristine layer is smooth, the annealed layer developed visible surface roughness. These structures might be due to crystal nuclei of specific phases. Another possible explanation would be phase separation. Smaller molecules within a mixture, which could be additives like chiral inducers or shorter polymer chains, have a tendency to move to the surface and could aggregate there. Higher curing temperatures and longer curing times generally increase this effect. However, it does not seem to have a negative impact on CPL-effects.

If viewed under a microscope (right pictures), the difference in structure becomes even more visible. These samples of F8BT-37 were spin-coated onto thin layers of XOTPD. Shown is a scale of magnification of 100x0.75. The vertical lines visible in these pictures are scratches in the underlying XOTPD layer. They are a result of the rubbing process, which was used in linear alignment experiments. For the demonstration of surface roughness structures, however, the presence of an alignment layer is inconsequential. Additionally, due to substrate handling outside a dust-free environment, dust particles on top of the layers are visible. These particles are not part of the layer, which can be confirmed in profilometry measurements, or by brushing them away. Such impurities are not present in a typical OLED fabrication process and therefore don't pose a problem.

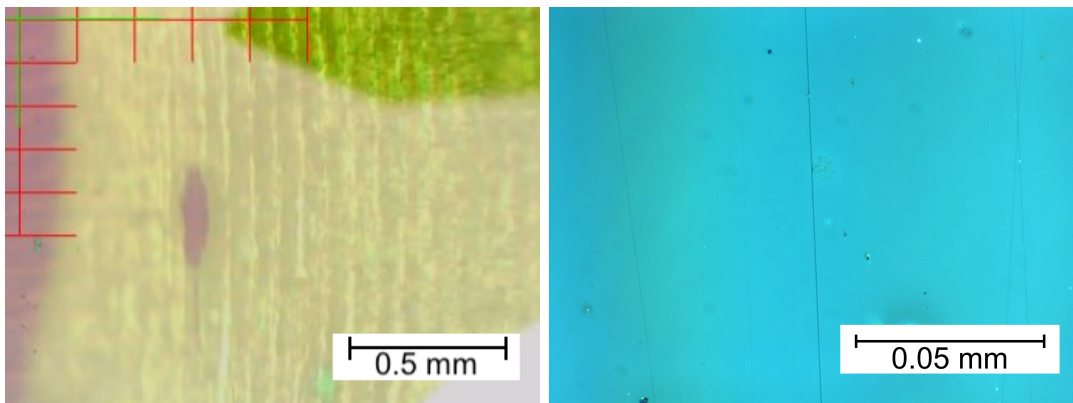
It can be seen that the pristine F8BT layer (a) is smooth and homogenous, even at higher magnification. After curing for 20 min@220 °C (bottom left) and 5 min at 300 °C (bottom right), however, surface roughness of the F8BT layer increases significantly. In contrast to the pristine layer, the visible particles do not lie on top of the layer, but are partially embedded. This observation is supported by pro-

3 Results and Discussion

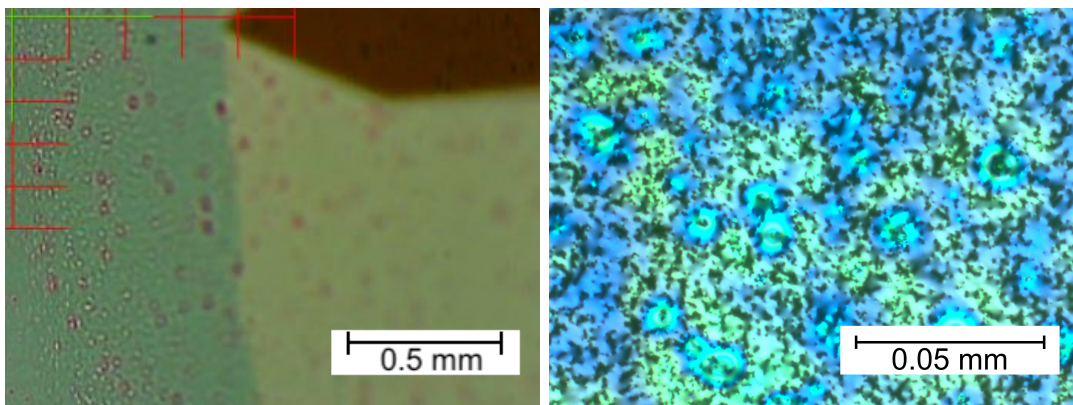
filometry measurements. Since sample fabrication, including curing, takes place inside a glove box, it can be excluded that impurities or dust were melted into the film. Instead, it is more likely that the particles represent specific phases or crystalline aggregates. At higher magnification, the pattern resembles a liquid crystalline phase, even though no polarisers or chiral elements were used here. This supports the assumption that during the short and hot annealing process, phase changes occurred simultaneously throughout the layer, resulting in a multidomain inhomogeneous phase.

The microscopy pictures shown in fig. 3.24 are taken without polarisers. However, polarisation microscopy (POM) was performed as well. For all measured samples, no light could pass the crossed polarisers, resulting in a black image. This includes thin films of F8BT, F8BT+R5011 and the chirally functionalised PF P(F4/c2-F8) (see chapter 3.7.2). Samples were measured with and without an underlying rubbed PI-based alignment layer. The samples were tested pristine and after curing for 20 min at 150 °C and 300 °C, respectively. Different layer thicknesses between 50 nm and 200 nm were analysed. However, it is possible that the structures were too small to be visible in POM. Other results could be achieved by analysing thicker layers.

3.4 Thermal annealing of F8BT thin films



(a) pristine



(b) cured

Fig. 3.24: Pictures of pristine (a) and cured (b) F8BT-37 thin film surfaces.

Images on the left were taken with the camera of a DEKTAK profilometer. In the top left picture, the underlying structure of the sample stage can be seen as vertical grooves.

Images on the right are microscopy pictures with a magnification of 100×0.75 .

The bottom samples were cured 20 min@220 °C (left) and 5 min@300 °C (right).

3.4.3 F8BT aggregation

It has been reported that F8BT can form non-emissive aggregates under certain conditions [48]. Such aggregates could already be present in solution and might be retained after spin-coating.

Fig. 3.26 shows UV/Vis absorption and PL data of F8BT thin films. The samples were produced using either freshly prepared or old F8BT solutions. The solutions were either spin-coated directly, or filtered through a syringe filter prior to spin-coating. The resulting layers were analysed in pristine condition, as well as after subsequent 15 min curing intervals at 115 °C and 175 °C. For the here used batch F8BT-21, the chosen curing conditions represent values slightly above T_g and the experimentally found ideal curing temperature for CPL experiments.

Curing leads to changes in the absorption and PL spectra for all samples. This aspect will be analysed in detail in chapter 3.4.4. This chapter, however, focuses only on the differences between freshly prepared and old, as well as unfiltered and filtered solutions. It can be said that the thin films of all four solutions produce almost identical spectral shapes for each curing condition. To clarify, the following example is given:

As shown in fig. 3.25 (a) and (c), the normalised absorption and PL spectra of all four layers cured at 115 °C are identical. There is, however, a spectral shift and maximum intensity difference between the absorption (b) and PL (d) spectra of uncured and cured samples, respectively. The size of this intensity difference depends on from which solution the sample was spin-coated.

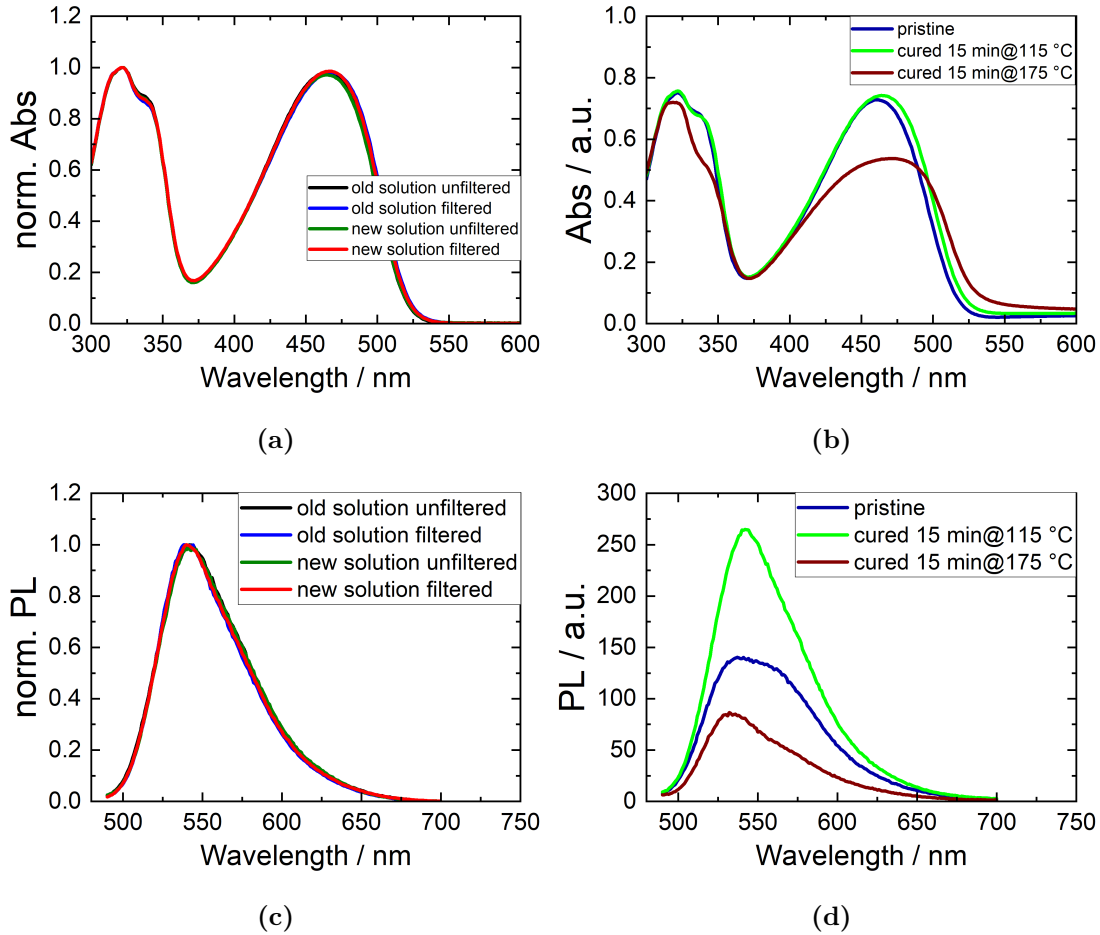


Fig. 3.25: Normalised absorption (a) and PL (c) spectra of F8BT-21 thin films. Samples were spin-coated from old unfiltered (black) or filtered (blue) solutions, or from new unfiltered (green) or filtered (red) solutions. All samples were cured 15 min at 115 °C. Absorption (b) and PL (d) spectra of an F8BT-21 thin film, spin-coated from an old, unfiltered solution. Sample is shown pristine (dark blue), and after 15 min curing at 115 °C (light green) and 175 °C (dark red), respectively. $\lambda_{\text{ex}} = 460$ nm.

3 Results and Discussion

Fig 3.26 shows the intensity differences for absorption (a) and PL (b) as relative values, as well as PLQY values (c) before and after curing.

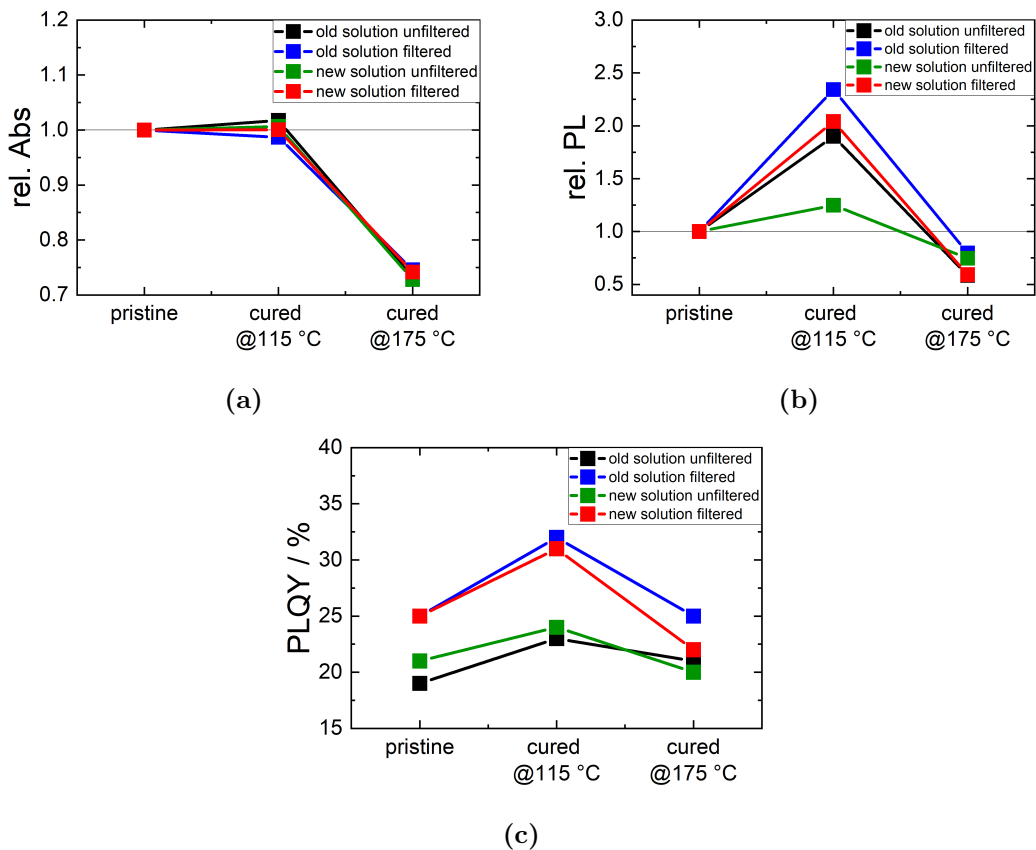


Fig. 3.26: Relative absorption at 462 nm (a), relative PL at 540 nm (b) and PLQY (c) of F8BT-21 thin films.

The layers were spin-coated from a freshly prepared or old solution, which was used directly or after filtering through a syringe filter. Those layers were then measured in pristine condition, and after 15 min curing at 115 °C and subsequently 175 °C. $\lambda_{\text{ex}} = 460$ nm.

For the relative absorption data in (a), no relative absorption difference between the preparation methods is found. Relative absorption decreases after curing at 175 °C, which is a side effect of rearranging the polymer chains.

An increased relative PL (b) is found after curing at 115 °C. This effect occurs for all samples, with the samples from filtered solutions experiencing a larger increase compared to the unfiltered solutions. Through curing above T_g the torsion angle between the F8 and BT units can change and the polymer chains start to rearrange. The now predominant alternating packing structure produces a more complex energetic structure, resulting in an increased emission [117, 118]. After curing at 175 °C, however, all samples fall below the original PL intensity, suggesting the formation of non-emissive aggregates [48].

While absorption and PL are layer thickness dependent and could only be compared as relative values, PLQY measurements can be compared directly. The PLQY values (c) of pristine layers illustrate the difference between filtered and unfiltered solutions. While a fresh F8BT solution has a slightly higher PLQY than an older solution, filtering both solutions results in an increased PLQY to the same level. This indicates that in both solutions, some non-emissive or quenching aggregates, or possibly impurities, might be present, which can be removed through filtering. Increased PLQY values are found after curing at 115 °C, which is analogous to the effect seen in (b) for PL. Likewise, PLQY values decrease after curing at 175 °C. While the samples from filtered solutions still possess the highest PLQY values, all samples display a similar performance around 23 ± 3 %, suggesting that, despite their different origins, a comparable state has been reached.

In conclusion, it can be assumed that freshly filtering F8BT solutions right before spin-coating might slightly increase efficiency by removing insoluble aggregates or impurities. Curing to T_g has an even greater benefit. However, curing to higher temperatures, which is necessary for F8BT based CP-OLEDs, revokes those advantages.

3.4.4 F8BT curing temperature

As shown in chapter 3.3, different F8BT batches react differently to thermal annealing, depending on their molecular weight. Also, as seen in fig. 3.25 (b) and (d) on the example of F8BT-21, thermal annealing of F8BT thin films leads to an absorption and PL spectral shift. In this chapter, the influence of different curing temperatures on the absorption, PL and photoluminescence quantum yield (PLQY) properties of F8BT thin films with different molecular weights is analysed.

Fig. 3.27 shows normalised absorption (left) and PL (right) spectra of pristine (top) and cured (bottom) F8BT+R5011 thin films². The samples contained 10 wt% of the non-emissive chiral inducer R5011. This is irrelevant for unpolarised measurements, as the presence of the chiral inducer does not influence the shown effects, as can be seen when comparing the spectra from fig. 3.27 with fig. 3.25. It allows, however, the additional acquisition of CD data, which is introduced in chapter 3.8.

Here, F8BT thin films with different molecular weights are compared. Curing for 15 min at 250 °C is above T_m for all F8BT batches. The wavelength of absorption and PL peaks of these spectra are also shown in fig. 3.28.

²Acquisition of some of the data shown in this chapter was supported by Annemarie Berger and Viktor Schlichting. Experiment planning and evaluation by Claudia Dillmann.

3.4 Thermal annealing of F8BT thin films

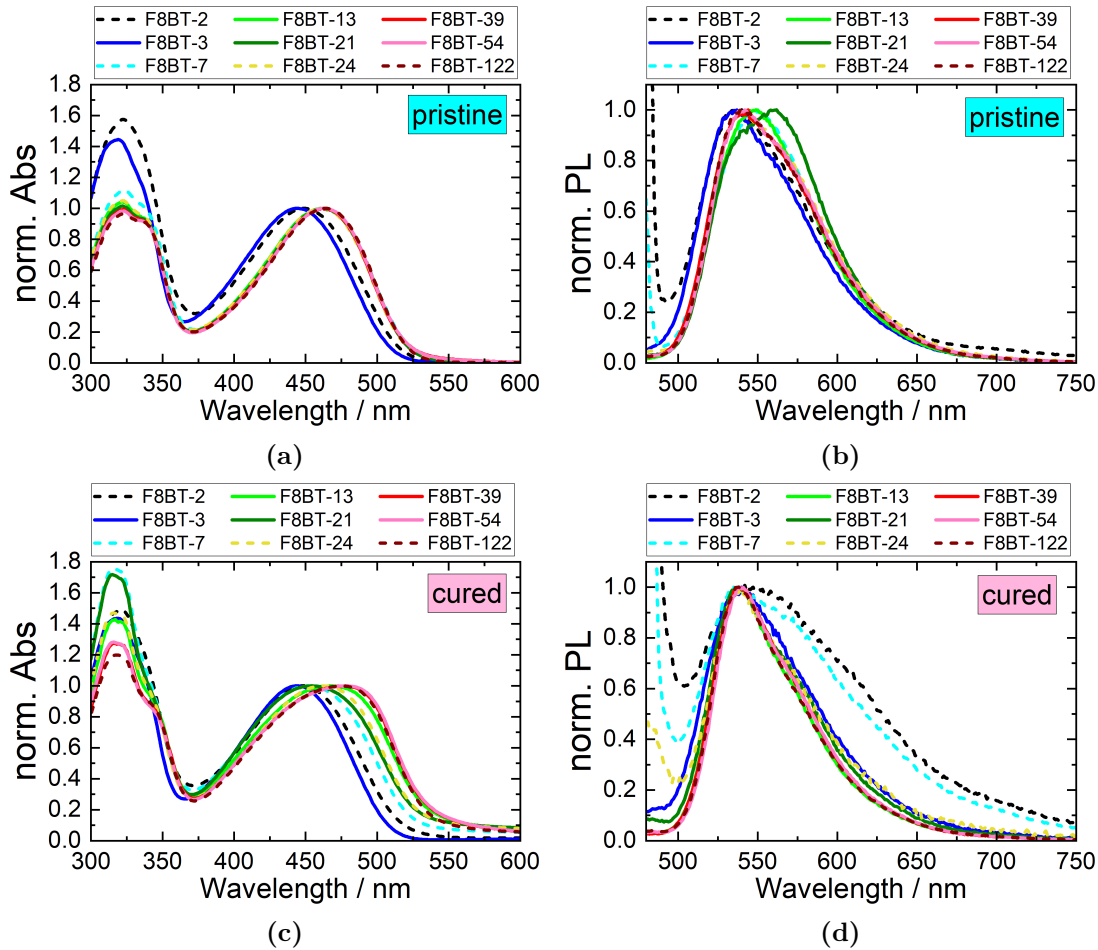


Fig. 3.27: Normalised absorption (left) and PL (right) spectra of F8BT + 10 wt% R5011 thin films with different molecular weights. Samples are shown pristine (top) and after curing for 15 min at 250 °C (bottom). Solid lines represent F8BT batches purchased from *1Material*, dashed lines represent F8BT batches synthesised by Dr. Jürgen Schelster. $\lambda_{\text{ex}} = 460 \text{ nm}$.

3 Results and Discussion

The spectral shift can be seen better in fig. 3.28. In (a), the absorption peak around 450 nm was chosen. While this is not the largest peak for most of the shown spectra, it is the more relevant signal.

The given trend-lines highlight the gradual absorption redshift with increasing molecular weight. While this is already the case for pristine thin films, the effect is even stronger for cured samples. This could indicate aggregation, which is a known effect, especially at higher curing temperatures.

From the PL data, an opposite trend for pristine and cured samples with medium molecular weights is found. Here, curing leads to a blueshifted emission.

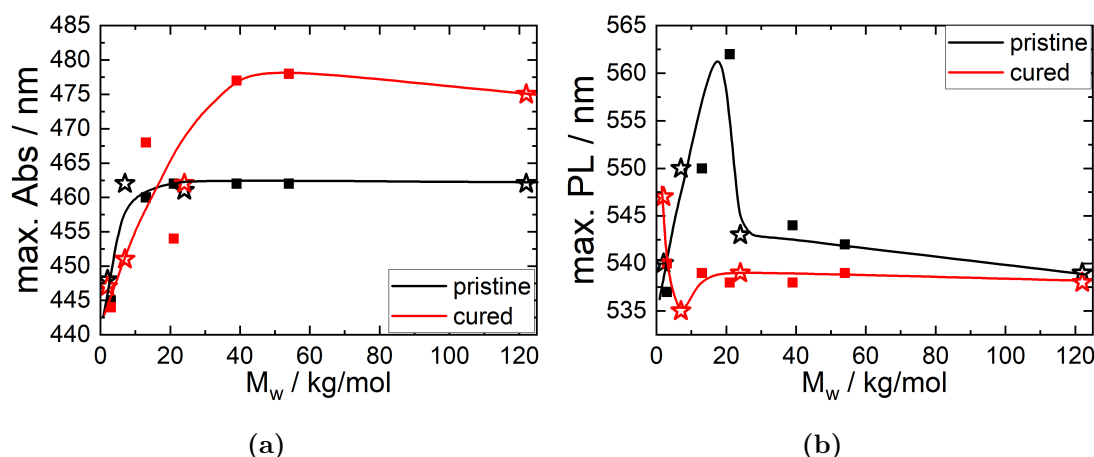


Fig. 3.28: Maximum absorption (a) and PL (b) wavelengths for F8BT + 10 wt% R5011 thin films with different molecular weights. Samples are shown pristine (black) and after curing for 15 min at 250 °C (red). For each dataset, a trend-line is drawn.

Batches synthesised by Dr. Jürgen Schelter are marked with a star. $\lambda_{\text{ex}} = 460$ nm.

To better analyse the absorption and PL behaviour of F8BT with different molecular weights, three representative examples from this data set are given and compared. Fig. 3.29 shows absorption (top row) and PL (bottom row) data for thin films of three F8BT batches. Shown here are measurements of pristine (blue) and cured at 250 °C (red) samples. To assure maximum comparability, all three

3.4 Thermal annealing of F8BT thin films

F8BT batches shown were purchased from the same supplier and synthesised with the same method.

As an example for a very short oligomer, data of F8BT-2 is given in (a). Even after curing, absorption spectra remain almost unchanged. At the same time, however, a significant decline in PL intensity occurs, which could indicate the formation of non-emissive aggregates.

F8BT-13 (b), despite its rather low molecular weight, proved to be one of the best batches for CPL applications. After curing, a decrease in absorption and PL intensity can be observed. Additionally, the second absorption peak around 450 nm is slightly red-shifted and broadened, which is a common effect reported in literature. PL intensity decreased, but the effect is not as strong as in F8BT-2. During curing, polymers can rearrange, thereby reducing the space between individual polymer chains. This increases the likelihood of aggregates (ground state) and excimers (excited state). The latter typically shows red-shifted emission. Since in this case, a blue-shift is observed, the presence of non-emissive aggregates is more likely [48].

F8BT-54 (c) was chosen as an example for a batch with much higher molecular weight. The same absorption intensity decrease and shift as observed in F8BT-13 are found, but less extensive. Both samples also display a non-zero absorption signal above 525 nm, indicative of light scattering caused by the rough surface [48]. However, the PL intensity remains almost constant, while the peak becomes slightly more narrow. This suggests that higher molecular weight batches might form less non-emissive aggregates upon curing.

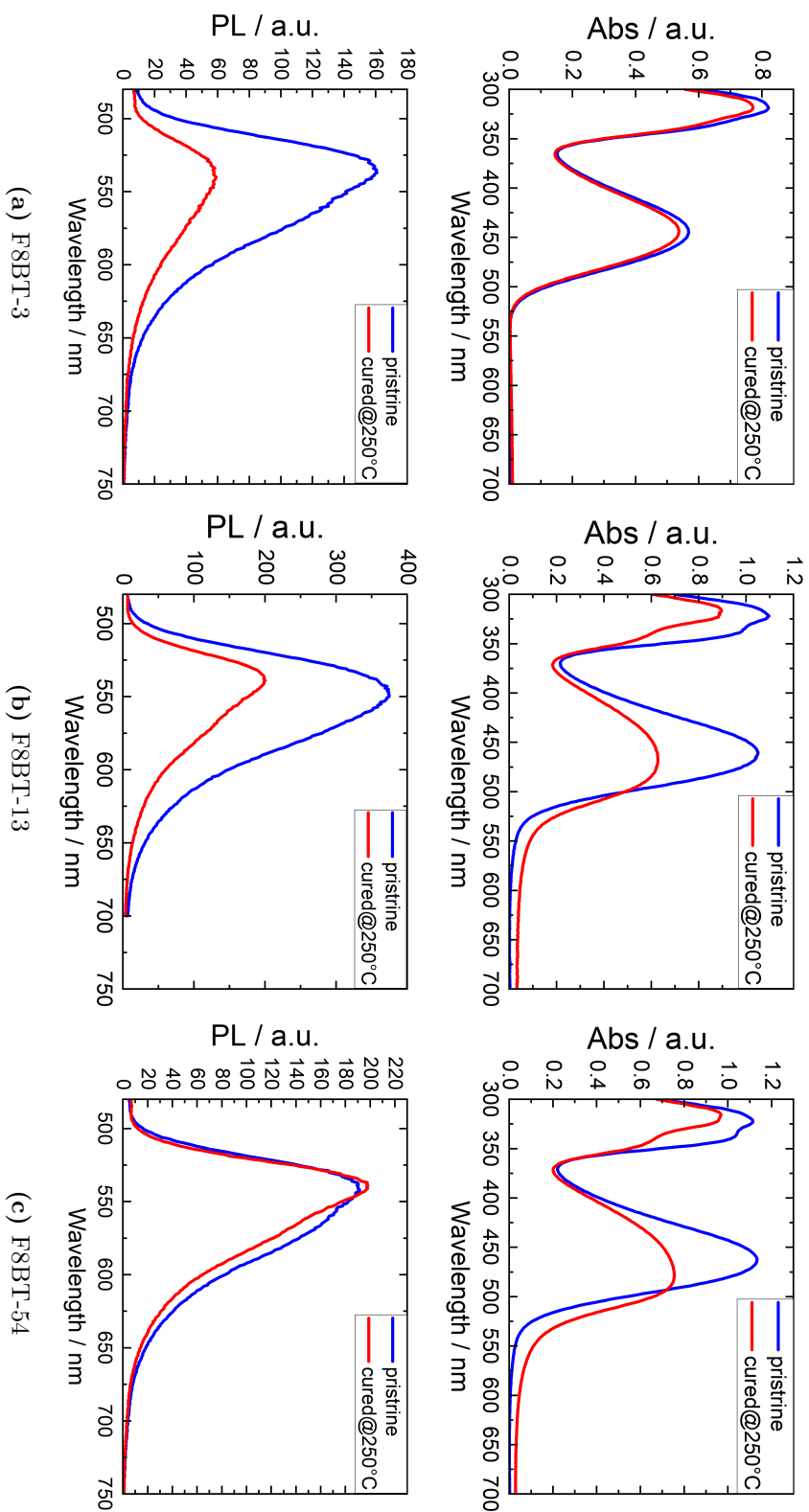


Fig. 3.29: Absorption (top row) and PL (bottom row) data of F8BT + 10 wt% R5011 thin films. Samples are shown in pristine condition (blue) and after curing for 15 min at 250 °C (red). Three exemplary molecular weights of F8BT were chosen, F8BT-3 (a), F8BT-13 (b) and F8BT-102 (c). For more information about these F8BT batches, see tab. [3.3](#)

Fig. 3.30 displays the relative absorption after curing for all batches. Shown are maximum absorption intensities of the signal around 460 nm.

In (a), a stepwise curing process is shown for the two examples F8BT-13 (red) and F8BT-39 (green). These samples were cured successively for 15 min at each given temperature. With increasing curing temperature, a gradual absorption intensity decrease is found. In accordance with DSC measurements (chapter 3.3), this decline sets in at lower temperatures for lower molecular weight batches like F8BT-13 and at higher temperatures for higher molecular weight batches like F8BT-39.

In (b), the molecular weight dependence of this absorption intensity decline is even more clear. Here, the relative absorption of pristine samples compared to samples cured at 250 °C is shown as a function of molecular weight. While low M_w batches remain almost unchanged and high M_w batches over 37 kg/mol seem to plateau at a constant value, the largest absorption decline is found for medium M_w batches.

As previously mentioned, batches synthesised by Dr. Jürgen Schelter (stars), while following the same trend, behave slightly different than commercially acquired batches (squares) and are therefore marked separately.

3 Results and Discussion

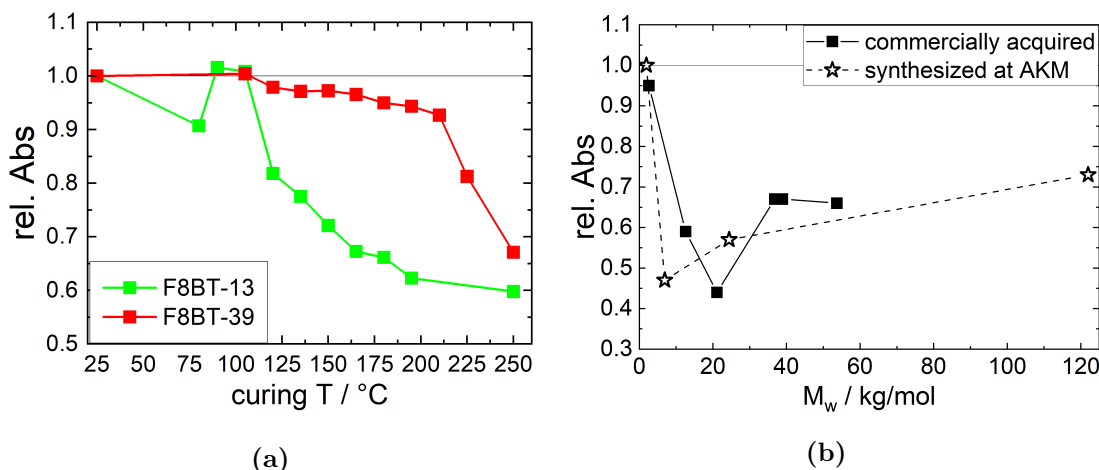


Fig. 3.30: Absorption change of thin films of different F8BT batches with 10 wt% R5011. Shown are maximum absorption intensities for the signal around 460 nm. Pristine samples are compared to cured samples. Samples were subsequently cured 15 min at different temperatures (a), with a maximum curing temperature of 250 °C (b). Batches synthesised by Dr. Jürgen Schelter are marked with a star.

Analogous to absorption data, fig. 3.31 highlights the emission behaviour after curing. The same F8BT + 10 wt% R5011 thin films were used for PL measurements as for the previously shown UV/Vis measurements. Shown are maximum PL intensities of the signal around 550 nm.

For the relative PL intensities of pristine samples compared to samples cured at 250 °C (b), a general trend can be found. Low M_w batches experience a significant PL intensity decline after curing, while high M_w batches remain constant or even show a slight increase. This curing temperature of 250 °C represents a value above T_m for all batches.

In contrast, curing at lower temperatures produces a more diverse picture. For this, the same examples shown in fig. 3.30 (a) are analysed here as well for a step-wise curing process. Both, the lower M_w example F8BT-13 (green) and higher M_w example F8BT-39 (red) show a relative PL increase when cured around their respective T_g . This result is in accordance with literature, as curing slightly above

T_g has been reported to boost OLED efficiency [48, 117]. Above T_g , however, further curing leads to a PL decrease, possibly due to the formation of non-emissive aggregates.

In contrast to absorption experiments, where low, medium and high M_w batches show different behaviour, the PL results follow a linear dependence with increasing M_w . Here, the relative PL (b) of pristine samples compared to samples cured at 250 °C is shown as a function of molecular weight. Lower M_w batches experience the highest relative PL decline, while high M_w batches show a relative PL increase. As with absorption, the synthesised batches (stars) follow the same trend, but are slightly shifted compared to the commercially acquired batches (squares).

In (c) and (d), absolute and relative PLQY values of pristine and cured F8BT + 10 wt%R5011 thin films are shown. Like the previously shown absorption and PL data, which were measured on the same samples, different F8BT batches are compared.

Absolute PLQY values of pristine and cured samples (c) and relative PLQY values (d) both show the same trend. After curing at 250 °C, lower M_w batches experience a decrease in PLQY, while higher M_w batches show an increase in PLQY. However, the highest PLQY values are achieved for medium M_w batches between 13 and 39 kg/mol. As before, the batches synthesised by Dr. Jürgen Schelter (stars) follow the same trend as the commercially acquired batches (squares), but with a generally lower PLQY.

3 Results and Discussion

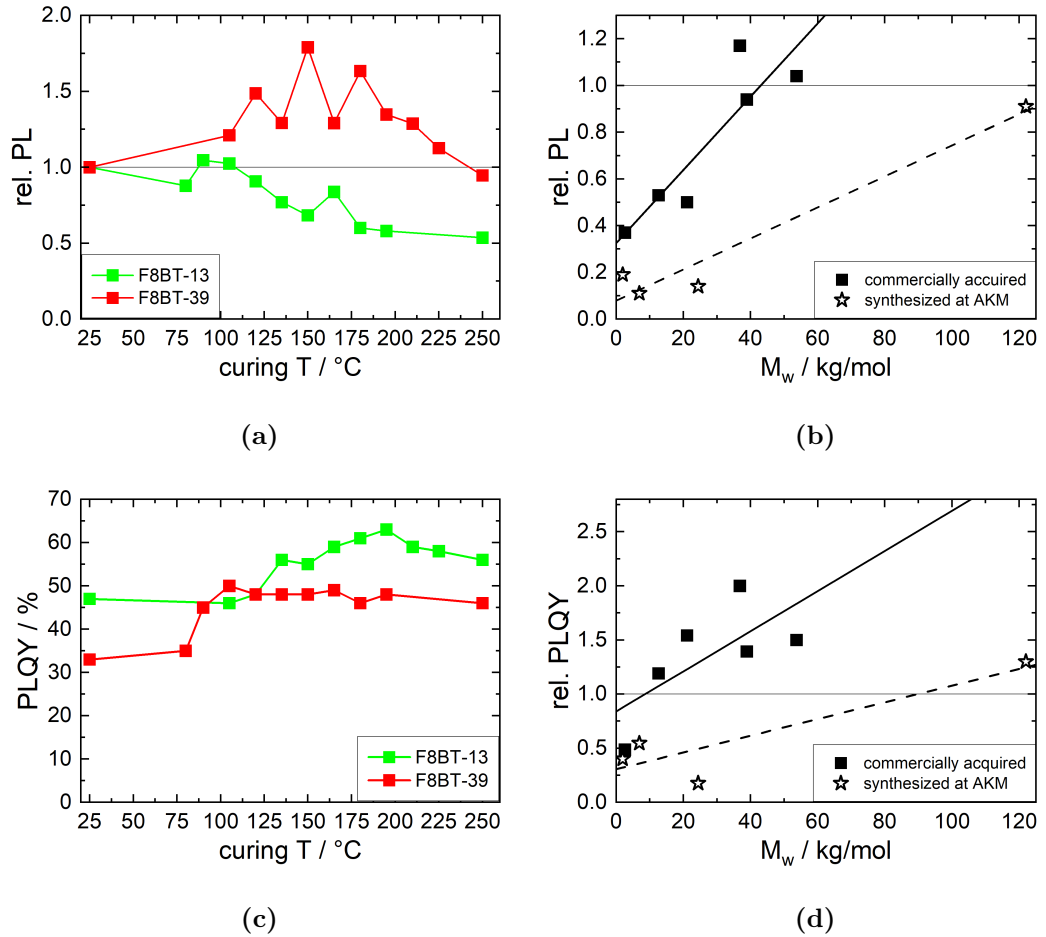


Fig. 3.31: Emission change of F8BT + 10 wt%R5011 thin films before and after curing. Different F8BT batches are compared. Shown are maximum PL intensities for the peak around 550 nm (top) and PLQY values (bottom). (a) and (c) samples cured 15 min at different temperatures, subsequently. (b) and (d) normalised PL and PLQY data of pristine samples compared to samples cured at 250 °C. Batches synthesised by Dr. Jürgen Schelter are marked with a star.

It is noticeable, that the relative PLQY in fig. 3.31 (d) increased, even though the relative PL in fig. 3.31 (b) decreased, or increased only slightly. To understand this behaviour, the relative absorption decrease shown in fig. 3.30 (b) has to be taken into account as well.

PLQY is calculated as a ratio of absorbed photons to emitted photons. Here, absorption decreased significantly for almost all samples. PL, on the other hand, decreased for low molecular weight batches and even increased slightly for high molecular weight batches. If the absorption decrease is larger than the PL decrease, it is possible to calculate an increased PLQY, despite a decrease in PL.

3.4.5 F8BT annealing conclusion

In this section, different aspects about cured F8BT thin films were introduced.

It was shown, that curing of F8BT thin films above T_m leads to volume reduction up to 17 % for a curing temperature of 300 °C. This is the result of the polymer melting and flattening out on the surface.

Already at lower curing temperatures, the originally smooth surface develops roughness, which increases with higher curing temperatures or longer curing times. Presumably, this indicates the formation of a different phase of crystalline aggregates.

Based on relative absorption, PL and PLQY measurements, it has to be assumed that F8BT solutions used for spin-coating can already contain non-emissive aggregates. This effect can be reduced by using freshly prepared solutions and filtering before spin-coating. However, after curing at larger temperatures typically required for the CP-OLEDs built in this work, the benefit gained through filtering is lost.

3 Results and Discussion

In chapter [3.3](#), the molecular weight dependence of thermal phase behaviour of F8BT was shown. In chapter [3.4.4](#), this could be related to changes in the optical behaviour. With increasing F8BT molecular weight, a red-shift of the absorption peak is observed, which increases after curing. In contrast, only the PL emission peak of medium molecular weight batches is red-shifted, and experiences a blue-shift upon curing. In general, curing leads to a decrease in relative absorption, which is strongest for medium molecular weight batches. For each F8BT, the decrease sets in at the respective experimentally identified ideal curing temperature for best CP-effects in CP-OLEDs. At the same time, curing leads to a change in relative PL, which follows a linear correlation with increasing molecular weight. Analogously, curing leads to a PLQY increase for most matches, which also follows a linear trend with increasing molecular weight.

For F8BT thin films containing a chiral inducer, the curing temperature dependent chiral phase behaviour can be analysed as well. These aspects are highlighted in chapter [3.9](#).

3.5 CP-OLED strategies

The aim of this work is the optimisation of CP-OLEDs. In chapters [3.2](#) to [3.4](#), the preliminary results for this goal, analysis of the behaviour of emissive polymers, were presented.

In the following chapters, these polymers and other materials are used to build CP-OLEDs. For this, three general strategies are used:

1. **I-CPL emitters**
2. **one component systems**
3. **mixed systems**

In chapter [3.6](#), two helicene based molecules are analysed as I-CPL emitters.

In chapter [3.7](#), several chiral polyfluorene polymers are used as one component system E-CPL emitters. The used materials including [BINOL](#) functionalised PF co-polymers (chapter [3.7.1](#)), PFs with chiral side chains (chapters [3.7.2](#) to [3.7.5](#)) and F8BT with chiral side chains (chapter [3.7.7](#)).

In chapter [3.8](#), the achiral emitter polymer F8BT is combined with the non-emissive chiral inducer R5011 to create a mixed system E-CP-effect. Following the same strategy, the helicene based molecules introduced in chapter [3.6](#) are used as chiral inducers here as well (chapter [3.8.1](#)).

To increase the CP-effect of CP-OLEDs, several factors are analysed in this work. This includes chiral phase behaviour for different polymer compositions and molecular weights, layer thickness variations, different curing conditions and chiral inducer concentrations.

3.6 Chiral small molecules as CPL-emitters

As described in chapter 2.6.2, chiral emitter molecules can be used to generate intrinsic CPL (I-CPL) effects. In this concept, the molecule directly emits CP-PL or -EL. The effect occurs in solution as well as in film.

In this chapter, two chiral emitter molecules, H1-Me₂ (chapter 3.6.1) and ThiahelalkBZT (chapter 3.6.2) are introduced. Both molecules are based on a helicene core, making them potential I-CPL emitters.

The reported $g_{\text{intrinsic}}$ values of these materials are low, typically in the range of 10^{-4} - 10^{-3} . With the CPL measuring set-up introduced in chapter 3.1, g_{EL} values of this magnitude cannot be measured with sufficient accuracy. Also, apart from their scientific significance, a low CP-effect of this magnitude would not have any benefits in applications.

Instead, the same chiral molecules can be used as non-emissive chiral inducers in an emissive achiral polymer matrix. This way, extrinsic CPL (E-CPL) effects would be promoted. For this kind of CP-OLED system, large $|g_{\text{EL}}|$ values of up to 1.1 have already been reported. In contrast to I-CPL systems, CP-effects of this magnitude can already be attractive for commercial applications.

Detailed information on E-CPL systems, chiral inducers and the influence of several device architecture and preparation parameters will be given in chapter 3.8.

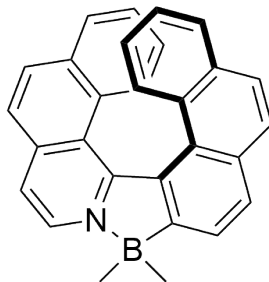
3.6.1 H1-Me₂

Fig. 3.32: Structure of *P*-**H1-Me₂**.

The structure shown in fig. 3.32 is called **H1-Me₂**³. The all-ortho-fused azabora[7]helicene displays structural chirality with exceptional configurational stability. The reported HOMO/LUMO energy levels for **H1-Me₂** derived from CV measurements are -6.08 eV and -3.04 eV, respectively [119].

As seen in fig. 3.33, neat thin films of **H1-Me₂** show two main absorption peaks around 415 nm and 435 nm. The PL emission spectrum features two peaks around 460 nm and 475 nm. The same peaks, while at a much lower intensity, can be found when 2.5 - 15 wt% **H1-Me₂** are embedded into a poly(9-vinylcarbazole) (PVK) matrix. **PLQY** measurements of said films result in overall low values of 7.6% for neat **H1-Me₂** and 1.7 - 4.0% in PVK.

³**H1-Me₂** was synthesised by Julian Full, working group of Prof. Agnieszka Nowak-Król, University of Würzburg.

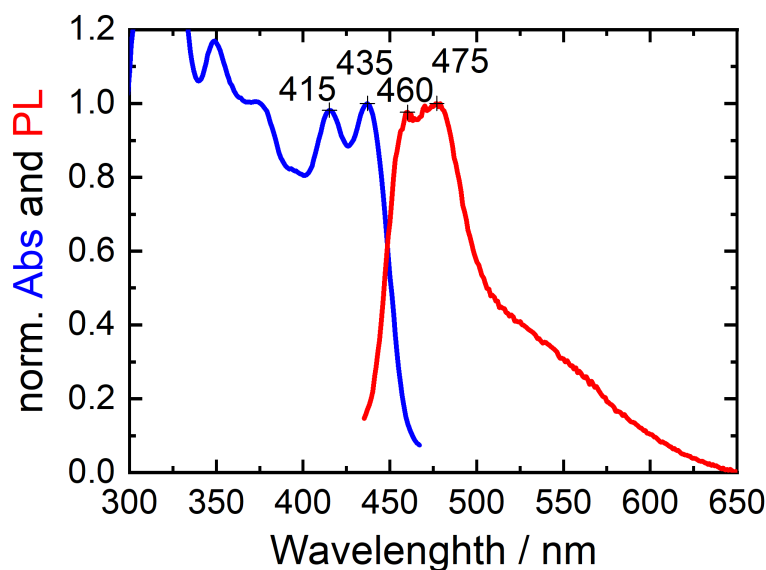


Fig. 3.33: Normalised absorption (blue) and PL (red) spectra of a spin-coated neat **H1-Me₂** thin film; PLQY = 7.6%, λ_{ex} = 410 nm.

With such low **PLQY** values, it is not surprising that OLEDs with **H1-Me₂** as emitter material ⁴ have poor device performances. A high V_{on} of 18 - 20 V is required to operate such a device. Still, only a maximum brightness of $L_{\text{max}} = 4 - 9 \text{ Cd/m}^2$ is achieved. The subsequent swift device degradation makes CP-EL measurements impossible.

While **H1-Me₂** is not suitable as I-CPL emitter, it was also tested as non-emissive chiral inducer in F8BT. The results of this E-CPL system are presented in chapter **3.8.1**.

⁴Device architecture: ITO / PEDOT / XQUPD / XOTPD / **H1-Me₂** neat or 5 - 15 wt% in PVK / CsF/Al

3.6.2 ThiahelalkBZT

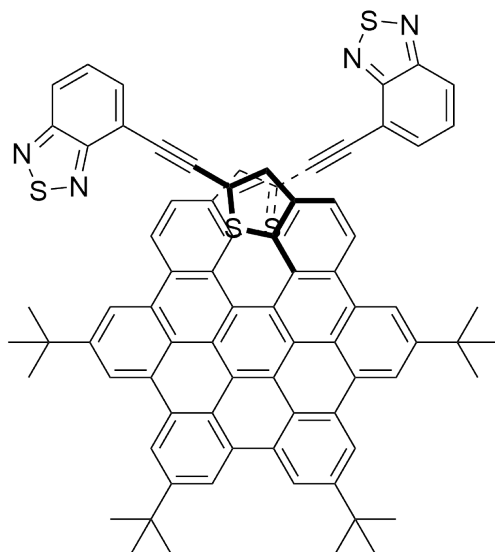


Fig. 3.34: Structure of *P*-ThiahelalkBZT

The structure shown in fig. 3.34 is called ThiahelalkBZT⁵. Like H1-Me₂, it is based on a [7]helicene core, only here in a π -extended form. The thiophene benzothiadiazole donor-acceptor structure not only improves electronic properties, but also increases steric hindrance and therefore enantiomeric stability. HOMO/LUMO energy levels derived from CV measurements are -5.61 eV and -2.95 eV, respectively⁶. The extensive, rigid, sterically chiral structure allows for an exceptionally high calculated maximum g_{PL} value of 1.5×10^{-2} . However, like all other intrinsic CP-effects found so far, it is much smaller than would be required for CP-OLED applications. And in fact, it is too small to be measured with the set-up introduced in chapter 3.1.

Other than H1-Me₂, ThiahelalkBZT performed reasonably well as emitter in an OLED. EL peaks at 495 nm and 525 nm can be observed when ThiahelalkBZT is embedded in a non-emissive PVK matrix. The achieved maximum brightness around 200 Cd/m² is even high enough for CP-EL measurements. However, the

⁵ThiahelalkBZT was synthesised in the working group of Prof. Klaus Müllen, MPIP Mainz.

⁶Max. g_{PL} calculations were performed by the group of Prof. Zikie Qiu, MPIP Mainz. CV measurements were performed by Stephanie RÜth in the group of Prof. Meerholz

3 Results and Discussion

CP-EL measurement set-up used in this work is not sensitive enough to detect a potential I-CP-effect in the typical range of 10^{-3} to 10^{-4} , resulting in a measured g_{EL} value of zero for this system.

Similar results are found when PFO is used as matrix material instead. While PFO can also be used as emitter material, the emission recorded from this system originates from [ThiahelalkBZT](#), because it acts as energetic trap. As shown in chapter [3.8](#), curing of such a system consisting of a polymer capable of forming a liquid crystalline phase and a chiral molecule, can lead to the formation of a chiral phase. As introduced at fig. [2.30](#) in chapter [2.6.3](#), this could lead to a CP-selective FRET from the chiral phase onto the I-CPL emitter, thereby boosting the CPL emission to a level that would be detectable by the here used measurement set-up [\[46\]](#). Unfortunately, this was not the case, as the measured g_{EL} value was still zero.

While [ThiahelalkBZT](#) is not suitable as I-CPL emitter, it was also tested as non-emissive chiral inducer in F8BT. The results of this E-CPL system are presented in chapter [3.8.1](#).

3.7 One component systems

A promising approach to achieve CP-OLEDs with excellent performance and high η_{GEL} values is combining a chiral element with a polymeric emitter capable of forming a liquid crystalline (LC) phase. Some of the earliest published examples for CP-OLEDs are from this category [3, 84, 89].

In this work, polyfluorene (PF) was chosen as base for this approach. PF is an extensively studied blue polymeric emitter, capable of forming a LC phase at temperatures appropriate for OLED applications. For CP-OLEDs, PFs with different chiral functionalities will be introduced in the following chapters.

Chiral functionalisation of a PF polymer can be done in different ways. Here, two main strategies are used. In chapter 3.7.1, achiral fluorene monomers are co-polymerised with another chiral monomer. The resulting polymer can form a helical structure. In chapter 3.7.2, PFs are functionalised with different chiral alkyl chains, which, upon curing, promote the formation of a chiral phase.

The names of the polymers used in this section obey the same system:

Homo- and co-polymers follow the pattern of P(**A**) and P(**A-B**), respectively, with the monomers **A** and **B**.

Fluorene monomers are indicated by the letter F, followed by a number, representing the total side chain length.

For chirally functionalised side chains, the position of the chiral centre is indicated by the letter c and its position, with the *R*- or *S*-handedness of the enantiomer set before the monomer.

As an example, P(*S*-F4/*c*2-F8), which is introduced in chapter 3.7.2, is a co-polymer, consisting of two fluorene monomers. The first monomer has side chains 4 C-units long, with an *S*-chiral centre at the second C-atom. The second monomer has achiral side chains 8 C-units long.

3 Results and Discussion

In this work, only chiral side chains with (*S*)-chirality are used. Therefore, and for better readability, the *S*-descriptor is omitted for these polymers after initial introduction of the full names.

3.7.1 BINOL functionalised polyfluorenes

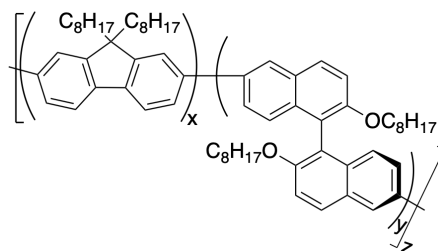


Fig. 3.35: Structure of P(*R*-BN-F8).

For this chapter, an achiral emissive unit is combined with a chiral non-emissive unit. The achiral emissive monomer, here dioctylfluorene, is co-polymerised with a chiral monomer, here a 1,1'-bi-2-naphthol (BINOL) structure [7](#) is given in fig. [3.35](#). The chemical structure of the resulting polymer P(BN-F8). In theory, the 8.0 - 8.5 % [8](#) of the BINOL component promotes a helical self-assembly, and thereby positions the emissive units in a regular, helical arrangement. It was previously shown that such structures are capable of generating CPL, with reported g_{PL} values up to -0.26 in solution [\[82\]](#).

As an indicator for chiral phase behaviour in thin film, circular dichroism (CD) measurements are extremely useful. Most CD spectrometers, however, are optimised for solution based measurements, which can cause problems when measuring thin film samples. Here, CD data is derived from ellipsometry measurements, specifically from *Müller* matrix (MM) measurements in transition. An extensive explanation of this measurement and evaluation process is given in chapters [2.4.5](#) and [3.1.4](#).

⁷P(BN-F8) was synthesised in the working group of Prof. Ullrich Scherf, University of Wuppertal.

⁸BN content determined via NMR.

Previous measurements of P(BN-F8) in the working group of Prof. Scherf indicated a CD effect in solution. Since these results support the hypothesis of helical self-assembly, the polymer was chosen to be tested for application in a CP-OLED. In thin film, however, no CD effect is found in either pristine or cured samples.

In fig. 3.36, CD data for P(BN-F8) thin films is shown. The shown samples are cured for 20 min at 300 °C. No CD effect is found here. The same results occur for pristine samples or samples cured at 150 °C.

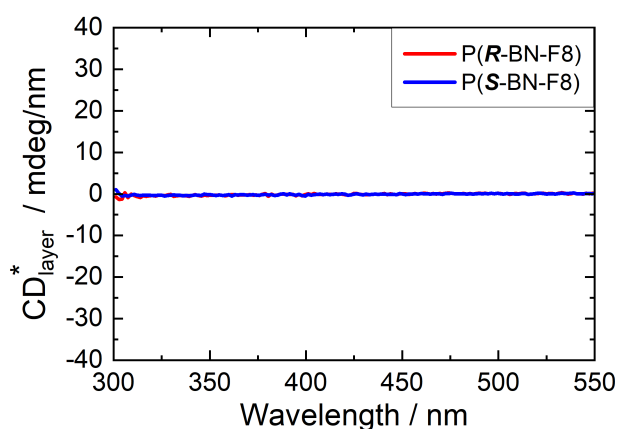


Fig. 3.36: CD* curves of P(*R*-BN-F8) (red) and P(*S*-BN-F8) (blue) thin films. Samples were cured for 20 min at 300 °C. Layer thickness 80 nm and 87 nm, respectively.

Fig. 3.37 shown LIV performance data (a), EL spectra (b) and g_{EL} values (c) of P(BN-F8) based OLEDs. The performance and spectral differences are a result of the different EML thicknesses.

In the g_{EL} curve of P(*S*-BN-F8) (c, blue), a very small non-zero g_{EL} value is visible. This is, however, an artefact caused by device degradation. As explained in chapter 3.1.3, an incorrect measurement sequence of LCP and RCP data can cause such artefacts, especially for poorly performing devices with a low brightness, as is the case here.

3 Results and Discussion

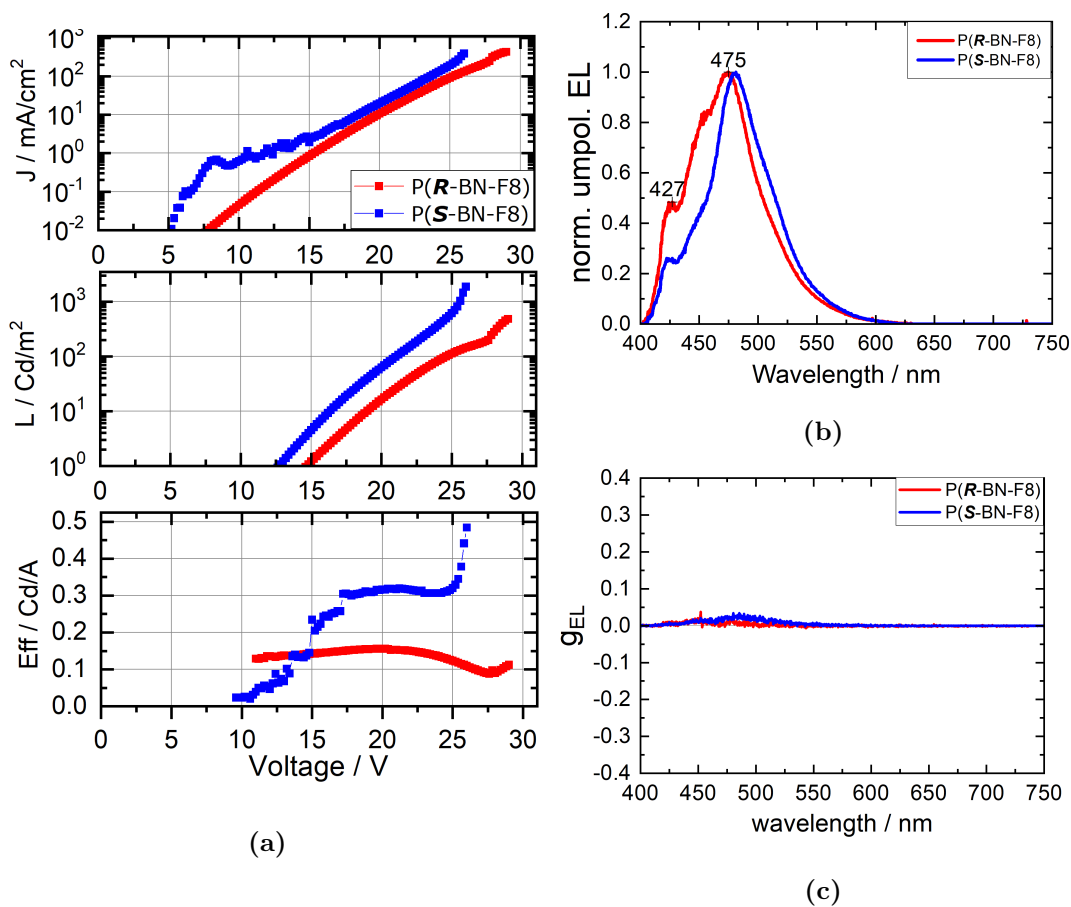


Fig. 3.37: LIV performance data (a), EL spectra (b) and g_{EL} values (c) of P(*R*-BN-F8) (red) and P(*S*-BN-F8) (blue) based OLEDs. Device architecture: ITO / PEDOT / XQUPD / XOTPD / P(*R/S*-BN-F8) (175 / 190 nm) / CsF/Al (cured 20 min@250 °C). M_w (P(*R/S*-BN-F8)) = 180 / 193 kg/mol.

In conclusion, it can be assumed that, while a stable helix is formed in solution, it disappears in thin film. However, those results are not entirely surprising. Helical self-aggregation in solution is rather slow. The polymer has to be stirred for several days before the maximum CD effect can be measured. In solid form, maintaining this fragile helical structure during spin-coating, or recreating it during curing, is certainly challenging.

To better understand these results, the nature of different CPL measurements has to be considered. CD measurements reflect the chirality of the absorption $S_0 \rightarrow S_1$. CP-PL and CP-EL measurements on the other hand reflect the chirality of the emission, in the case of the here used fluorescence emitters $S_1 \rightarrow S_0$ [120]. In most cases, the chirality is expected to be similar or equal in both states (except for Stokes shift), which makes CD an easy and reasonable measurement to estimate CPL behaviour of a material. For PL and especially for EL, however, optical effects like CP-selective reabsorption, optical rotation, reflection of interfaces and electrodes and the position of the recombination zone influence the outcoupled CPL. g_{abs} , g_{PL} and g_{EL} values of the same material or system found in literature sometimes differ significantly. Therefore, while absorption based measurements allow a fast and easy estimation of potential CP-effects, it is important to also measure the emissive CPL behaviour of a material.

While P(BN-F8) in particular is not a suitable material for CP-OLEDs, the copolymerisation of an emissive unit and a chiral unit might still be a valid approach. Since DSC measurements of the polymer do not exhibit any features, it is difficult to judge whether the tested curing conditions are suitable. However, even the highest tested curing temperature of 300 °C is already unsuitable for OLED fabrication. Therefore, even if a CD effect was to be found at even higher curing temperatures, the polymer still could not be used in devices. On the other hand, as introduced in chapter 3.3, the molecular weight of the polymer has a large influence on its phase behaviour. The here used P(BN-F8) polymers have a M_w of 180 - 193 kg/mol. Lower molecular weight batches of P(BN-F8) might show better results. Alternatively, it might be possible to imitate the solution environment in which a helix could be formed by mixing P(BN-F8) with a matrix material. Alternatively, some kind of stabilisation, either chemically through bridging or physically through support or spacer molecules, could help to form and maintain the helical structure.

3.7.2 Polyfluorenes with chiral side chains

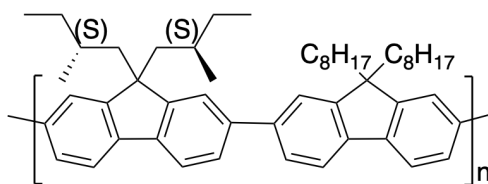


Fig. 3.38: Structure of the alternating co-polymer P(*S*-F4/*c2*-F8).

Instead of co-polymerisation with a chiral co-monomer, chiral functionalisation of PF side chains are also a promising approach for CP-OLEDs. In accordance with the naming system introduced in chapter 3.7, fig. 3.38 shows the chemical structure of P(*S*-F4/*c2*-F8), an alternating co-polymer with equal amounts of chiral di(*2S*)-2-methylbutyl-fluorene monomers F4/*c2* and achiral dioctyl-fluorene F8⁹.

P(F4/*c2*-F8) is designed as a co-polymer for solubility reasons. A P(F4/*c2*) homopolymer, due to its very short alkyl chains, would suffer from poor solubility. It would not be possible to process this polymer via spin-coating. Therefore, the co-monomer F8 with longer alkyl chains is introduced. While this unit does not contain a chiral functionality and therefore does not induce a CP-effect, it aids solubility and therefore processability.

In contrast to P(BN-F8), thin films of P(F4/*c2*-F8) exhibit significant CD values after curing. Fig. 3.39 (bottom) shows CD curves for different layer thicknesses of this polymer after curing for 20 min at 230 °C. For comparison, an absorption spectrum is given (top), with the absorption maximum in both graphs marked with a dashed line.

⁹P(F4/*c2*-F8) was synthesised by Heinz-Georg Nothofer and later again by Christin Barron in the working group of Prof. Ullrich Scherf, University of Wuppertal.

In the mainchain π - π^* transition region between 320 nm and 420 nm, both, positive and negative CD values are found. This phenomenon, called a bisignate Cotton effect, is a result of optical activity within the measured sample. The position of the sign flip is usually at or close to the wavelength of the absorption maximum, as is the case here [84].

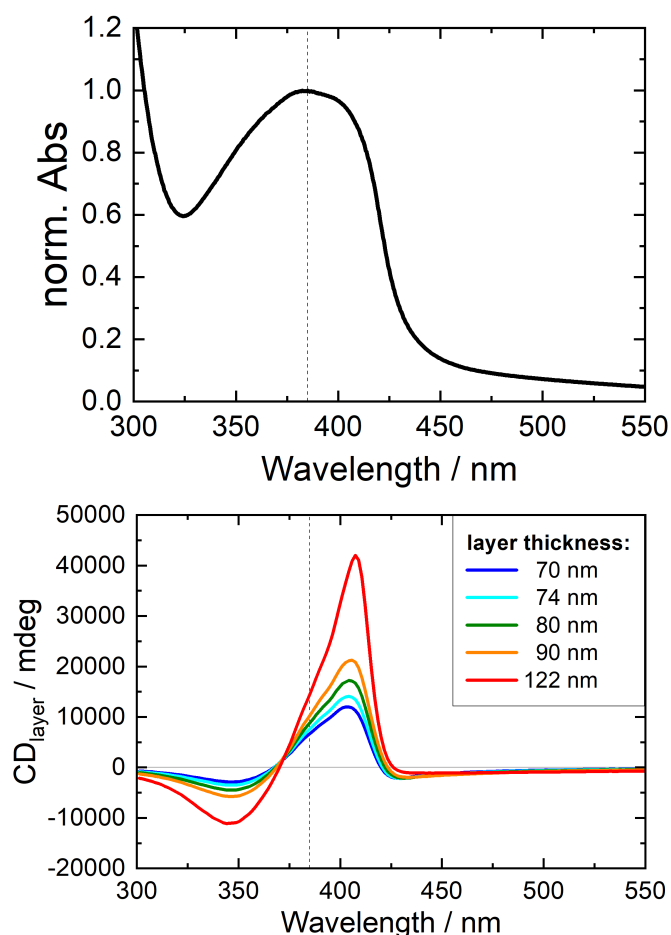


Fig. 3.39: Normalised absorption spectrum (top) and CD curves (middle) for P(F4/c2-F8) thin films of various thicknesses. Position of the absorption maximum at 385 nm is marked with a dashed line.

Samples were cured for 15 min at 250 °C (absorption spectrum) and 20 min at 230 °C (CD data). M_w (P(F4/c2-F8)) = 247 kg/mol.

Similar to the typical behaviour of solution based CD measurements when increasing the concentration or cuvette thicknesses, the CD effect in layer increases with

3 Results and Discussion

increasing layer thickness. Typically, CD values of the largest signal peak are compared, but as explained in chapter 3.1.4, other signal peaks can be used as well, since they all follow the same trend. In fig. 3.40, a linear correlation between $|\text{CD}|$ (a) or respectively $|\text{CD}^*|$ (b) values of the signal peaks at 406 nm and 344 nm and the layer thickness is shown.

To compare samples with different layer thicknesses, CD values can be divided by the layer thickness, resulting in CD^* values (see chapter 3.1.4). Fig. 3.40 (b) shows the $|\text{CD}^*|$ values corresponding to the $|\text{CD}|$ data shown in (a). Contrary to what might be expected, the CD^* for P(F4/c2-F8) is not a constant, but increases with increasing layer thickness. This behaviour is found for all chiral phase systems shown in this work, independent of material, layer thickness and curing conditions, as long as a chiral phase is present. As previously explained, this behaviour indicates that the size of the chiral domain responsible for the CD effect is larger than the layer thickness.

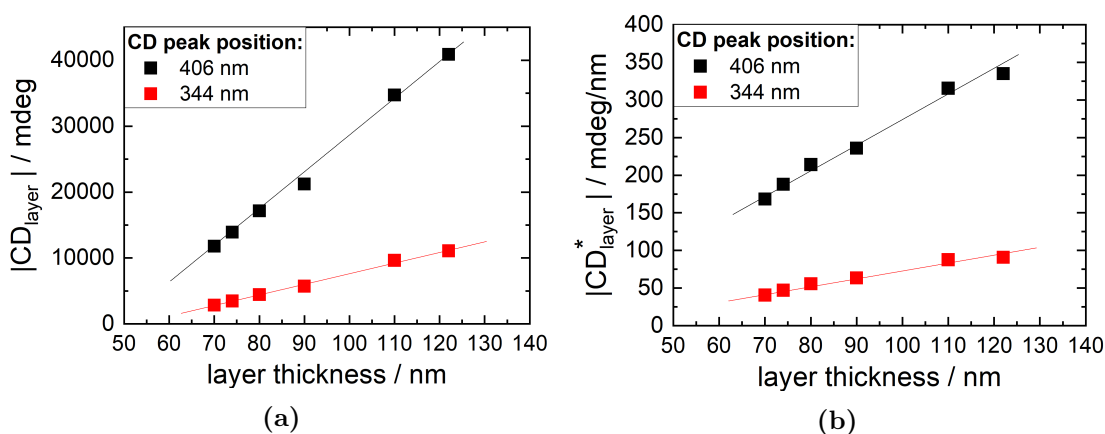


Fig. 3.40: $|\text{CD}|$ values (a) and $|\text{CD}^*|$ (b) at 406 nm (black) and 344 nm (red) over layer thickness for P(F4/c2-F8) thin films of various thicknesses. Samples were cured for 20 min at 230 °C . $M_w(\text{P}(\text{F4}/\text{c2-F8})) = 247 \text{ kg/mol}$.

Naturally, no CD effect occurs for pristine layers, as curing above T_g is necessary to form the desired chiral phase. Unfortunately, DSC measurements are not conclusive about the phase behaviour of this polymer, with no clear features for either

heating rates of 10 °C/min or 30 °C/min, so the position of T_g is unclear. Therefore, the correlation between curing temperature and resulting CD value has to be measured directly. For this, a thin film sample is cured successively at different temperatures and measured after each interval.

As expressed earlier, CD data of different measurements are usually compared at the largest CD signal peak. For larger layer thicknesses with large CD effects, however, the absorption limit can be reached during measurement, resulting in unphysical CD values in this region (see explanation in chapter 3.1.4). In this case, to still be able to compare samples of different layer thicknesses, the second, lower signal peak can be used instead, which follows the same trend as the main peak. Comparison of CD data from different PFs is also possible, but must be made at the same signal peak.

This obstacle occurs in the experiment shown in fig. 3.41. For some of the measurements, the absorption limit is reached, resulting in invalid CD data around the main signal peak. Therefore, the lower signal peak at 344 nm (analogous to the red data set in fig. 3.40) is chosen here instead of the main signal at 406 nm. Shown here are CD* values of P(F4/c2-F8) thin films for different curing temperatures.

P(F4/c2-F8) was synthesized twice, resulting in two batches with different molecular weights of $M_w = 172$ kg/mol and 247 kg/mol, respectively. As previously shown, CD is layer thickness dependent. For the two batches of P(F4/c2-F8), however, no data from samples with comparable layer thicknesses is available. To account for the difference, data from multiple samples with different layer thicknesses is shown for the higher M_w batch. Based only on layer thickness, the 75 nm sample (black triangles) would be expected to lie between the 55 nm (blue squares) and 104 nm (green squares) samples. Since the samples represent different polymer molecular weights, however, this is not the case. Instead, two trends can be deduced from this plot.

Contrary to the expected behaviour based only on layer thickness, the lower M_w polymer (black) reaches a higher maximum CD value than similar layer thick-

3 Results and Discussion

nesses of the higher M_w polymer (blue and green). At first, this behaviour is contra intuitive, as one would expect longer polymer chains able to create a more elaborate chiral phase. On the other hand, increasing chain length also leads to an increased steric demand, which could hinder or eventually even prevent the proper formation of a chiral phase. The same behaviour is also observed for F8BT based CP-OLEDs, which will be explained in detail in chapter 3.11.

As shown in chapter 3.3 for F8BT, the thermal phase behaviour of a polymer is influenced significantly by its molecular weight. It is, therefore, not surprising that, while both batches of P(F4/c2-F8) are processed and measured the same way, the largest CD effect is achieved at different curing temperatures. For all samples, curing at lower temperatures leads to no or only very low CD effects. Above a certain temperature, though, CD abruptly rises. For the lower M_w polymer (black triangles), this jump occurs around 200 °C. The higher M_w polymer (blue, green and red squares), however, exhibits a much flatter rise, still increasing even at 300 °C. This behaviour is to be expected, since a lower M_w polymer typically has a lower T_g than its M_w version, as was previously explained.

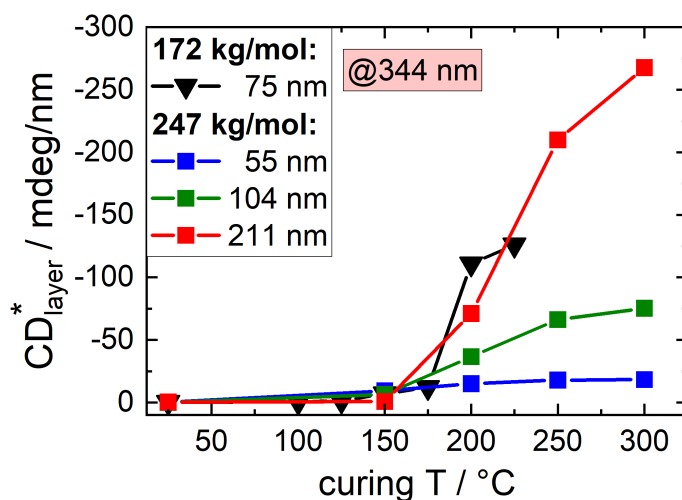


Fig. 3.41: CD* values at 344 nm for P(F4/c2-F8) thin films. Both batches are shown, with a M_w of 172 kg/mol and 247 kg/mol. Samples were cured successively for 15 - 20 min at the given temperatures.

For a constant curing temperature of 230 °C, fig. 3.42 shows the influence of different curing times on CD*. For this, P(F4/c2-F8) thin films of different layer thicknesses are cured and measured successively. Initially, CD* increases rapidly with increasing curing times, indicating the gradual development of the chiral phase. Eventually, however, a stable maximum is reached, which occurs between 20 min and 40 min, depending on the layer thickness. Just like in the previously shown plots, larger CD* values are found for larger layer thicknesses.

For all thinner samples, a slight decrease from the maximum CD* after 20 min is found. Degradation of the material, aggregation or conversion into another phase might account for this result. However, layer thickness volume reduction is a much more likely explanation. This behaviour, which was introduced in chapter 3.4.1, is also observed for F8BT layers. While the heated polymer strands rearrange into a chiral phase, the layer can flatten out over the substrate surface. Since CD is thickness dependent, it is to be expected that a thinner layer thickness would result in lower CD values. To account for this artefact, the exact layer thickness would have to be measured after each curing step with a non-invasive method, for example variable angle spectroscopic ellipsometry (VASE). In this example, however, the layer thickness was measured only once via profilometry, after annealing.

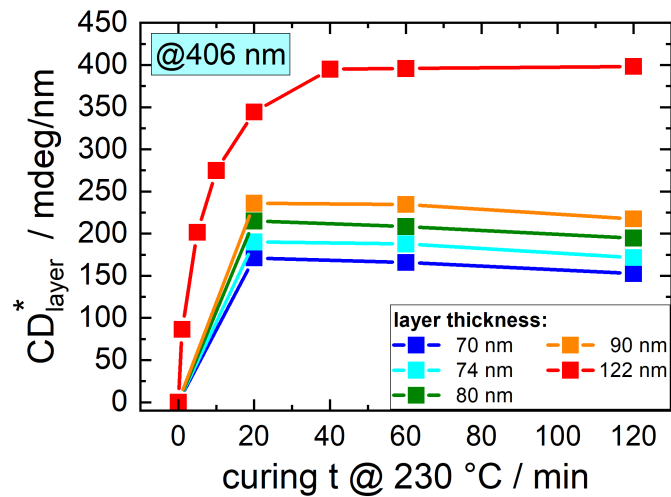


Fig. 3.42: CD* values at 406 nm for P(F4/c2-F8) thin films.

Samples were cured successively for 1 - 120 min at 230 °C. M_w (P(F4/c2-F8)) = 247 kg/mol.

From these measurements, the ideal curing conditions for P(F4/c2-F8) can be interpreted. For the polymer molecular weight of 172 kg/mol, best results are achieved with 20 min curing at approximately 210 °C. For the polymer molecular weight of 247 kg/mol, best results are achieved with 20 - 40 min curing at 230 °C. However, for application in OLEDs, these conditions are not suitable. Curing temperatures above 200 °C and longer curing times, as would be ideal for this polymer, bring the risk of efficiency loss through degradation of the other contained layers, especially ITO. Therefore, a compromise between high CP-effects and good device performance has to be made. Otherwise, device performance losses have to be accepted instead.

Fig. 3.43 and 3.44 display multiple aspects of P(F4/c2-F8) based CP-OLEDs with different EML thicknesses.

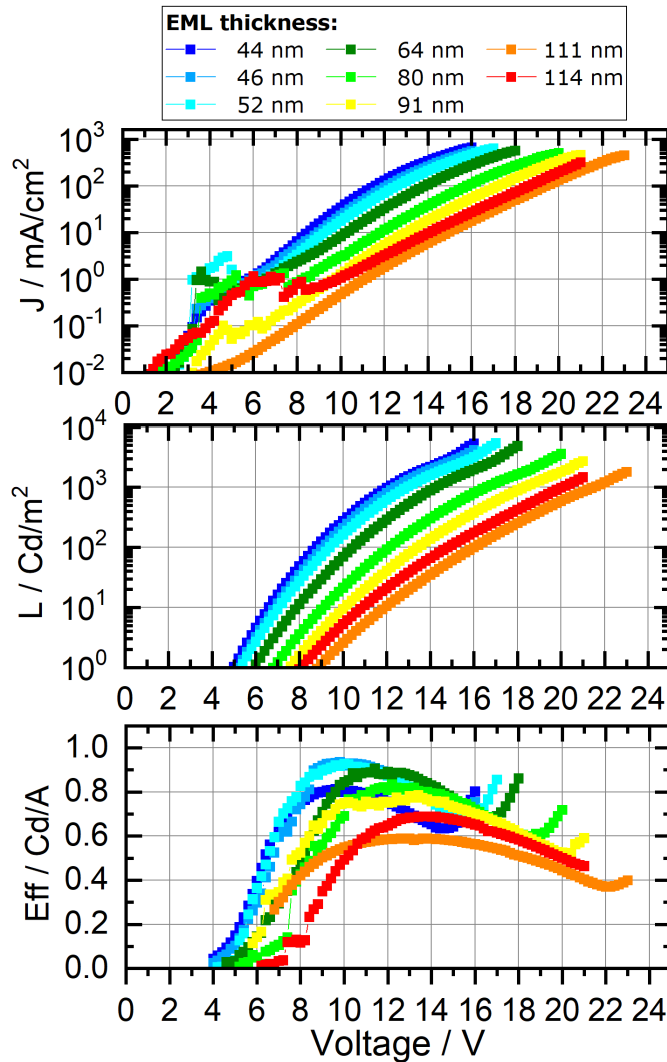
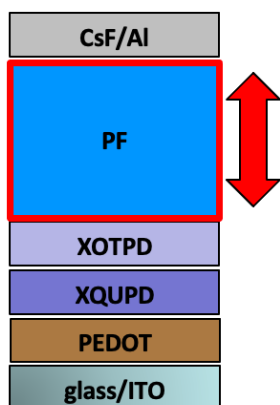


Fig. 3.43: LIV performance data of P(F4/c2-F8) based CP-OLEDs with different EML thicknesses.

Device architecture: ITO / PEDOT / XQUPD / XOTPD / P(F4/c2-F8) / CsF/Al (cured 20 min@240 °C) M_w (P(F4/c2-F8)) = 247 kg/mol.



Analogous to the results for F8BT explained in chapter 3.2.4, the normalised EL spectra in fig. 3.44 (a) exhibit a thickness dependent spectral shift, resulting from optical interference. In contrast to F8BT, however, which features only one broad emission band, PFs typically have several emission peaks, consisting of distinct vibrational transitions. For F8BT, this thickness dependent optical effect manifested as a wavelike spectral shift of the EL maximum back and forth. For PFs, however, the emission peak positions remain almost fixed. Instead, the ratio of the individual peaks to each other changes. As explained before, this behaviour is a result of the varying distance between the recombination zone and reflective cathode, and the resultant interference pattern between light beams in forward direction and reflected light previously in backward direction.

Just like the thickness dependent spectral shift, the associated g_{EL} curves (b) experience a wavelike progression, both, in intensity and spectrally. Many of the shown curves feature one or even two sign flips. This trend is seen even clearer in the g_w curves shown in (c). The magnitude and sign of g_w values for each EL peak shift significantly. For the single emission peak of F8BT, this effect is analysed in depth in chapter 3.10. Here, the multiple varying EL peaks make analysis more complex. Instead of plotting $g@maxEL$ over EML thickness, g_{EL} values of the peaks are plotted individually in (d). Overall, a maximum $g@maxEL$ of -0.55 is found.

It appears that the overall trend for all peaks is similar. Just like for F8BT, g_{EL} experiences a wave like intensity shift with varying EML thickness. However, with increasing wavelength of the EL peak, this trend curve flattens out. The maximum intensity of the trend curve decreases while the distance between two zero crossings increases. The CP-effect appears strongest for the lowest wavelength EL peak. This result could, however, be distorted. To confirm this thesis, optical and CP-effects would have to be decoupled and evaluated individually. Several methods to achieve this are suggested in chapter 4.

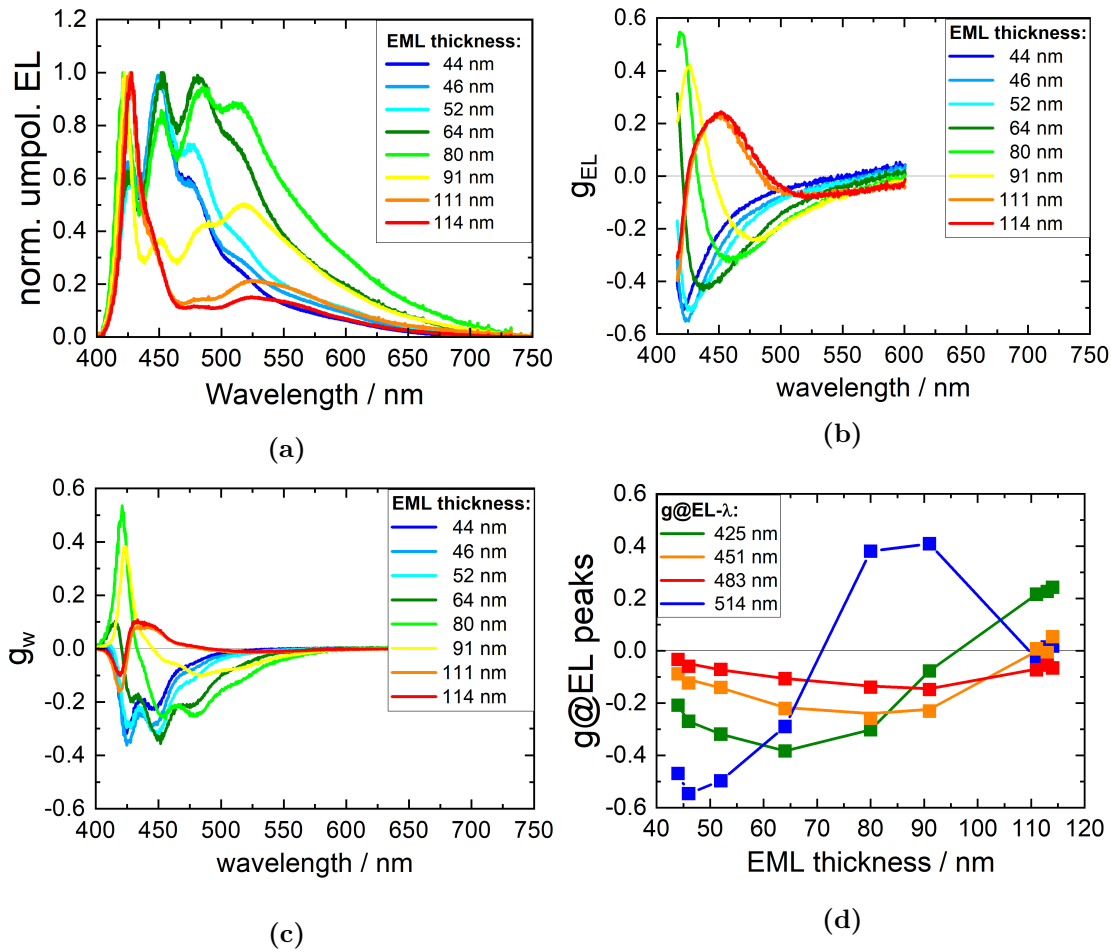


Fig. 3.44: Normalised unpolarised EL spectra (a), g_{EL} curves (b) and g_w curves (c) of P(F4/c2-F8) based CP-OLEDs with different EML thicknesses. (d) g_{EL} values with trend curves for four different EL peaks over EML thickness.

Device architecture: ITO / PEDOT / XQUPD / XOTPD / P(F4/c2-F8) / CsF/Al (cured 20 min@240 °C). M_w (P(F4/c2-F8)) = 247 kg/mol.

3.7.3 Cavity CP-OLEDs

In the previous chapter, the thickness dependent shift of g_{EL} values of a P(F4/c2-F8) based CP-OLED appeared different for each EL peak. Within one device, it is possible that both, LCP and RCP emission are found. For commercial application, however, this behaviour is problematic. Ideally, a CP-OLED would emit only light of a uniform polarisation state. While for an EML thickness around 55 nm, g_{EL} values for all peaks at least have the same sign (see fig. 3.44), it is unlikely to find one perfect layer thickness or architecture where g_{EL} values for all peaks would be equally high. Suppression of optical interference effects, as suggested in chapters 3.10 and 4, might be a solution to this problem. A more simple approach, however, could be to use a cavity architecture to single out only one emission wavelength, and suppress all others, like it was explained in chapter 2.4.2.

The difference between regular and cavity OLEDs is the addition of a second reflective metal layer on the anode side. Here, a semitransparent layer consisting of 30 nm Ag is evaporated onto the ITO layer. This way, light is consecutively reflected on both electrodes before it is eventually outcoupled. Like in a Fabry-Pérot resonator, light waves with the correct resonance wavelength can create a standing wave. The resonance wavelength depends on the distance between both mirrors, which is called cavity length. Through constructive and destructive interference, this specific wavelength is amplified compared to other wavelengths, a process originally used for lasers.

Fig. 3.45 (top) shows EL spectra of a regular OLED (blue) compared to a cavity OLED (red) with the same architecture. While there is still some emission present above 470 nm, the intensity of all EL peaks besides the first peak around 425 nm is significantly dampened in the cavity device. For this area, g_{EL} values could be calculated, but since the normalised EL intensity is below 0.2, the values are cropped, as explained in chapter 3.1.2. Through optimisation of the thickness of all layers, especially the semitransparent Ag layer, this wavelength selection effect could be further improved. Through variation of the Ag layer thickness, a better cavity can be created, resulting in a smoother and narrower EL spectrum.

The shape and size of the g_{EL} curve peak at the first EL peak around 425 nm is similar for both, regular and cavity OLED. The g_{EL} curve peaks are not identical, however, which is not surprising. Differences of this magnitude can be the result of even a small EML thickness difference of a few nanometers.

To the left and right of this g_{EL} curve peak, the regular OLED exhibits large g_{EL} values of the opposite handedness as well, which indicate a spectral shift between the LCP and RCP spectra, caused by optical interference effects after reflection on the cathode.

The g_{EL} curve (middle) of the regular OLED experiences two sign flips and both, large positive and negative g_{EL} values, with a $g_{\text{@maxEL}}$ of -0.12 at the main emission peak of 428 nm. For the cavity OLED, $g_{\text{@maxEL}}$ is even higher with -0.34 . The difference between the two devices is even clearer in the g_{w} curves (bottom). While g_{max} is very similar, the difference in g_{w} is obvious.

As mentioned before, this difference could have been caused by slight EML thickness differences in the range of a typical batch to batch variation. Since EML thickness influences the optical interference pattern after reflection, even slight thickness differences can cause a spectral shift between the RCP and LCP spectra, resulting in a shifted g_{EL} curve. However, it is also possible that the larger $g_{\text{@maxEL}}$ of the cavity OLED is caused by the cavity effect. Because of the repeated reflection of the light within the cavity, the light travels through the chiral EML multiple times. During interaction with this layer, CP-selective absorption or optical rotation can occur, thereby influencing the polarisation state of the out-coupled light. To estimate the influence of this effect compared to typical batch to batch variations, further experiments would be necessary, including optimisation of the Ag layer thickness and an EML thickness variation of the cavity OLED, analogous the results shown in fig. 3.44. Creating a CP-OLED with a sharp spectral peak and CPL emission of one handedness only is a basic requirement for use in a CPL display. As demonstrated here, cavity CP-OLEDs could provide just that.

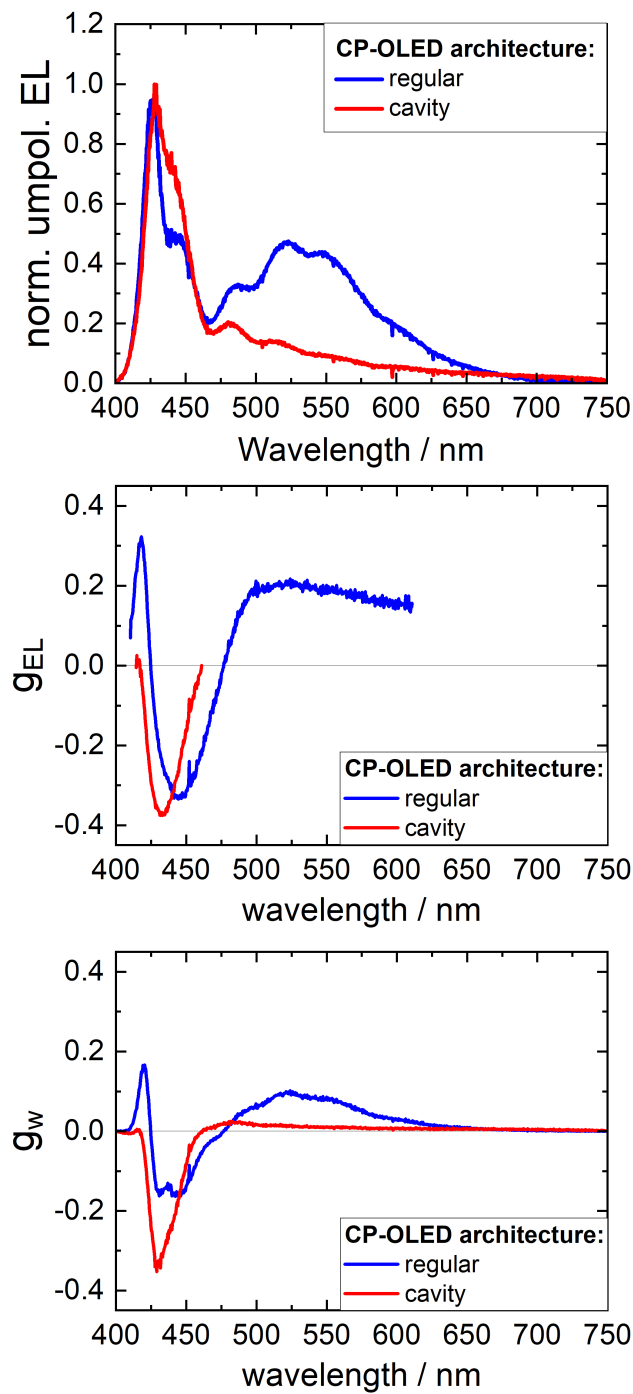


Fig. 3.45: Normalised unpolarised EL spectra (top), g_{EL} curves (middle) and g_w curves (bottom) of P(F4/c2-F8) based CP-OLEDs. Compared are a regular device (blue) with a cavity device (red).
 Device architecture: ITO / (30 nm Ag) / PEDOT / XQUPD / XOTPD / P(F4/c2-F8) (100 nm) / CsF/Al (cured 15 min@200 °C). M_w (P(F4/c2-F8)) = 172 kg/mol.)

3.7.4 Oxidation of chirally functionalised PFs

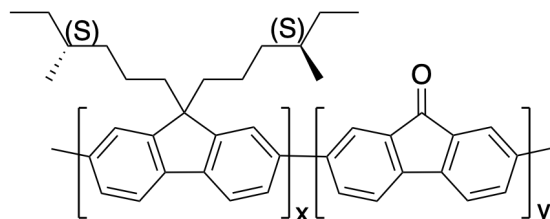


Fig. 3.46: Structure of the chiral polymer P(*S*-F6/*c4*-FN) with statistically distributed oxidised degradation product fluorenone.

PF is a rather stable material which can even be spin-coated in air. Nevertheless, it is susceptible to oxidation under certain conditions. Because of their aromaticity, the two benzyl rings are chemically very stable. The covalent bridge, however, is prone to photooxidation. This vulnerability for keto-defects is particularly high in PFs with, even accidentally, only one side chain present instead of two [121].

The structure given in fig. 3.46 shows one such example, where, during its synthesis, the chiral monomer F6/*c4* (left monomer) or its homo-polymer P(F6/*c4*) was partially oxidised to fluorene (FN, right monomer), resulting in a co-polymer of the form P(F6/*c4*-FN) [10]. Through this oxidation, the chirally functionalised side chains of each affected monomer are replaced with a keto function. While the resulting polymer still contains chiral units and might even be able to form a chiral phase, the absorption and emission behaviour changes.

Fig. 3.47 shows normalised thin film absorption (a) and PL (b) spectra of the oxidised P(F6/*c4*-FN) polymer. Measured were samples of the polymer directly after synthesis ("mix", red) with $M_w = 82$ kg/mol, as well as all three GPC fractions of 31 kg/mol (blue), 82 kg/mol (green) and 177 kg/mol (orange). As an example of a chirally functionalised PF without keto-defects, data of P(F8/*c3*-F8) ("PF", black) is shown in comparison.

¹⁰P(F6/*c4*-FN) was synthesised and separated via GPC by Christin Barron in the working group of Prof. Ullrich Scherf, University of Wuppertal.

3 Results and Discussion

The main absorption peak of fluorenone is located below 300 nm and is not visible in measurements on glass substrates. A second absorption peak occurs around 390 nm. However, this absorption peak is very weak and superimposed with the main fluorene absorption peak [122]. It is, therefore, not surprising that all shown absorption spectra are almost identical.

PL spectra, however, show significant differences. P(F8/c3), as a chirally functionalised PF without keto-defects for comparison, shows PL peaks around 420 nm and 445 nm from the fluorene unit. While these peaks are also visible for the oxidised P(F6/c4-FN), a second, broad emission around 540 nm appears, which is typical for fluorenone [121, 122]. Directly after synthesis ("mix"), P(F6/c4-FN) only contains a small fluorenone PL peak. After GPC separation, however, all three fractions show significantly larger fluorenone emissions than fluorene emissions, indicating a gradually advancing oxidation. If compared with each other, the three fractions have a similar ratio of fluorene to fluorenone, with the largest molecular weight fraction slightly less oxidised.

Becker *et al.* analysed statistical polyfluorenes containing small percentages of fluorene units. They report a linear correlation between the ratio of the green to total PL intensities on a logarithmic scale and the fluorenone concentration. However, this only applies to dilute solutions of fluorene co-polymers with very low fluorenone concentrations up to 5 %. Also, when analysing PL data, it has to be considered that the PL emission intensity of the fluorenone is sensitive to air. The green emission is quenched by a factor of 4.5 if measured in vacuum instead of in air, a process that is almost completely reversible, though [123].

De Freitas *et al.* also report an increased PL intensity of the red-shifted fluorenone emission with increasing fluorenone content in similar polymers. This is attributed to an interchain FRET in solid state [124]. Since the results of this source are based on thin film PL spectra, they are comparable to the spectra shown in fig. 3.47 (b). By comparing the PL intensities at 420 nm (fluorene) and 540 nm (fluorenone) and assuming a linear correlation, the fluorenone concentration in the here used polymers could be roughly estimated, resulting in fluorenone

concentrations of 0.1 mol% for the mixed polymer and 0.8 mol% for the polymer fractions after GPC separation.

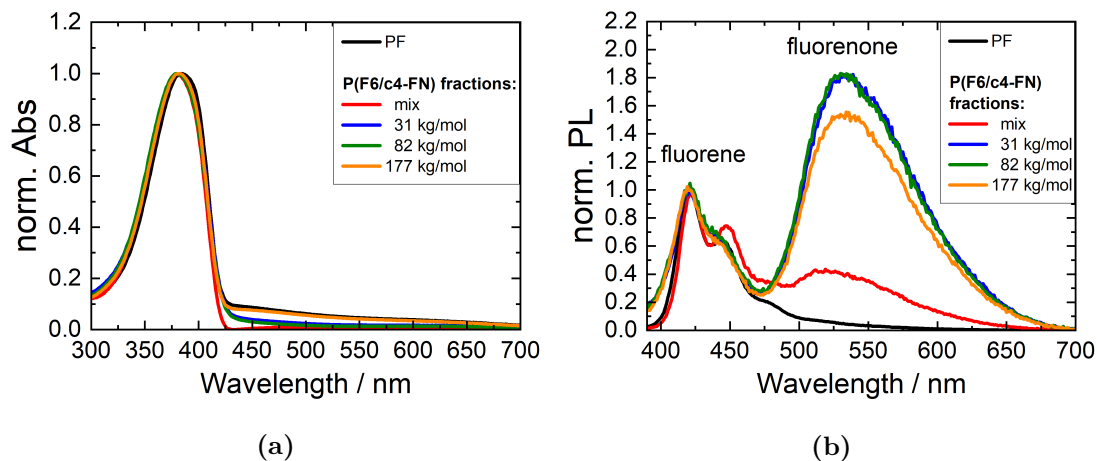


Fig. 3.47: Normalised thin film absorption (a) and PL (b, $\lambda_{ex} = 370$ nm) spectra of P(F6/c4-FN). The oxidised polymer P(F6/c4-FN) is shown as synthesised (red) and three fractions after GPC separation with a M_w of 31, 82 and 177 kg/mol (blue, green and orange). As comparison without keto-defects, the chiral side chain polymer P(F8/c3-F8) is shown in black.

Since oxidation results in cleavage of the side chains in favour of a keto function, the chiral information at this monomer unit is lost. However, the polymer can still form a chiral phase, despite some keto defects. As seen in fig. 3.48, a CD effect is still present. This indicates that, even with a significant amount of keto-defects as seen in PL data, sufficient chirally functionalised units still remain to produce a chiral phase.

As explained in chapter 3.3, batches or fractions of a polymer with different M_w s require different curing temperatures to produce the desired chiral LP phase. As indicated by fig. 3.42 in chapter 3.7.2, it is possible that, especially for the larger M_w fractions, higher curing temperatures or much longer curing times might have lead to even higher CD values here. It appears that the phase behaviour of the mixed P(F6/c4-FN) sample (green) is dominated by the behaviour of the larger M_w fractions. With decreasing M_w , a stronger CD effect can be observed. A sim-

3 Results and Discussion

ilar trend is found for F8BT based CP-OLEDs and will be analysed in detail in chapter [3.11](#).

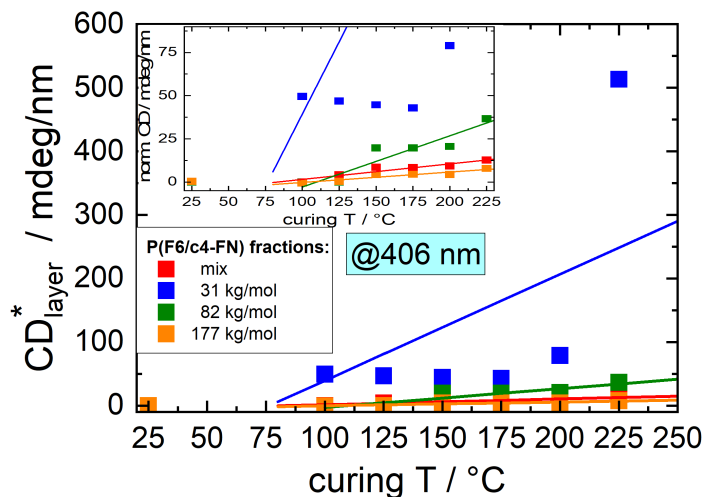


Fig. 3.48: CD* values at 406 nm for different P(F6/c4-FN) fractions. Thin films were successively cured for 15 min at different temperatures. Because of the large spread of the data points, a close up section is shown as inset.

Even though a CD effect can be measured, in CP-OLEDs, the same material does not exhibit a CP-effect. Fig. [3.49](#) shows the EL spectrum (black) and associated g_{EL}^{EL} data (red) of a P(F6/c4-FN) based OLED. No non-zero g_{EL}^{EL} values are found for this device, or any other devices from this material. An explanation for this behaviour can be found in the EL spectrum. Only a very small fluorene emission signal around 450 nm is present, compared to a very large fluorenone emission signal around 540 nm. The ratio of fluorene to fluorenone emission signals for EL is significantly smaller than for PL. But this effect is not a result of further oxidation, but due to the different energetic levels of the two materials.

In PL, all molecules are excited equally, as excitons are formed and recombine within one molecule only. While fluorenone molecules have a low [PLQY](#), their oscillator strength is enhanced when co-polymerised with fluorene. A light-harvesting effect of the polymer backbone promotes exciton trapping in the fluorenone, leading

to preferential population of the fluorenone excited state [123]. However, emission of fluorene units is still prominent as well. In EL, however, excitons are formed by the recombination of charge carriers from different molecules. Naturally, this is favoured for lower energetic levels. Since fluorenone has a lower HOMO level around -6.15 eV [125] compared to PF around -5.9 eV [49], it forms an energetic trap for electrons. The resulting EL emission spectrum is largely dominated by fluorenone emission, despite its lower content in the material. Even though a chiral phase might still be formed through the remaining fluorene units, the observed EL emission is unpolarised.

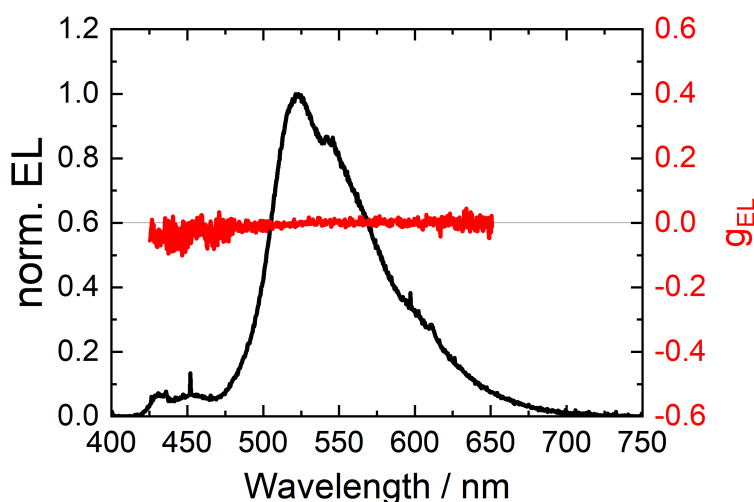


Fig. 3.49: P(F6/c4-FN) based CP-OLED. Shown are the normalised unpolarised EL spectrum (black) and the resulting g_{EL} curve (red).
 Device architecture: ITO / PEDOT / XQUPD / XOTPD / P(F6/c4-FN) (210 nm) / CsF/Al (cured 15 min@230 °C). M_w (P(F6/c4-FN)) = 82 kg/mol.

3.7.5 Odd-Even-Effect

Some differentiators between the chirally functionalised PFs shown in this work, for example molecular weight, have been analysed in previous chapters. One significant difference, however, has not been addressed yet. Like the other analysed factors, the position of the chiral centre has a noticeable influence of CPL behaviour.

Fig. 3.50 shows CD* spectra of cured thin films of the three polymers P(F4/c2-F8) (a), P(F8/c3) (b) and P(F6/c4-FN) (c). All samples are spin-coated with a layer thickness of 90 nm and cured at their respective ideal curing temperature.

The Cotton effect introduced in chapter 3.7.2 can be divided into two subcategories. For this, the development of the CD curve with increasing wavelength is analysed. If the signal transitions from negative to positive values, it is called a positive Cotton effect. Likewise, if the signal transitions from positive to negative values, it is called a negative Cotton effect.

While the three compared polymers all contain *S*-chirality, they exhibit different Cotton effects depending on the position of the chiral centre. P(F4/c2-F8) (a) and P(F6/c4-FN) (c) both have a chiral centre on an even numbered C-atom and, subsequently exhibit a positive Cotton effect (blue). P(F8/c3) (b) on the other hand has its chiral centre on an odd numbered C-atom. As a result, it exhibits a negative Cotton effect (red). This behaviour, known as odd-even-effect, has previously been reported for chirally functionalised PFs [84] and other materials [80, 126, 127].

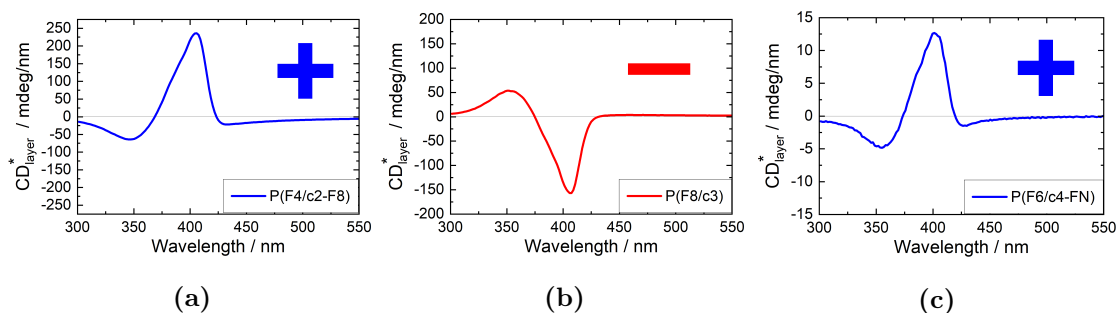


Fig. 3.50: CD* curves of 90 nm thick cured thin films of P(F4/c2-F8) (a), P(F8/c3) (b) and P(F6/c4-FN) (c). Depending on the position of the chiral centre, a positive (blue, +) or negative (red, -) Cotton-effect is observed.

Because of the differences especially in molecular weight, a quantitative comparison of maximum possible CD values would not be robust. Based on the here shown data, it, therefore, cannot be judged how much the position of the chiral centre influences CPL behaviour. A qualitative statement, on the other hand, can be made.

In Table 3.4, the three polymers with their molecular weight, maximum CD* and Cotton effect sign, are compared. With 236 mdeg/nm, P(F4/c2-F8) has the largest CD* of the three polymers. This is surprising, since P(F4/c2-F8) has the largest M_w , which, as shown in chapter 3.7.2, typically produces lower CD effects. Also, the polymer only contains 50 % chiral monomer, a factor also expected to reduce the CD effect. Following this trend, P(F8/c3) and P(F6/c4-FN), both with decreasing M_w , have lower CD* values of -157 mdeg/nm and 13 mdeg/nm, respectively. This indicates that with increasing distance between the chiral centre and the emissive core or polymer backbone, the CD effect is reduced.

3 Results and Discussion

Tab. 3.4: Polymers shown in fig. 3.50, with M_w maximum CD* values and Cotton effect.

Polymer	M_w / kg/mol	max. CD coeff. / mdeg/nm	Cotton effect
P(F4/c2-F8)	172	236	+
P(F8/c3)	130	-157	-
P(F6/c4-FN)	82	13	+

Interestingly, the odd-even-effect also occurs in CP-EL measurements. Fig. 3.51 shows g_{EL} curves of P(F4/c2-F8) (blue) and P(F8/c3) (red) based CP-OLEDs with comparable device architectures. Other than two equal devices with opposite enantiomers of the same chiral material, the here shown curves are not perfect mirror images of each other. Partly, this can be explained by the slight differences between the two devices. Especially the 5 nm EML thickness difference and varying curing temperature have a large impact on the shape and size of the g_{EL} curves.

A qualitative comparison, however, can certainly be made. For the first EL peak around 422 nm, P(F4/c2-F8) and P(F8/c3) achieve a g_{EL} value of +0.88 and -0.60, respectively. Likewise, the g_{EL} curves for the more redshifted EL peaks of both polymers have opposite signs.

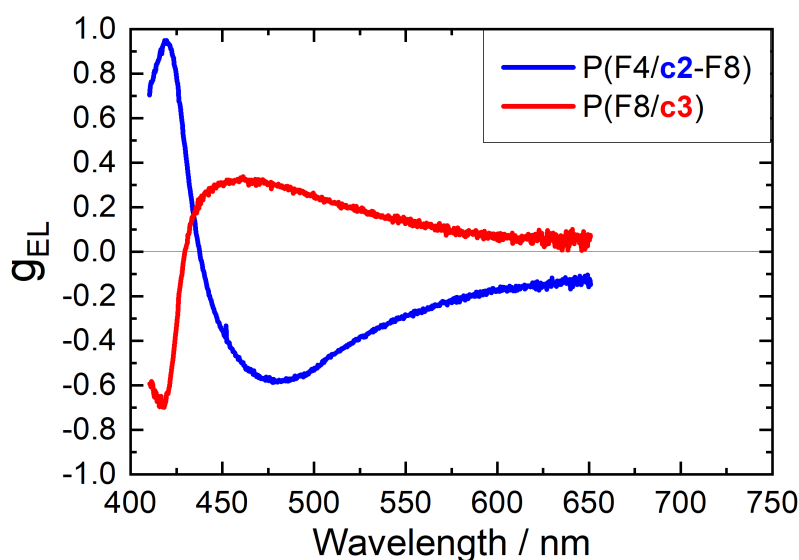


Fig. 3.51: g_{EL} curves of CP-OLEDs with P(F4/c2-F8) (blue) or P(F8/c3) (red) as EML. EML thickness is 90 nm and 85 nm, and curing was performed for 15 min at 200 °C and 180 °C, respectively. Device architecture: ITO / PEDOT / XQUPD / XOTPD / emitter polymer / CsF/Al.

The odd-even-effect offers a unique opportunity for CP-OLEDs based on chirally functionalised polymers. Usually, the two enantiomers of chiral functional groups offered for synthesis have a significant price difference, with the *R* enantiomer often being more than twice as expensive than the *S* enantiomer. Such materials are often synthesised with the help of enzymes, profiting of their built in stereoselectivity. In nature, however, most compounds and enzymes only appear in one chiral form. Using artificial instead of naturally occurring enzymes and raw materials, therefore, increases production costs significantly. For 3D displays based on CP-OLEDs, however, equal CPL pixels of both handednesses would be required. Using two polymers with their chiral centre on different positions rather than two enantiomers of the same polymer might have significant cost advantages without performance detriments.

3.7.6 Chirally functionalised homo- vs. co-polymers

Since chiral functionalisation of the fluorene unit occurs prior to polymerisation, it is just as easy to create homo-polymers as it is to create co-polymers with other monomer units. In the case of P(F4/c2-F8) in chapter [3.7.2](#), this co-polymerisation was performed to increase solubility, and therefore usability of the material.

F8, the co-monomer chosen for this work, is the most common fluorene monomer. It provides great solubility properties and is extensively studied. However, the linear alkyl chains do not contain a chiral centre.

Because of its low solubility, it is not possible to compare the CP-effect of homo-versus co-polymer for P(F4/c2). Instead, another chirally functionalised fluorene unit has to be found.

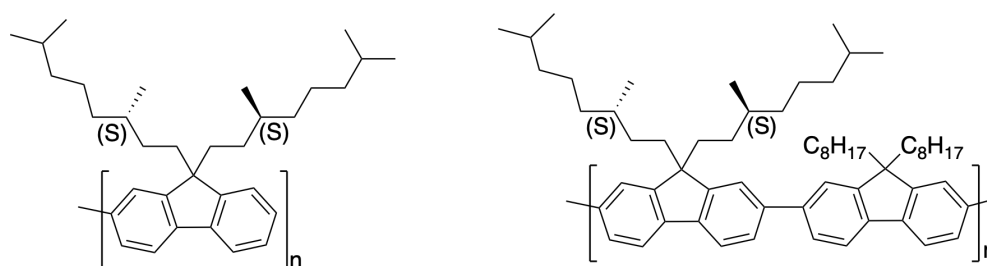


Fig. 3.52: Structure of P(S-F8/c3) (left) and P(S-F8/c3-F8) (right).

Fig. [3.52](#) shows the chemical structures of P(F8/c3) (left) and P(F8/c3-F8) (right), homo- and co-polymers of the same chirally functionalised unit [11](#). Here, the alkyl chains of both, chiral and achiral functionality, are based on octyle chains and feature comparable solubility and steric behaviour.

While the additional methyl groups in the chiral unit are not expected to have a big impact on any of the here compared properties besides chirality driven effects, the different molecular weights of the polymers do. Polymerisations of this

¹¹P(F8/c3) and P(F8/c3-F8) were synthesised by Christin Barron in the working group of Prof. Ullrich Scherf, University of Wuppertal.

kind always produce a certain batch to batch variation concerning their molecular weight and $\overline{\text{PDI}}$. In this case, P(F8/c3) has a lower $\overline{M_w}$ of 130 kg/mol compared to P(F8/c3-F8) with a $\overline{M_w}$ of 157 kg/mol. As introduced in chapter 3.3 for F8BT, the phase behaviour of PF based polymers changes significantly with molecular weight. Additionally, molecular weight is also a factor for the CP-effect, which will be analysed in detail in chapter 3.11. It is, therefore, important to keep both these factors in mind while comparing the here used batches of P(F8/c3) and P(F8/c3-F8).

In this chapter, P(F8/c3) is first introduced and analysed individually. Afterwards, both polymers are compared to assess the influence of achiral co-monomers within a chiral polymer.

To determine the ideal curing conditions for P(F8/c3), fig. 3.53 shows CD* values of thin films after different curing temperatures. Shown is data from two different layer thicknesses, 90 nm (red) and 225 nm (black). Typical for PFs, the largest CD signal peak is located at 406 nm. For many of these measurements, however, the data for this signal peak is unphysical. With a larger layer thickness, the absorption limit is reached and CD values around the largest CD signal cannot be calculated. To circumvent this problem, evaluation of CD data is performed for the second CD signal peak at 344 nm. For comparison, CD* data of the 406 nm signal peak for the 90 nm sample can be found in fig. 3.54 (red curve).

While the 90 nm sample reaches a stable CD maximum already at 175 °C, the maximum for the 225 nm sample is located around 200 °C with a subsequent decline. As shown for P(F4/c2-F8) in fig. 3.42 (chapter 3.7.2), samples with a larger layer thickness tend to require longer curing times. It is likely that, given a longer curing time, the thicker sample would also have reached its maximum CD at a lower temperature. Additionally, shrinking during curing, as introduced in chapter 3.4.1, can have a larger impact on the CD* values for larger layer thickness samples. Here, only the final layer thickness after curing is measured via DEKTAK profilometry and used for all data points. Very likely, the observed CD decline above 200 °C for the 225 nm sample can be explained as such an artefact

created by the unaccounted thickness shrinkage.

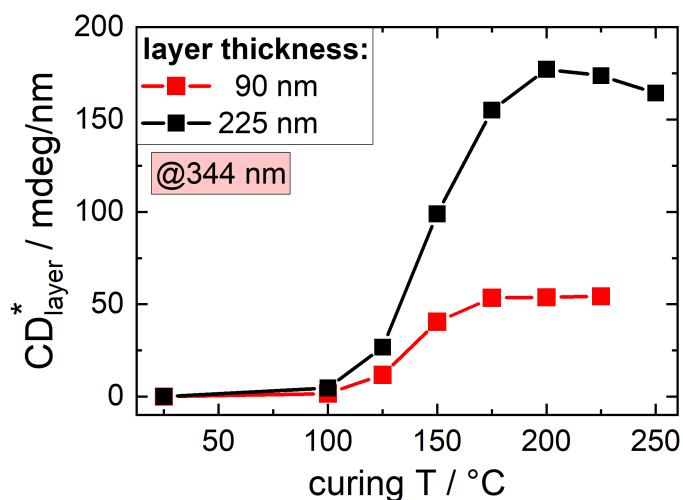


Fig. 3.53: CD* values at 344 nm of P(F8/c3) thin films with two different layer thicknesses. Samples were cured successively for 15 min at different temperatures. M_w (P(F8/c3)) = 130 kg/mol.

Fig. 3.54 compares CD* values of P(F8/c3) (red) and P(F8/c3-F8) (blue). In contrast to fig. 3.53, where positive CD values from the smaller signal peak at 344 nm are shown, fig. 3.54 contains negative CD values from the larger signal peak at 406 nm. The red data sets in both figures are taken from the same sample and represent the two signal peaks of one measurement. Thin films of both polymers are cured successive at different temperatures. For comparability, both samples are prepared with the same layer thickness of approximately 90 nm.

While P(F8/c3) (M_w = 130 kg/mol) achieves a CD plateau with a curing temperature around 175 °C, P(F8/c3-F8) (M_w = 157 kg/mol) requires a curing temperature around 235 °C for best results. Considering the difference in molecular weight between both polymers, different curing temperatures are not surprising. For the lower M_w polymer to require a lower curing temperature is in accordance with the previous results illustrated in this work.

The maximum possible CD* of 157 mdeg/nm for P(F8/c3) is significantly larger

than for P(F8/c3-F8) with 24 mdeg/nm. A larger CD effect for the lower M_w polymer is in accordance with the results for F8BT in chapter 3.11. It cannot be excluded that the difference in CD intensity might be based purely on the molecular weight difference between the polymers. However, the observed CD difference is much larger than would be expected for such small M_w differences of this magnitude. It is more likely that the achiral F8 units in P(F8/c3-F8) have a disruptive effect on the desired chiral phase. P(F8/c3) on the other hand only contains chirally functionalised side chains and might, therefore, be able to form a more continuous chiral phase.

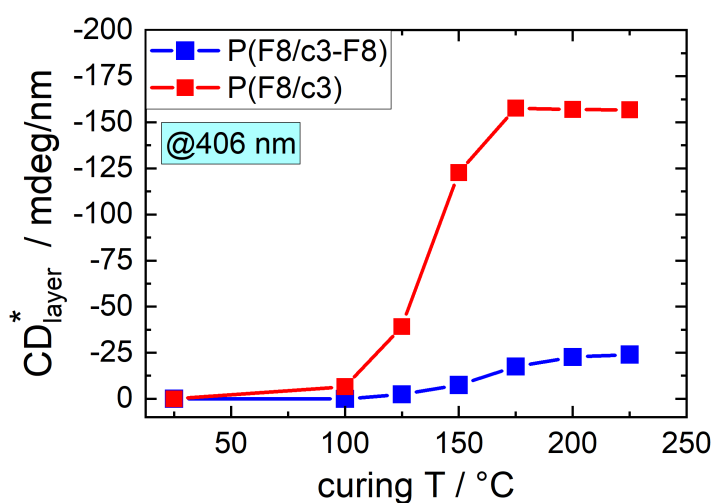


Fig. 3.54: CD* values at 406 nm of P(F8/c3-F8) (blue) and P(F8/c3) (red) thin films with approximately 90 nm thickness. Samples were cured successively for 15 min at different temperatures. M_w (P(F8/c3)) = 130 kg/mol and M_w (P(F8/c3-F8)) = 157 kg/mol.

3 Results and Discussion

As emitter material in CP-OLEDs, both polymers show polarised electroluminescence. For P(F8/c3), g_{EL} values of the four main emission peaks are plotted against EML thickness in fig. 3.55. Similar to the results of P(F4/c2-F8) (see fig. 3.44 (d) in chapter 3.7.2), a thickness dependent size and sign change of g_{EL} occurs.

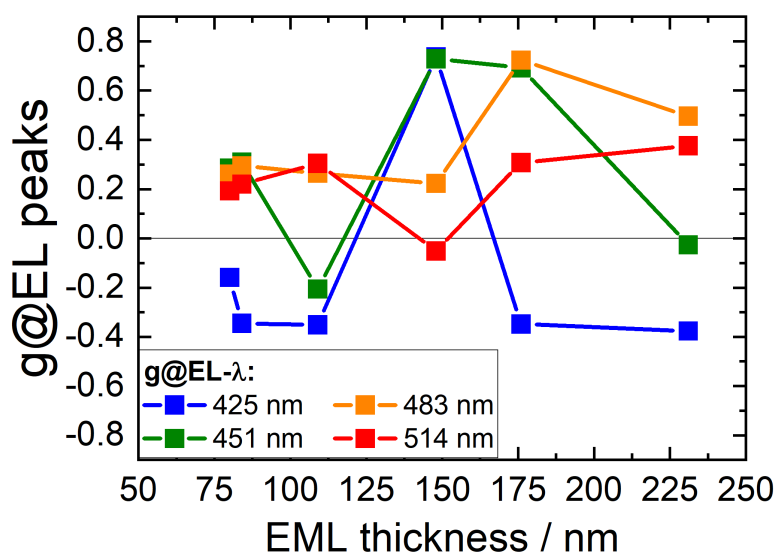


Fig. 3.55: g_{EL} values of P(F8/c3) based CP-OLEDs with different EML thicknesses.

Device architecture: ITO / PEDOT / XQUPD / XOTPD / P(F8/c3) / CsF/Al (cured 15 min@180 °C) M_w (P(F8/c3) = 130 kg/mol.

Fig. 3.56 compares g_{EL} values at 425 nm for CP-OLEDs with different EML thicknesses of P(F4/c2-F8) (black) and P(F8/c3) (purple). The data is equivalent to the blue data sets shown in fig. 3.44 (d) and 3.55.

While a larger layer thickness range is covered for P(F8/c3), the likewise larger increments between individual measurements make the overall trend less obvious. Based on data for EML thicknesses between 75 nm and 125 nm, which is available for both polymers, one can, however, estimate that the curves of P(F4/c2-F8) and P(F8/c3) are generally mirror images along the line of $g_{EL} = 0$. This effect, called odd-even-effect, was explained in chapter 3.7.5.

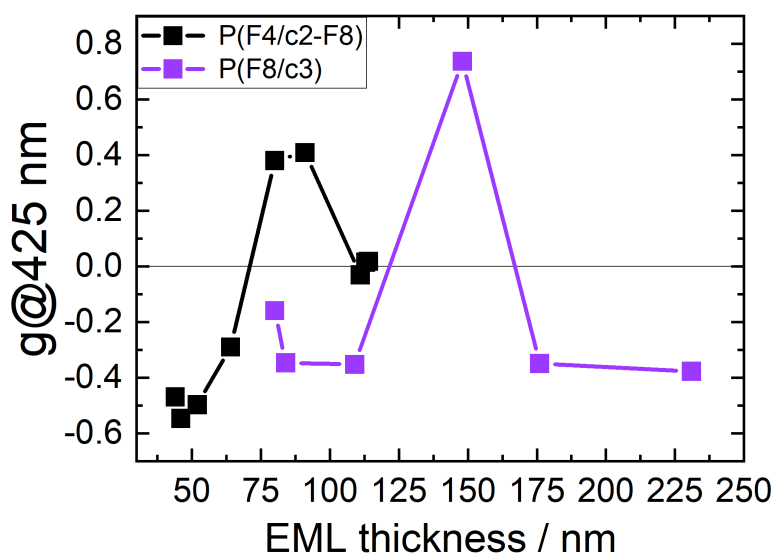


Fig. 3.56: Comparison of g_{EL} values at 425 nm for P(F4/c2-F8) (black) and P(F8/c3) (purple) based CP-OLEDs with different EML thicknesses. Device architecture: ITO / PEDOT / XQUPD / XOTPD / emissive polymer / CsF/Al. Cured 20 min@240 °C or 15 min@180 °C, respectively.

To estimate the difference between homo- and co-polymers, similar CP-OLEDs based on P(F8/c3) and P(F8/c3-F8) can be compared. For the first EL peak at 425 nm, a g_{EL} value of -0.18 is found for P(F8/c3-F8) (EML = 120 nm, cured 15 min@225 °C). A similar device based on P(F8/c3) achieves a g_{EL} value of -0.33 (EML = 110 nm, cured 15 min@180 °C). Considering the EML thickness difference between the compared devices, it can be said that both polymers achieve similar CP-effects.

In order to quantify the effect of achiral units within a chirally functionalised co-polymer, those polymers would have to be synthesised with a molecular weight as close as possible to each other. Naturally, only devices with the same EML thickness should be directly compared. But to fully estimate the potential of each polymer, it would be ideal to analyse devices with a wide range of EML thicknesses

3 Results and Discussion

to find the maximum possible g_{EL} value. Comparison of different polymers at this thickness would give the most robust data possible.

Additionally, it would be interesting to compare polymers containing different ratios of chiral to achiral monomer units. While it is to be expected that the fully chiral homo-polymer would achieve the highest CP-effect, small amounts of achiral F8 units might not disturb the chiral phase, yet still increase polymer solubility. This way, the use of shorter chirally functionalised side chains, like in the F4/c2 unit, could be realised despite their poor processability.

3.7.7 Chirally functionalised F8BT

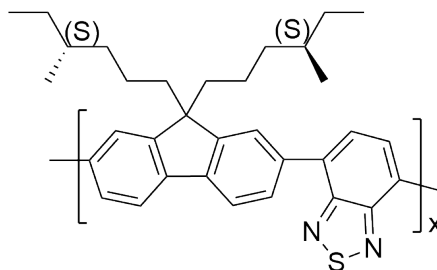


Fig. 3.57: Structure of P(*S*-F6/c4-BT).

The previously introduced PFs, with the exception of the oxidised fluorenone compound, all produce a blue emission colour. To achieve other emission colours, PF can be co-polymerised with a different monomer. A typical example is F8BT, which was introduced in chapter [3.2.2](#). In chapter [3.8](#), achiral F8BT is used in combination with a chiral inducer to produce mixed system CP-OLEDs. It is, however, also possible to use chirally functionalised PF units instead of the typically used achiral F8 units.

Fig. [3.57](#) shows the structure of one such example. Just like its achiral version F8BT, the chiral co-polymer P(*S*-F6/c4-BT) shows green emission.

In fig. [3.58](#), absorption (top) and CD (bottom) data of a P(F6/c4-BT) thin film

is shown. The sample was cured successively for 15 min at different temperatures. Similar to the oxidised homo-polymer P(F6/c4-FN) of the monomer F6/c4, which was introduced in chapter 3.7.4, P(F6/c4-BT) can form a chiral phase, indicated by the CD curve.

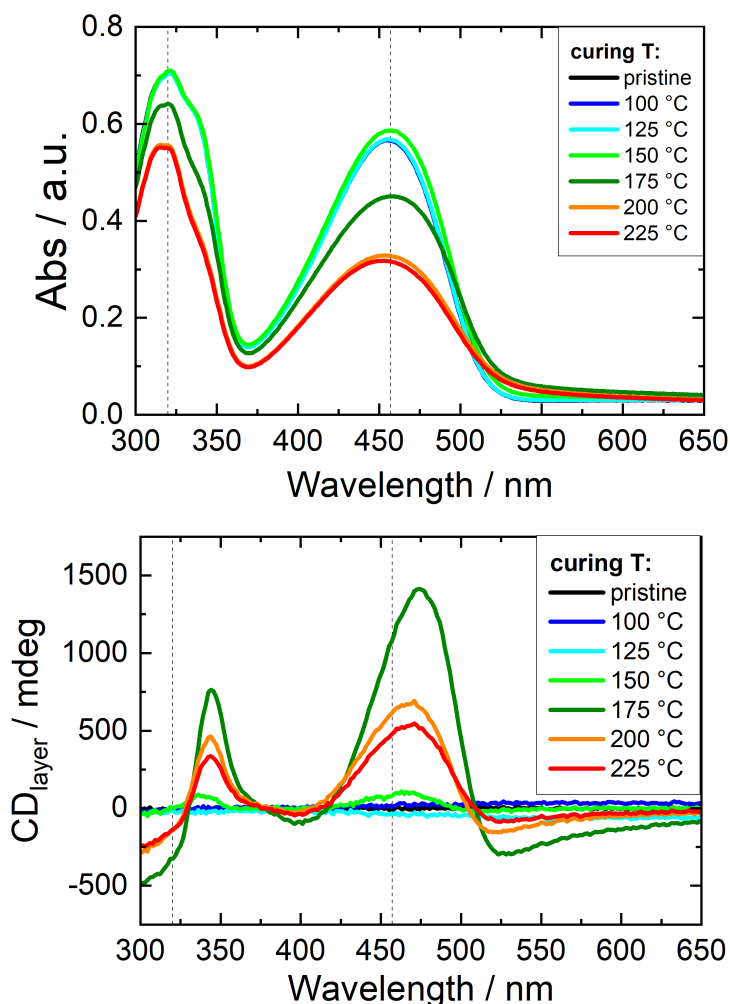


Fig. 3.58: Absorption intensities (top) and corresponding CD curves (bottom) of a 100 nm P(F6/c4-BT) thin film. The sample was cured successively for 15 min at different temperatures.

With a molecular weight of 12 kg/mol, this polymer is best compared with F8BT-13 in chapter 3.3. Analogous to the behaviour of F8BT, absorption decreases with increasing curing temperature.

3 Results and Discussion

In contrast to PF, F8BT exhibits two absorption peaks, here at 320 nm and 457 nm, which are marked with a dashed line. As a result, the shape of the CD curves contains multiple signal peaks. With increasing curing temperature, CD increases up to 175 °C. Afterwards, it decreases again.

This trend is better visible in fig. 3.59, which shows CD* values from the largest signal peak at 470 nm. The maximum value of 15 mdeg/nm is in the same range as P(F6/c4-FN) (see fig. 3.48). An ideal curing temperature around 175 °C can be interpreted, above which the CD intensity decreases again.

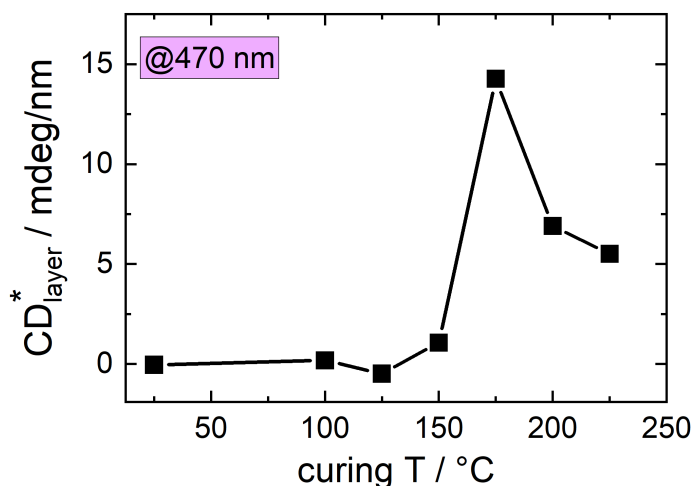


Fig. 3.59: CD* values at 470 nm for P(F6/c4-BT) thin films cured successively for 15 min at different temperatures.

One more aspect has to be considered during evaluation of the results in this chapter. In chapter 3.7.4, the effect of oxidation on the polymer P(F6/c4-FN) was shown. Some monomer units were oxidised to fluorenone, which had a negative impact on CD and g_{EL} values. It is not clear at what point this oxidation occurred, whether it was during the synthesis of the monomer or its polymerisation.

P(F6/c4-BT) was polymerised from the same batch of F6/c4 monomer as P(F6/c4-

FN). Therefore, if the monomer was already oxidised, or contained the impurities which lead to oxidation, P(F6/c4-BT) could also contain keto defects.

In P(F6/c4-FN), fluorenone could easily be detected by its specific PL and EL emission around 540 nm. Unfortunately, this signal is directly superimposed with the typical emission of F8BT. It is, therefore, difficult to evaluate whether P(F6/c4-BT) also contains oxidised impurities, and if so, how much and whether further oxidation occurs during device preparation, measurement and storage.

To evaluate the potency of a chirally functionally polymer compared to its achiral version mixed with a chiral inducer, it would be necessary to repeat the synthesis of the chirally functionalised monomer and, afterwards, its polymerisation. With this approach, different functionalisations could also be compared to different chiral inducers. This would provide valuable information and potential for optimisation.

In fig. 3.60, P(F6/c4-BT) (red) is compared to two other polymers, which are similar in certain aspects. P(F6/c4-FN) (blue) is the oxidised homo-polymer of the F6/c4 monomer, on which both polymers are based. Both polymers are examples of one component systems, and potentially suffer from keto defects. In contrast, the third example, F8BT + R5011 (green), represents a mixed system. For best comparability, F8BT-13 was chosen here.

Despite their commonalities, these polymers and the shown thin film samples have many differences, which are listed in tab. 3.5, and have to be considered.

As expected, the absorption spectrum (top) of P(F6/c4-FN) is blue-shifted compared to both F8BT derivatives. There is, however, also a slight difference between the absorption spectra of P(F6/c4-BT) and F8BT + R5011. Both polymers have similar M_w s, but the required curing temperature for P(F6/c4-BT) is significantly higher than for F8BT. As shown in chapter 3.4.4, curing leads to spectral shifts in absorption and PL. Therefore, the different curing temperatures could be responsible for the difference.

3 Results and Discussion

Since they are correlated to the shape of the absorption spectra, the normalised CD spectra (middle) exhibit a similar variance in shape. More interesting, however, are the differences in CD* intensity (bottom). Here, CD* values are compared not at the same wavelength, but at each sample's largest CD signal. In addition, the layer thicknesses of the shown samples vary. It was previously demonstrated that CD* is not constant for the systems shown in this work. Rather, it increases with increasing layer thickness, because the size of the chiral domain is expected to be larger than the layer thickness. Naturally, these conditions only allow for a qualitative comparison at this point.

P(F6/c4-BT) and P(F6/c4-FN) achieve almost identical maximum CD* values of 14 mdeg/nm and 13 mdeg/nm, respectively. However, with its much lower \overline{M}_w , P(F6/c4-BT) would be expected to reach much larger CD* values. In comparison, F8BT-13 + R5011 with a similar \overline{M}_w achieves a maximum CD* value of 232 mdeg/nm. A difference of this magnitude can not be explained by the difference in layer thickness alone. It can, therefore, be said that P(F6/c4-BT) exhibits a significantly lower CD effect than would be expected.

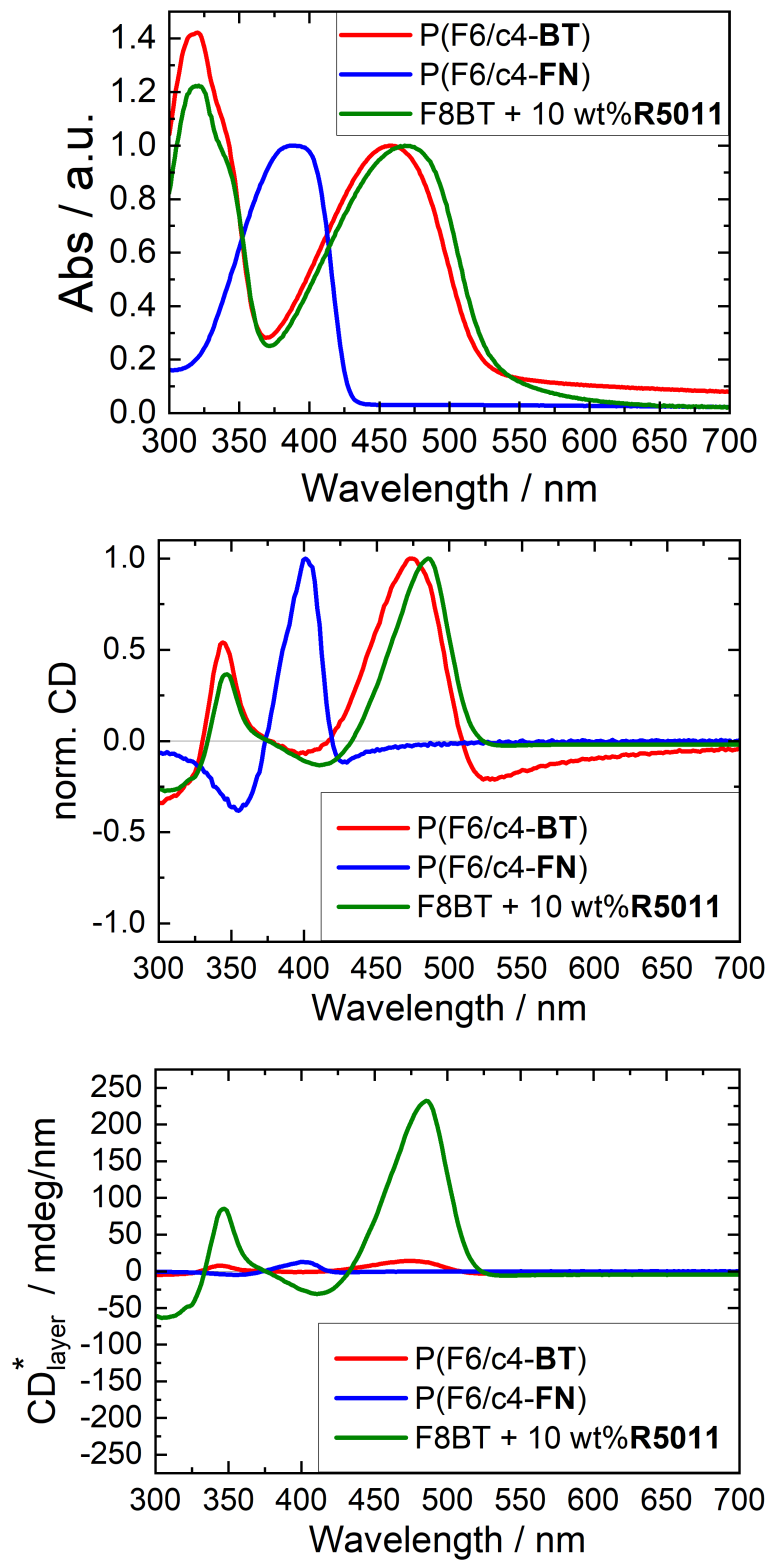


Fig. 3.60: Normalised absorption intensities (top) and corresponding normalised CD (middle) and CD* (bottom) curves of P(F6/c4-BT) (red), P(F6/c4-FN) (blue) and F8BT + 10 wt%R5011 (green) thin films. 171
 Respective thin film specifications: Layer thickness = 100 / 90 / 145 nm.
 Cured for 15 min at 175 / 225 / 120 °C. M_w = 12 / 82 / 13 kg/mol.

3 Results and Discussion

Tab. 3.5: Key data of P(F6/c4-BT), P(F6/c4-FN) and F8BT + 10 wt%R5011 thin films and CP-OLEDs. See also fig. 3.60.

	P(F6/c4-BT)	P(F6/c4-FN)	F8BT + 10 wt%R5011
M_w / kg/mol	12	82	13
layer thickness / nm	100	90	145
curing T / °C	175	225	120
Abs peak λ / nm	457	388	468
max. CD signal λ / nm	470	406	485
max. CD* / mdeg/nm	14	13	232
max. found $g_{\text{@maxEL}}$	-0.13	0	-1.08

Fig. 3.61 shows LIV performance data (a), normalised EL spectra (b), g_{EL} (c) and g_w (d) curves of P(F6/c4-BT) based OLEDs with different EML thicknesses.

Device performance and EM spectra are similar to F8BT based mixed system CP-OLEDs (see chapter 3.8). The achieved g_{EL} values are, however, much lower. Due to the large spectral shift between RCP and LCP spectra, the shape of these g_{EL} curves is significantly different than the EL spectrum. Here, trends are much clearer and easier to see in g_w curves. However, $g_{\text{@maxEL}}$ values are also shown below in fig. 3.62.

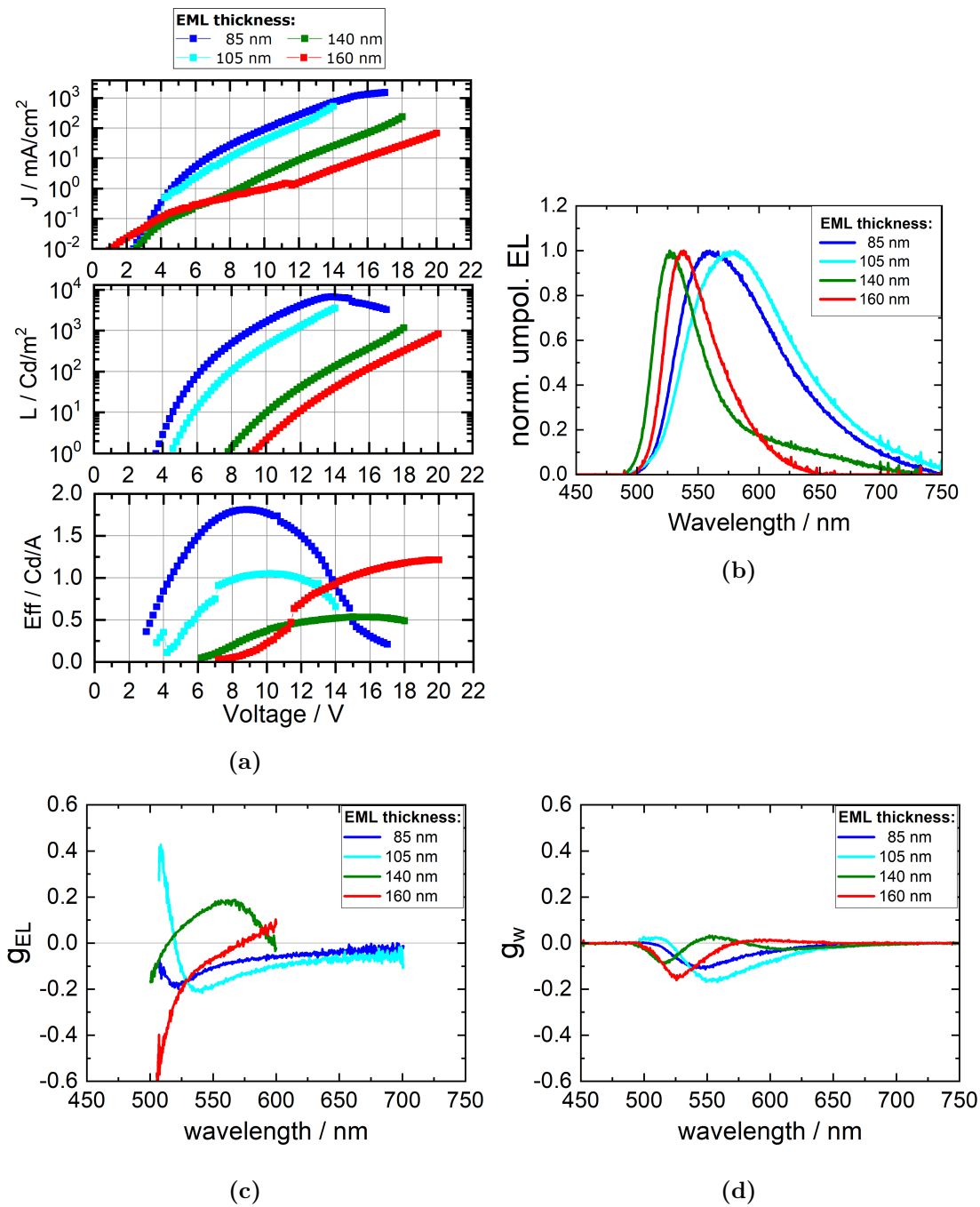


Fig. 3.61: LIV performance data (a), normalised EL spectra (b), g_{EL} (c) and g_w (d) curves of P(F6/c4-BT) based OLEDs with different EML thicknesses. Device architecture: ITO / PEDOT / XQUPD / XOTPD / P(F6/c4-BT) / CsF/Al (cured 15 min@180 °C) M_w (P(F6/c4-BT)) = 12 kg/mol.

3 Results and Discussion

Fig. 3.62 shows $g@maxEL$ values of the P(F6/c4-BT) based CP-OLEDs introduced in fig. 3.61. With varying EML thickness, $g@maxEL$ exhibits a sign flip. This behaviour is also found for F8BT mixed systems containing a chiral inducer and will be analysed in detail in chapter 3.10. However, with a maximum $g@maxEL$ of -0.13 , the CP-effect of P(F6/c4-BT) is lower than found in a comparable mixed system with an F8BT polymer of similar molecular weight. For example, a P(F6/c4-BT) and a F8BT-13 + 10 wt%R5011 based CP-OLED with EML thicknesses of 158 nm and 161 nm achieved $g@maxEL$ values of -0.11 and -0.25 , respectively.

As shown in chapter 3.10, the largest $g@maxEL$ values for F8BT + R5011 based CP-OLEDs are achieved with an EML thickness around 200 nm. It is possible that P(F6/c4-BT) based CP-OLEDs with EML thicknesses in this range would exhibit larger g_{EL} values as well. However, this aspect was not analysed in this work.

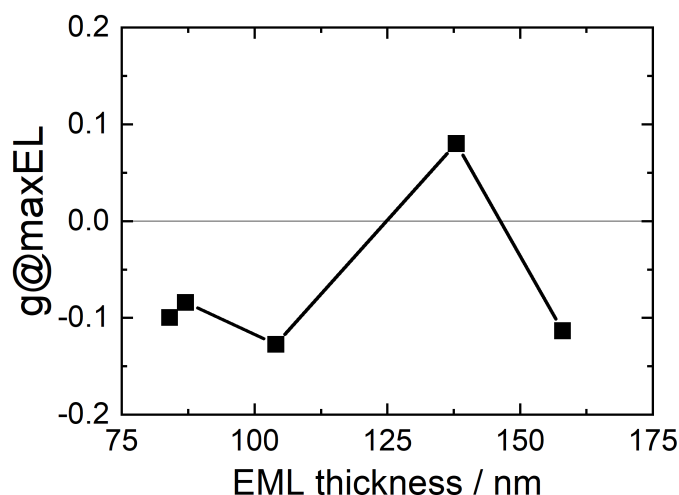


Fig. 3.62: $g@maxEL$ values of P(F6/c4-BT) based CP-OLEDs with different EML thicknesses.

Device architecture: ITO / PEDOT / XQUPD / XOTPD / P(F6/c4-BT) / CsF/Al (cured 15 min@180 °C) $M_w(P(F6/c4-BT)) = 12$ kg/mol.

3.8 Mixed systems

To initiate the formation of a chiral phase, the chiral element does not necessarily have to be connected to the polymer. As introduced in chapter [2.6.2](#), a non-emissive chiral molecule can be combined with an emissive achiral polymer. Curing the system at an appropriate temperature can lead to the formation of a chiral liquid crystalline phase. The chiral molecule thereby acts as chiral inducer. This is a typical example of an E-CP-effect. Enantiomerically pure synthesis or separation of a chiral small molecule is usually easier than of a chirally functionalised polymer, which could make this mixed approach less complex and, therefore, less expensive.

In the following chapters, different aspects of a mixed system consisting of F8BT with a chiral inducer are highlighted. While the enantiomer R5011 is used for most experiments, the statements apply for S5011 just the same. In comparison, the two helicene based molecules [H1-Me₂](#) and [ThiahelalkBZT](#), which were analysed as I-CPL emitters in chapter [3.6](#), are also used here as non-emissive chiral inducers in an F8BT matrix.

The properties of F8BT as polymer matrix and emitter material (chapter [3.2](#)), its curing behaviour (chapter [3.4](#)) as well as the influence of the polymer molecular weight (chapter [3.3](#)), were previously discussed and likewise apply for mixtures with a chiral inducer. In the following, it shall be analysed how these parameters affect CP-OLED performance specifically, especially in terms of g_{EL} curves.

3.8.1 Chiral inducers for E-CPL mixed systems

The **BINOL** based enantiomers R5011 and S5011 shown in fig. 3.63 are relatively inexpensive commercially available materials typically utilised in LCD technologies. Used as chiral inducers in CP-OLEDs, the largest g_{EL} values reported for a reasonably well performing CP-OLED so far are achieved [4].

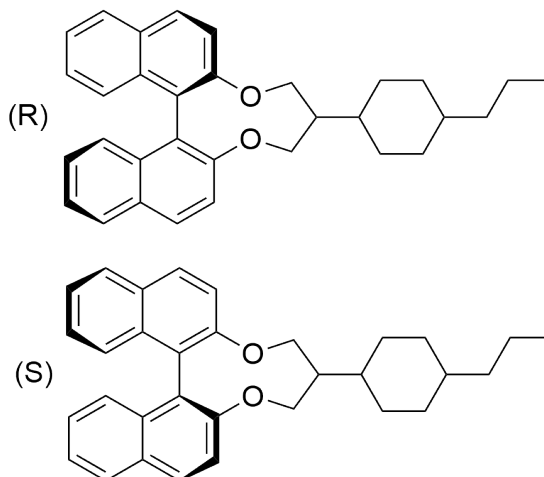


Fig. 3.63: Structure of the chiral inducers R5011 and S5011.

Fig. 3.64 shows how, for a comparable device architecture with equal chiral inducer concentrations and similar layer thicknesses, R5011 and S5011 produce mirror image CD curves (a) and g_{EL} curves (b). The chiral phase generated through annealing remains thermodynamically stable even after cooling.

In (b), two chiral inducer concentrations, 5 and 10 wt%, are compared. With 10 wt%, a larger CP-effect is achieved. The chiral inducer concentration dependence of F8BT + R5011 based CP-OLEDs is analysed in chapter 3.12.

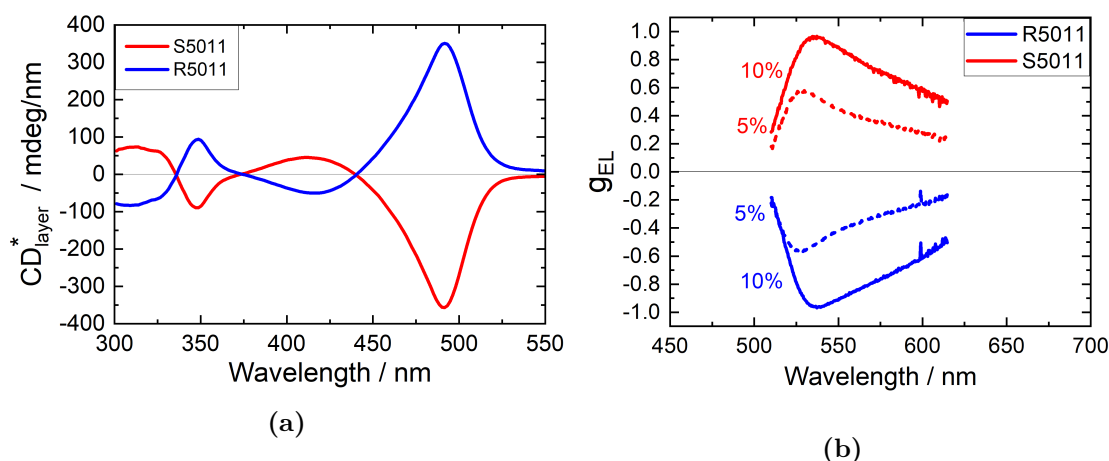


Fig. 3.64: CP-OLEDs containing equal concentrations of the two chiral inducers R5011 (blue) or S5011 (red) produce mirror image CD* curves (a) and g curves (b). For each pair, device architecture and layer thickness is comparable.

Analogously, the two helicene based molecules [H1-Me₂](#) and [ThiahelalkBZT](#), which were used as I-CPL emitters in chapter [3.6](#), are used as non-emissive chiral inducers.

While [H1-Me₂](#) does not perform well as emitter material, it can still be used in CP-OLEDs.

[H1-Me₂](#) was mixed with F8BT. Fig. [3.65](#) shows g_{EL} curves of CP-OLEDs with F8BT as emitter and [H1-Me₂](#) as chiral inducer. As would be expected, the two enantiomers M - and P -[H1-Me₂](#) produce mirror image g_{EL} curves with opposite signs. g_{max} values of +0.54 and -0.49, or respectively, $g@maxEL$ values of +0.43 and -0.39 can be derived. The different values for the two enantiomers can be explained by EML thickness variations. The shown g_{EL} curves originate from CP-OLEDs with an EML thickness of 180 nm (M -[H1-Me₂](#), red) and 200 nm (P -[H1-Me₂](#), blue), respectively.

3 Results and Discussion

These values are in the range of other published systems based on helicene chiral inducers. Wan *et al.*, for example, used a similar system consisting of F8BT mixed with 10 wt% aza[6]helicene. They published a maximum g_{EL} of 0.57 [70, 96].

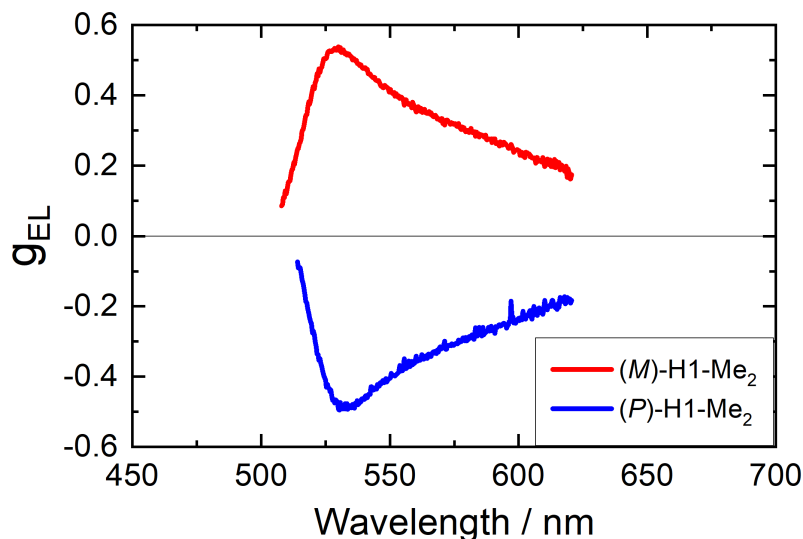


Fig. 3.65: CP-OLEDs with $H1-Me_2$ as chiral inducer and F8BT as emitter. The two enantiomers produce g_{EL} curves with opposite handedness. Device architecture: ITO / PEDOT / XQUPD / XOTPD / F8BT + 10 wt% $H1-Me_2$ / CsF/Al. Cured 15 min@180 °C. EML thickness = 180 - 200 nm. M_w (F8BT) = 37 kg/mol.

Just like $H1-Me_2$, $ThiahelalkBZT$ can be used as chiral inducer in an F8BT based CP-OLED. Fig. 3.66 shows the g_{EL} curve of a CP-OLED with F8BT as emitter and M - $ThiahelalkBZT$ as chiral inducer. A g_{max} value of +0.43, or respectively, a $g@maxEL$ value of +0.42 is found.

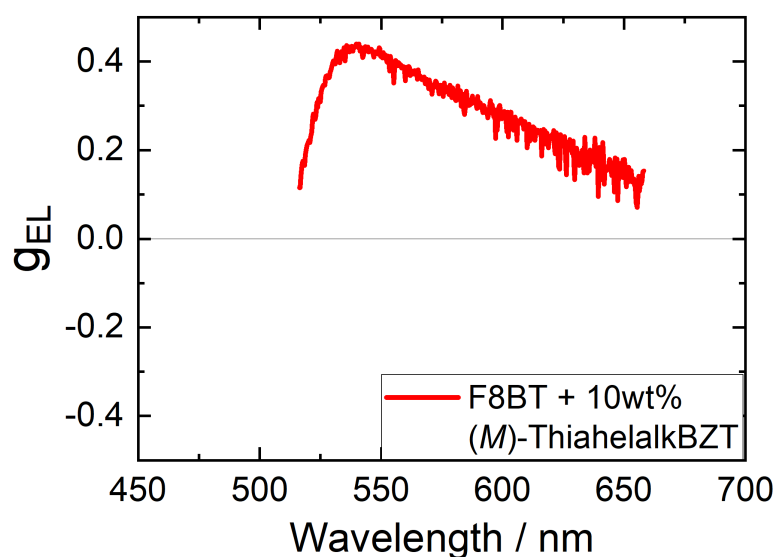


Fig. 3.66: CP-OLED with **ThiahelalkBZT** as chiral inducer and F8BT as emitter. Device architecture: ITO / PEDOT / XQUPD / XOTPD / F8BT + 10 wt% **M-ThiahelalkBZT** / CsF/Al. Cured 15 min@180 °C. EML thickness = 215 nm. M_w (F8BT) = 37 kg/mol.

In fig. 3.67, g_{EL} curves of CP-OLEDs with these three chiral inducers are shown. For comparability, all three devices are based on the same device architecture. The same F8BT batch (F8BT-37), chiral inducer concentration and curing condition is used. However, the EML thickness of the shown examples varies between 180 nm and 215 nm. The influence of EML thickness variations in F8BT based CP-OLEDs on g_{EL} is analysed and explained in chapter 3.10.

It can be seen that the two helicene based molecules perform relatively similar. **H1-Me₂** and **ThiahelalkBZT** achieve $g@maxEL$ values of 0.42 and 0.41, respectively. S5011, however, achieves a much larger $g@maxEL$ value of 0.93, making it a more promising choice.

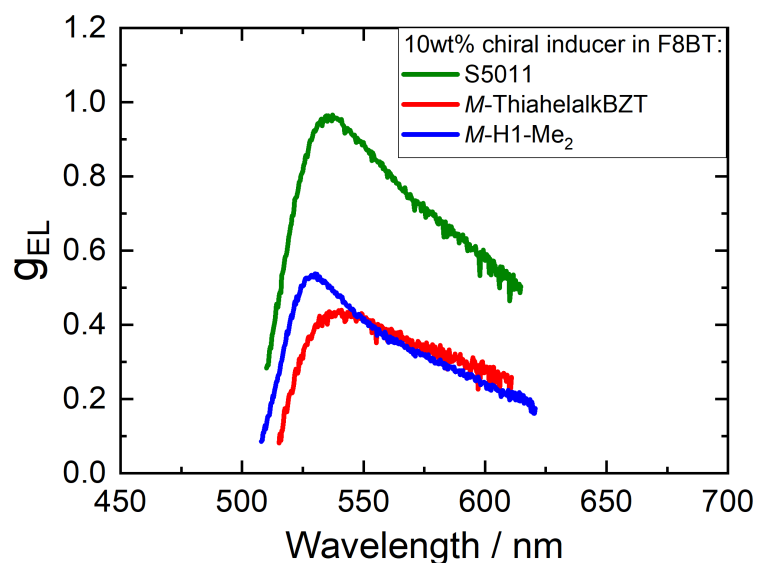


Fig. 3.67: CP-OLEDs with F8BT + 10 wt% chiral inducer. Used were S5011 (green), *M*-ThiahelalkBZT (red) and *M*-H1-Me₂ (blue). Device architecture: ITO / PEDOT / XQUPD / XOTPD / F8BT + 10 wt% chiral inducer / CsF/Al. Cured 15 min@180 °C. EML thickness = 206 / 215 / 180 nm. M_w (F8BT) = 37 kg/mol.

The chiral inducer concentration in mixed system CP-OLEDs is typically given in wt%. To compare different chiral inducers, however, mol% values would be more useful.

For batch F8BT-37, which was used in this example, a chiral inducer concentration of 10 wt% is equivalent to 9.3 mol% for H1-Me₂, 3.1 mol% for ThiahelalkBZT and 8.1 mol% for S5011.

Since in this work, F8BT batches with different molecular weights are used, a ratio of mol chiral inducer per gram F8BT is the over all most comparable value. For the examples in fig. 3.67, this results in concentrations of 2.53×10^{-4} mol for H1-Me₂, 0.85×10^{-4} mol for ThiahelalkBZT and 2.21×10^{-4} mol for S5011 per gram F8BT.

While good CP-effects can also be achieved with [H1-Me₂](#) and [ThiahelalkBZT](#), the large synthetic effort in creating and purifying these helicene based molecules makes them too precious to be used as mere chiral inducers. Therefore, the results in the following section are only based on the chiral inducer R5011.

3.8.2 F8BT + R5011 operating voltage

Different CP-OLED materials and device architectures naturally have to be measured at different operating voltages. To achieve a good signal to noise ratio and minimise device degradation, CP-EL measurement were performed at a typical brightness around 100 Cd/m². Fig. 3.68 (a) shows different g_{EL} curves of one F8BT + R5011 based CP-OLED, measured at different operating voltages. Apart from small fluctuations, the g_{max} values displayed in (b) are constant.

While the operating voltage might still have an influence on the position of the recombination zone and, therefore, possibly also on g , this does not seem to be the case for the F8BT based systems predominantly used in this work. It is, therefore, possible to compare different devices measured at different operating voltages.

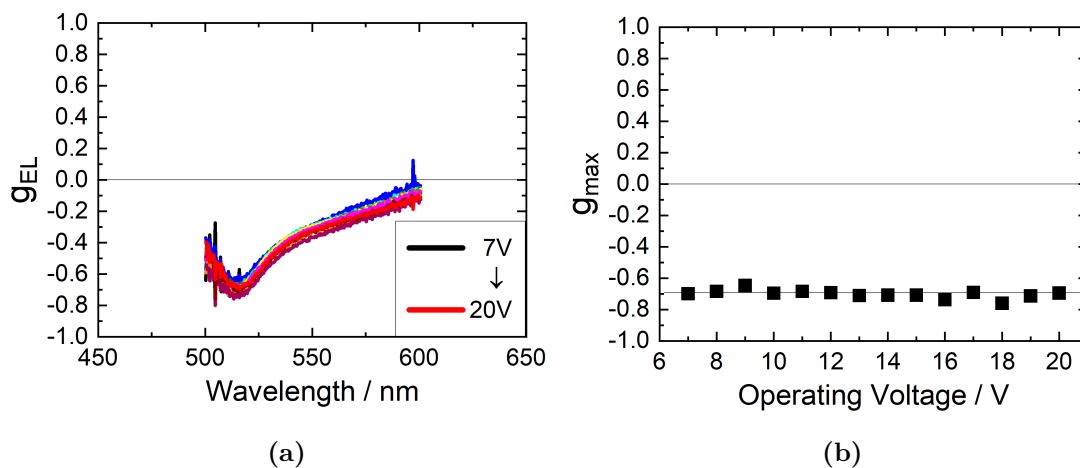


Fig. 3.68: g_{EL} curves (a) and g_{max} values (b) of an F8BT + R5011 based CP-OLED, measured at different operating voltages.

3.9 Thermal annealing of F8BT + R5011 thin films

In chapter [3.4](#), different aspects of how curing influences F8BT thin films and OLEDs were introduced, including layer thickness volume reduction, surface roughness, aggregation and the influence of different curing conditions. While these aspects generally also apply for F8BT + R5011 mixed systems, the thermal phase behaviour is slightly changed. Small molecules like the chiral inducer R5011 used here act as plasticisers, which typically shifts the thermal phase behaviour towards lower temperatures, for example reducing T_g and T_m . A detailed analysis of the influence of different chiral inducer concentrations on the phase behaviour and resulting CP-effects is given in chapter [3.12](#).

Also, in mixed systems, especially at high curing temperature and long curing times, phase separation can occur. This could impact the chiral phase, surface roughness and layer thickness volume reduction, an aspect that is highlighted in chapter [3.9.1](#).

Most examples in the following chapters are based on the system F8BT + 10 wt%R5011. It is, however, likely that the shown trends, for example concerning the curing behaviour, also apply to other chiral inducer concentrations, and possibly even other chiral inducers. Naturally, for a different system, the specific values, like ideal curing temperature or layer thickness volume reduction, may change. On the influence of different R5011 concentrations, further information is given in chapter [3.12](#).

3.9.1 F8BT + R5011 thin film volume reduction

In chapter [3.4.1](#) the aspect of F8BT thin film volume reduction was introduced. It was shown that curing above T_m of a pure F8BT-37 thin film resulted in a volume reduction up to 17 % at 300 °C.

Fig. [3.69](#) shows the gradual shrinking of a polymer layer through curing for a mixed system F8BT-37 + R5011 thin film. In contrast to pure F8BT-37 samples, volume reduction sets in at much lower temperatures. While pure F8BT-37 thin film thickness remains constant up to 200 °C, volume reduction of F8BT-37 + 10 wt%R5011 thin films already sets in around 170 °C.

As shown in (a), higher curing temperatures promote more significant shrinking effects. In this example, the final layer thickness after curing decreased by up to 13 % at only 250 °C. While for pure F8BT thin films, volume reduction could only be observed at curing temperatures above T_m , a gradual layer thickness reduction already sets in at 180 °C in this example.

In (b), the influence of different curing times on volume reduction is shown for two curing temperatures, 180 °C and 200 °C. The layer thickness decreases with increasing curing times, rapidly in the beginning and more slowly at the end. In this example, the final layer thickness after 60 min decreased by up to 12 % for both temperatures.

3 Results and Discussion

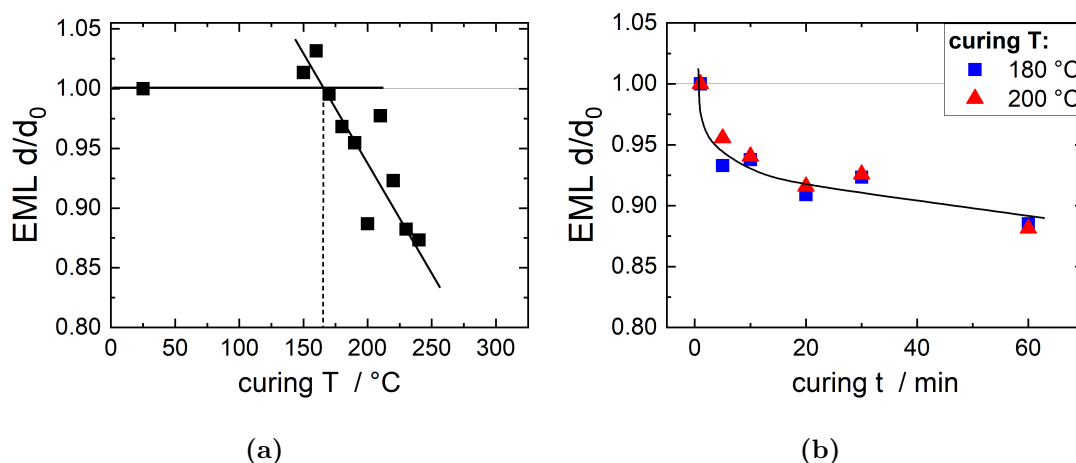


Fig. 3.69: Ratio of pristine to cured layer thickness d/d_0 of an F8BT-37 + 10 wt%R5011 thin film. The sample was cured successively for 15 min at different temperatures (a) or cured at 180 °C (blue squares) or 200 °C (red triangles) for different curing times (b).

This example shows that layer thickness shrinking becomes an increasingly important factor for F8BT + R5011 mixed systems, especially at higher curing temperatures and longer curing times and for thicker EMLs.

An explanation for this volume reduction effect is given in chapter [3.4.1](#) for pure F8BT thin films. Here, R5011 acts as plasticiser, which shift the thermal phase behaviour toward lower temperatures. This could explain why the volume reduction sets in at lower temperatures. In addition, R5011 acts as a chiral inducer. In contrast to pure F8BT, it promotes a preferential phase arrangement. This chiral phase differs from the achiral, amorphous phase of pure F8BT. Layer thickness shrinking could be a result of the phase rearrangement. Lastly, it might also be possible that R5011 evaporates during curing. In this case, the volume reduction could be explained by the loss of material.

In mixed systems, one more aspect has to be considered. In thin films consisting of a polymer and a small molecule, phase separation can be an issue, especially at higher temperatures. This can already apply for pure F8BT thin films, as was demonstrated in chapter [3.4.2](#). There, a significant surface roughness after cur-

ing was detected, most likely indicating crystallisation nuclei of different phases or phase separation of lower molecular weight components in the polymer. With small molecules like R5011, phase separation is even more likely. There was, however, no difference detectable between the surface roughness of pure F8BT and mixed F8BT + R5011 thin films. More importantly, the observed surface roughness did not seem to impact device performance or CP-effect negatively.

3.9.2 F8BT + R5011 curing temperature

As explained in chapters [3.3](#) and [3.4.4](#), the molecular weight of different F8BT batches determines their respective curing behaviour. It was also shown how curing of F8BT thin films leads to thin film volume reduction, increased surface roughness and changes in absorption, PL and PLQY behaviour. Naturally, the same applies for F8BT and chiral inducer mixtures. In this chapter, a focus shall be put on CD and CPL behaviour, instead. The molecular weight dependence of CD and g_{EL} values, specifically, is analysed in chapter [3.11](#).

Different F8BT batches were used for different experiments, so it should be noted that ideal curing conditions may vary. F8BT molecular weight also impacts CPL behaviour. This topic will be addressed in detail in chapter [3.11](#).

While curing is not necessary for pure F8BT OLEDs, it is a crucial step for their respective CP-OLEDs. Through addition of a chiral inducer, a preferential twisting direction of the polymer backbone can be induced while the polymer is in a liquid crystalline phase. A device without added chiral inducer or omitted curing will not produce CPL. For best results, ideal curing conditions need to be used for each system.

Absorption spectra of different molecular weight batches of F8BT with 10 % R5011, including changes resulting from curing, were presented in [fig. 3.27](#). In comparison, a typical CD spectrum of the chiral F8BT P(F6/c4-BT) is given in [fig. 3.58](#). [Fig. 3.70](#) shows CD curves (a), CD^* (b) and $g@maxEL$ (c) data for F8BT

3 Results and Discussion

+ 10 wt% based CP-OLEDs cured for 15 min at different temperatures. The black data set is based on F8BT-21, and the red data set is based on F8BT-37.

As demonstrated in chapter [3.2.4](#), the best device performance for F8BT based OLEDs is found for an EML thickness around 200 nm. For this reason, the devices shown here feature EML thicknesses of 165 - 190 nm for F8BT-21, and 175 - 230 nm for F8BT-37. As explained in chapter [3.4.1](#) for F8BT and chapter [3.9.1](#) for F8BT + R5011, the difference in EML thickness is caused by gradual volume reduction through curing.

The possibility of unphysical CD values when the absorption limit is reached was explained in chapter [3.1.4](#). Due to the large layer thickness and strong CD effect, this is the case here for the largest CD signal at 488 nm, as shown in (a). Therefore, (b) shows CD* values of the CD signal at 349 nm.

Contrary to what might be assumed, higher temperatures do not lead to better results, but rather an ideal curing temperature is found. Curing at higher temperatures, for the here used F8BT-37 batch (red) above 175 °C, leads to a decrease in CD and g_{EL} values. In comparison, g_{EL} values are also shown for a comparable device set with F8BT-21 (black). For this batch, the ideal curing temperature lies around 190 °C. In both cases, the ideal curing temperature indicated by CD and g_{EL} values matches the position of the second exothermic signal found in DSC measurements of F8BT (see fig. [3.22](#) in chapter [3.3](#)).

3.9 Thermal annealing of F8BT + R5011 thin films

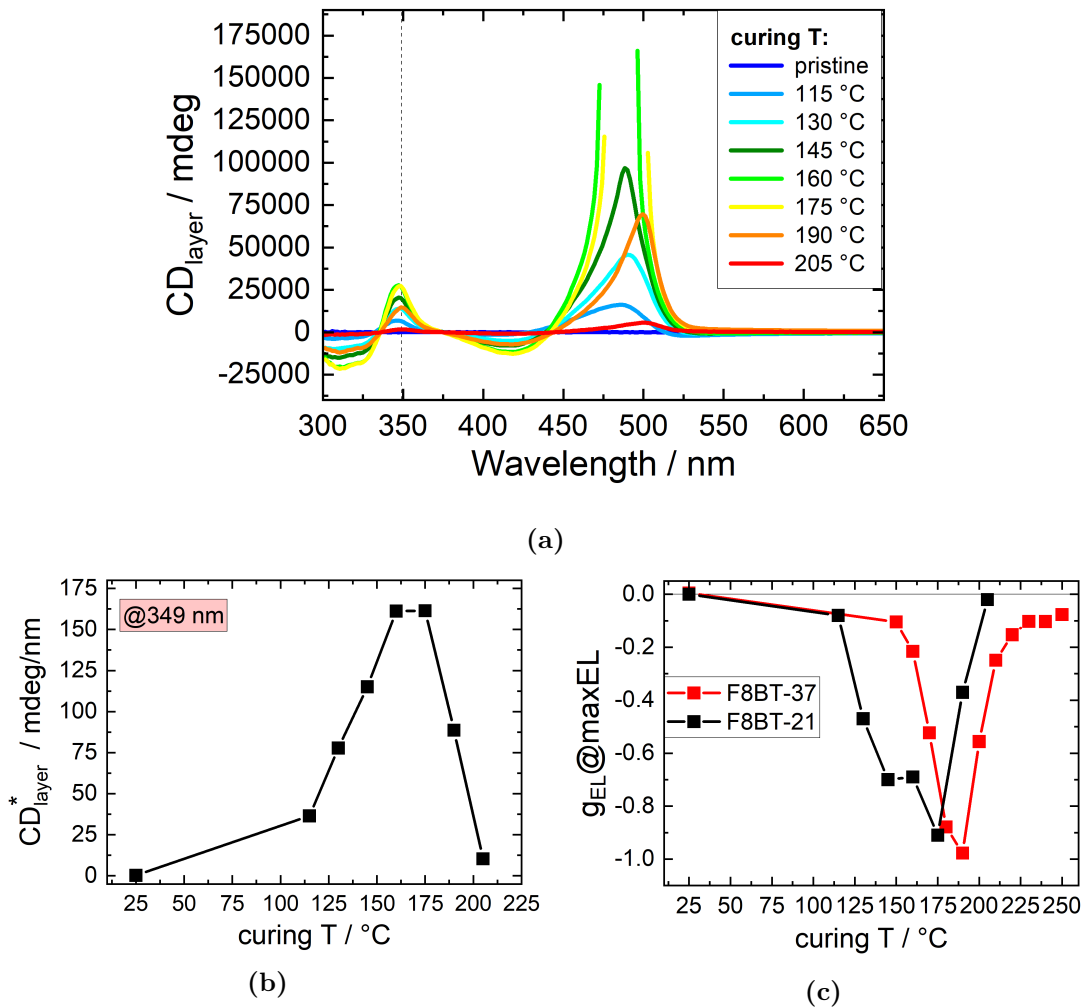


Fig. 3.70: CD curves (a), CD^* values at 349 nm (indicated by dashed line in (a)) (b) and $g_{\text{EL}} @ \text{maxEL}$ values (c) for CP-OLEDs cured at different temperatures. The black CD and g_{EL} data points are measured from the same devices based on F8BT-21. The red data points originate from a comparable device based on F8BT-37.

Device architecture: ITO / PEDOT / XQUPD / XOTPD / F8BT + 10 wt%R5011 / CsF/Al (cured 15 min@115 - 250 °C). EML thickness 165 - 190 nm for F8BT-21 and 175 - 230 nm for F8BT-37.

3 Results and Discussion

Like the ideal curing temperature, an ideal curing time needs to be found. The polymer needs enough time to fully rearrange into the desired chiral phase structure. If the curing time is too short, the intended phase might not be able to fully form. With longer polymer chains, the required minimum curing time is expected to increase.

Longer than necessary curing times, however, can also be detrimental, as shown in fig. 3.71. For the here shown example, curing times above 10 min result in a decreased $g_{\text{EL@maxEL}}$, even at the ideal curing temperature (blue). For very short curing times, even a slightly higher than ideal curing temperature (red) is acceptable. But very short curing times have the risk of not fully forming the required chiral LC phase. Also, g_{EL} value decrease due to longer curing times occurs faster for higher curing temperatures, shrinking the window for fabrication errors. For a reliable and reproducible device preparation procedure, it is not advisable to deviate too far from ideal curing conditions.

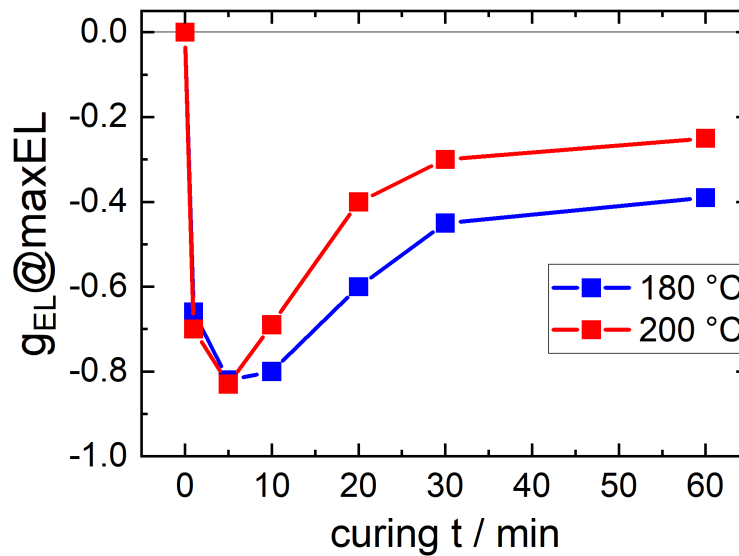


Fig. 3.71: $g_{\text{EL@maxEL}}$ values of F8BT-37 + 10 wt%R5011 based CP-OLEDs cured at 180 °C (blue) or 200 °C (red) for different curing times.

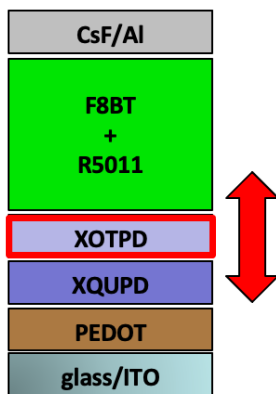
3.9 Thermal annealing of F8BT + R5011 thin films

One aspect that has not been extensively studied here, but should still be mentioned, are heating and cooling rates. All samples in this work were placed on a preheated heating plate, making the heating process almost instant. For cooling, the differences between quenched samples (placed on a cold metal surface) and non-quenched samples (placed directly into the Teflon substrate holder) were within the range of normal sample to sample or batch to batch variations. On this result alone, however, the possibility can not be excluded that larger CP-effects might be achievable with more sophisticated heating and cooling procedures. Especially the difference between immediately quenched and very slowly, gradually cooled samples might be an interesting field to study.

3.10 F8BT + R5011 layer thickness variation

In chapter [3.2.4](#), the OLED stack architecture was varied and optimised for performance improvement, and a standard stack was chosen. One of the analysed aspects featured a thickness variation of the layers in the stack. In this chapter, the impact of such layer thickness variation on CPL performance is highlighted.

3.10.1 HTL thickness variation



In fig. [3.72](#) and [3.73](#), the HTL thickness of XOTPD is varied between 0 nm and 85 nm. LIV performance trends (fig. [3.72](#)) are analogous to the results shown in chapter [3.2.4](#). Compared to a device without OTPD (dark blue), a 22 nm thick OTPD layer (cyan) greatly improves LIV performance. Further increasing the thickness, however, leads to a gradual performance decrease due to the higher resistance. For this reason, OTPD layers in the range of 20 - 25 nm were chosen as standard in this work, as previously stated.

3.10 F8BT + R5011 layer thickness variation

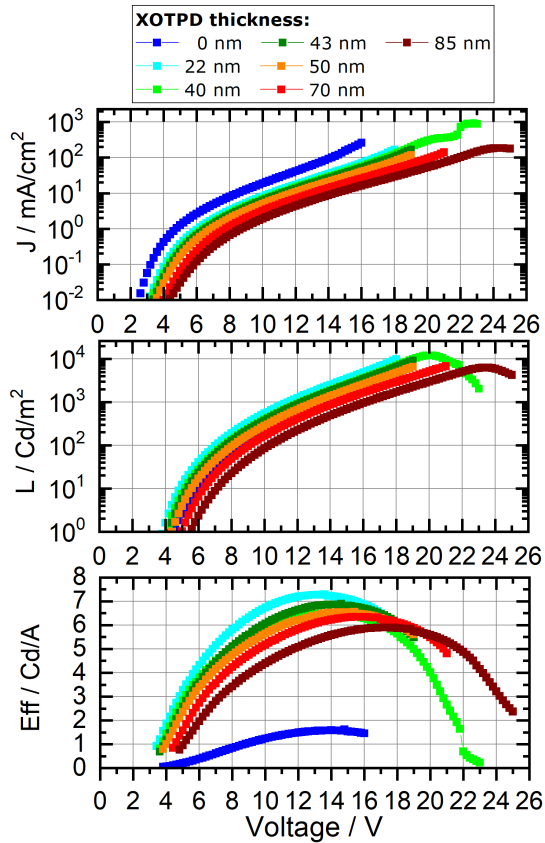


Fig. 3.72: LIV performance data for CP-OLEDs with varying XOTPD layer thickness.

Device architecture: ITO / PEDOT (37 nm) / XQUPD (22 nm) / XOTPD / F8BT + 10 wt% R5011 (217 - 225 nm) / CsF/Al (cured 10 min@180 °C) M_w (F8BT) = 37 kg/mol.

While the XOTPD thickness variation influences device performance, there seems to be no impact on the CPL behaviour, as demonstrated in fig. 3.73. EL spectra (b), g_{EL} curves (a) and g_w curves (c) are almost identical for all XOTPD thicknesses. The differences can be explained by a slight EML thickness variation between 217 nm and 225 nm, which is in the typical range of sample to sample variations. Therefore, $g_{@maxEL}$ values (d) are almost constant for all HTL thicknesses. As previously explained, this result can be explained by optical effects. In F8BT based OLEDs, the recombination zone is expected to be located close to the HTL-EML interface. Because of the energetic electron blocking step between

3 Results and Discussion

the LUMOs of OTPD and F8BT, variation of the OTPD thickness should not significantly influence the position of the recombination zone. Also, since none of the HTMs contain chiral elements, the polarisation state of CPL traversing these layers is not expected to be altered, for example through optical rotation. Since the EML thickness is kept constant, the distance between recombination zone and reflective cathode remains constant as well. In conclusion, the unchanged g_{EL} value with varying HTL thickness is not surprising. Other changes within the device architecture can, however, potentially influence the position of the recombination zone, or its distance to the cathode.

3.10 F8BT + R5011 layer thickness variation

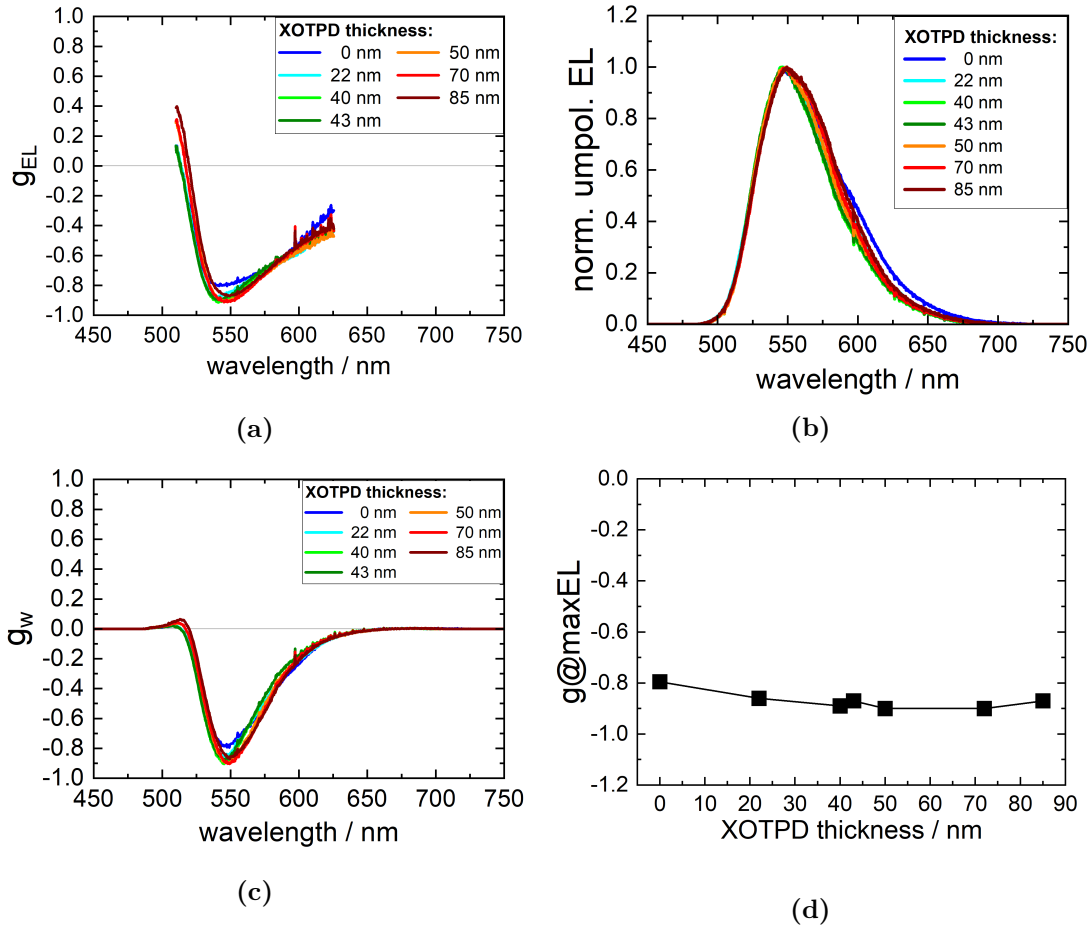
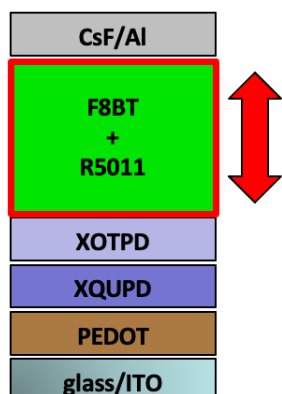


Fig. 3.73: g_{EL} curves (a), normalised EL spectra (b), g_w curves (c) and $g@maxEL$ values (d) for CP-OLEDs with varying XOTPD layer thickness. Device architecture: ITO / PEDOT (37 nm) / XQUPD (22 nm) / XOTPD / F8BT + 10 wt% R5011 (217 - 225 nm) / CsF/Al (cured 10 min@180 °C) M_w (F8BT) = 37 kg/mol.

3.10.2 EML thickness variation



For F8BT based OLEDs, variation of the EML thickness and subsequently the distance between recombination zone and reflective cathode leads to different EL interference patterns.

In fig. 3.74 and 3.76, the EML thickness of a F8BT + 10 wt%R5011 based CP-OLED is varied. As previously mentioned, the recombination zone for F8BT based OLEDs is expected to be located at the HTL/EML interface. By varying the EML thickness, the position of the recombination zone does not change, but the distance between the recombination zone and the reflective cathode does

As introduced in chapter 2.4.2 and demonstrated in chapter 3.2.4 for regular F8BT OLEDs, the outcoupled EL spectrum and its polarisation state is the interference product of all light waves in forward direction and reflected light waves initially in backward direction. Therefore, this variation of the EML thickness has a significant impact on OLED performance and optical properties.

In fig. 3.74, LIV performance data (a), normalised EL spectra (b), efficiency values at 13 V (c) and spectral positions of EL peaks (d) is shown. The general trends are analogous to fig. 3.18 in chapter 3.2.4, where a similar EML thickness variation is discussed for unpolarised F8BT OLEDs. Larger EML thicknesses lead to an increased V_{on} due to the higher resistance. Here, the efficiency is compared at 13 V, instead of 10 V for the neat F8BT example. The CP-OLED follows the same wave-like trend as the regular OLED. Neither the curing temperature of 180 °C (see fig. 3.19), nor the chiral inducer concentration of 10 wt% (see fig. 3.82) influence device performance negatively. Again, no linear correlation between EML thickness and Eff_{max} is found, because of its dependence on the EL spectrum. Here, two resonant modes, presumably $\frac{\lambda}{2}$ (left) and λ (right) are found.

3.10 F8BT + R5011 layer thickness variation

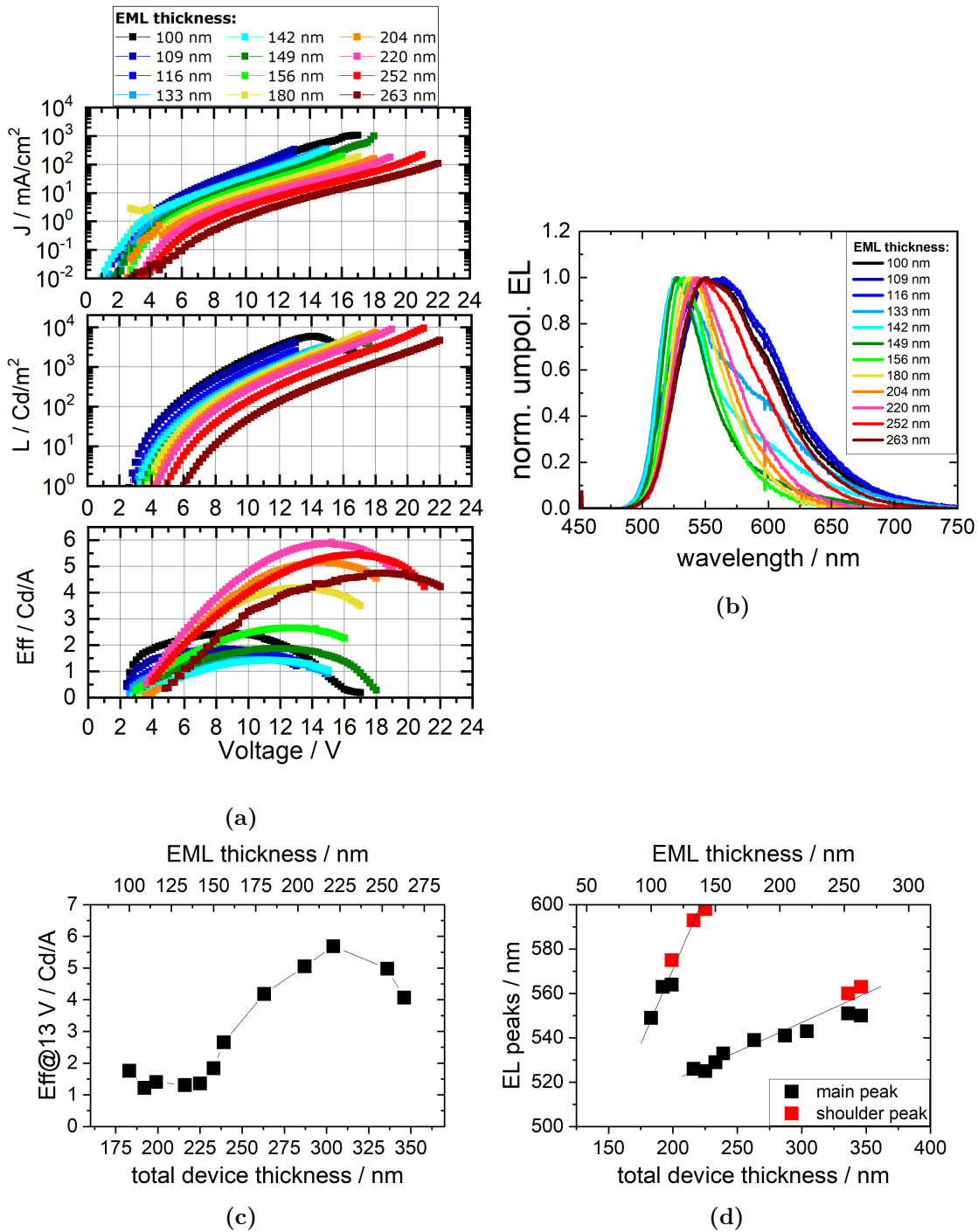


Fig. 3.74: LIV performance data (a) and normalised unpolarised EL spectra (b) of F8BT + 10 wt%R5011 based OLEDs with different EML thicknesses. Efficiencies at 13 V (c) and main peak (black) and shoulder peak (red) spectral positions (d) are shown for different total device thicknesses. In (d), trend-lines of two resonant modes are added as guide to the eye. Device architecture: ITO / PEDOT (37 nm) / XQUPD (21 nm) / XOTPD (25 nm) / F8BT + 10 wt% R5011 / CsF/Al (cured 15 min@180 °C) M_w (F8BT) = 37 kg/mol. 195

3 Results and Discussion

In fig. 3.75, device efficiencies (top) and EL peak positions (bottom) of F8BT + 10 wt%R5011 based CP-OLEDs and regular F8BT based OLEDs are compared. Both examples are built with the same F8BT-37 batch. Because of the differences in HTL thicknesses, the data shown here is plotted over EML thickness instead of total device thickness, which represents the more relevant factor.

Efficiencies are plotted at 13 V and 10 V, respectively. Both data sets follow the same wave-like trend, but the mixed system set has a slightly poorer performance. This is, however, in the range of a typical experiment batch to batch variation.

In both cases, multiple resonant modes can be seen. The jump between those modes occurs at the same total device thicknesses for both systems. The trend line slopes, however, differ noticeably. This indicates that the optical properties of these systems are not identical. It is likely that the differences are a result of the added chiral inducer, the chiral phase, or the curing process.

As previously demonstrated, curing of F8BT neat or mixed systems leads to spectral shifts in absorption, PL and EL. To separate this aspect of the chiral aspect, this experiment would have to be repeated with cured neat F8BT OLEDs and the results compared to the data shown here.

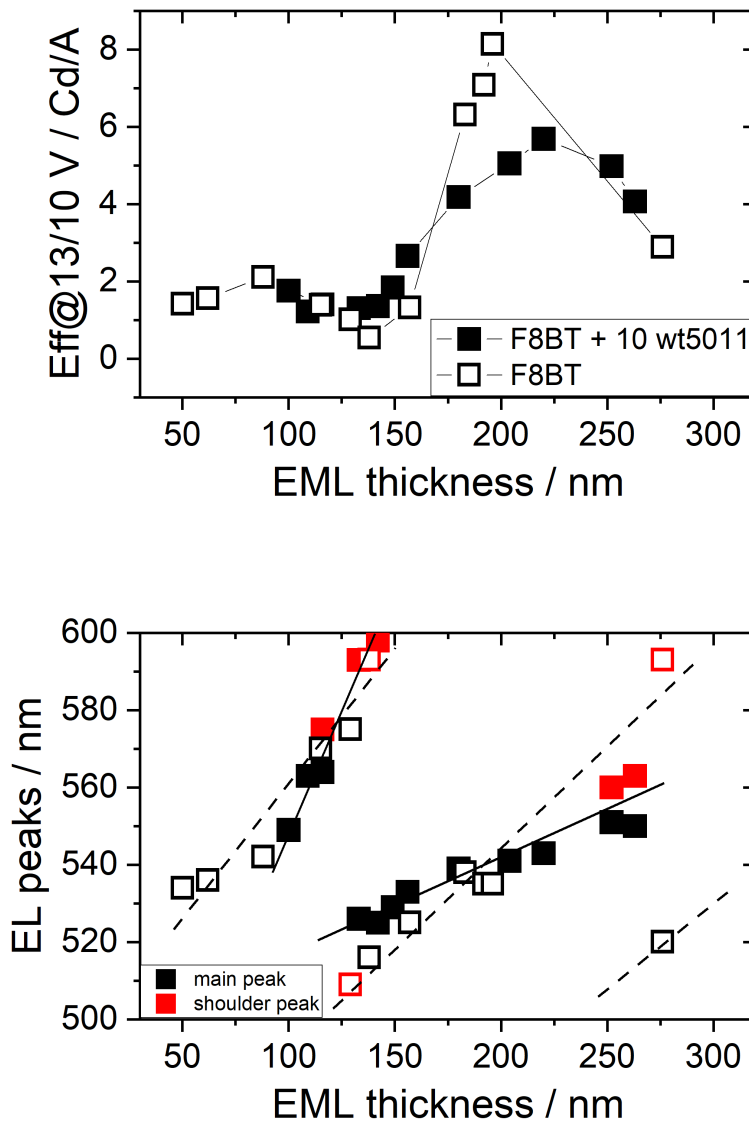


Fig. 3.75: Device efficiencies (top) and main (black) and shoulder (red) peak spectral positions (bottom) for F8BT + 10 wt%R5011 based CP-OLEDs (filled symbols, solid trend lines, Eff@13 V) and F8BT based OLEDs (open symbols, dashed trend lines, Eff@10 V).

Device architectures: ITO / PEDOT (37 / 32 nm) / XQUPD (21 / 31 nm) / XOTPD (25 / 31 nm) / F8BT + 10 wt% R5011 or F8BT / CsF/Al (cured 15 min@180 °C or uncured) \overline{M}_w (F8BT) = 37 kg/mol.

3 Results and Discussion

Analogous to the EL spectral shift, optical interference also affects the polarisation state, resulting in an intensity and polarisation distribution. Fig. 3.76 shows g_{EL} (a) and g_w (b) curves for the same devices.

With increasing EML thickness, an almost wavelike progression of the g_{EL} curves occurs. This behaviour is partly explained by the previously introduced spectral shift. The effect can be seen even better on g_w curves. The position of the g_w peaks moves left and right, analogous to the shift of the EM maximum. Additionally, the intensity of the g_w peak and $g@maxEL$ varies and even exhibits a sign flip. This trend is highlighted in (c), where $g@maxEL$ values are shown over EML thickness.

As explained in chapter 2.4.2, both, the EL spectral shift and the changing g_{EL} curve are a result of optical interference. When CPL in backward direction is reflected on the cathode, its handedness is reversed. Additionally, the chiral EML itself shows CPL-selective absorption (i.e. CD), which can influence the polarisation state of light travelling through this layer. Upon interaction with the light in forward direction, optical interference occurs, leading to an interference pattern. The resulting intensity distribution determines the EL spectral shape, and the polarisation distribution determines the polarisation state of the outcoupled light.

In the here shown example, $g@maxEL$ values between +0.52 and -0.83 are reached. These values are not yet sufficient for commercial application as 3D displays. However, the fact that large g_{EL} values of an opposite handedness can be achieved, simply through layer thickness variation, poses great promise in this direction.

3.10 F8BT + R5011 layer thickness variation

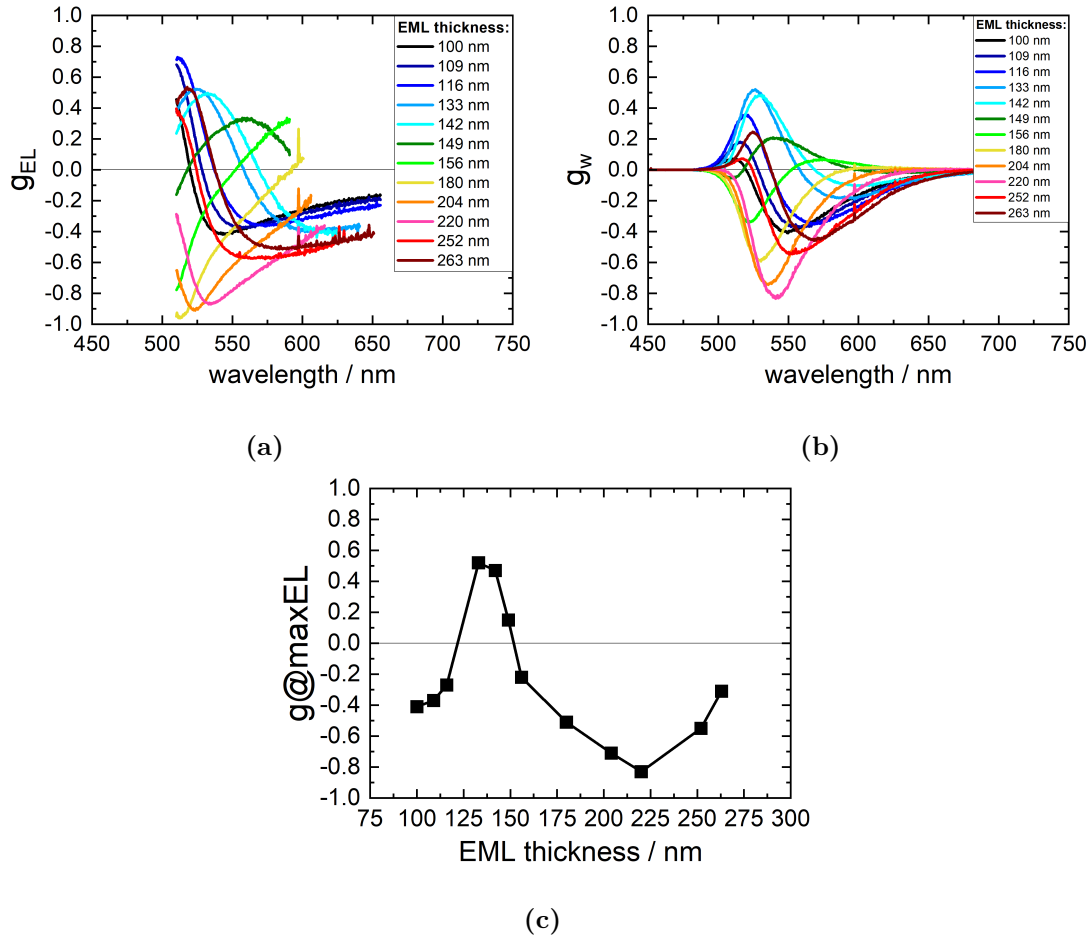
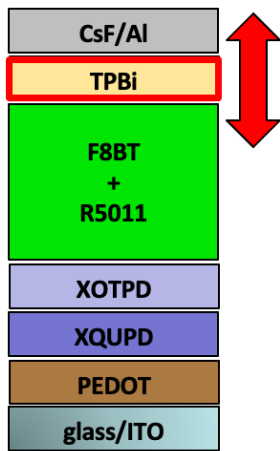


Fig. 3.76: g_{EL} curves (a), g_w curves (b) and $g@maxEL$ values (c) for CP-OLEDs with different EML thicknesses.

Device architecture: ITO / PEDOT (37 nm) / XQUPD (21 nm) / XOTPD (25 nm) / F8BT + 10 wt% R5011 / CsF/Al (cured 15 min@180 °C) M_w (F8BT) = 37 kg/mol.

3.10.3 ETL thickness variation



The effect of the introduction and thickness variation of an **ETL**, here TPBi, into the standard stack is analysed in this chapter.

Fig. 3.77 (b) shows how TPBi fits into the stack energetically. With its LUMO energy level of -2.7 eV, TPBi lowers the electron injection barrier and acts as an **ETL**. At the same time, the low HOMO energy level of -6.2 eV provides an energetic hole blocking step.

However, the LIV performance data (a) indicates that the material is not ideal. With increasing TPBi layer thicknesses, higher resistance leads to a significant rise in V_{on} . At the same time, device efficiency decreases. While, based on these results, TPBi does not seem like an ideal ETM for F8BT based OLEDs, it might still be possible that thinner TPBi layers, for example 10 nm, could be beneficial to the performance.

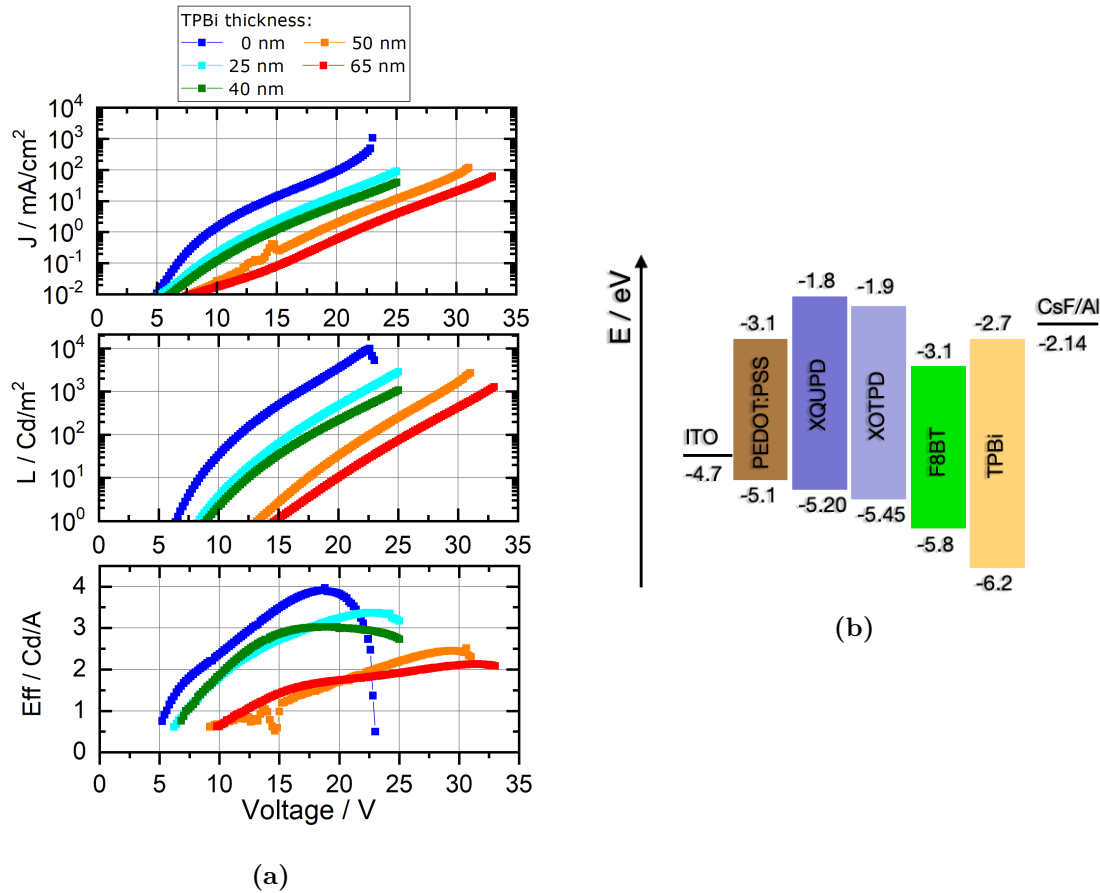


Fig. 3.77: LIV performance data (a) and energy diagram (b) for CP-OLEDs with varying TPBi layer thickness.

Device architecture: ITO / PEDOT (33 nm) / XQUPD (23 nm) / XOTPD (22 nm) / F8BT + 10 wt% R5011 (210 nm) / TPBi / CsF/Al (cured 15 min@200 °C) M_w (F8BT) = 54 kg/mol.

In fig. 3.78, the impact of an added TPBi ETL on the optical properties is shown. In contrast to the HTL thickness variation in chapter 3.10.1, the here shown ETL thickness variation influences the EL spectra (b) and g_{EL} curves (a). Again, the effect is better visible by means of g_w curves (c).

$g@maxEL$ (d) shifts with increasing ETL thickness, even to the point of a sign flip. In this case, even with a constant EML thickness, the distance between recombination zone and reflective cathode changes through the additional layer. It is, however, also possible that, because of the new energetic environment with this

3 Results and Discussion

additional material, the position of the recombination zone within the EML is influenced. In both cases, the observed $g@maxEL$ shift can be explained through the changed distance between recombination zone and reflective cathode, and the subsequent interference.

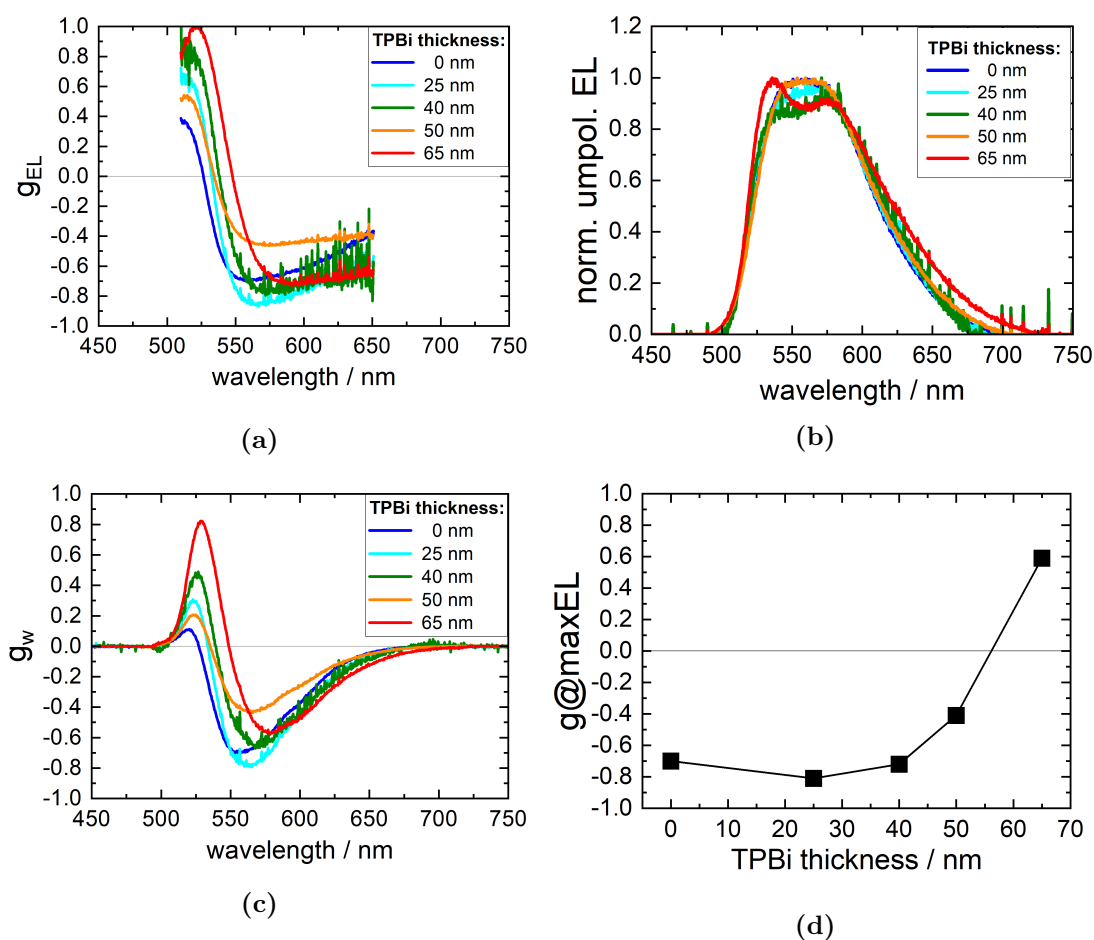


Fig. 3.78: g_{EL} curves (a), normalised EL spectra (b), g_w curves (c) and $g@maxEL$ values (d) for F8BT + R5011 based CP-OLEDs with varying TPBi layer thickness.

Device architecture: ITO / PEDOT (33 nm) / XQUPD (23 nm) / XOTPD (22 nm) / F8BT + 10 wt%R5011 (210 nm) / TPBi / CsF/Al (M_w (F8BT) = 54 kg/mol).

3.11 F8BT + R5011 molecular weight

As previously explained, the molecular weight of the used F8BT batch determines the required curing conditions. The trend shown in fig. 3.70 (b) for the F8BT-21 batch is found in other batches as well in fig. 3.79. Each batch possesses an ideal curing temperature, shifting to higher temperatures with increasing M_w , analogous to the results found in DSC measurements. But interestingly, not all F8BT batches produce equally large CP-effects, even if processed under their respective ideal conditions. Fig. 3.79 (b) shows how, for the same chiral inducer concentration and layer thickness, the maximum achievable CD* value differs significantly for different batches.

For very low M_w batches, low CD values are not surprising. For the desired chiral LC phase, both, intramolecular polymer chain twisting and intermolecular polymer chain arrangement play a role. For oligomers, the first aspect naturally loses potency. Likewise, an increasing CD effect for medium M_w batches is to be expected. Lastly, for very high M_w batches, the decreasing CD effect can be explained by the growing steric factor. For larger polymer chains, it becomes increasingly difficult to detangle from another and rearrange into the desired chiral LC phase. It might be possible that much longer curing times in the range of hours or days could improve the CD effect for those batches. But this particular aspect was not studied here, as such extensive curing routines would undoubtedly damage the stack and thereby decrease device performance. Since the aim of this work was to develop a CP-OLED with good performance and large CP-effect, both aspects need to be fulfilled equally. Therefore, an F8BT M_w range of approximately 7 to 24 kg/mol was identified as ideal for application in mixed system CP-OLEDs.

3 Results and Discussion

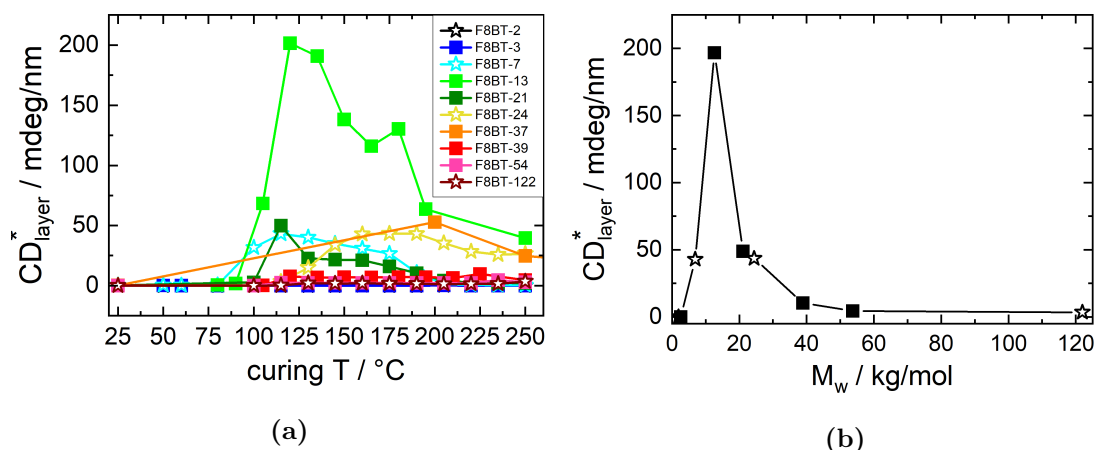


Fig. 3.79: CD* values at 480 nm for thin films of different F8BT batches containing 10 wt% R5011. CD* values are plotted against curing temperature (a) or against M_w (b). Batches synthesised by Dr. Jürgen Schelter are marked with a star.

The same trends are found for g_{EL} values, as shown in fig. 3.80. The dependency between layer thickness and g_{EL} value was explained in chapter 3.10. And it shows now that g_{EL} is not only thickness dependent, but the maximum achievable g_{EL} also strongly depends on the F8BT batch molecular weight. Just like with CD results, very low M_w (F8BT-2 and F8BT-3, black and blue) and very high M_w (F8BT-122, burgundy) batches perform poorly, only achieving low $g@maxEL$ values. Therefore, the reasonable M_w range of F8BT polymers for CP-OLED applications lies between 7 kg/mol and 54 kg/mol.

Based on these results, an additional differentiation can be made. With the unviable batches omitted, the remaining F8BT batches are separated into lower M_w (7 - 21 kg/mol, red) and higher M_w (37 - 54 kg/mol, black) groups in fig. 3.80 (bottom). While the general trend for both groups is the same, the lower M_w group could achieve a higher maximum $g@maxEL$ of up to -1.12 compared to a maximum $g@maxEL$ of -0.93 for the higher M_w group. This confirms the trend found in CD data shown above.

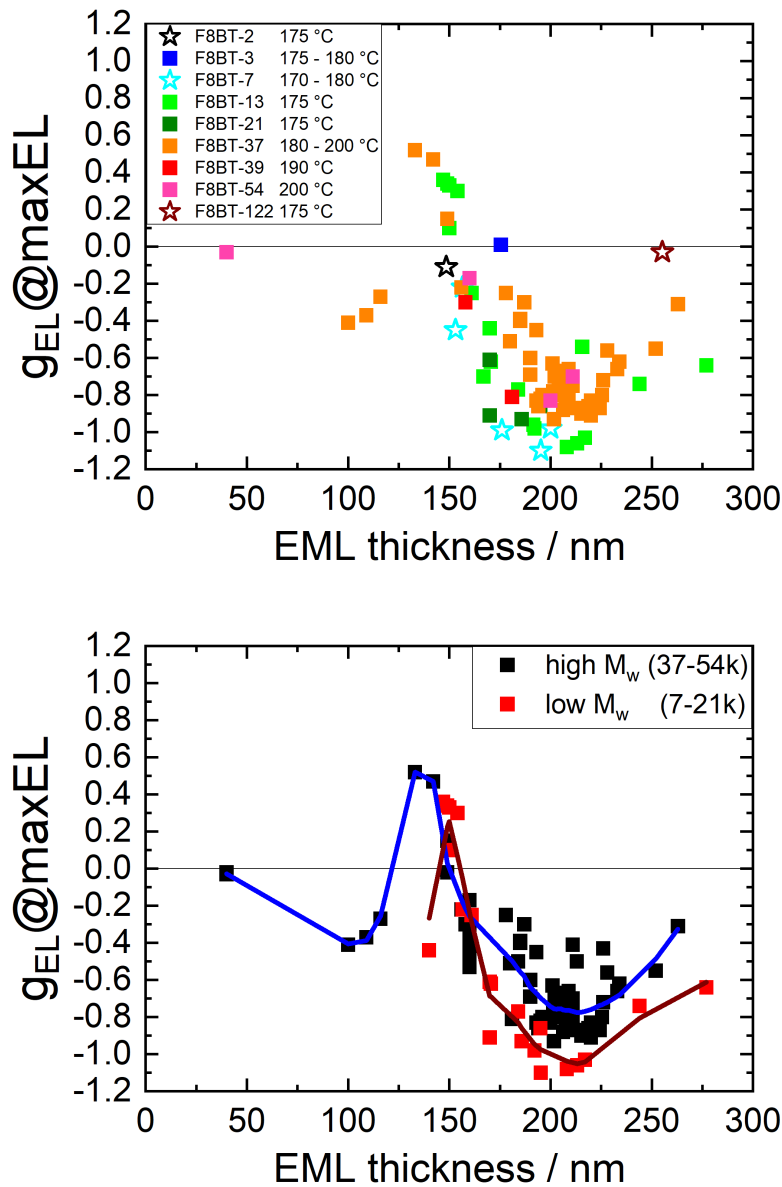


Fig. 3.80: $g_{EL}@maxEL$ values for F8BT + 10 wt% R5011 based CP-OLEDs with different EML thicknesses. F8BT batches with different M_w are distinguished through data point colours (top) or grouped into M_w (7 - 21 kg/mol, red) and high M_w (37 - 54 kg/mol, black) groups, for which trend lines are shown (bottom).

Batches synthesised by Dr. Jürgen Schelter are marked with a star.

3.12 F8BT + R5011 chiral inducer concentration

F8BT based OLEDs without chiral inducer do not show any CPL, even if cured. It is not surprising that for small chiral inducer concentrations, CP-effect intensity increases with increasing chiral inducer concentration. However, it is to be assumed that at some point, an ideal chiral phase is formed. Adding more chiral inducer afterwards could even disturb the chiral phase, thereby decreasing the amount of CPL. However, to understand how the changing chiral inducer concentration influences the amount of outcoupled CPL, some additional factors have to be considered.

Fig. 3.81 shows how increasing chiral inducer concentrations also influence the thermal phase behaviour. With a reported T_m of 152 - 156 °C [128], R5011 acts as a plasticiser, slightly shifting phase peaks towards lower temperatures, but much more significantly dampening signal intensities. In contrast to the neat F8BT DSC measurements shown in chapter 3.3, signal intensity could not be increased by increasing the heating rate in this case.

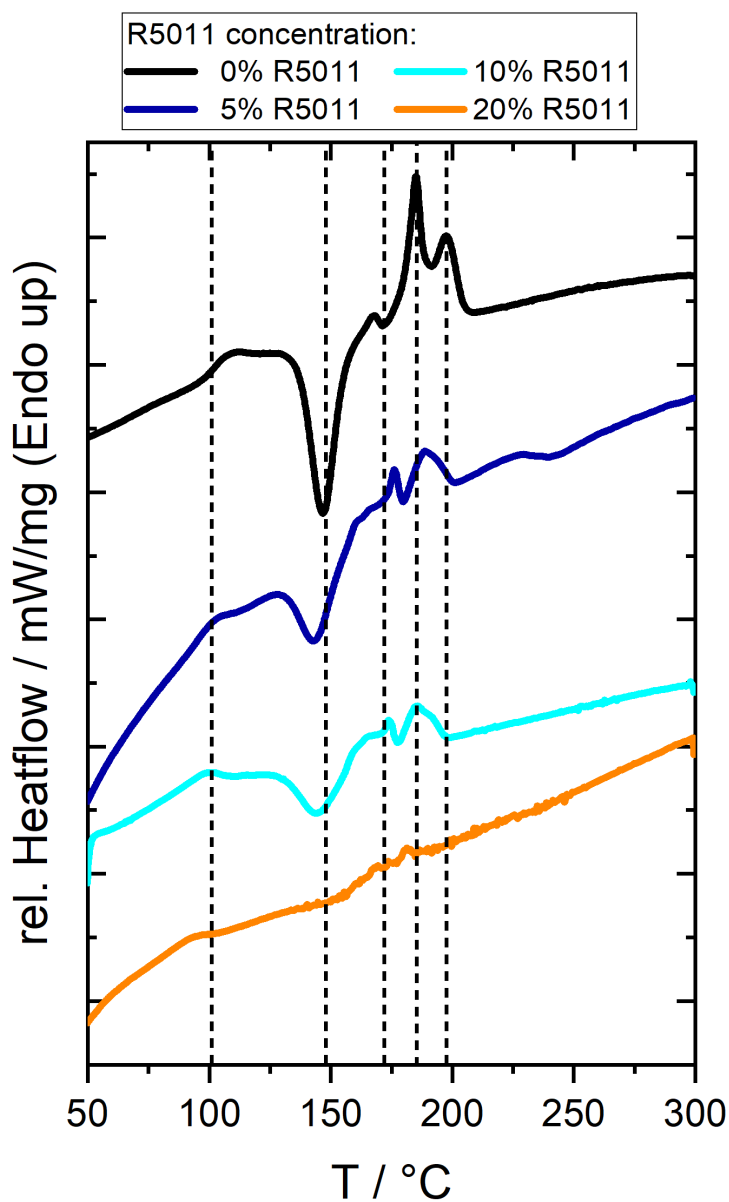


Fig. 3.81: DSC measurements of F8BT-21 with different concentrations of R5011. Materials were mixed in solution and solvent was subsequently evaporated before DSC measurement. Heating rate: 10 °C/min, second heating scans are shown. Heatflow was divided by sample mass, curves are levelled and stacked. For comparison, the signal positions of the neat F8BT measurements are indicated through dashed lines superimposed for better visibility.

3.12.1 F8BT + R5011 total chiral inducer concentration

Fig. 3.82 (a) shows LIV performance data for F8BT + S5011 based CP-OLEDs with varying chiral inducer concentrations. Even though it is difficult to see on the logarithmic scale, brightness L and current density J increase slightly with increasing chiral inducer concentration. Likewise, and better so see on the linear scale, the maximum efficiency increases for larger chiral inducer concentrations. Since all shown devices are relatively comparable with EML thicknesses of 201 - 206 nm, it can be assumed that the chiral inducer influences the electrical properties of the mixed layer.

In comparison, fig. 3.82 (b) shows LIV performance data for F8BT + R5011 based CP-OLEDs with a wider variation of the chiral inducer concentration than shown in the previous example. For the evaluation of this example, however, the EML thickness variation of 188 – 229 nm, with the EML thickness decreasing for higher chiral inducer concentrations, has to be considered as well. For this, a comparison to the EML thickness variation of F8BT + 10 %R5011 based CP-OLEDs shown in fig. 3.74 in chapter 3.10.2 can be made. While an EML thickness variation of the magnitude shown here does also lead to performance differences in the previous example, the effect shown here is larger than would be expected for a thickness variation.

This result reinforces the assumption, that the added chiral inducer influences the electric properties of the EML. Considering this, it can be said that device efficiency and brightness improve with chiral inducer concentrations up to 20 wt%. Increasing the concentration further, however, leads to performance losses.

Optical measurements, including CD, EL and g_{EL} data, for both examples are shown on the following pages.

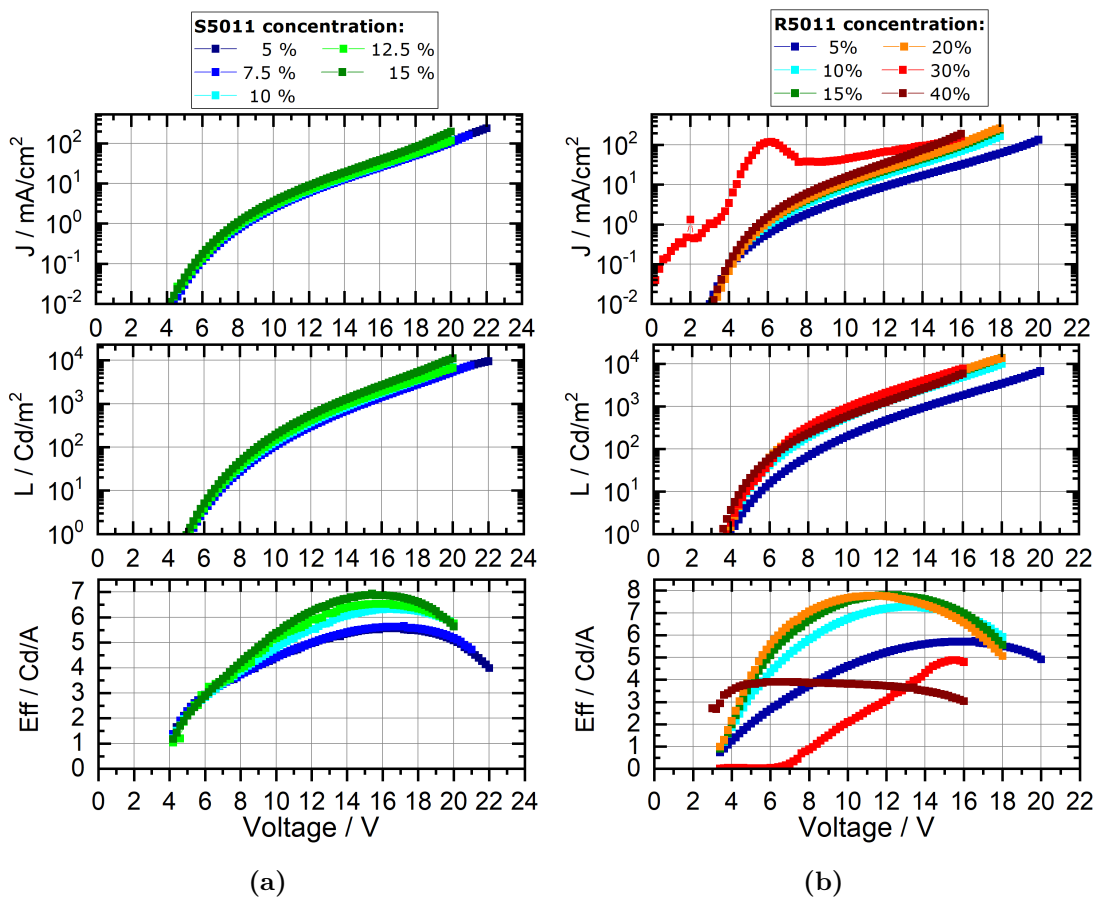


Fig. 3.82: LIV performance data for F8BT + S5011 (a) or R5011 (b) CP-OLEDs with varying chiral inducer concentrations.

Device architecture (a): ITO / PEDOT (36 nm) / XQUPD (35 nm) / XOTPD (21 nm) / F8BT + S5011 (201 - 206 nm) / CsF/Al (cured 15 min@180 °C) M_w (F8BT) = 37 kg/mol.

Device architecture (b): ITO / PEDOT (37 nm) / XQUPD (22 nm) / XOTPD (22 nm) / F8BT + R5011 (188 - 229 nm) / CsF/Al (cured 10 min@180 °C) M_w (F8BT) = 37 kg/mol.

Fig. 3.83 shows CD curves (a) and CD* values at 349 nm (b) of the devices shown in fig. 3.82 (a). It should be pointed out that the data shown in this chapter is based on CP-OLEDs with either R5011 or S5011. As previously mentioned, chiral inducer enantiomers produce mirror image CD and g_{EL} curves to each other. Data sets based on R5011 and S5011, if otherwise equivalent, can be compared by using the modulus instead of the absolute values. For the two data sets in this chapter,

3 Results and Discussion

however, the difference in EML thickness has to be considered.

Due to the large EML thickness, all samples with S5011 concentrations above 7.5 wt% contain unphysical values. Because the absorption limit is reached at the largest signal peak, data analysis is performed on the second signal peak at 349 nm, which is indicated with a dashed line.

CD* values shown in (b) increase with larger S5011 concentrations. This illustrates the gradually forming chiral phase. Above 12.5 wt%, however, the value remains constant, suggesting that at this concentration, the chiral phase is fully formed. Further increase of the chiral inducer concentration does not lead to an increased CP-effect.

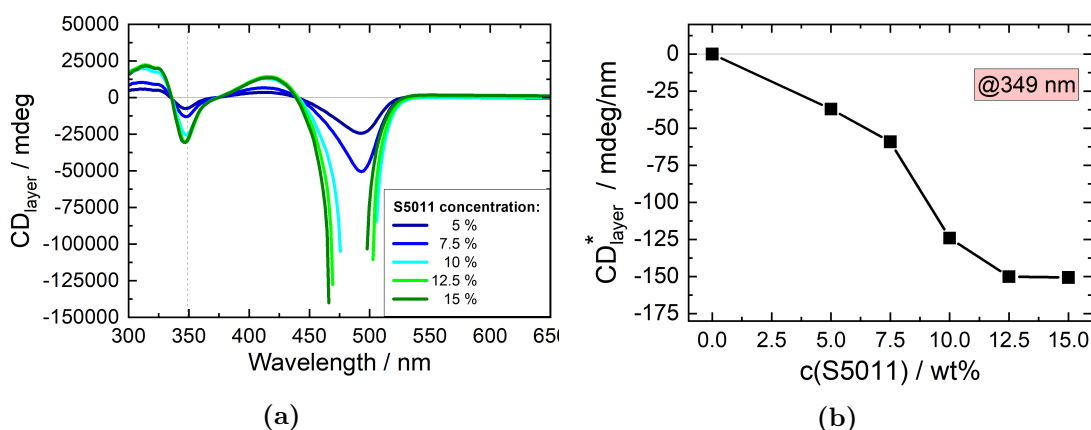


Fig. 3.83: CD curves (a) and resulting CD* values at 349 nm (b) of CP-OLEDs with varying chiral inducer concentrations.

Device architecture (a): ITO / PEDOT (36 nm) / XQUPD (35 nm) / XOTPD (21 nm) / F8BT + S5011 (201 - 206 nm) / CsF/Al (cured 15 min@180 °C) M_w (F8BT) = 37 kg/mol.

In fig. 3.84, the influence of S5011 on the EL properties and CP-effect of the EML is demonstrated. A small spectral shift is found in the normalised EL spectra (b), with EL maxima varying between 538 nm and 543 nm. This indicates that S5011 also influences the optical properties of the EML. This is not surprising, since small non-absorbing molecules like the here used chiral inducer S5011 are expected to have a lower refractive index than the polymer.

3.12 F8BT + R5011 chiral inducer concentration

In the g_{EL} (a) and g_w (c) curves, the impact of different S5011 concentrations on the CP-effect can be seen. In (d), $g@maxEL$ is plotted over chiral inducer concentration. With the given device architecture and layer thickness, a maximum $g@maxEL$ value of 0.96 is achieved for a 10 wt%S5011 concentration. Smaller or larger concentrations only produce lower g_{EL} values. Interestingly, $g@maxEL$ already declines at a concentration of 12.5 wt%S5011, even though CD^* still increases up to this point. This result, however, could be explained by optical interference effects due to reflection on the cathode.

3 Results and Discussion

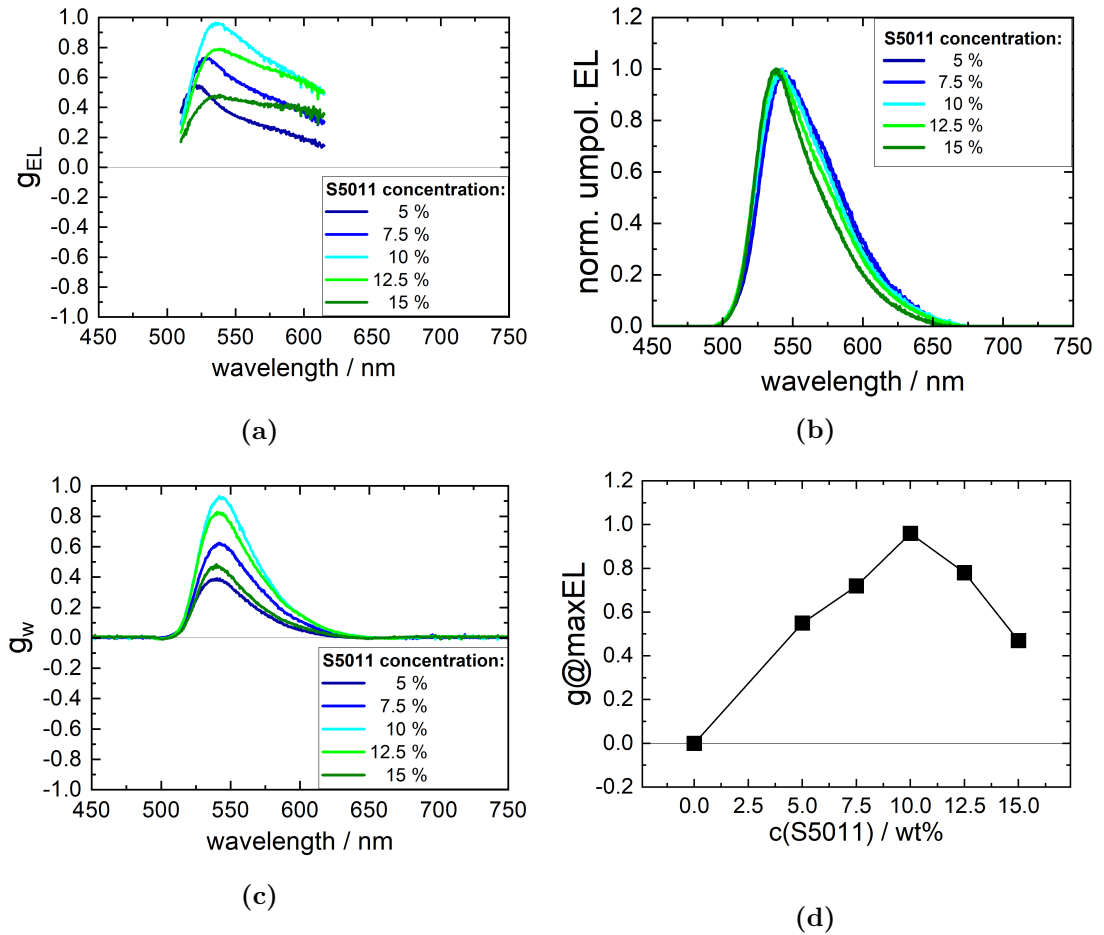


Fig. 3.84: g_{EL} curves (a), normalised EL spectra (b), g_w curves (c) and $g@maxEL$ values (d) for F8BT + S5011 CP-OLEDs with varying chiral inducer concentrations.

Device architecture (a): ITO / PEDOT (36 nm) / XQUPD (35 nm) / XOTPD (21 nm) / F8BT + S5011 (201 - 206 nm) / CsF/Al (cured 15 min@180 °C) $M_w(F8BT) = 37$ kg/mol.

3.12 F8BT + R5011 chiral inducer concentration

Analogous to fig. 3.84 for S5011, fig. 3.85 shows optical measurements of the F8BT + R5011 CP-OLED example introduced in fig. 3.82 (b). Here, the effect of even larger chiral inducer concentrations is demonstrated.

A significant spectral shift is found in the normalised EL spectra (b), with EL maxima varying between 533 nm and 557 nm. As seen in fig. 3.74, however, a comparable EML thickness variation for F8BT + 10 wt%R5011 only resulted in a 4 nm shift of EL maxima. It can, therefore, be assumed that R5011 also influences the optical properties of the EML.

In the g_{EL} (a) and g_w (c) curves, a significant impact of the chiral inducer concentration on the CP-effect can be seen. In (d), $g@maxEL$ is plotted over chiral inducer concentration and reveals a varying size and sign of the CP-effect, similar to the previously shown correlation between $g@maxEL$ and EML thickness. $g@maxEL$ first increases with increasing chiral inducer concentration. The maximum achievable $g@maxEL$ for the chosen device architecture and layer thicknesses is found, again, for 10 wt%R5011, which is a value often found in literature as the ideal concentration [4, 46, 99]. Above 10 wt%, however, the outcoupled CPL decreases, with $g@maxEL$ even exhibiting a sign flip at 20 wt%.

3 Results and Discussion

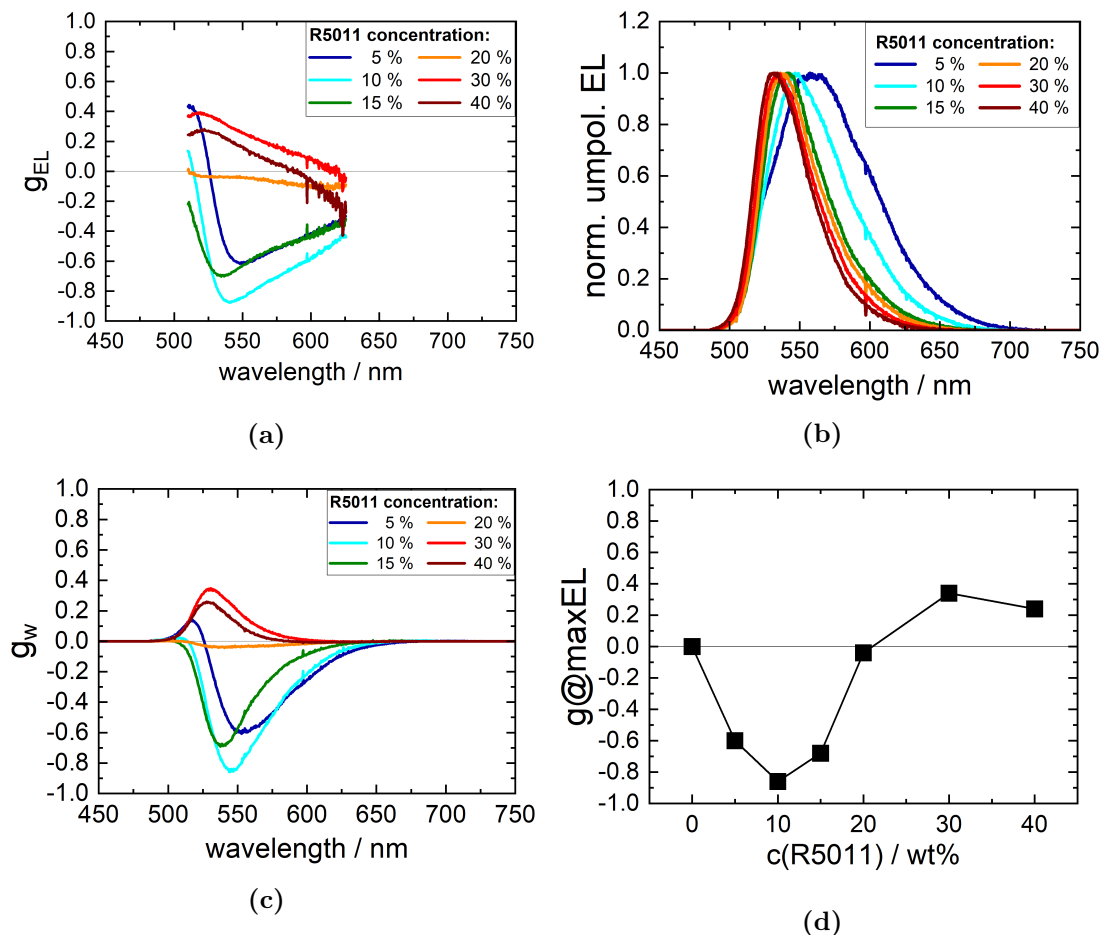


Fig. 3.85: g_{EL} curves (a), normalised EL spectra (b), g_w curves (c) and $g@maxEL$ values (d) for F8BT + R5011 CP-OLEDs with varying chiral inducer concentrations.

Device architecture: ITO / PEDOT (37 nm) / XQUPD (22 nm) / XOTPD (22 nm) / F8BT + R5011 (188 - 229 nm) / CsF/Al (cured 10 min@180 °C) $M_w(F8BT) = 37$ kg/mol.

As previously shown, g_{EL} does not only depend on the chiral inducer concentration, but also on the EML layer thickness. Therefore, to achieve a full picture of the concentration dependence of g_{EL} , both parameters would have to be changed systematically. This means analysing a set of CP-OLEDs with varying EML thicknesses for several chiral inducer concentrations, resulting in a 3D plot which aligns $g@maxEL$, EML thickness and chiral inducer concentration.

3.12.2 F8BT + R5011 chiral inducer *e.e.*

It was shown that the chiral inducer concentration has an impact on the electrical and optical properties of the mixed layer. It is, therefore, not ideal to simply change the chiral inducer concentration in the system. To mitigate these problems, a different approach shall be introduced here. Instead of adding different concentrations of one chiral inducer enantiomer, different ratios of both enantiomers are used at a given total chiral inducer concentration. In analogy to organic synthesis, those mixtures can be declared in terms of enantiomeric excess (*e.e.*) as calculated with eq. 3.6, with the weight of both enantiomers m_1 and m_2 .

$$e.e. = \frac{|m_1 - m_2|}{m_1 + m_2} \cdot 100\% \quad (3.6)$$

Alternatively, since equal amounts of R5011 and S5011 are expected to cancel each other out in terms of chiral induction, one could refer to the excess concentration of one enantiomer as effective concentration.

Tab. 3.6 gives some representative enantiomeric mixtures and their calculated *e.e.* and effective concentrations, corresponding to the examples shown in this chapter.

3 Results and Discussion

Tab. 3.6: Examples for different mixtures of R5011 and S5011 with calculated combined additive and effective chiral inducer concentrations, as well as *e.e.*

c(R5011) / wt%	c(S5011) / wt%	combined additive concentration / wt%	<i>e.e.</i> / %	effective chiral inducer concentration / wt%
5	5	10	0	0
8	2	10	60	6
10	0	10	100	10
10	5	15	33	5
12.5	2.5	15	67	10
15	0	15	100	15

Fig. 3.86 demonstrates this effect on three CP-OLEDs with an equal total chiral inducer concentration of 10 wt%, but different R/S5011 *e.e.*

The black example contains equal amounts of R5011 and S5011, resulting in an effective concentration and *e.e.* of 0 %. As previously stated, the two enantiomers cancel each other out. As a result, no CD is visible.

By changing the ratio between the enantiomers, different CD intensities are observed, corresponding to the effective concentration and *e.e.*

At this point, the behaviour of the excess chiral inducer molecules that have been cancelled out is not known. One possibility is that, like in mixtures with only one enantiomer, each molecule induces a twist in the F8BT polymer chains, with the preferential twisting direction determined by their chirality. This could lead to a more racemic than helical polymer arrangement in some places, which could produce unpolarised light rather than CPL.

Alternatively, different domains with preferentially left or right handed twisting directions could be formed, leading to RCP and LCP emission, depending on the domain. The outcoupled light would be a combination of both polarisations.

It is also possible that two opposite chiral inducer enantiomers could aggregate, leading to no chiral induction whatsoever. This way, the chiral phase is only influenced by the predominant enantiomer.

To answer this question, further analysis of the mixed enantiomer chiral phase would have to be made, for example through polarisation microscopy (POM) of thin films with different chiral inducer *e.e.s* and total concentrations. Since the chiral domain has been shown to be smaller than the typical layer thickness used in this work, it is likely that larger film thicknesses would produce better results with POM. With this method, it might also be possible to determine the domain size and whether only chiral domains of one handedness, of both handednesses, or racemic mixtures are present.

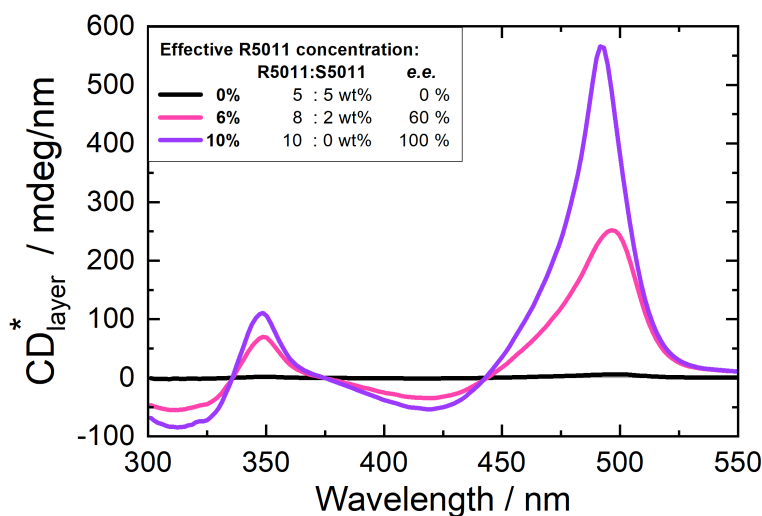


Fig. 3.86: CD* values of F8BT + R/S5011 based CP-OLEDs with a total chiral inducer concentration of 10 wt%, but different *e.e.s*.
 Device architecture: ITO / PEDOT (33 nm) / XQUPD (26 nm) / XOTPD (22 nm) / F8BT + 10 wt%R/S5011 (163 - 170 nm) / CsF/Al (cured 15 min@175 °C) M_w (F8BT) = 21 kg/mol.

3 Results and Discussion

Fig. 3.87 shows LIV performance data of three sets of F8TB + R/S5011 based CP-OLEDs with EML thickness variations¹². While all devices contain a total chiral inducer concentration of 15 wt%, the sets have different effective concentrations of 5 wt% (b), 10 wt% (c) and 15 wt% (d) R5011, respectively.

(a) compares one device from each set with an EML thickness of 217 nm. In chapter 3.12.1, varying the chiral inducer concentration directly produced different electrical and optical properties, which lead to a concentration dependent shift in device performance. In contrast, all devices shown here contain the same total chiral inducer concentration. Therefore, no electrical differences should occur. As expected, LIV performance differences in (a) are only marginal and in the range of typical sample to sample variations.

For these three devices, performance values at 15 V, EL peaks and $g@maxEL$ values, are given in tab. 3.7 on page 224.

In general, the EML thickness dependence for all three sets (b - d) is analogous to the results discussed in chapter 3.10.

¹²Acquisition of this data was supported by Annemarie Berger. Experiment planning and evaluation by Claudia Dillmann.

3.12 F8BT + R5011 chiral inducer concentration

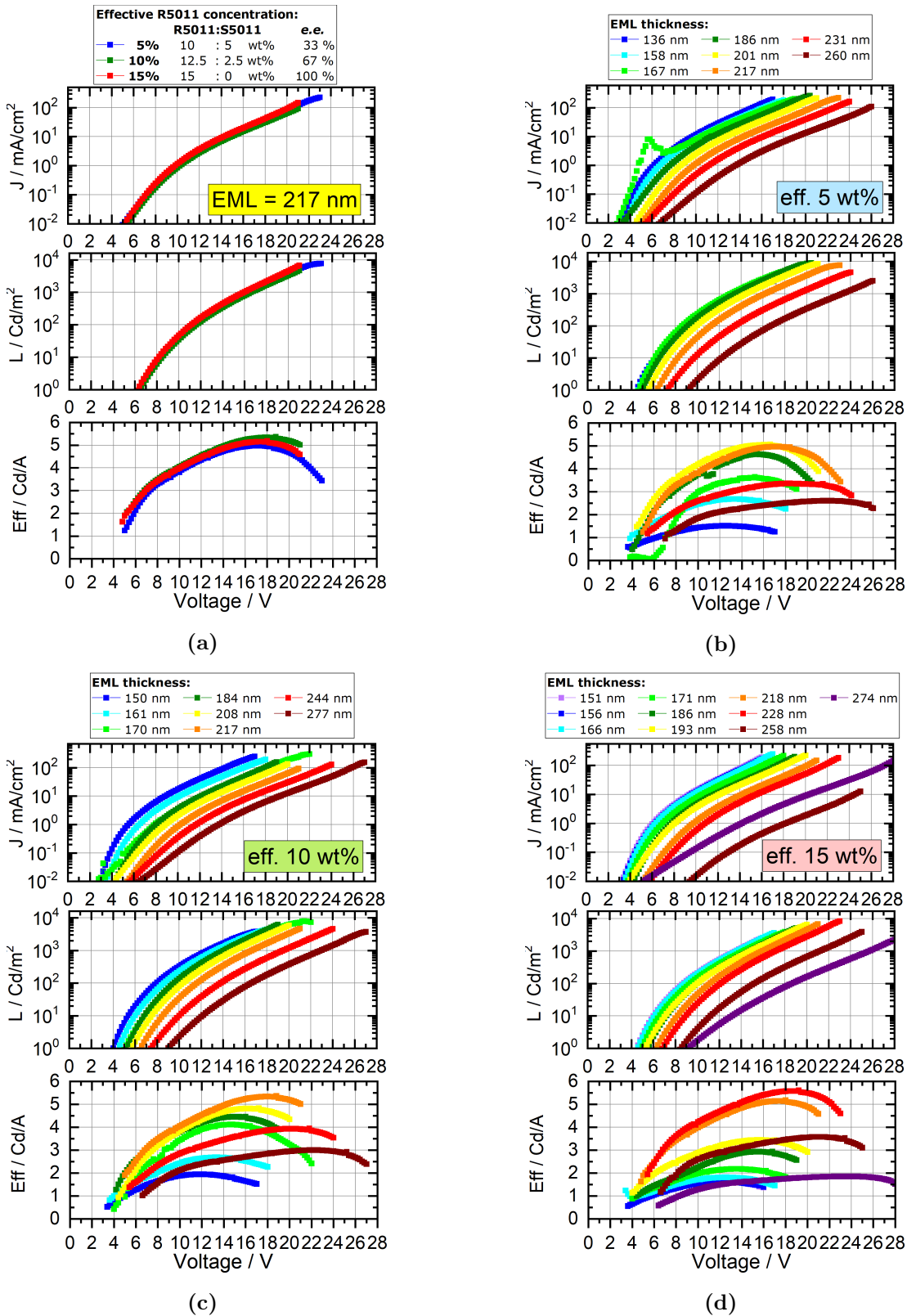


Fig. 3.87: LIV device performance of F8BT + R/S5011 based CP-OLEDs with a total chiral inducer concentration of 15 wt% and effective concentrations of 5 % (b), 10 % (c) and 15 % (d) R5011. (a) compares all three *e.e.*s at an EML thickness of 217 nm.

Device architecture: ITO / PEDOT (35 nm) / XQUPD (25 nm) / XOTPD (25 nm) / F8BT + 15 wt%R/S5011 / CsF/Al (cured 10 min@180 °C) (M_w (F8BT) = 13 kg/mol).

3 Results and Discussion

Fig. 3.88 shows normalised EL spectra of the same devices shown in fig. 3.87. Analogous, (b - d) contain the EML thickness dependent EL spectra of each set. (a) compares the three devices with an EML thickness of 217 nm. Here, a large spectral shift is noticeable, with EL maxima varying between 538 nm and 551 nm. Since the device architecture, layer thicknesses and total chiral inducer concentration are equal, this shift must be caused by the different chiral phases. Fig. 3.84 (b) shows the same effect for a total R5011 concentration variation.

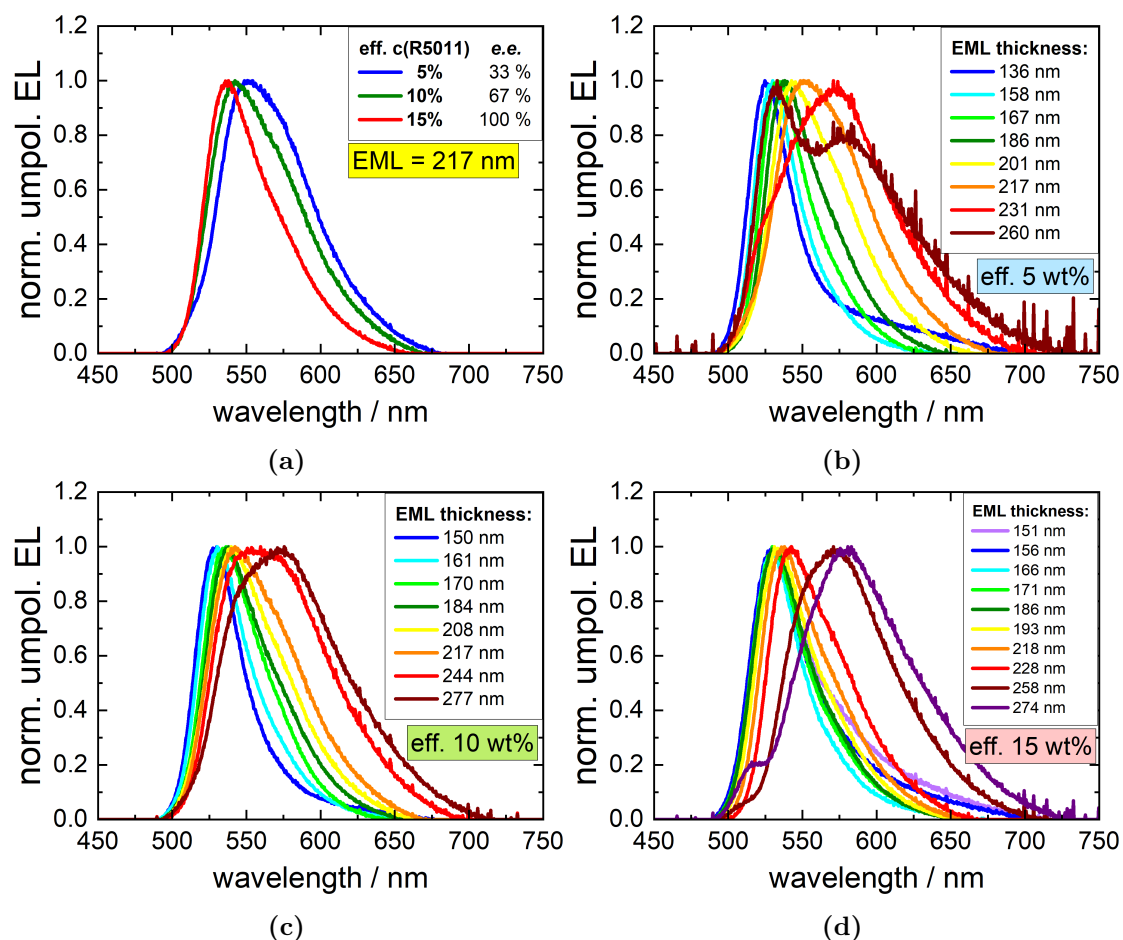


Fig. 3.88: Normalised EL spectra of F8BT + R/S5011 based CP-OLEDs with a total chiral inducer concentration of 15 wt% and effective concentrations of 5 % (b), 10 % (c) and 15 % (d) R5011. (a) compares all three *e.c.s* at an EML thickness of 217 nm.

Device architecture: ITO / PEDOT (35 nm) / XQUPD (25 nm) / XOTPD (25 nm) / F8BT + 15 wt%R/S5011 / CsF/Al (cured 10 min@180 °C) M_w (F8BT) = 13 kg/mol.

Fig. 3.89 and 3.90 show g_{EL} and g_w curves, respectively, of the same devices shown in fig. 3.87. Analogous, (b - d) contain the EML thickness dependent g_{EL} and g_w curves of each set. Like above, (a) compares the three devices with an EML thickness of 217 nm. As previously shown for mixtures with only one chiral inducer enantiomer, the largest CP-effect is found for the sample containing an effective R5011 concentration of 10 %. In both cases, lower or higher concentrations result in lower g_{EL} values.

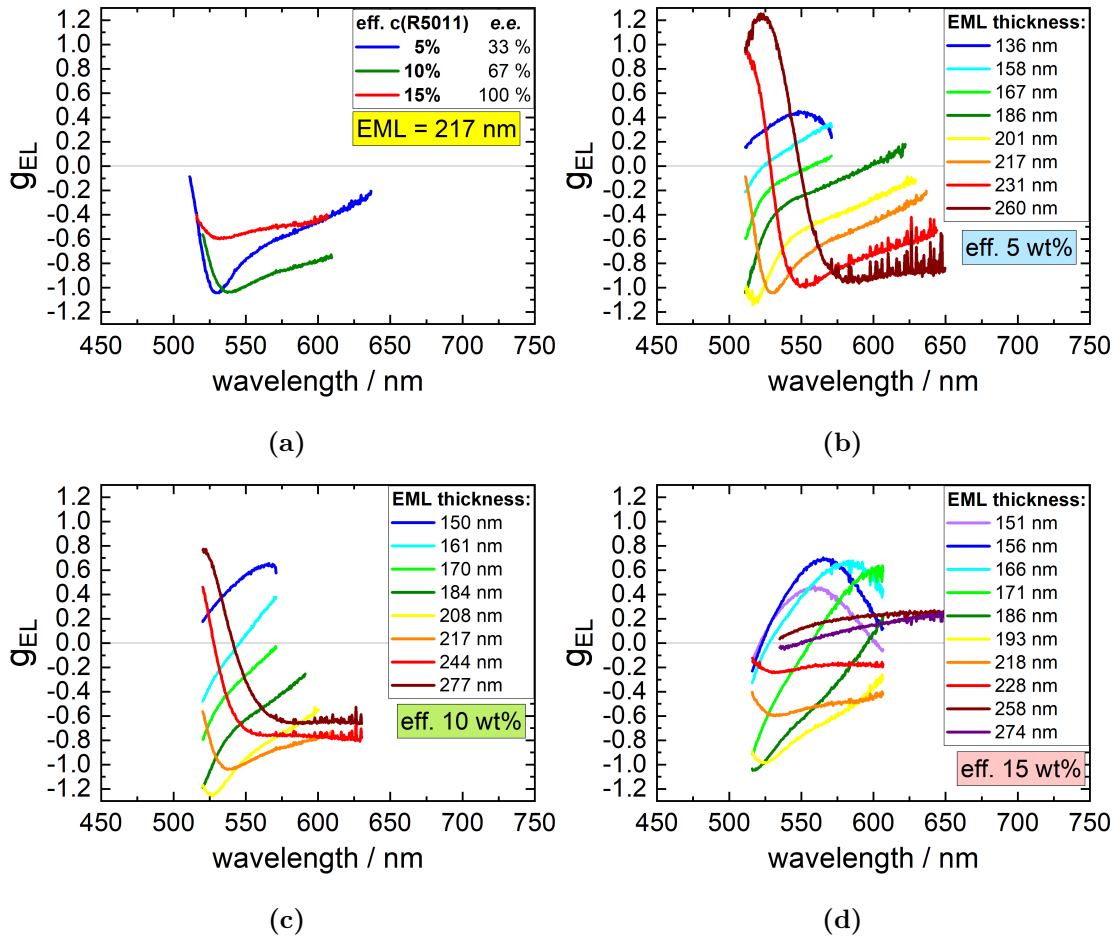


Fig. 3.89: g_{EL} curves of F8BT + R/S5011 based CP-OLEDs with a total chiral inducer concentration of 15 wt% and effective concentrations of 5 % (b), 10 % (c) and 15 % (d) R5011. (a) compares all three *c.e.s* at an EML thickness of 217 nm.

Device architecture: ITO / PEDOT (35 nm) / XQUPD (25 nm) / XOTPD (25 nm) / F8BT + 15 wt%R/S5011 / CsF/Al (cured 10 min@180 °C) M_w (F8BT) = 13 kg/mol.

3 Results and Discussion

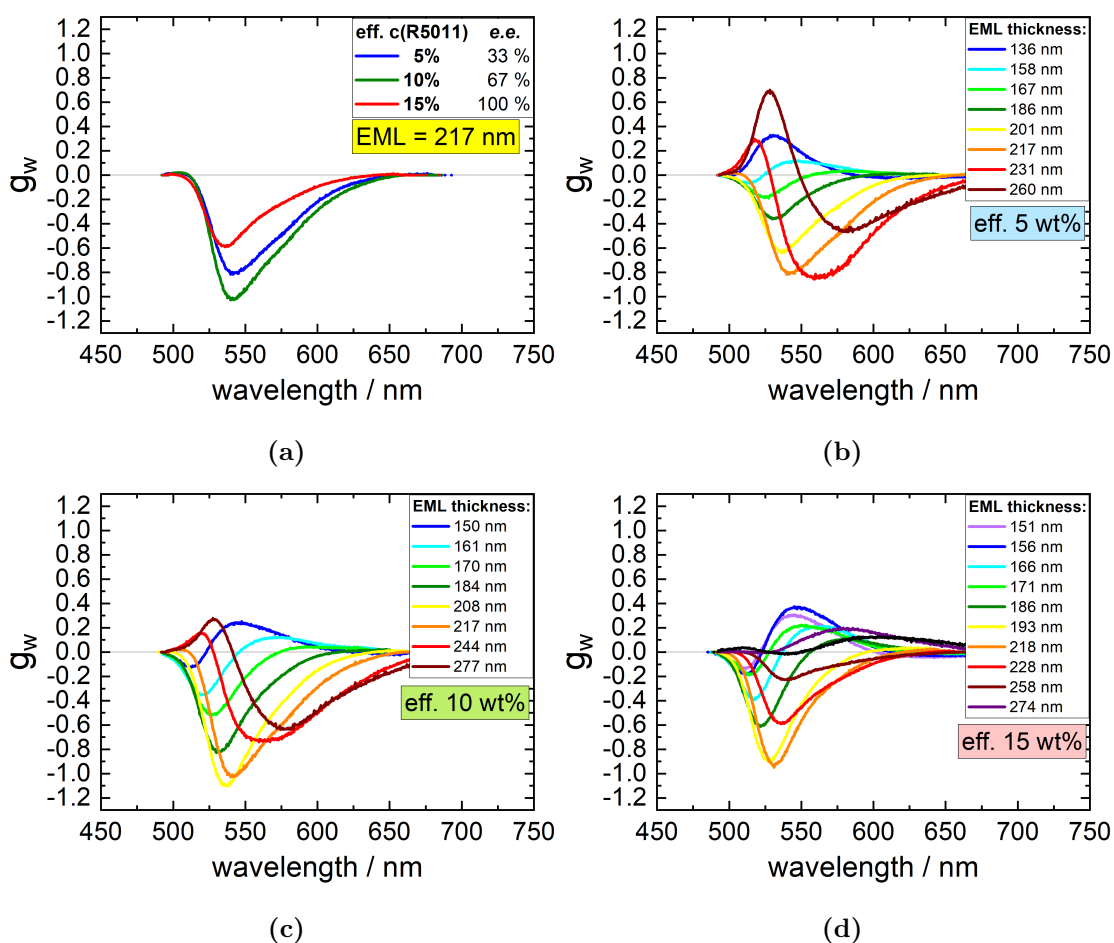


Fig. 3.90: G_w curves of F8BT + R/S5011 based CP-OLEDs with a total chiral inducer concentration of 15 wt% and effective concentrations of 5 % (b), 10 % (c) and 15 % (d) R5011. (a) compares all three $e.e.s$ at an EML thickness of 217 nm.

Device architecture: ITO / PEDOT (35 nm) / XQUPD (25 nm) / XOTPD (25 nm) / F8BT + 15 wt%R/S5011 / CsF/Al (cured 10 min@180 °C) M_w (F8BT) = 13 kg/mol.

Fig. 3.91 (a) shows CD^* values. Like previously mentioned, samples with larger layer thicknesses and CP-effects can contain unphysical CD values on the main signal peak at 490 nm. This is the case here as well. Therefore, the smaller signal peak at 349 nm is used for comparison here.

In accordance with previously shown results, CD^* increases for higher EML thicknesses. Also, analogous to fig. 3.83 (b), an increased effective R5011 concentration produces an overall larger CD effect. However, while a clear increase from 5 wt% to 10 wt% is found, there is almost no difference between the 10 wt% and 15 wt% data points. This could indicate a saturation effect, supporting previously shown results and common procedures from literature, that 10 wt% is the ideal chiral inducer concentration.

In (b), $g@maxEL$ is shown over EML thickness for the same devices. The general thickness dependency trend for all concentrations is comparable and in accordance with the results from chapter 3.10. However, differences between the three shown concentrations are found.

At lower EML thicknesses between 130 nm and 160 nm, a range with typically low g_{EL} values due to the g_{EL} sign flip, only very small differences are found between the three concentrations. But within the EML thickness region between 175 nm and 230 nm, which typically produces the largest achievable g_{EL} values, the maximum possible $g@maxEL$ shifts towards lower EML thicknesses with increasing R5011 concentration. Nonetheless, the overall largest $g@maxEL$ value is found for an effective concentration of 10 wt% R5011, with 5 wt% and 15 wt% falling slightly short. This supports the theory that with 10 wt% chiral inducer, an ideal chiral phase is formed. With lower concentrations, this phase cannot fully form, and higher concentrations seem to disturb this phase.

3 Results and Discussion

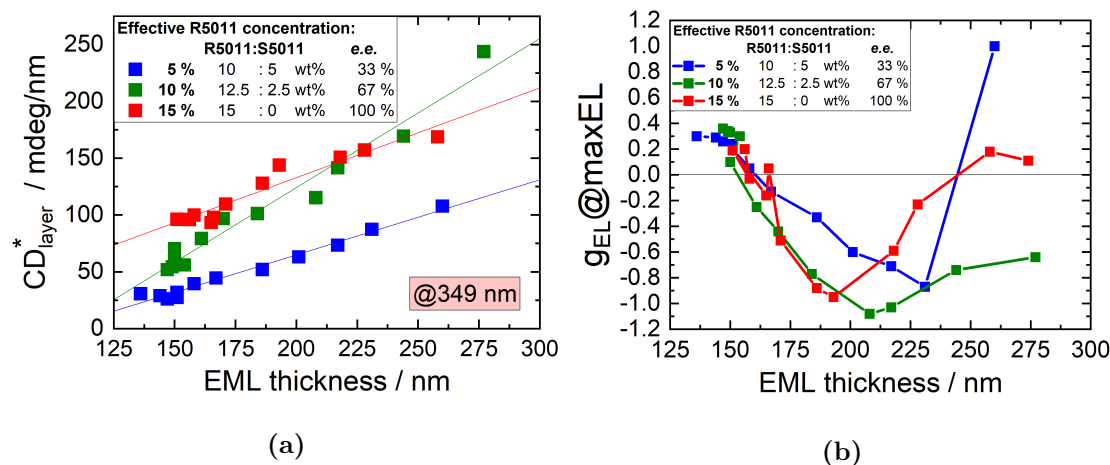


Fig. 3.91: CD* values at 349 nm (a) and $g_{\text{EL}}@_{\text{maxEL}}$ values (b) of F8BT + R/S5011 based CP-OLEDs with a total chiral inducer concentration of 15 wt% and effective concentrations of 5 % (blue), 10 % (green) and 15 % (red) R5011.

Device architecture: ITO / PEDOT (35 nm) / XQUPD (25 nm) / XOTPD (25 nm) / F8BT + 15 wt%R/S5011 / CsF/Al (cured 10 min@180 °C) M_w (F8BT) = 13 kg/mol.

Tab. 3.7: LIV performance details at 15 V, EL peaks and $g_{\text{EL}}@_{\text{maxEL}}$ values for three F8BT + 15 wt%R/S5011 based CP-OLEDs with different *e.e.*s, all with an EML thickness of 217 nm. Data is taken from fig. 3.87 to 3.90.

effective R5011 concentration	5 %	10 %	15 %
$e.e.$ / %	33	67	100
$J@15 \text{ V}$ / mA/cm ²	13.1	10.4	13.8
$L@15 \text{ V}$ / Cd/m ²	636	531	690
$\text{Eff}@15 \text{ V}$ / Cd/A	4.9	5.1	5.0
max. EL λ / nm	551	542	538
$g_{\text{EL}}@_{\text{maxEL}}$	-0.76	-1.03	-0.59

Even outside of one specific experiment set, devices with different effective chiral inducer concentrations can be compared. Fig. 3.92 with chiral inducer enantiomeric mixtures shows the same general trend as fig. 3.85 (d), which used absolute chiral inducer concentrations of one enantiomer only. The variations here can be explained by the device differences, specified in tab. 3.8. Individual experiment sets are indicated by different data point shapes. Variations between these experiments include total chiral inducer concentration, chiral inducer enantiomeric mixtures and F8BT molecular weight. Also, the shown devices have a slight EML thickness variation, a typical drawback in batch to batch comparison, which is difficult to avoid completely. However, based on the data shown in fig. 3.80 in chapter 3.10, the here shown EML range of 170 - 230 nm should result in g_{EL} values in the same range.

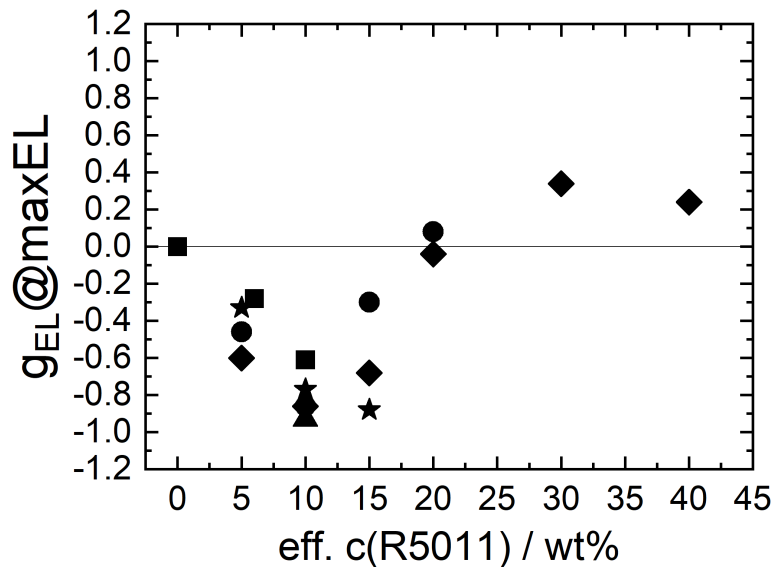


Fig. 3.92: $g_{EL}@maxEL$ values for CP-OLEDs with different effective R5011 concentrations. Different data point shapes indicate different experiment sets. Variations between these sets include total chiral inducer concentration, chiral inducer enantiomeric mixtures, F8BT molecular weight and EML thickness variation. Experimental conditions are listed in tab. 3.8.

Tab. 3.8: Experimental condition of the data shown in fig. 3.92.

data point	square	diamond	circle	triangle	star
F8BT batch	F8BT-21	F8BT-37	F8BT-21	F8BT-21	F8BT-13
curing t / min	15	10	15	15	15
curing T / °C	175	180	175	175	180
EML thickness / nm	163 - 170	188 - 229	195 - 197	186	184 - 186
total chiral ind. conc. / wt%	10	5 - 40	20	10	15
<u>e.e.</u> / %	0 - 100	100	25 - 100	100	33 - 100

4 Conclusion and perspectives

4.1 Summary and Conclusion

In this work, different aspects of CP-OLEDs were introduced.

In chapter 3.1, a **measurement set-up** and procedure for circularly polarised EL was introduced. Potential errors and artefacts were addressed and three different ways to evaluate and present CP-EL data, through g_{EL} curves, g_w curves and $g@maxEL$ values, were given. The possibilities and limitations of CD measurements and the thickness-normalised CD coefficient CD^* were demonstrated.

Basic aspects of the two used emitter classes, **PFs** and **F8BT**, were given in chapters 3.2 to 3.4.

Optical and phase behaviour of pristine and cured thin films from these polymers was highlighted.

Based on energetic aspects, a standard OLED stack architecture was chosen and optimised. On the example of F8BT, this included thickness variations of the EML, as well as different curing temperatures. LIV device performance and EL spectral shifts due to optical interference after reflection on the cathode were explained.

F8BT polymers with different molecular weights were compared, with a focus on the influence of different curing conditions.

As potential obstacles, layer thickness volume reduction, surface roughness and aggregation were analysed.

The influence of different curing times and temperatures on the absorption, PL and PLQY behaviour of various F8BT batches with different M_w s was studied.

CP-OLEDs based on three different strategies were presented:

1. **I-CPL emitters**
2. **one component systems**
3. **mixed systems**

In chapter 3.6, the two helicene based molecules **H1-Me₂** and **ThiahelalkBZT** were introduced. Both materials did not perform well as emitters, achieving a maximum device brightness too low to measure a potential I-CP-effect (strategy 1). Both materials did, however, perform well as non-emissive chiral inducers within an F8BT matrix, achieving $g_{\text{@maxEL}}$ values up to 0.42, which is shown in chapter 3.8.1 (strategy 3).

Different groups of **chirally functionalised PFs and F8BT** were analysed in chapter 3.7 (strategy 2).

The BINOL based co-polymer **P(BN-F8)**, while promising in solution, could not create a chiral phase in layer. All other polymers, however, achieved significant CP-effects. The best results, with maximum g_{EL} values on the first EL peak of up to 0.74 and -0.55, were found for **P(F8/c3)** and **P(F4/c2-F8)** based CP-OLEDs, respectively. Based on other results of this work, it is likely that, through optimisation of the device architecture, preparation conditions and polymer properties, these values could be significantly improved.

As representative example, **P(F4/c2-F8)** was analysed more thoroughly. The layer thickness dependence, molecular weight dependence, as well as curing temperature and time dependence of CD* was demonstrated. For **P(F4/c2-F8)** based CP-OLEDs, different EML thicknesses lead to a wave-like shift of g_{EL} values for all EL peaks.

With the same polymer, the potential benefit of cavity OLEDs was illustrated.

The effect of oxidation of the chirally functionalised polymer on absorption, PL, CD* and CPL behaviour was analysed on the example of **P(F6/c4-FN)**.

The influence of the position of the chiral centre on the handedness of the resulting CD and CPL was explained, introducing the odd-even-effect.

To analyse the effect of co-polymerisation with achiral units, **P(F8/c3)** was compared to **P(F8/c3-F8)**.

As an example for chirally functionalised F8BT, **P(F6/c4-BT)** was analysed, resulting in $g_{\text{@maxEL}}$ values up to -0.13. A comparison to **P(F6/c4-FN)** and **F8BT-13 + 10 wt%R5011** was made, which both share similarities with **P(F6/c4-BT)**. In conclusion, it was found that **P(F6/c4-BT)** produced a much smaller CP-effect than expected.

4 Conclusion and perspectives

In chapter 3.8, a mixed system (strategy 3) consisting of an **F8BT** matrix and the BINOL based additives **R5011** or **S5011** was introduced. The two chiral inducer enantiomers were shown to produce mirror image CD and g_{EL} curves.

It was shown that g_{EL} is independent of operating voltage for F8BT + R5011 based CP-OLEDs.

Analogous to neat F8BT thin films in chapter 3.4, chapter 3.9 analysed the influence of different curing temperatures and times on F8BT + R5011 mixed system thin films.

While, for the example of F8BT-37, neat thin film thicknesses remained constant up to 200 °C, volume reduction for the mixed system with 10 wt%R5011 already set in at 170 °C.

On the example of F8BT-21 and F8BT-37, it was confirmed that the ideal curing temperature and time is M_w dependent. Lower or higher curing temperatures, as well as shorter or longer curing times resulted in a reduced CP-effect.

In chapter 3.10, the impact of layer thickness variations of LIV performance and CP-effect of F8BT + 10 wt%R5011 based CP-OLEDs was analysed and interpreted based on optical reflection and interference effects.

Increasing the HTL thickness gradually reduced device performance due to increased resistance. However, $g@maxEL$ remained almost constant.

Changing the EML thickness resulted in a wave-like progress of $Eff@13 V$. Similar to neat F8BT OLEDs, the spectral shift of EL peaks revealed multiple optical modes, however, with different slopes. A strong EML thickness dependence of $g@maxEL$ was found, with the values varying not only in size, but even in sign.

Similarly, the addition and thickness increase of an ETL resulted in decreasing performance, as well as shifting EL spectra and $g@maxEL$ values.

In chapter 3.11, the F8BT molecular weight was shown to have a large influence on the maximum achievable CP-effect, with M_w s between 7 kg/mol and 21 kg/mol producing best results.

Additionally, the chiral inducer concentration was varied in chapter 3.12. On samples containing 5 - 40 wt% R5011 or S5011, the dependence of $g@maxEL$ on the chiral inducer concentration was illustrated. The largest CP-effects were achieved with a concentration of 10 wt%.

Since directly changing the concentration had some drawbacks, the feasibility of using enantiomeric mixtures instead was proven. It could be shown that with increasing effective chiral inducer concentration, the maximum possible $g@maxEL$ shifts towards lower EML thicknesses. However, 10 wt% chiral inducer remains the ideal concentration, achieving $g@maxEL$ values up to a modulus of -1.12 .

In conclusion, this work shows several successful approaches to create CP-OLEDs with great device performance and outstanding CP-effects. The most important factors influencing the outcoupled CPL are analysed, providing extensive guidance to optimise CP-OLED systems. The maximum $g@maxEL$ values up to 1.1 are reproducible and on level with the highest g_{EL} values reported for CP-OLEDs with good performance to this day. It is often unclear whether a published g_{EL} value is based on $g@maxEL$, or if the less meaningful but usually higher maximum g_{EL} value is given. This work might, therefore, even surpass these results.

4.2 Perspectives

While large g_{EL} values, as required for device applications, are easily measurable with the introduced optical CP-EL measurement set-up, it might still be valuable to **increase measurement sensitivity**, for example to study I-CPL emitter materials, or measure CP-OLEDs with lower brightness. This could be achieved by replacing the optical polariser components with a photoelastic modulator. The advantage of this method, in addition to its higher sensitivity, is the possibility to automate the measurement process. A significant drawback, however, is that it would no longer be possible to measure complete EL spectra, but only intensities at specific wavelengths. Measuring wavelength by wavelength might still be possible, but for quickly degrading devices, this would certainly result in errors. Unstable CP-OLEDs, which experience significant degradation within the time frame of the measurement, are in danger of producing incorrect g_{EL} values or measurement artefacts. With decreasing size of the g_{EL} value, those artefacts can even be larger than the CP-effect, making it hard to quantify.

Currently, there is no solution for the poor performance of **I-CPL emitters**. The requirements on the electric and magnetic transition dipole moments for large CP-effects and high luminance simply could not be brought in accordance so far. Intrinsic CPL is, however, still the most elegant concept and more attempts will surely be made in the future. It has already been shown that the combination of I-CPL and E-CPL components can lead to increased overall CP-effects [46]. It would, therefore, be of great value to continue the individual research of both concepts to be able to combine them in the most profitable way.

Chiral functionalisation of polymers, as shown in this work, resulted in great results. Compared to mixed systems, this approach, while more synthetically demanding, allows for a more stable chiral environment without the risk of phase separation between the polymer and the chiral inducer. It would be extremely valuable to continue the research on how different parameters influence the CP-effect. Interesting factors could be the length and branching of the chiral side chain, different ratios of chiral to achiral monomers and the position of the chiral

centre. Using different chiral functionalities or multiple chiral centres could also result in valuable insights. It should, however, not be disregarded that molecular weight is a significant factor for CPL, so the M_w of compared polymers from different groups should match as close as possible.

For **mixed systems**, it would be interesting to compare **different chiral inducers**. Since such molecules can vary significantly in size, it would be preferable to use molecular concentrations rather than the mass concentrations used in this work and most publications. To quickly test whether and how well a chiral molecule could function as chiral inducer, a parameter commonly used in the field of LCD technology could be used, called helical twisting power (HTP). It is usually measured in an LCD cell with a liquid crystalline matrix material. Using this established procedure would allow the comparison with other chiral inducer materials from literature. On the other hand, results found for this system might not be transferable to thin layers in CP-OLEDs. Establishing a comparable process with thin films of emissive polymers as matrix material might produce more realistic results. For example, it is possible to calculate the twisting angle of spring shaped nanowires from ellipsometry measurements. With the same process, it might be possible to calculate HTP values and directly compare them to CD or g_{EL} values of the same thin film or even CP-OLED. This process would allow extensive analysis of the same device, thereby reducing preparation effort and errors caused by batch to batch variations.

Apart from the here used emissive polymers PF and F8BT, many **other emitter polymers** could be tested. The most important requirement for these materials would be the existence of a liquid crystalline phase, ideally in a temperature range unharmed for other OLED materials. For ideal results, the correlation between molecular weight, phase behaviour and temperature would have to be studied for each new polymer, just as shown in this work. Through the great potential for customization of polymers, the CP-effect could be optimised for polymers with different emission colours. This way, the first step towards a CP-OLED display, possibly even a 3D display, could be made.

To better analyse CP-effects in all CP-OLEDs, it would be extremely beneficial to prevent optical interference within the device, and the resulting intensity and polarisation distribution of the outcoupled light. Light reflection on the cathode and the subsequent CPL handedness reversal has the largest influence on the EL spectral shape and polarisation state of the outcoupled light. Therefore, three strategies shall be introduced here to **suppress cathode reflection**:

The first strategy, using a **transparent cathode** instead of a reflective cathode, has already been attempted for CP-OLEDs. The working principle and examples from literature were introduced in chapter [2.6.5](#).

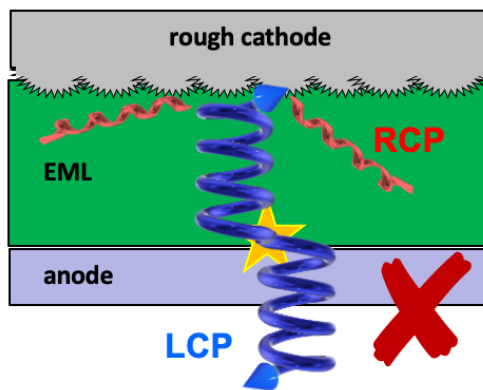


Fig. 4.1: Strategy 2: CP-OLED with rough cathode.

As second strategy, a **rough cathode** could be used. A typical evaporated cathode, following the surface of the underlying organic layer, is smooth and, therefore, highly reflective. Using a rough cathode, however, could lead to scattering rather than reflection, thereby outcoupling the unwanted light in backward direction to the sides rather than in forward direction. Interestingly, this approach has typically been researched for the opposite reason, namely to increase light outcoupling efficiencies in cavity OLEDs [\[114\]](#). It would, therefore, have to be adapted for this purpose and device architecture.

As third strategy, an additional **light absorbing layer** could be introduced into the device stack. This layer, ideally placed between the EML and cathode, would absorb all light in backward direction, and, therefore, remove it from the system. But changing a device stack so severely is always difficult. Even for highly absorbing materials, this absorbing layer would certainly have to be a few hundred nanometers thick, which would drastically influence the electrical properties of the device.

To maintain good CPL results, device efficiency should be influenced as little as possible by the new layer. Perovskites, due to their high conductivity and absorbance, might be an excellent material choice for this purpose.

Naturally, all three proposed strategies to suppress cathode reflection would result in reduced device efficiency in "normal" forward outcoupling geometry. Half of the generated light, the light produced in backward direction, would be removed and not be outcoupled in forward direction. While this process might not be suitable for eventual commercial device designs, it would be an immensely valuable step towards studying and understanding CP-OLEDs. The knowledge gained this way would benefit all types of CP-OLEDs, not just E-CPL systems.

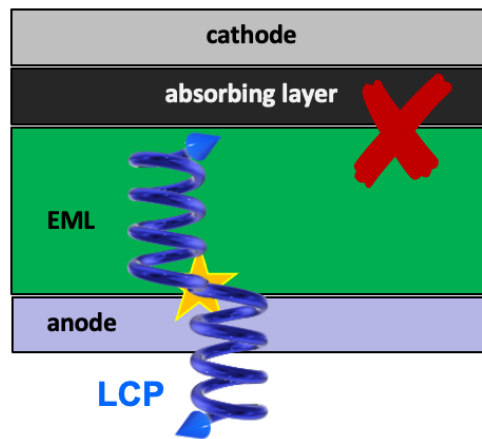


Fig. 4.2: Strategy 3: CP-OLED with an absorbing electron transport layer.

5 Experimental Section

5.1 General Procedures

5.1.1 Substrates

As substrates, float glass or ITO coated glass sheets were cut into 1 inch² sized squares. For device application, ITO substrates were structured via etching in a mixture of 5 M FeCl₃ and 6 M HCl solution with a ratio of 1:1. All substrates were washed before use. Washing was done successively in an ultrasonic bath with CHCl₃, acetone and 2 % Mucosal solution. Afterwards, the substrates were washed in a spin-rinse-dryer with deionized water. Immediately before spin-coating PE-DOT:PSS, the substrates were treated in an ozone chamber for 10 min, to remove organic residues and increase surface polarity.

5.1.2 Materials

All materials were either used pure or mixed with a matrix material. To avoid impurities, high grade materials like HPCL grade or at least 99% purity were used. Only dried organic solvents were used. Materials synthesised from collaboration partners were used as given.

5.1.3 Spin-coating of organic materials

Deposition of organic materials (e.g. HTM and EM) via spin-coating was performed in N₂ protective atmosphere (H₂O and O₂ < 1 ppm). If not otherwise stated, solutions were prepared in toluene. Other used organic solvents include chlorobenzene (CB), cyclopentanone (CPN), tetrahydrofuran (THF), chloroform (CHCl₃), dichloromethane (DCM), methanol (MeOH), or mixtures thereof. Solvent and concentration were chosen depending on spin-coating properties and desired layer thickness.

Typical spin-coating concentrations for were 10 - 30 mg/ml. Typical doping concentrations for small molecule emitters or chiral inducers were 2.5 - 40 wt% in

solution. Depending on the desired properties, spin-coater settings from 500 – 5000 rpm for 20 s were used, yielding EML thicknesses of 20 - 300 nm. Typical EML thicknesses for polymer-based OLEDs were 160 - 190 nm.

Spin-coating was used for single- or multi-layer samples on glass or ITO-substrates, as well as for layers in OLED devices.

5.1.4 PEDOT:PSS deposition

PEDOT:PSS deposition was performed in ambient atmosphere via spin-coating. The PEDOT:PSS solution was filtered through a 0.45 μm syringe filter and spin-coated at 4000 rpm for 30 s, resulting in an average layer thickness of 35 nm. The PEDOT:PSS layer was subsequently heated to 150 °C for 10 min to remove residual water. Afterwards, the samples were immediately transferred into N_2 protective atmosphere to avoid phase separation of PEDOT and PSS due to air humidity.

5.1.5 Cross-linking

Cross-linking of oxetane-functionalised HTM molecules QUPD and OTPD was performed through a CROP reaction with OPPI as photo-acid. HTMs were spin-coated from a 5 mg/ml solution with 2 mol% OPPI. Afterwards, the layers were illuminated with UV light (365 nm) for 15 s. Curing was performed at 110 °C for 90 s, followed by a dynamic rinsing step with 3 x 100 μl toluene. This process typically yielded solvent-resistant layers of around 25 nm thickness.

5.1.6 Alignment layer preparation

As alignment layer, the polyimide (PI) precursor Liquicoat[®] PI-kit ZLI-2650 from Merck was used. Solutions in CPN with concentrations of 11 - 30 mg/ml were spin-coated at 1000 - 4000 rpm for 20 s. Afterwards, the PI precursor layer was pre-annealed at 65 °C for 15 min to remove residual solvent and annealed at 210-350 °C for 30 - 60 min to imidize the material.

5 Experimental Section

After cooling, the layer was rubbed multiple times to create an alignment layer. Different kinds of materials were used as rubbing material, e.g. a woven microfibre cloth, a piece of velvet or a thick microfibre material with long and soft fibres, a polymer block or a carbon fibre brush.

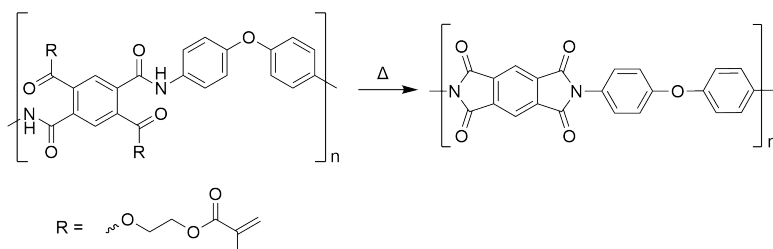


Fig. 5.1: Imidization reaction of the PI-precursor through thermal treatment.

Other materials tested for their usability as alignment layer were mixtures of PI with 30 - 70 wt% OTPD, PEDOT:PSS, XOTPD and graphene nano ribbons (GNR).

5.1.7 Vacuum deposition

Vacuum deposition of the metallic cathode was performed in an evaporation chamber. A 2 nm layer of CsF, followed by a 75 – 100 nm layer of Al were deposited. For devices with an electron transporting layer, TPBi was deposited via vacuum deposited in a *K.J.Lesker* spectroscopy evaporation chamber.

For cavity OLEDs, 30 nm Ag was evaporated on top of the ITO substrate to form a semitransparent mirror layer.

5.2 Analytical Methods

5.2.1 UV/Vis spectroscopy (UV/Vis)

UV/Vis absorption spectra were measured with a Cary 50 Bio spectrometer by *Varian* in transmission geometry. A zero and baseline correction were performed

before measurement. For linearly polarised absorption, a Lambda 1050 UV/VIS/NIR spectrometer from *PerkinElmer* was used with a rotating linear polariser.

5.2.2 Photoluminescence spectroscopy (PL)

Photoluminescence spectra were measured with a Cary Eclipse spectrometer by *Varian*. Measurements were performed in N₂ protective atmosphere with a fixed double-fiber at a 30° angle to sample surface. As excitation wavelength, fitting values depending on the absorption properties of the tested material were used.

5.2.3 Photoluminescence quantum yield (PLQY)

PLQY was measured with a C9920-02 absolute PL quantum yield measurement system by *Hamamatsu*. Measurements were performed in N₂ protective atmosphere with the same excitation wavelength as used in PL spectroscopy.

5.2.4 Profilometry

Layer thickness was measured with tactile profilometry using a Dektak XT profilometer by *Bruker*. To estimate the total layer thickness, the organic material was partially removed with a scalpel. A highly sensitive measurement tip was directed perpendicular over the scratch. This measurement was performed at three positions. The depth of each resulting valley was measured at three positions. An average value was calculated from those nine point measurements.

5.2.5 Ellipsometry

Ellipsometry measurements were performed on an M-2000XI ellipsometer with EC-400 controller and ESM-300 stage by *J.A.Woollam*. Measurements in reflection were performed with scotch tape on the back of the substrate to suppress backside

5 Experimental Section

reflections. All measurements in reflection were repeated at four angles ([VASE](#)). Measurements in transmission were performed in a substrate holder oriented at 90° in respect to the light beam. As measurement mode, either standard ellipsometers (SE) or Müller Matrix ellipsometry (MM) were used.

Evaluation of SE data was performed on the Complete EASE software by *J.A. Woollam*. For layer thickness measurements, the material was only fitted with a Cauchy in the transparent region. For optic material constants n and k , the fit was extended over the whole wavelength region with B-Spline and Gen-Osc functions. CD values were calculated from MM data with a Matlab script from [\[61\]](#). Samples with larger layer thicknesses of strongly absorbing materials, like in many OLED device stacks used here, can border on the absorption limit. In these samples, it might not be possible to calculate realistic CD values for the complete spectral range. Usually, the missing wavelength range occurs around the most intense CD peak. However, for materials with multiple CD peaks, it is possible to analyse a second, smaller peak instead of the incomplete, largest peak.

5.2.6 Electric characterization (LIV) and electroluminescence (EL) of OLEDs

Current-voltage-characteristics of OLEDs were measured with a 2004 source meter by *Keithley*. Measurements were performed in an Ar protective atmosphere. The brightness of the device was measured using an eye-corrected photodiode. All measurements were performed on 3 individual pixels. For this work, the turn-on voltage V_{on} was defined as the lowest driving voltage that produced a brightness of 1 Cd/m².

5.2.7 Electroluminescence (EL) and polarised electroluminescence

This measurement was performed subsequently to the LIV measurements. Electroluminescence of OLEDs was measured with a USB2000 fibre optic spectrometer

by *OCEAN OPTICS* and a M93L02 fibre patch cable \varnothing 1500 μm , 0.39 NA, 300 - 1200 nm (High OH) from *ThorLabs*. The device was operated with the same power source as LIV measurements, but on a custom built OLED-holder with xyz-stage. To achieve a collimated light beam, several lenses were used, e.g. an RMS4X Olympus Plan N 4x/0.10/ ∞ /-/FN22 achromatic objective and a A390TM-A mounted rochester spheric lens ($f = 4.6$, NA = 0.53, 350 - 700 nm), both from *ThorLabs*. The measured scope mode spectra were converted into relative irradiance, based on a calibration file for the whole set-up.

For polarised measurements, a linear polariser and an AQWP10M-580 1" achromatic quarter-wave plate (qwp) SM1-Threaded Mount, 350-850nm, both from *ThorLabs* with rotating mounts, were used. All rotation angles are defined from the point of view of the detector, with the 12 o'clock position as 0° . Whenever possible, devices were measured at approximately 100 Cd/m^2 to ensure sufficient brightness. To measure linear polarisation, only the linear polariser was placed in the path of the collimated light beam and rotated between measurements. To measure circular polarisation, the qwp was inserted between the linear polariser and device. The linear polariser was set in 90° orientation and the qwp was set in $+45^\circ$ position for LCPL and -45° for RCPL. Each polarisation was measured four times. To avoid artefacts due to device degradation, measurement sequence was L-R-R-L-L-R-R-L.

5.2.8 Microscopy

Microscopy pictures were prepared digitally with an Axio Scope.A1 microscope from *Zeiss*. Samples were illuminated with a backlight and analysed at different magnifications, depending on the structure.

5.2.9 Differential scanning calorimetric (DSC)

DSC measurements were performed on a DSC821e calorimeter from *Mettler Toledo*. Sample sizes were 3 - 10 mg material in ME-27331 40 μl Al-crucibles. A small hole was pinned into the closed crucibles to avoid pressure built up. Samples were

5 *Experimental Section*

measured with a heating rate of 10 °C/min (slow) or 30 °C/min (fast). All shown measurements are second or later measurements.

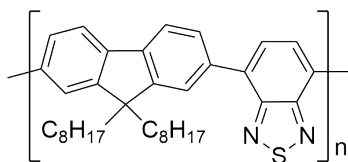
5.2.10 Gel permeation chromatography (GPC)

Molar mass distribution of several polymers were measured by Sylwia Adamczyk in the working group of Prof. Scherf, Bergische Universität Wuppertal. As solvent, CHCl₃ was used.

6 Appendix

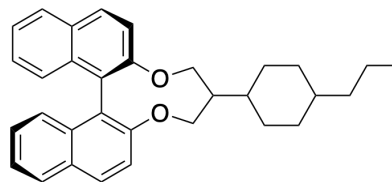
6.1 Materials

Chemicals were, if not otherwise stated, used as purchased or provided.



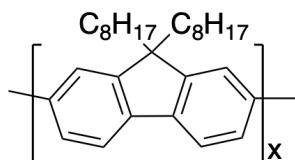
F8BT

poly(dioctylfluorene-co-benzothiadiazole)



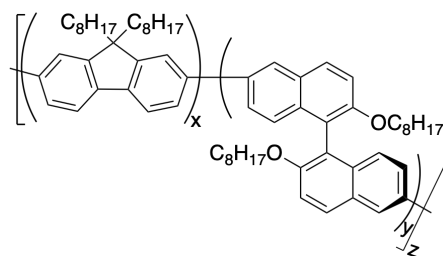
R5011

(13bR)-5,6-Dihydro-5-(trans-4-propylcyclohexyl)-4H-dinaphtho[2,1-f:1',2'-h][1,5]dioxin



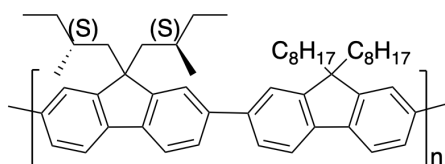
PFO or P(F8)

poly(dioctylfluorene)



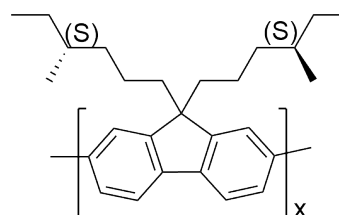
P(R-BN-F8)

poly(dioctylfluorene-co-6,6'-(2,2'-dioctyloxy-1,1'-binaphthalene))



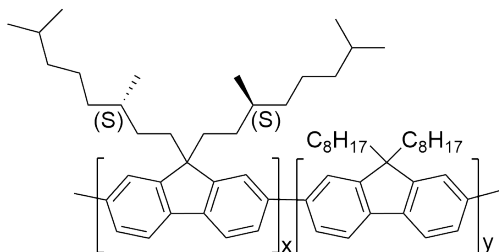
P(S-F4/c2-F8)

poly(dioctyl-co-di((2S)-methylbutylfluorene))



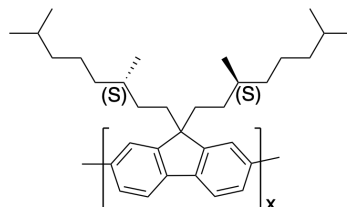
P(S-PF6/c4)

poly(di((4S)-hexylfluorene))



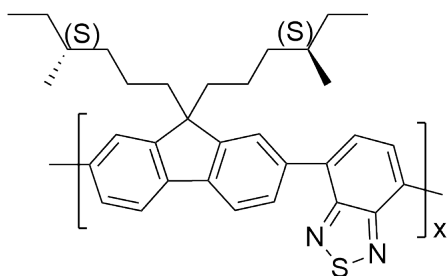
P(*S*-F8/c3-F8)

poly(dioctyl-co-di((3*S*),7-dimethyloctylfluorene))



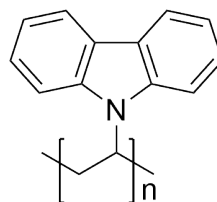
P(*S*-F8/c3)

poly(di((3*S*),7-dimethyloctylfluorene))



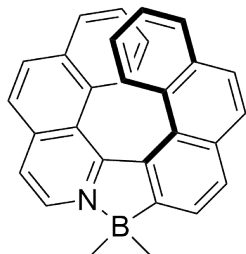
P(*S*-F6/c4-BT)

poly(di((4*S*)-methylhexylfluorene)-co-benzothiadiazole)

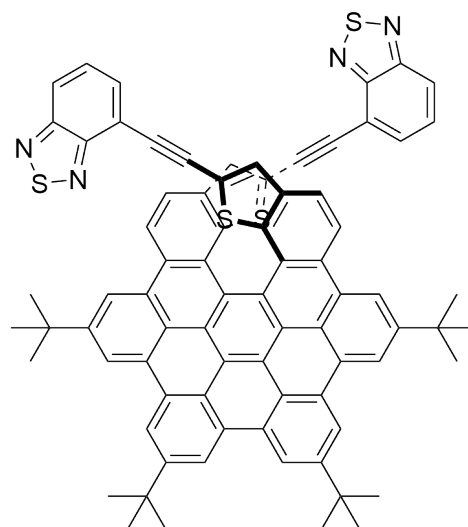


PVK

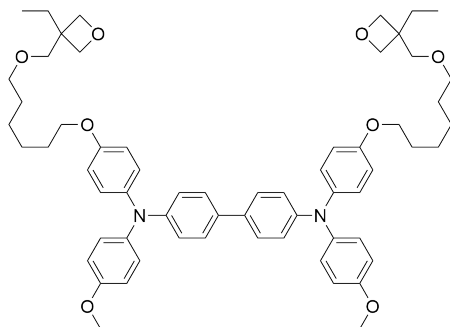
poly(9-vinylcarbazole)

**H1-Me2**

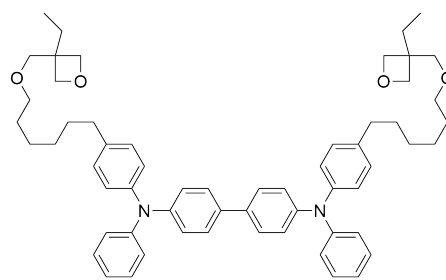
16,16-dimethyl-15lambda4-aza-16lambda4-boraheptacyclo[15.12.0.0^{2,15}.0^{3,12}.0^{4,9}.0^{20,29}.0^{23,28}]nonacosa-1(17),2(15),3(12),4(9),5,7,10,13,18,20(29),21,23(28),24,26-tetradecaene

**Thiahelalk-BZT**

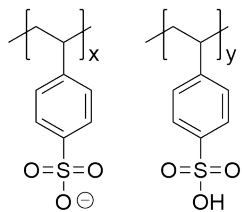
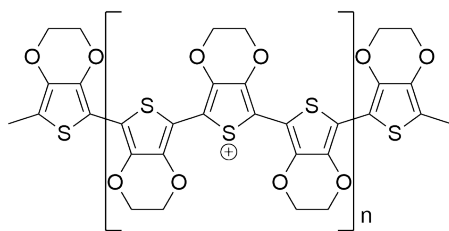
4-(2-28-[2-(2,1,3-benzothiadiazol-4-yl)dddd ethynyl]-6,11,20,45-tetra-tert-butyl-29 lambda3,36-dithiatetradecacyclo[31.15.0.0^{2,15}.0^{3,8}.0^{4,47}.0^{9,14}.0^{13,18}.0^{16,32}.0^{17,22}.0^{23,31}.0^{26,30}.0^{34,42}.0^{35,39}.0^{43,48}]octatetraconta-1,3,5,7,9,11,13,15,17(22),18,20,23(31),24,26(30),28,32,34(42),35(39),37,40,43(48),44,46-tricosaen-37-ylethynyl)-2,1,3-benzothiadiazole

**QUPD**

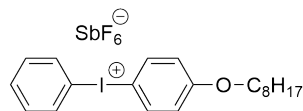
N4,N4'-bis(4-(6-((3-ethyloxetan-3-yl)methoxy)hexyloxy)phenyl)-N4,N4'-bis(4-methoxyphenyl)biphenyl-4,4'-diamine

**OTPD**

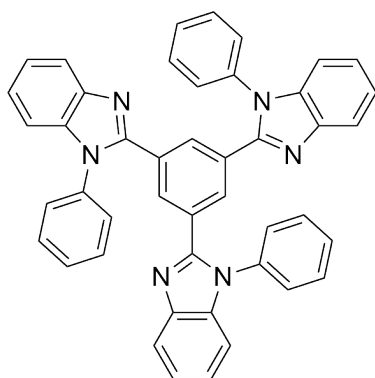
N,N-bis(4-(6-((3-ethyloxetane-3-yl)methoxy)-hexylphenyl))-N,N'-biphenyl-4,4'-diamine

**PEDOT:PSS**

poly(3,4-ethylene dioxythiophene) doped
with poly(styrene sulfonate)

**OPPI**

(4-octyloxyphenyl) phenyliodonium
hexafluoroantimonate

**TPBi**

2,2',2''-(1,3,5-benzinetriyl)-tris(1-
phenyl-1-H-benzimidazole)

Tab. 6.1: Polymeric emitter materials: F8BT.

Material	M_w / g/mol	M_n / g/mol	PDI	Purchased from or synthesised by
F8BT-2 (Lot# SR218)	1,920	1,103	1.74	Stephanie R�uth, AK Meerholz
F8BT-3 (Lot# X131025)	2,590	1,880	1.38	1 Material, Canada
F8BT-7 (Lot# SR222)	6,850	2,403	2.85	Stephanie R�uth, AK Meerholz
F8BT-13 (Lot# SX10074C85)	12,600	7,000	1.8	1Material, Canada
F8BT-21 (Lot# YY7082CH)	21,100	12,500	1.68	1 Material, Canada
F8BT-24 (Lot# JS254)	24,400	9,138	2.67	Dr. J�rgen Schelter, AK Meerholz
F8BT-28 (Lot# SX10138C85)	28,000	14,000	2	1Material, Canada
F8BT-37 (Lot# YY6208TH)	36,800	17,300	2.13	1Material, Canada
F8BT-39 (Lot# YY22088TH)	38,863	17,400	2.23	1Material, Canada
F8BT-54 (Lot# YY16136TH)	53,700	28,400	1.89	1Material, Canada
F8BT-122 (Lot# SR237)	122,000	13,260	9.20	Stephanie R�uth, AK Meerholz

Tab. 6.2: Polymeric emitter materials: PFs.

Material	M_w / g/mol	M_n / g/mol	PDI	Purchased from or synthesised by
PFO (Lot# mf1-p200)	270,000	99,400	2.17	AK Scherf
PFO (Lot# YY7162P)	32,326	14,716	2.19	1Material, Canada
P(R-BN-F8) (Lot# mctj04r1)	180,000	90,400	2.0	AK Scherf
P(S-BN-F8) (Lot# mctj04r3)	193,000	92,800	2.1	AK Scherf
P(F4/c2-F8) (Lot# HNA 93)	247,000	116,000	2.13	Heinz-Georg Nothofer, AK Scherf
P(F4/c2-F8) (Lot# CBCP2)	172,000	91,700	1.88	Christin Barron, AK Scherf
P(F6/c4-FN) (Lot# CBHP3)	81,800	50,800	1.61	Christin Barron, AK Scherf
P(F8/c3) (Lot# CBPF08602)	130,000	69,700	1.86	Christin Barron, AK Scherf
P(F8/c3-F8) (Lot# CBCP4)	101,000	59,000	1.71	Christin Barron, AK Scherf
P(F6/c4-BT) (Lot# CBCP3-BT)	12,300	8,500	1.45	Christin Barron, AK Scherf

Tab. 6.3: Other materials used.

Material	purity	Purchased from or synthesised by
QUPD	n.a.	Stephanie R�uth and Anne Bergen, AK Meerholz
OTPD	n.a.	Stephanie R�uth and Anne Bergen, AK Meerholz
OPPI	n.a.	ABCR GmbH
PEDOT:PSS (Lot# 9001853423)	n.a.	Clevios
PVK (25 - 50k av. M_w)	n.a.	Aldrich
R5011	99.9%	Daken Chemical Limited, China
S5011	99.9%	Daken Chemical Limited, China
CsF	99.99%	Puratronic
Al	99%, 2.38 metal spheres	n.a.

Tab. 6.4: Solvents used.

Solvent	purity	Purchased from
Toluene	SeccoSolv dried 99.9%	Merck
THF	99.5%, extra dry	ACROS
CHCl ₃	99.9%, extra dry over mol. sieve, stabilised	ACROS
CH ₂ Cl ₂ (DCM)	99.8%, extra dry over mol. sieve, stabilised	ACROS
Cyclopentanone (CPN)	≥99.0% (GC)	Fluka
Methanol (MeOH)	99.8%, extra dry over mol. sieve	ACROS
Chlorobenzene (CB)	HPLC-grade 99.9%	Sigma Aldrich

Bibliography

- [1] Tang, C. W.; VanSlyke, S. A. Organic electroluminescent diodes. *Appl. Phys. Lett.* **1987**, *51*, 913–915.
- [2] Dyreklev, P.; Berggren, M.; Inganäs, O.; Andersson, M. R.; Wennerström, O.; Hjertberg, T. Polarized electroluminescence from an oriented substituted polythiophene in a light emitting diode. *Adv. Mater.* **1995**, *7*, 43–45.
- [3] Peeters, E.; Christiaans, M. P. T.; Janssen, R. A. J.; Schoo, H. F. M.; Dekkers, H. P. J. M.; Meijer, E. W. Circularly Polarized Electroluminescence from a Polymer Light-Emitting Diode. *J. Am. Chem. Soc.* **1997**, *119*, 9909–9910.
- [4] Lee, D. M.; Song, J. W.; Lee, Y. J.; Yu, C. J.; Kim, J. H. Control of Circularly Polarized Electroluminescence in Induced Twist Structure of Conjugate Polymer. *Adv. Mater.* **2017**, *29*, 1700907.
- [5] Guenes, S.; Neugebauer, H.; Sariciftci, N. S. Conjugated polymer-based organic solar cells. *Chem. Rev.* **2007**, *107*, 1324–1338.
- [6] Jaffe, H. H.; Miller, A. L. The fates of electronic excitation energy. *J. Chem. Educ.* **1966**, *43*, 469.
- [7] Hertel, D.; Müller, C. D.; Meerholz, K. Bilderzeugung: Organische Leuchtdioden. *Chem. Unserer Zeit* **2005**, *39*, 336–347.
- [8] Atkins, P.; de Paula, J. *Physical Chemistry*, 9th ed.; Oxford University Press, 2010.
- [9] Baldo, M. A.; Thompson, M. E.; Forrest, S. R. High-efficiency fluorescent organic light-emitting devices using a phosphorescent sensitizer. *Nature* **2000**, *403*, 750–753.

Bibliography

- [10] Uoyama, H.; Goushi, K.; Shizu, K.; Nomura, H.; Adachi, C. Highly efficient organic light-emitting diodes from delayed fluorescence. *Nature* **2012**, *492*, 234–238.
- [11] Hirai, H.; Nakajima, K.; Nakatsuka, S.; Shiren, K.; Ni, J.; Nomura, S.; Ikuta, T.; Hatakeyama, T. One-Step Borylation of 1,3-Diaryloxybenzenes Towards Efficient Materials for Organic Light-Emitting Diodes. *Angew. Chem. Int. Ed.* **2015**, *54*, 13581–13585.
- [12] Frédéric, L.; Desmarchelier, A.; Favereau, L.; Pieters, G. Designs and Applications of Circularly Polarized Thermally Activated Delayed Fluorescence Molecules. *Adv. Funct. Mater.* **2021**, *31*, 2010281.
- [13] Zacharias, P.; Gather, M. C.; Rojahn, M.; Nuyken, O.; Meerholz, K. New crosslinkable hole conductors for blue-phosphorescent organic light-emitting diodes. *Angew. Chem. Int. Ed.* **2007**, *46*, 4388–4392.
- [14] Deußen, M.; Bäessler, H. Organische Leuchtdioden. *Chem. Unserer Zeit* **1997**, *2*, 76–86.
- [15] Purandare, S.; Gomez, E. F.; Steckl, A. J. High brightness phosphorescent organic light emitting diodes on transparent and flexible cellulose films. *Nanotechnol.* **2014**, *25*, 094012.
- [16] Zhang, M.; Höfle, S.; Czolk, J.; Mertens, A.; Colsmann, A. All-solution processed transparent organic light emitting diodes. *Nanoscale* **2015**, *7*, 20009–20014.
- [17] www.transparent-oled.de, accessed on 26.08.2022.
- [18] <https://oledera.samsungdisplay.com/eng/flex-oled>, accessed on 26.08.2022.
- [19] Bäessler, H.; Köhler, A. *Chapter: Charge Transport in Organic Semiconductors*, In: Metzger, R. (eds) *Unimolecular and Supramolecular Electronics I*; Springer-Verlag, Berlin, Heidelberg, 2011; Vol. 312.
- [20] Frohne, H.; Müller, D. C.; Meerholz, K. Continuously Variable Hole Injection in Organic Light Emitting Diodes. *ChemPhysChem* **2002**, *3*, 707–711.

- [21] Bäessler, H. Charge Transport in Disordered Organic Photoconductors. *Phys. Status Solidi (B)* **1993**, *175*, 15–56.
- [22] Friend, R. H.; Gymer, R. W.; Holmes, A. B.; Burroughes, J. H.; Marks, R. N.; Taliani, C.; Bradley, D. D.; Dos Santos, D. A.; Brédas, J. L.; Lögdlund, M.; Salaneck, W. R. Electroluminescence in conjugated polymers. *Nature* **1999**, *397*, 121–128.
- [23] Lower, S. K.; El-Sayed, M. A. The triplet state and molecular electronic processes in organic molecules. *Chem. Rev.* **1966**, *66*, 199–241.
- [24] VanSlyke, S. A.; Tang, C. W.; Roberts, L. C. Electroluminescent device with organic luminescent medium, US Patent US4720432A, 1987.
- [25] Van Slyke, S. A.; Chen, C. H.; Tang, C. W. Organic electroluminescent devices with improved stability. *Appl. Phys. Lett.* **1996**, *69*, 2160–2162.
- [26] Wong, M. Y.; Zysman-Colman, E. Purely Organic Thermally Activated Delayed Fluorescence Materials for Organic Light-Emitting Diodes. *Adv. Mater.* **2017**, *29*, 1605444.
- [27] Romanovskii, Y.; Bäessler, H. Phosphorescence from a ladder-type conjugated polymer in solid solutions at low temperature. *Chem. Phys. Lett.* **2000**, *326*, 51–57.
- [28] Hong, G.; Gan, X.; Leonhardt, C.; Zhang, Z.; Seibert, J.; Busch, J. M.; Bräse, S. A Brief History of OLEDs—Emitter Development and Industry Milestones. *Adv. Mater.* **2021**, *33*, 2005630.
- [29] Zhang, Q.; Li, B.; Huang, S.; Nomura, H.; Tanaka, H.; Adachi, C. Efficient blue organic light-emitting diodes employing thermally activated delayed fluorescence. *Nat. Photonics* **2014**, *8*, 326–332.
- [30] Chen, X. L.; Jia, J. H.; Yu, R.; Liao, J. Z.; Yang, M. X.; Lu, C. Z. Combining Charge-Transfer Pathways to Achieve Unique Thermally Activated Delayed Fluorescence Emitters for High-Performance Solution-Processed, Non-doped Blue OLEDs. *Angew. Chem. Int. Ed.* **2017**, *56*, 15006–15009.

Bibliography

- [31] Nakanotani, H.; Higuchi, T.; Furukawa, T.; Masui, K.; Morimoto, K.; Numata, M.; Tanaka, H.; Sagara, Y.; Yasuda, T.; Adachi, C. High-efficiency organic light-emitting diodes with fluorescent emitters. *Nat. Commun.* **2014**, *5*, 4016.
- [32] Lee, K. H.; Lee, J. Y. High External Quantum Efficiency in Fluorescent OLED by Cascade Singlet Harvesting Mechanism. *Adv. Optical Mater.* **2020**, *8*, 2000328.
- [33] Bayerl, M. S.; Braig, T.; Nuyken, O.; Müller, D. C.; Groß, M.; Meerholz, K.; Mu, D. C. Crosslinkable hole-transport materials for preparation of multi-layer organic light emitting devices by spin-coating. *Macromol. Rapid Commun.* **1999**, *20*, 224–228.
- [34] Köhnen, A.; Riegel, N.; Müller, D. C.; Meerholz, K. Surface-initiated phase separation-fabrication of two-layer organic light-emitting devices in a single processing step. *Adv. Mater.* **2011**, *23*, 4301–4305.
- [35] Köhnen, A.; Riegel, N.; Kremer, J. H.; Lademann, H.; Müller, D. C.; Meerholz, K. The simple way to solution-processed multilayer OLEDs - Layered block-copolymer networks by living cationic polymerization. *Adv. Mater.* **2009**, *21*, 879–884.
- [36] Feser, S.; Meerholz, K. Investigation of the photocross-linking mechanism in oxetane-functionalized semiconductors. *Chem. Mater.* **2011**, *23*, 5001–5005.
- [37] Tieke, B. *Makromolekulare Chemie: eine Einführung*, 3rd ed.; Wiley-VCH: Weinheim.
- [38] Yang, S. H.; Hsu, C. S. Liquid crystalline conjugated polymers and their applications in organic electronics. *J. Polym. Sci. A* **2009**, *47*, 2713–2733.
- [39] Misaki, M.; Chikamatsu, M.; Yoshida, Y.; Azumi, R.; Tanigaki, N.; Yase, K.; Nagamatsu, S.; Ueda, Y. Highly efficient polarized polymer light-emitting diodes utilizing oriented films of β -phase poly(9,9-dioctylfluorene). *Appl. Phys. Lett.* **2008**, *93*, 023304.

- [40] Wilhelm, P.; Blank, D.; Lupton, J. M.; Vogelsang, J. Control of Intrachain Morphology in the Formation of Polyfluorene Aggregates on the Single-Molecule Level. *ChemPhysChem* **2020**, *21*, 961–965.
- [41] Zhang, Q.; Chi, L.; Hai, G.; Fang, Y.; Li, X.; Xia, R.; Huang, W.; Gu, E. An Easy Approach to Control Beta-Phase Formation in PFO Films for Optimized Emission Properties. *Molecules* **2017**, *22*.
- [42] Rabe, T.; Hoping, M.; Schneider, D.; Becker, E.; Johannes, H. H.; Kowalsky, W.; Weimann, T.; Wang, J.; Hinze, P.; Nehls, B. S.; Scherf, U.; Farrell, T.; Riedl, T. Threshold reduction in polymer lasers based on poly(9,9-dioctylfluorene) with statistical binaphthyl units. *Adv. Funct. Mater.* **2005**, *15*, 1188–1192.
- [43] Seideman, T. The liquid-crystalline blue phases. *Rep. Prog. Phys.* **1990**, *53*, 659–705.
- [44] Wright, D. C.; Mermin, N. D. Crystalline liquids: The blue phases. *Rev. Mod. Phys.* **1989**, *61*, 385–432.
- [45] Greenfield, J. L.; Wade, J.; Brandt, J. R.; Shi, X.; Penfold, T. J.; Fuchter, M. J. Pathways to increase the dissymmetry in the interaction of chiral light and chiral molecules. *Chem. Sci.* **2021**, *12*, 8589–8602.
- [46] Wade, J.; Brandt, J. R.; Reger, D.; Zinna, F.; Amsharov, K. Y.; Jux, N.; Andrews, D. L.; Fuchter, M. J. 500-Fold Amplification of Small Molecule Circularly Polarised Luminescence through Circularly Polarised FRET. *Angew. Chem. Int. Ed.* **2021**, *60*, 222–227.
- [47] Lakhwani, G.; Meskers, S. C. Insights from chiral polyfluorene on the unification of molecular exciton and cholesteric liquid crystal theories for chiroptical phenomena. *J. Phys. Chem. A* **2012**, *116*, 1121–1128.
- [48] Donley, C. L.; Zaumseil, J.; Andreasen, J. W.; Nielsen, M. M.; Sirringhaus, H.; Friend, R. H.; Kim, J. S. Effects of packing structure on the optoelectronic and charge transport properties in poly(9,9-di-n-octylfluorene-alt-benzothiadiazole). *J. Am. Chem. Soc.* **2005**, *127*, 12890–12899.

Bibliography

- [49] Morgado, J.; Friend, R. H.; Cacialli, F. Improved efficiency of light-emitting diodes based on polyfluorene blends upon insertion of a poly(p-phenylene vinylene) electron-confinement layer. *Appl. Phys. Lett.* **2002**, *80*, 2436–2438.
- [50] Wang, B.; Ye, H.; Riede, M.; Bradley, D. D. Chain conformation control of fluorene-benzothiadiazole copolymer light-emitting diode efficiency and lifetime. *ACS Applied Materials and Interfaces* **2021**, *13*, 2919–2931.
- [51] Jones, R. C. A New Calculus for the Treatment of Optical Systems I Description and Discussion of the Calculus. *J. Opt. Soc. Am.* **1941**, *31*, 488–503.
- [52] Berova, N.; Bari, L. D.; Pescitelli, G. Application of electronic circular dichroism in configurational and conformational analysis of organic compounds. *Chem. Soc. Rev.* **2007**, *36*, 914–931.
- [53] Hecht, E. *Optik*, 2nd ed.; Addison Wesley: Berlin, 1992.
- [54] Yan, Z. P.; Luo, X. F.; Liu, W. Q.; Wu, Z. G.; Liang, X.; Liao, K.; Wang, Y.; Zheng, Y. X.; Zhou, L.; Zuo, J. L.; Pan, Y.; Zhang, H. Configurationally Stable Platinahelicene Enantiomers for Efficient Circularly Polarized Phosphorescent Organic Light-Emitting Diodes. *Chem. Eur. J.* **2019**, *25*, 5672–5676.
- [55] Zhang, H.; Ma, L.; Zhang, Q.; Shi, Y.; Fang, Y.; Xia, R.; Hu, W.; Bradley, D. D. C. Azobenzene Sulphonic Dye Photoalignment as a Means to Fabricate Liquid Crystalline Conjugated Polymer Chain-Orientation-Based Optical Structures. *Advanced Optical Materials* **2020**, *8*, 1901958.
- [56] Dahal, E.; Allemeier, D.; Isenhardt, B.; Cianciulli, K.; White, M. S. Characterization of higher harmonic modes in Fabry–Pérot microcavity organic light emitting diodes. *Sci. Rep.* **2021**, *11*, 8456.
- [57] Bannwarth, H.; Kremer, B. P.; Schulz, A. *Basiswissen Physik, Chemie und Biochemie*; Springer: Berlin, Heidelberg, 2007.
- [58] Mendoza-Galván, A.; Muñoz-Pineda, E.; Ribeiro, S. J. L.; Santos, M. V.; Järrendahl, K.; Arwin, H. Mueller matrix spectroscopic ellipsometry study of chiral nanocrystalline cellulose films. *J. Opt.* **2018**, *20*, 024001.

- [59] Schaefer, B.; Collett, E.; Smyth, R.; Barrett, D.; Fraher, B. Measuring the Stokes polarization parameters. *Am. J. Phys.* **2007**, *75*, 163–168.
- [60] Hilfiker, J. N.; Hale, J. S.; Herzinger, C. M.; Tiwald, T.; Hong, N.; Schöche, S.; Arwin, H. Estimating Depolarization with the Jones Matrix Quality Factor. *Appl. Surf. Sci.* **2017**, *421*, 494–499.
- [61] Schulz, M.; Zablocki, J.; Abdullaeva, O. S.; Brück, S.; Balzer, F.; Lützen, A.; Arteaga, O.; Schiek, M. Giant intrinsic circular dichroism of prolinol-derived squaraine thin films. *Nat. Commun.* **2018**, *9*, 2413.
- [62] Anslyn, E. V.; Dougherty, D. A. *Modern Physical Organic Chemistry*; University Science Books, 2006.
- [63] Banach, M. J.; Friend, R. H.; Siringhaus, H. Influence of the Casting Solvent on the Thermotropic Alignment of Thin Liquid Crystalline Polyfluorene Copolymer Films. *Macromol.* **2004**, *37*, 6079–6085.
- [64] Grell, M.; Knoll, W.; Lupo, D.; Meisel, A.; Miteva, T.; Neher, D.; Nothofer, H. G.; Scherf, U.; Yasuda, A. Blue polarized electroluminescence from a liquid crystalline polyfluorene. *Adv. Funct. Mater.* **1999**, *11*, 671–675.
- [65] Jo, S. I.; Kim, Y.; Baek, J.-H.; Yu, C.-J.; Kim, J.-H. Highly polarized emission of the liquid crystalline conjugated polymer by controlling the surface anchoring energy. *Jap. J. Appl. Phys.* **2014**, *53*, 03CD04.
- [66] Zhu, J.; Wang, J.; Lu, H.; Qiu, L. Solution-processed polarized light-emitting diodes. *J. Mater. Chem. C* **2020**, *8*, 9147–9162.
- [67] Sainova, D.; Zen, A.; Nothofer, H.-G.; Asawapirom, U.; Scherf, U.; Hagen, R.; Bieringer, T.; Kostromine, S.; Neher, D. Photoaddressable Alignment Layers for Fluorescent Polymers in Polarized Electroluminescence Devices. *Adv. Funct. Mater.* **2002**, *12*, 49.
- [68] Choi, G. J.; Van Le, Q.; Choi, K. S.; Kwon, K. C.; Jang, H. W.; Gwag, J. S.; Kim, S. Y. Polarized Light-Emitting Diodes Based on Patterned MoS₂ Nanosheet Hole Transport Layer. *Adv. Mater.* **2017**, *29*, 1702598.

Bibliography

- [69] Ward, M. D.; Wade, J.; Shi, X.; Nelson, J.; Campbell, A. J.; Fuchter, M. J. Highly Selective High-Speed Circularly Polarized Photodiodes Based on π -Conjugated Polymers. *Adv. Optical Mater.* **2022**, *10*, 2101044.
- [70] Wan, L.; Wade, J.; Salerno, F.; Arteaga, O.; Laidlaw, B.; Wang, X.; Penfold, T.; Fuchter, M. J.; Campbell, A. J. Inverting the Handedness of Circularly Polarized Luminescence from Light Emitting Polymers Using Film Thickness. *ACS Nano* **2019**, *13*, 8099–8105.
- [71] dos Santos, J. M.; Sun, D.; Moreno-Naranjo, J. M.; Hall, D.; Zinna, F.; Ryan, S. T. J.; Shi, W.; Matulaitis, T.; Cordes, D. B.; Slawin, A. M. Z.; Beljonne, D.; Warriner, S. L.; Olivier, Y.; Fuchter, M. J.; Zysman-Colman, E. An S-shaped double helicene showing both multi-resonance thermally activated delayed fluorescence and circularly polarized luminescence. *J. Mater. Chem. C* **2022**, *10*, 4861–4870.
- [72] Blok, P. M.; Dekkers, H. P. Discrimination between $3\pi\pi^*$ and $3n\pi^*$ states in organic molecules by circular polarization of phosphorescence. *Chem. Phys. Lett.* **1989**, *161*, 188–194.
- [73] Kubo, H.; Shimizu, D.; Hirose, T.; Matsuda, K. Circularly Polarized Luminescence Designed from Molecular Orbitals: A Figure-Eight-Shaped [5]Helicene Dimer with D₂ Symmetry. *Org. Lett.* **2020**, *22*, 9276–9281.
- [74] Kubo, H.; Hirose, T.; Nakashima, T.; Kawai, T.; Hasegawa, J.-y.; Matsuda, K. Tuning Transition Electric and Magnetic Dipole Moments: [7]Helicenes Showing Intense Circularly Polarized Luminescence. *J. Phys. Chem. Lett.* **2021**, *12*, 686–695.
- [75] Zinna, F.; Giovanella, U.; Bari, L. D. Highly Circularly Polarized Electroluminescence from a Chiral Europium Complex. *Adv. Mater.* **2015**, *27*, 1791–1795.
- [76] Zinna, F.; Pasini, M.; Galeotti, F.; Botta, C.; Di Bari, L.; Giovanella, U. Design of Lanthanide-Based OLEDs with Remarkable Circularly Polarized Electroluminescence. *Adv. Funct. Mater.* **2017**, *27*, 1603719.

- [77] Wu, Z.-G.; Yan, Z.-P.; Luo, X.-F.; Yuan, L.; Liang, W.-Q.; Wang, Y.; Zheng, Y.-X.; Zuo, J.-L.; Pan, Y. Non-doped and doped circularly polarized organic light-emitting diodes with high performances based on chiral octahydro-binaphthyl delayed fluorescence luminophores. *J. Mater. Chem. C* **2019**, *7*, 7045–7052.
- [78] Chen, S. H.; Katsis, D.; Schmid, A. W.; Mastrangelo, J. C.; Tsutsui, T.; Blanton, T. N. Circularly polarized light generated by photoexcitation of luminophores in glassy liquid-crystal films. *Nature* **1999**, *397*, 506–508.
- [79] Zhang, D.-W.; Li, M.; Chen, C.-F. Recent advances in circularly polarized electroluminescence based on organic light-emitting diodes. *Chem. Soc. Rev.* **2020**, *49*, 1331–1343.
- [80] Yashima, E.; Ousaka, N.; Taura, D.; Shimomura, K.; Ikai, T.; Maeda, K. Supramolecular Helical Systems: Helical Assemblies of Small Molecules, Foldamers, and Polymers with Chiral Amplification and Their Functions. *Chem. Rev.* **2016**, *116*, 13752–13990.
- [81] Kulkarni, C.; van Son, M. H. C.; Di Nuzzo, D.; Meskers, S. C. J.; Palmans, A. R. A.; Meijer, E. W. Molecular Design Principles for Achieving Strong Chiroptical Properties of Fluorene Copolymers in Thin Films. *Chem. Mater.* **2019**, *31*, 6633–6641.
- [82] Zhao, B.; Pan, K.; Deng, J. Intense Circularly Polarized Luminescence Contributed by Helical Chirality of Monosubstituted Polyacetylenes. *Macromol.* **2018**, *51*, 7104–7111.
- [83] Zhao, B.; Pan, K.; Deng, J. Combining Chiral Helical Polymer with Achiral Luminophores for Generating Full-Color, On-Off, and Switchable Circularly Polarized Luminescence. *Macromol.* **2019**, *52*, 376–384.
- [84] Oda, M.; Nothofer, H. G.; Lieser, G.; Scherf, U.; Meskers, S. C.; Nether, D. Circularly polarized electroluminescence from liquid-crystalline chiral polyfluorenes. *Adv. Mater.* **2000**, *12*, 362–365.

Bibliography

- [85] Lee, D. M.; Jung, J. H.; Kang, B. J.; Cho, Y.; Yu, C. J.; Kim, J. H. Luminance Enhancement of the OLED by Direct Emission of Circular Polarization. *SID DIGEST* **2018**, *49*, 1835–1837.
- [86] Baek, K.; Lee, D. M.; Lee, Y. J.; Choi, H.; Seo, J.; Kang, I.; Yu, C. J.; Kim, J. H. Simultaneous emission of orthogonal handedness in circular polarization from a single luminophore. *Light Sci. Appl.* **2019**, *8*.
- [87] Di Nuzzo, D.; Kulkarni, C.; Zhao, B.; Smolinsky, E.; Tassinari, F.; Meskers, S. C.; Naaman, R.; Meijer, E. W.; Friend, R. H. High Circular Polarization of Electroluminescence Achieved via Self-Assembly of a Light-Emitting Chiral Conjugated Polymer into Multidomain Cholesteric Films. *ACS Nano* **2017**, *11*, 12713–12722.
- [88] Wade, J. et al. Natural optical activity as the origin of the large chiroptical properties in pi-conjugated polymer thin films. *Nat. Commun.* **2020**, *11*, 6137.
- [89] Geng, Y.; Trajkovska, A.; Culligan, S. W.; Ou, J. J.; Chen, H. M.; Katsis, D.; Chen, S. H. Origin of Strong Chiroptical Activities in Films of Nonfluorenes with a Varying Extent of Pendant Chirality. *J. Am. Chem. Soc.* **2003**, *125*, 14032–14038.
- [90] Yang, Y.; Da Costa, R. C.; Smilgies, D. M.; Campbell, A. J.; Fuchter, M. J. Induction of circularly polarized electroluminescence from an achiral light-emitting polymer via a chiral small-molecule dopant. *Adv. Mater.* **2013**, *25*, 2624–2628.
- [91] Li, T. Y.; Jing, Y. M.; Liu, X.; Zhao, Y.; Shi, L.; Tang, Z.; Zheng, Y. X.; Zuo, J. L. Circularly polarised phosphorescent photoluminescence and electroluminescence of iridium complexes. *Sci. Rep.* **2015**, *5*, 14912.
- [92] Albano, G.; Aronica, L. A.; Minotto, A.; Cacialli, F.; Di Bari, L. Chiral Oligothiophenes with Remarkable Circularly Polarized Luminescence and Electroluminescence in Thin Films. *Chem. - Eur. J.* **2020**, *26*, 16622–16627.

- [93] Morgenroth, M.; Scholz, M.; Cho, M. J.; Choi, D. H.; Oum, K.; Lenzer, T. Mapping the broadband circular dichroism of copolymer films with supramolecular chirality in time and space. *Nat. Commun.* **2022**, *13*, 210.
- [94] Jung, J. H.; Lee, D. M.; Kim, J. H.; Yu, C. J. Circularly polarized electroluminescence by controlling the emission zone in a twisted mesogenic conjugate polymer. *J. Mater. Chem. C* **2018**, *6*, 726–730.
- [95] Jung, J. H.; Lee, D. M.; Park, H. B.; Lee, Y. J.; Lee, G. D.; Yu, C. J.; Kim, J. H. An orthogonally polarized OLED for high brightness 3D display. *IDW/AD* **2016**, *2*, 1219–1222.
- [96] Wan, L.; Wade, J.; Shi, X.; Xu, S.; Fuchter, M. J.; Campbell, A. J. Highly Efficient Inverted Circularly Polarized Organic Light-Emitting Diodes. *ACS Appl. Mater. Interfac.* **2020**, *12*, 39471–39478.
- [97] Wan, L.; Wade, J.; Wang, X.; Campbell, A. J.; Fuchter, M. J. Engineering the sign of circularly polarized emission in achiral polymer – chiral small molecule blends as a function of blend ratio. *J. Mater. Chem. C* **2022**, *10*, 5168–5172.
- [98] Wan, L.; Liu, Y.; Fuchter, M. J.; Yan, B. Anomalous circularly polarized light emission caused by the chirality-driven topological electronic properties. **2022**,
- [99] Zhang, X.; Xu, Z.; Zhang, Y.; Quan, Y.; Cheng, Y. High brightness circularly polarized electroluminescence from conjugated polymer F8BT induced by chiral binaphthyl-pyrene. *J. Mater. Chem. C* **2020**, *8*, 15669–15676.
- [100] Yan, Z.-p.; Liao, K.; Han, H.-b.; Su, J.; Zheng, Y.-x.; Zuo, J.-l. Chiral iridium(III) complexes with four-membered Ir–S–P–S chelating rings for high-performance circularly polarized OLEDs. *Chem. Commun.* **2019**, *55*, 8215–8218.
- [101] Han, J.; Guo, S.; Wang, J.; Wei, L.; Zhuang, Y.; Liu, S.; Zhao, Q.; Zhang, X.; Huang, W. Circularly Polarized Phosphorescent Electroluminescence from

Bibliography

- Chiral Cationic Iridium(III) Isocyanide Complexes. *Adv. Optical Mater.* **2017**, *5*, 1700359.
- [102] Brandt, J. R.; Wang, X.; Yang, Y.; Campbell, A. J.; Fuchter, M. J. Circularly Polarized Phosphorescent Electroluminescence with a High Dissymmetry Factor from PHOLEDs Based on a Platinahelicene. *J. Am. Chem. Soc.* **2016**, *138*, 9743–9746.
- [103] Fu, G.; He, Y.; Li, W.; Wang, B.; Lu, X.; He, H.; Wong, W.-y. Efficient polymer light-emitting diodes (PLEDs) based on chiral [Pt(C-N)(N-O)] complexes with near-infrared (NIR) luminescence and circularly polarized (CP) light. *J. Mater. Chem. C* **2019**, *7*, 13743–13747.
- [104] Zinna, F.; Albano, G.; Taddeucci, A.; Colli, T.; Aronica, L. A.; Pescitelli, G.; Bari, L. D. Emergent Nonreciprocal Circularly Polarized Emission from an Organic Thin Film. *Adv. Mater.* **2020**, 2002575.
- [105] Zhang, X.; Zhang, Y.; Zhang, H.; Quan, Y.; Li, Y.; Cheng, Y.; Ye, S. High Brightness Circularly Polarized Organic Light-Emitting Diodes Based on Nondoped Aggregation-Induced Emission (AIE)-Active Chiral Binaphthyl Emitters. *Org. Lett.* **2019**, *21*, 439–443.
- [106] Wu, Z.-G.; Han, H.-B.; Yan, Z.-P.; Luo, X.-F.; Wang, Y.; Zheng, Y.-X.; Zuo, J.; Pan, Y. Chiral Octahydro-Binaphthol Compound-Based Thermally Activated Delayed Fluorescence Materials for Circularly Polarized Electroluminescence with Superior EQE of 32.6% and Extremely Low Efficiency Roll-Off. *Adv. Mater.* **2019**, *31*, 1900524.
- [107] Wang, Y.; Zhang, Y.; Hu, W.; Quan, Y.; Li, Y.; Cheng, Y. Circularly Polarized Electroluminescence of Thermally Activated Delayed Fluorescence-Active Chiral Binaphthyl-Based Luminogens. *ACS Appl. Mater. Interfac.* **2019**, *11*, 26165–26173.
- [108] Wang, Y.-f.; Lu, H.-y.; Chen, C.; Li, M.; Chen, C.-f. 1,8-Naphthalimide-based circularly polarized TADF enantiomers as the emitters for efficient orange-red OLEDs. *Org. Electron.* **2019**, *70*, 71–77.

- [109] Li, M.; Li, S. H.; Zhang, D.; Cai, M.; Duan, L.; Fung, M. K.; Chen, C. F. Stable Enantiomers Displaying Thermally Activated Delayed Fluorescence: Efficient OLEDs with Circularly Polarized Electroluminescence. *Angew. Chem. Int. Ed.* **2018**, *57*, 2889–2893.
- [110] Sharma, N.; Spuling, E.; Mattern, C. M.; Li, W.; Fuhr, O.; Tsuchiya, Y.; Adachi, C.; Bräse, S.; Samuel, I. D. W.; Zysman-Colman, E. Turn on of sky-blue thermally activated delayed fluorescence and circularly polarized luminescence (CPL) via increased torsion by a bulky carbazolophane donor. *Chem. Sci.* **2019**, *10*, 6689–6696.
- [111] Dhbaibi, K.; Abella, L.; Meunier-Della-Gatta, S.; Roisnel, T.; Vanthuyne, N.; Jamoussi, B.; Pieters, G.; Racine, B.; Quesnel, E.; Autschbach, J.; Crasous, J.; Favereau, L. Achieving high circularly polarized luminescence with push-pull heliogenic systems: From rationalized design to top-emission CP-OLED applications. *Chem. Sci.* **2021**, *12*, 5522–5533.
- [112] Qiu, Z.; Ju, C.-w.; Frédéric, L.; Hu, Y.; Schollmeyer, D.; Pieters, G.; Müllen, K.; Narita, A. Amplification of Dissymmetry Factors in π -Extended [7]- and [9]Helicenes. *J. Am. Chem. Soc.* **2021**,
- [113] Tanaka, H.; Inoue, Y.; Mori, T. Circularly Polarized Luminescence and Circular Dichroisms in Small Organic Molecules: Correlation between Excitation and Emission Dissymmetry Factors. *ChemPhotoChem* **2018**, *2*, 386–402.
- [114] Kourkoulos, D.; Patron, C.; Umbach, T. E.; Umbach, A. M.; Meerholz, K. Enhancing Light Outcoupling in Organic Light-Emitting Devices by Integration of Scattering Electrodes. *Phys. Status Solidi (A)* **2020**, *217*, 1–7.
- [115] Chen, H.-W.; Lee, J.-H.; Lin, B.-Y.; Chen, S.; Wu, S.-T. Liquid crystal display and organic light-emitting diode display: present status and future perspectives. *Light-Sci. Appl.* **2018**, *7*, 17168.
- [116] Schärftl, W. *Basic Physical Chemistry*, 1st ed.

Bibliography

- [117] Xiong, Y.; Peng, J. B.; Wu, H. B.; Wang, J. Improved performance of polymer light-emitting diodes with an electron transport emitter by post-annealing. *Chin. Phys. Lett.* **2009**, *26*, 097801/1–4.
- [118] Ghasemi, B.; Ševčík, J.; Nádaždy, V.; Végső, K.; Šiffalovič, P.; Urbánek, P.; Kuřitka, I. Thickness Dependence of Electronic Structure and Optical Properties of F8BT Thin Films. *Polymers* **2022**, *14*.
- [119] Full, J.; Panchal, S. P.; Götz, J.; Krause, A. M.; Nowak-Król, A. Modular Synthesis of Organoboron Helically Chiral Compounds: Cutouts from Extended Helices. *Angew. Chem. Int. Ed.* **2021**, *60*, 4350–4357.
- [120] Duong, S. T.; Fujiki, M. The origin of bisignate circularly polarized luminescence (CPL) spectra from chiral polymer aggregates and molecular camphor: Anti-Kasha's rule revealed by CPL excitation (CPLE) spectra. *Polym. Chem.* **2017**, *8*, 4673–4679.
- [121] Köhler, A.; Bässler, H. *Electric Processes in Organic Semiconductors*; Wiley-VCH: Weinheim, 2015.
- [122] Dias, F. B.; Maiti, M.; Hintschich, S. I.; Monkman, A. P. Intramolecular fluorescence quenching in luminescent copolymers containing fluorenone and fluorene units: A direct measurement of intrachain exciton hopping rate. *J. Chem. Phys.* **2005**, *122*, 054904.
- [123] Becker, K.; Lupton, J. M.; Feldmann, J.; Nehls, B. S.; Galbrecht, F.; Gao, D. Q.; Scherf, U. On-Chain Fluorenone Defect Emission from Single Polyfluorene Molecules in the Absence of Intermolecular Interactions. *Adv. Funct. Mater.* **2006**, *16*, 364–370.
- [124] Scandiucci de Freitas, P.; Scherf, U.; Collon, M.; List, E. J. W. (9,9-Dialkylfluorene-co-fluorenone) copolymers containing low fluorenone fractions as model systems for degradation-induced changes in polyfluorene-type semiconducting materials. *e-Polym.* **2002**, *2*, pp. 008.
- [125] Eakins, G. L.; Alford, J. S.; Tiegs, B. J.; Breyfogle, B. E.; Stearman, C. J. Tuning HOMO-LUMO levels: trends leading to the design of 9-fluorenone

- scaffolds with predictable electronic and optoelectronic properties. *J. Phys. Org. Chem.* **2011**, *24*, 1119–1128.
- [126] Hoogboom, J.; Rasing, T.; Rowan, A. E.; Nolte, R. J. LCD alignment layers. Controlling nematic domain properties. *J. Mater. Chem.* **2006**, *16*, 1305–1314.
- [127] Yashima, E.; Maeda, K.; Lida, H.; Furusho, Y.; Nagai, K. Helical polymers: Synthesis, structures, and functions. *Chem. Rev.* **2009**, *109*, 6102–6211.
- [128] www.echemi.com/produce/pr2207254662-r5011-right-99-kanbei.html, accessed on 20.02.2023.

Abbreviations

AL	alignment layer
BINOL	1,1'-bi-2-naphthol
CB	circular birefringence
CD	circular dichroism
CP	circularly polarised
CPL	circularly polarised light
CP-OLED	circularly polarised OLED
CROP	cationic ring-opening polymerization
DOS	density of energetic states
E_F	Fermi-level
EBL	electron blocking layer
<i>e.e.</i>	enantiomeric excess
EL	electroluminescence
EM	emitter material
EML	emissive layer
ETL	electron-transport layer
EQE	external quantum efficiency
F8BT	poly(9,9-dioctylfluorene- <i>alt</i> -benzo thiadiazole)
FMO	frontier molecular orbital

Bibliography

FRET	Förster resonance energy transfer
g	CPL dissymmetry factor
g_{max}	maximum g-value
g@maxEL	g _{EL} value at the wavelength of the EL spectrum maximum
g_w	g weighted EL spectrum
HIL	hole-injection layer
H1-Me₂	azabora[7]helicene
HOMO	highest occupied molecular orbital
HTL	hole-transport layer
HTM	hole-transport material
IQE	internal quantum efficiency
ITO	indium tin oxide ((In ₂ O ₃) ₉ (Sn ₂) ₁)
LC	liquid crystalline
LCP	left-handed circularly polarised
LP	linearly polarised
LPL	linearly polarised light
LUMO	lowest unoccupied molecular orbital
MM	<i>Müller matrix</i>
M_n	number average molecular mass
M_w	weight average molecular mass
OLED	organic light emitting diode
OPPI	(4-octyloxyphenyl) phenyliodonium hexafluoroantimonate

PDI	polydispersity index
PF	polyfluorene
PFO	poly(9,9-dioctylfluorene)
PI	polyimide
PL	photoluminescence
PLQY	photoluminescence quantum yield
qwp	quarter-wave plate (also written as $\lambda/4$ plate)
RCP	right-handed circularly polarised
RISC	reverse intersystem crossing
RT	room temperature
SVA	solvent vapour annealing
TADF	thermally activated delayed fluorescence
T_g	glass transition temperature
ThiahelalkBZT	π -extended [7]helicene
T_m	melting temperature
TPA	triphenylamine
VASE	variable angle spectroscopic ellipsometry
V_{on}	turn on voltage (defined here as operating voltage to achieve $L = 1 \text{ Cd/m}^2$)
w_i	weight fraction
x_i	molar fraction

Acknowledgment

The pursuit of knowledge is a winding road. And like any journey, it improves with company. I thank you, with whom I shared this path during the last four years, for your companionship, patience and support.

I am deeply indebted to my supervisor, Prof. Dr. Klaus Meerholz, for the opportunity to join his group. Thank you, Klaus, for your guidance and the view beyond the horizon. I was honoured to work in this atmosphere of creative freedom and trust, at a topic I fell in love with from the moment I switched on my first self-built OLED.

I would like to express my inmost gratitude to Prof. Dr. Arne Lützen, for accepting the position as second reviewer for this thesis. I appreciate the time investment and commitment this requires.

I am grateful for the funding received from Ti-DE and DFG.

This thesis would not have been possible without excellent materials. For the synthesis and characterisation of many of these materials, I would like to thank, in chronological order:

Dr. Michael Forster, Heinz-Georg Nothofer and Christin Barron in the working group of Prof. Dr. Ullrich Scherf, University of Wuppertal, for a multitude of chiral polyfluorenes.

Julian Full in the working group of Prof. Dr. Agnieszka Nowak-Król, University of Würzburg, for the helicene emitter H1-Me₂.

Dr. Hao Wu and Dr. Zijie Qiu under supervision of Prof. Dr. Klaus Müllen, for the helicene emitter ThiahelalkBZT.

I want to thank the "constants" of Team Meerholz, who made working in this team the best possible experience. I thank Dr. Dirk Hertel for his unique com-

Bibliography

ination of incredible know-how and deep understanding, and for always saying his mind. I'm grateful for the amazing support from Anne Berngen, Ruth Bruker, Kai-Uwe Fritz, Stephanie R uth and Tanja Tegender in the lab, and from Peter M uller and Petra Sablotny outside of the lab.

I salute my travel companions that reached the summit before me.

Steffi, thank you for your amazing support, but even more for the lovely tea talks.

I wish you all the best on your grand journey around the world.

Meike, thank you for leading me onto the path of tea, for long game nights in the face of evil, and most of all, for staying a great friend, even now.

Simon, thank you for the office talks about bikes and wine. Your presence always grounded me when things got stressful.

Flo, thank you for the quirky conversations and showing me a different side of life.

To the ones that follow on the same path, I hold out my hand.

Eva, thank you for your explosive energy and dedication. There is no one I enjoy freaking out and drinking some Weinchen with more. You motivate me to be better!

Lisa, thank you for dragging me through Cologne during my first bike ride in centuries, for delicious Belgian waffles, and for your lovely singing in the office. K-K-K-Kaktus!

Chris, thank you for the many passionate tips about everything green. Our smoking Gin and Tonic will always be the best.

Annemarie, to you, my padawan, I pass the circularly polarised torch. Thank you for the long days in the lab where you did great work. I enjoyed teaming up with you.

I want to thank Team Meerholz for the great atmosphere and for many long and short office talks. Your views on our projects and methods gave me invaluable scientific insights. But most of all, I thank you for the christmas baking, soup cooking, rage cage rampages, flask sharing during hikes, canoe crashes, and stories around the campfire. It was a pleasure to walk with you all, and I await your at the summit!

My deepest gratitude goes out to my family. To my parents, who held my hand from my first steps until today. To my favourite sister, who will achieve GREAT things! And to my partner, who appreciates me for all my quirks. You are my rock!

Eidesstattliche Erklärung

Hiermit versichere ich an Eides statt, dass ich die vorliegende Dissertation selbstständig und ohne die Benutzung anderer als der angegebenen Hilfsmittel und Literatur angefertigt habe. Alle Stellen, die wörtlich oder sinngemäß aus veröffentlichten und nicht veröffentlichten Werken dem Wortlaut oder dem Sinn nach entnommen wurden, sind als solche kenntlich gemacht. Ich versichere an Eides statt, dass diese Dissertation noch keiner anderen Fakultät oder Universität zur Prüfung vorgelegen hat; dass sie - abgesehen von unten angegebenen Teilpublikationen und eingebundenen Artikeln und Manuskripten - noch nicht veröffentlicht worden ist sowie, dass ich eine Veröffentlichung der Dissertation vor Abschluss der Promotion nicht ohne Genehmigung des Promotionsausschusses vornehmen werde. Die Bestimmungen dieser Ordnung sind mir bekannt. Darüber hinaus erkläre ich hiermit, dass ich die Ordnung zur Sicherung guter wissenschaftlicher Praxis und zum Umgang mit wissenschaftlichem Fehlverhalten der Universität zu Köln gelesen und sie bei der Durchführung der Dissertation zugrundeliegenden Arbeiten und der schriftlich verfassten Dissertation beachtet habe und verpflichte mich hiermit, die dort genannten Vorgaben bei allen wissenschaftlichen Tätigkeiten zu beachten und umzusetzen. Ich versichere, dass die eingereichte elektronische Fassung der eingereichten Druckfassung vollständig entspricht.



Claudia Dillmann, 19. März 2023

Die Primärdaten und Versuchsprotokolle dieser Arbeit liegen in mehrfacher Ausführung vor. Alle Rohdaten sind auf dem AK Meerholz Server gespeichert. Versuchsprotokolle und Auswertungen (Laborjournal) liegen dem AK Meerholz vor. Zusätzlich sind alle Rohdaten und Auswertungen bei mir gespeichert.

Bibliography

Journal Articles and Conference Contributions

Optimisation of Mixed System CP-OLEDs

Dillmann, C.; Berger, A.; Meerholz, K.

in preparation.

Impact of Truncation on Optoelectronic Properties of Azaborole Helicenes

Full, J.; Wildervanck, M.; Dillmann, C.; Panchal, S.; Volland, D.; Full, F.; Meerholz, K.; Nowak-Król, A.

Chem. Eur. J. **2023**, e202302808.


Development of a Circularly Polarized OLED (CP-OLED)


International Conference on Science and Technology of Synthetic Materials (ISCM), Glasgow, **july 2022**.



Claudia Dillmann

Personal Info

 born 05.06.1989
in Nürtingen, Germany

 c.dillmann@mailbox.org

Conferences and Awards

ISCM 2022, Glasgow
delegate speaker (07/22)
"Analysis and Optimisation of
different Circularly Polarised
OLED Systems"

BIGS Summer School, Bonn
speaker (08/19)
"Development of a CP-OLED"

Förderpreis Chemie 2019,
Cologne
finalist (06/19)

Work Experience

- Since 01/23 Research Scientist at **ZOEK gGmbH**,
Cologne
- 11/21 - 12/22 Strategic Project Support at
IMCD Germany, Cologne
- Since 10/12 Active and Reserve Officer of the
German Air force

Education

- 07.06.23 PhD **defense**
- 09/19 - 03/23 **PhD** in the group of Prof. Meerholz,
University of Cologne
"Optimisation and Analysis of a Circularly
Polarised Organic Light Emitting Diode
(CP-OLED)"
- 10/14 - 03/19 **Master of Science** Chemistry at
University of Cologne
"Photophysical properties and OLED
applications of new D-A-D type emitters"
- 10/09 - 09/12 **Bachelor of Science** Chemistry at
University of Stuttgart
"Influence of sugar and sugar-based
surfactants on enzyme catalyzed reactions"
- 08/99 - 07/08 **Abitur** at Max-Planck-Gymnasium,
Nürtingen
- 09/05 - 02-06 **Exchange Student** at Cascade Locks High
School and Mt. Hood Community College,
Oregon, USA
- 08/95 - 07/99 Friedrich Glück **Grundschule**,
Oberensingen